



Institute of Mechanics,
Materials & Civil Engineering

Processing and experimental micromechanics of Elium[®] thermoplastic composites

Sarah F. Gayot

Thesis submitted in partial fulfillment
of the requirements for the degree of
docteur en Sciences de l'Ingénieur

Dissertation committee:

Prof Hervé JEANMART, UCLouvain - President of the Jury

Prof Véronique MICHAUD, Ecole Polytechnique Fédérale de Lausanne (CH)

Dr Julie DIANI, Ecole Polytechnique (FR)

Pr Yentl SWOLFS, KULeuven (BE)

Dr Pierre GERARD, Arkema (FR)

Prof Bernard NYSTEN, UCLouvain

Prof Christian BAILLY, UCLouvain - Supervisor

Prof Thomas PARDOEN, UCLouvain - Supervisor

Version of 07/08/2023.

Acknowledgements

J'ai longtemps repoussé l'écriture de cette section, tant il me paraissait insurmontable de parvenir à remercier en quelques lignes l'ensemble des personnes ayant contribué au succès de cette thèse. Vous êtes si nombreux et vous m'avez tellement apporté – je voulais que l'hommage soit à la hauteur.

Aux membres de mon jury, j'aimerais tout d'abord dire combien j'ai apprécié les échanges que nous avons eus lors de ma défense privée. Merci pour vos commentaires constructifs et toujours bienveillants, qui ont permis d'aboutir à une meilleure version de ce manuscrit. Merci pour tout le temps que vous avez consacré à mon travail; c'est un honneur d'avoir pu vous le présenter.

A tous ceux qui ont joué pour moi le rôle de mentor au fil des années: Jawad Amokhtari, Sophie Rémy, Armand Lattes, Russell Bassindale, Ahmad Jiblaoui, Vincent Chaleix, Sandra Tavares, Lucien Bildstein et Frederik Van Loock. Je vous dois ma réussite professionnelle, vous qui avez cru en moi à ma place et m'avez donné la confiance nécessaire pour prendre le relais. Sans vous, je n'aurais sans doute ni repris mes études, ni réussi ma reprise d'études, ni osé sonner aux bonnes portes, ni même estimé avoir la légitimité pour le faire. A la manière des petits cailloux blancs du Petit Poucet, chacun d'entre vous m'a aidée à tracer une partie du chemin que j'ai emprunté.

Un grand merci à mes professeurs de collège et lycée qui m'ont donné le goût des sciences, mes professeurs d'université à Limoges et à Lille qui m'ont accompagnée dans la construction de mon projet de thèse, et à Marie-Josée Marti qui a porté la double casquette (peu commune) de directrice des études et maman de substitution lors de mon expatriation dans le Nord. On reconnaît les bons professeurs au nombre de petits frag-

ments d'eux qu'on emporte en fin d'année: une expression, une anecdote, une petite maniaquerie scientifique (dans mon cas, les chiffres significatifs et l'analyse dimensionnelle)...Merci d'avoir glissé toutes ces petites choses dans mes bagages d'étudiante.

A Christian Collette, Michel Glotin et Jean-Paul Moulin d'Arkema, j'aimerais exprimer toute ma reconnaissance pour leur confiance, leur humanité, leur simplicité et leur gentillesse. Grâce à vous, j'ai bénéficié des meilleures conditions possibles pour effectuer ma recherche, et je mesure pleinement l'ampleur de ce privilège. J'espère pouvoir continuer ma route à vos côtés, car je crois qu'Arkema est une entreprise comme il en existe peu.

Je remercie, du fond du cœur, les quatre personnes que je considère comme mes promoteurs de thèse (même si sur le papier seuls deux d'entre eux le sont): Thomas Pardoën, Christian Bailly, Bernard Nysten et Pierre Gérard. Grâce à vous qui m'avez maintes fois conseillée (mais aussi écoutée et rassurée), j'ai le sentiment d'avoir pu devenir une « vraie scientifique » malgré les obstacles rencontrés en chemin. Vous rendre fiers a toujours été un moteur et j'espère un jour pouvoir transmettre, à mon tour, un peu de ce que vous m'avez enseigné durant ces cinq années. Mention spéciale pour Aude Simar, qui m'a également beaucoup soutenue sur les plans professionnel et humain et mérite à ce titre le titre de promotrice *Honoris Causa* !

En tant que chercheuse, j'aimerais remercier l'ensemble du personnel administratif et technique du pôle IMAP (et plus largement de l'institut IMMC) ainsi que les équipes polymères et microscopie du pôle BSMA pour leurs compétences et leur dévouement au service de notre recherche. Vous êtes la version contemporaine des caryatides, ces statues grecques qui soutiennent les temples anciens - et les empêchent de s'effondrer. Nous avons tant de chance de vous avoir; merci de supporter nos visites impromptues, nos demandes farfelues, nos expériences mal foutues, nos erreurs, retards, urgences, oublis administratifs et autres questions idiotes (en tous cas en ce qui me concerne).

Merci à l'équipe Elium du GRL : Anne-Marie, Sylvie, Romane, la triplète des Pierres, Alex, Xavier, Henri, Gene, Sylvain et Christelle. Comme je vous l'ai récemment écrit, vous avez tous contribué au succès de cette thèse par vos conseils, votre aide, votre énergie et votre gentillesse - sans mentionner votre sens de l'humour. Je me réjouissais de chacune de

mes visites à Lacq, car je savais qu’au-delà du travail accompli ensemble, nous aurions aussi (surtout) l’occasion de nous retrouver. En commençant la thèse, j’étais loin d’imaginer que nous aurions le temps de développer de tels liens humains à l’occasion de mes courts séjours - et pourtant ce fut le cas. Votre soutien dans mes travaux de thèse, mais aussi face aux autres épreuves que j’ai dû affronter, resteront toujours bien au chaud dans ma tête et dans mon cœur.

Merci aux trois « grands frères de thèse » qui m’ont tant apporté professionnellement : Jérémy, qui m’a aidée à démarrer et a répondu à de nombreuses questions bêtes, Florent qui m’a aidée à terminer et a répondu à de nombreuses questions un peu moins bêtes, et bien sûr Fred qui m’a non seulement supervisée au quotidien pendant 18 mois et inculqué la rigueur scientifique qui me manquait, mais a surtout été un ami qui m’a motivée, coachée et fait tellement rire – et Dieu sait que j’en avais besoin pour oublier Matlab.

Et il y a bien sûr la « core team » d’IMAP : les fous du 2ème, Maïté, Charline, Catherine et Nathan, les non-moins-folles du 1^{er}, Sophinette et Marion, l’incroyable équipe « GD » constituée de Marc, Maxence, Bruno, Alban et John, et bien sûr ma Cécillette au Boltzmann. Vous m’avez offert une véritable seconde famille, dont l’affection et le soutien ont tout changé dans les moments difficiles – et rendu les (nombreux) bons moments encore plus beaux. Merci d’avoir fait de chaque jour au labo une vraie petite fête; grâce à vous je n’ai jamais eu l’impression d’aller travailler. Je remercie également tous mes collègues devenus amis, en particulier Mariia, Farzan, Vida, Sanjay, Matthieu L, Marie-Stéphane alias MS, Nelson, Audrey, Isabelle, Rania, Vincent, Pierre, Benoît, Jeroen, Mélanie et Delphine. J’adresse aussi un petit clin d’œil à mes compagnons de pause vapote au pied du Réaumur, Marco, Vanessa et Christophe, que je me réjouissais de croiser dehors malgré le froid, la pluie ou (plus rarement) les chaleurs caniculaires.

Merci à Pierre-Yves Gousenbourger, que je ne connais pas directement mais qui m’a gentiment permis d’utiliser son propre template LaTeX pour rédiger ma thèse. Si la mise en page qui va suivre vous plaît, sachez donc que je n’y suis absolument pour rien.

Merci aux sponsors non-officiels de ma thèse, qui s’ignorent sans doute : le Proxy Delhaize de la place des Wallons et ses sandwiches « triangle », le Pain Quot’ de Nivelles où j’ai souvent rédigé à grand

renfort de café, le Quick, la friterie « Chez Marielle » et le bar « La Bourse » à Nivelles – qui m’ont fourni les calories nécessaires pour faire tourner mon cerveau à plein régime, sans oublier le goéland de Galway qui m’a fait réfléchir à la notion de gaspillage alimentaire. Merci à La Pée, et merci à Microsoft PowerPoint aussi. On peut vraiment tout faire avec PowerPoint.

Plus sérieusement, j’aimerais à présent dire à mes parents, à mes sœurs Jeanne et Clara, à ma fille Esther et à mon mari Paul combien je les aime. Merci de m’avoir portée, que ce soit depuis ma naissance, depuis votre naissance, ou depuis notre rencontre sur les bancs de la fac. Papa, maman, je n’aurais pu avoir de meilleurs parents et je suis fière d’être votre fille. Cette réussite je vous la dois amplement, même si vous refusez souvent de l’admettre ! Merci de nous avoir tout donné, de m’avoir accompagnée dans toutes mes aventures, soutenue dans tous mes projets et toutes mes lubies, et surtout de m’avoir écoutée et aimée de façon inconditionnelle. Désormais « grand enfant » de 31 ans, j’ai toujours besoin de vous pour avancer au quotidien – et vous êtes là; pour moi, mais aussi pour votre petite-fille, que je veux aussi remercier (même si elle ne pourra lire ces lignes que dans quelques années). Ma Esthie, ta joie de vivre et ton courage nous ramènent sans cesse à l’essentiel, dont les petits tracas de la vie d’adulte nous détournent parfois. Si fragile mais pourtant si forte, tu nous as aidés, papa et moi, à devenir la meilleure version de nous-mêmes. A toi mon Paulo, je veux dire combien je me sens chanceuse de t’avoir à mes côtés, « pour le meilleur et pour le pire ». Il n’y a qu’avec toi que je me vois continuer à grandir et vieillir, car tu rends le meilleur encore meilleur et le pire franchement moins pire, car tu me fais rire comme personne, car j’adore parler avec toi d’absolument tout et d’absolument rien, car ensemble on fait les 400 coups, et car grâce à toi j’ai une alimentation un peu plus équilibrée (non je rigole, même si le fait que tu cuisines merveilleusement bien ne gâte rien). Merci pour ton soutien indéfectible pendant ces cinq années, pour toutes les heures passées à m’écouter me plaindre, pester, tout remettre en question, mais aussi à entendre le récit de mes petites victoires, à m’aider à répéter mes présentations et à relire mon manuscrit. Tout cela a beaucoup, beaucoup compté - cette thèse, c’est aussi un peu la tienne.

Je remercie aussi du fond du cœur la petite armée qui marche derrière notre famille depuis la naissance d’Esther, en plus de tous mes collègues : la team 24h vélo, mes chers amis Rowanne, Skyler, Marion, Yann, Linh,

Loki et Guix, mes petits anges gardiens tata Hélène et tata Françoise, ma mamie Jacqueline et tous mes cousin(e)s, ma belle-maman alias mamie Ninie et ma belle-soeur Charlotte, mes précieuses alliées Gaëlle et Cécile, les extraordinaires équipes Kites et EB de l'UZLeuven, le Pr Tennstedt, l'association Debra France et Belgique, ainsi que Kjetil et ses collègues de Nanomedic. Vous serez sans doute surpris de voir vos noms apparaître dans cette section; pourtant, vous avez joué un rôle crucial dans cette thèse en m'aidant à toujours garder le cap.

Enfin, je dédie cette thèse à ceux qui l'ont rendue possible: Armand Lattes et Christian Collette. A Christian, dont l'intelligence, la bienveillance et la simplicité nous manquent, j'aimerais exprimer toute ma gratitude et mon admiration pour ce que tu étais en tant que scientifique et en tant qu'être humain. Merci de m'avoir fait confiance et accueillie telle que j'étais, avec mon parcours atypique, ma sensibilité et mon vœu de suivre mon Paul en Belgique alors que vous aviez tant de partenariats académiques déjà bien établis par ailleurs. Merci d'avoir toujours répondu à mes mails comme s'ils étaient importants, alors que tu en recevais des centaines d'autres tous les jours dont les enjeux étaient autrement plus grands. A Armand, qui a suivi mes pérégrinations de ces douze dernières années avec toujours autant d'enthousiasme, je voudrais adresser les derniers « mercis » de cette section : merci d'avoir été le plus grand supporter de tous mes choix professionnels (même les plus farfelus), merci d'avoir ravivé ma passion pour la chimie après mes débuts chaotiques dans le supérieur, et merci de m'avoir recommandée à notre cher Christian au détour d'une conférence – il semble que cela ait plutôt bien fonctionné.

Contents

Contents	i
List of Figures	v
List of acronyms	xvii
1 Introduction	1
2 State of the art	11
2.1 A brief history of PMMA	11
2.2 Structure-property relationships in PMMA	13
2.3 The peculiar thermokinetics of MMA polymerisation	14
2.4 PMMA in composites: from dentures to wind turbines	15
2.5 Elium composites for wind energy: current state of the art	20
2.5.1 <i>The Elium polymer</i>	20
2.5.2 <i>Elium composites</i>	26
2.5.3 <i>Conclusions</i>	35
3 Top-down preliminary exercise on thick Elium composites	37
3.1 Introduction	38
3.2 Materials and experimental methods	38
3.2.1 <i>Materials</i>	38
3.2.2 <i>Preparation of composite specimens</i>	38
3.2.3 <i>Mechanical characterisation</i>	42
3.2.4 <i>Chemical analysis</i>	43
3.2.5 <i>Thermal analysis</i>	44
3.2.6 <i>2D and 3D imaging</i>	44
3.3 Results and discussion	45
3.3.1 <i>Thermal behaviour of the laminate during in-situ polymerisation</i>	45

3.3.2	<i>Characterisation of porosity patterns in the composite</i>	47
3.3.3	<i>Chain length distribution and residual monomer content in Elium</i>	50
3.3.4	<i>Thermal properties</i>	52
3.3.5	<i>Micromechanical response of the composite matrix</i>	55
3.3.6	<i>Influence of porosity on transverse compression response</i>	56
3.4	Conclusions	62
4	Thermokinetic behaviour of thick Elium laminates during in-situ polymerisation	65
4.1	Introduction	66
4.2	Materials and experimental methods	68
4.2.1	<i>Materials</i>	68
4.2.2	<i>Composite manufacturing</i>	69
4.2.3	<i>Composite characterisation</i>	71
4.3	Thermochemical model	72
4.3.1	<i>Theory</i>	72
4.3.2	<i>Numerical implementation of the model</i>	78
4.4	Results and discussion	79
4.4.1	<i>Infusion test results</i>	79
4.4.2	<i>Model calibration</i>	82
4.4.3	<i>Model validation based on temperature profile predictions</i>	84
4.4.4	<i>Conversion predictions</i>	85
4.4.5	<i>Processing maps</i>	88
4.5	Concluding remarks	92
4.6	Supplementary information	93
4.6.1	<i>Influence of diffusional effects on kinetic coefficients</i>	93
4.6.2	<i>Validity of the quasi-steady state approximation (QSSA) in the presence of diffusional effects</i>	97
4.6.3	<i>Characterisation of plate microstructure by X-ray tomography [1]</i>	98
5	4D-XCT monitoring of void formation in thick Elium composites produced by infusion	103
5.1	Introduction	104
5.2	Materials and experimental methods	106
5.2.1	<i>Materials</i>	106
5.2.2	<i>Miniature infusion setup</i>	106
5.2.3	<i>In-situ infusion experiment</i>	106
5.2.4	<i>XCT scanning parameters</i>	109
5.2.5	<i>Processing of XCT results</i>	110

5.3	Results and discussion	110
5.3.1	<i>Cross-sectional images of the composite specimen</i>	110
5.3.2	<i>Evolution of porosity</i>	113
5.3.3	<i>Evolution of void size</i>	116
5.3.4	<i>Assessment of dynamic scan uncertainty</i>	119
5.3.5	<i>Identification of void formation mechanisms</i>	120
5.4	Conclusions and perspectives	121
5.5	Acknowledgements	122
5.6	Appendix	123
6	Nanoscale digital image correlation at elementary fibre/matrix level in polymer-based composites	125
6.1	Introduction	126
6.2	Materials and experimental methods	130
6.2.1	<i>Manufacturing of composite specimens</i>	130
6.2.2	<i>Speckle pattern deposition</i>	132
6.2.3	<i>SEM imaging and in-situ compression testing</i>	132
6.2.4	<i>DIC data processing</i>	134
6.2.5	<i>Atomic force microscopy</i>	136
6.2.6	<i>Finite element modelling</i>	136
6.3	Results and discussion	138
6.3.1	<i>Optimisation and validation of the DIC method</i>	138
6.3.2	<i>DIC results</i>	144
6.4	Comparison to FE simulations	157
6.5	Conclusion	160
6.6	Acknowledgements	161
6.7	Appendix	161
7	Influence of physical ageing and fibre proximity on the local mechanical response of Elium	165
7.1	Introduction	166
7.2	Theoretical background	169
7.2.1	<i>Instrumented indentation techniques [101]</i>	169
7.2.2	<i>Linear mixed models [288] and confidence intervals in statistics</i>	172
7.3	Materials and methods	173
7.3.1	<i>Materials</i>	173
7.3.2	<i>Preparation of polymer and composite specimens</i>	173
7.3.3	<i>Micromechanical characterisation by nanoindentation and AFM</i>	175
7.3.4	<i>Statistical analysis of nanoindentation results</i>	179

7.4	Results and discussion	180
7.4.1	<i>Thickness and mechanical properties of the interphase region</i> .	180
7.4.2	<i>Influence of fibre proximity and physical ageing on nanoindentation properties</i>	183
7.4.3	<i>Comparison with PFT-QNM AFM measurements</i>	190
7.5	Conclusion	191
7.6	Acknowledgements	192
7.7	Supplementary information	192
7.7.1	<i>Sectioning diagram of composite plate</i>	192
7.7.2	<i>Polishing protocol for composite specimens</i>	193
7.7.3	<i>FE simulations of AFM and nanoindentation experiments near the fibre-matrix interface</i>	194
8	Conclusions and perspectives	203
8.1	General conclusions	203
8.1.1	<i>Mitigating porosity in Elium composites</i>	205
8.1.2	<i>Small-scale mechanical response of Elium matrix and interphase</i>	206
8.2	Recommendations for future work	207
9	Annexes	209
9.1	ANNEX 1: Macroscopic characterisation of Elium resins	210
9.1.1	<i>Materials and methods</i>	210
9.1.2	<i>Results and discussion</i>	211
9.1.3	<i>Tensile test results</i>	216
9.1.4	<i>Identification of Drucker-Prager model parameters</i>	217
9.2	ANNEX 2: Application for synchrotron beamtime	218
9.2.1	<i>Goal of the experiment</i>	218
9.2.2	<i>Background</i>	218
9.2.3	<i>Experimental method and specific requirements</i>	221
9.2.4	<i>Results expected</i>	223
9.2.5	<i>Estimate and justification of the beamtime</i>	223
	List of publications and awards	225
	Bibliography	227

List of Figures

1.1	Current obstacles met by the wind energy sector: (a) catastrophic blade failure event near Drumkeen, Ireland and (b) decommissioned blades being buried in a landfill in Wyoming, USA. Photo credit: (a) D. Doherty, 2016 and (b) B. Rasmussen, 2020.	2
1.2	Successful repurposing of wind turbine blades into (a) a bike garage in Denmark and (b) a children playground in the Netherlands. Photo credit: (a) D. Guzzo and (b) C. Yelland.	3
1.3	Thermoplastic blade manufactured as part of the ZEBRA project in 2022. Photo credit: ZEBRA consortium.	5
1.4	Lengthscales of interest in Chapters 4 to 7, as compared to those of a wind turbine blade composite structure.	8
2.1	From acrolein to methyl methacrylate.	12
2.2	Relationship between the molecular structure of PMMA and its physical properties at the macroscale.	14
2.3	Typical structure of a wind turbine blade. Adapted from [29].	16
2.4	Time evolution of offshore wind power generation capacity and blade rotor dimensions (with Belgian Atomium for scale). Data obtained from [37–42].	18
2.5	Influence of the chemical nature and amount of peroxide initiator on the polymerisation time of Elium at 105 °C, adapted from Zoller [71]. Both experimental measurements and model predictions are shown.	22
2.6	State of the art on unreinforced Elium resins. Colours indicate the level of completeness achieved in each field of study; green: comprehensive studies, orange: partially-investigated topics and red: gaps in the literature.	25

★ | List of Figures

2.7 Recycling glass fibre reinforced Elium composites by dissolution: (a) principle of the method and nature of recovered materials, and (b) comparison of ultimate tensile “mass-normalised force σ_{\max} ” values for virgin fibres *versus* fibres recycled by dissolution. Adapted from Cousins [44]. 26

2.8 Obande’s [84] work on the mechanical characterisation of glass fibre (GF) reinforced Elium and epoxy composites, including (a) comparison of static properties and (b) fractography images following Mode-I interlaminar fracture testing. 31

2.9 Void patterns observed in glass fibre reinforced Elium composites produced by infusion (a) at the ply level [51], and (b) through the thickness of a 25 mm laminate [98]. Red circles and yellow arrows have been added to Fig. (a) in order to indicate intra- and inter-tow voids, respectively. Note that only inter-tow voids are visible in Fig. (b). 34

2.10 State of the art on Elium composites. Colours indicate the level of completeness achieved in each field of study; green: comprehensive studies, orange: partially-investigated topics and red: gaps in the literature. 36

3.1 Experimental setup used for the vacuum infusion of plates A and B ($h = 73$ mm, $L = 60$ cm, $W = 40$ cm) with associated coordinate system. 39

3.2 (a) First sectioning diagram of composite plate samples, exemplified in the case of sample A, and (b) final sectioning diagram applied, from left to right, to subparts a to d, and associated nomenclature indicating specimen location with respect to the y and z -axes. Note that only a few specimens were labelled (in red) for the sake of clarity, the logic of numerotation should be self-obvious from the provided examples. 41

3.3 A speckled composite specimen after installation in the compression setup. 42

3.4 Temperature profiles recorded in plates A (dashed line) and B (full lines) during the in-situ polymerisation of Elium, at different locations along the y -axis. The grey-shaded area corresponds to temperature values equal to or exceeding the boiling point of MMA at atmospheric pressure, i.e. 101 °C. 46

3.5	Optical micrographs of (a) plate A and (b) plate B cross-sectional specimens extracted at various locations along the y -axis.	49
3.6	3D volume rendering of void patterns across the thickness of plate B in (from left to right) the bottom, middle and top third of the laminate, with associated porosity Φ	49
3.7	Molecular weight distributions determined by SEC for plates (a) A and (b) B at different locations across the thickness direction, alongside with the calculated values of \overline{M}_n , \overline{M}_w and I_p for each specimen.	50
3.8	Weight percentage of residual MMA in Elium along the y -axis of plates A (grey) and B (red). Each bar plot is obtained by averaging the results of two analyses, whose values are displayed via the error bars.	51
3.9	Variation of the glass transition temperature T_g of a PMMA/MMA mixture as a function of the mass fraction ω_p of PMMA, adapted from Fontanier [46]. The dashed and full black lines respectively indicate the crystallisation and melting temperatures of MMA.	54
3.10	Elastic modulus and hardness of the Elium matrix measured by nanoindentation along the y -axis of (a), (c) plate A and (b), (d) plate B, respectively.)	55
3.11	Stress-strain curves obtained from the transverse compression testing of composite specimens extracted from plates (a) A and (b) B.	57
3.12	Vertical strain ε_y fields obtained from the DIC analysis of plate B specimens c_{11} , c_{31} and c_{51} , from bottom to top. Arrows and ellipses respectively indicate areas of high strain concentration within and between fibre tows. Yellow and blue ellipses are used to distinguish acute ($\varepsilon_y \geq 0.1$) from more diffuse ($0.05 \leq \varepsilon_y < 0.1$) strain localisation phenomena.	59
3.13	Definition of fibre and void orientation in the work of Becker and Hopmann [111]. Aspect ratio α is defined as a_2/a_1 . Directions 2 and 1 respectively correspond to the y - and z -axes for plate A and the y - and x -axes for B, see section 3.2.2.	61
3.14	Evolution of the Young's modulus E of the Elium composite in transverse compression with porosity Φ , as measured experimentally <i>versus</i> as predicted from Voigt (full line) and B-H models (dashed lines) for several values of void aspect ratio α	61

★ | List of Figures

4.1 Experimental setup for the vacuum infusion of laminates of variable thickness c_1 ($L = 60$ cm, $W = 40$ cm). 69

4.2 Heating mould temperature T_m versus process time t for test conditions A, B and C, where T_{ext} denotes the ambient temperature, T_p ($= 50$ °C) the mould set temperature, t_1 (≈ 25 min) the end of the infusion stage, t_2 (≈ 75 min) the end of the heating ramp, and t_3 (≈ 105 min) the end of the temperature plateau at $T_m = T_p$ 70

4.3 Sectioning diagram for the characterisation of plates A and B ($L = 60$ cm, $W = 40$ cm, $c_1 = 73$ mm). 71

4.4 Boundary conditions used in the 1D thermochemical model. Note that c_1 refers to preform thickness ($c_1 = 49$ mm for condition C and $c_1 = 73$ mm for conditions A and B) and c_2 is the thickness of the mould ($c_2 = 15$ mm). The time-dependent temperature profile applied at node $y = -\delta y$ for testing conditions B and C is given in Fig. 4.2). 79

4.5 Dependence of the measured porosity Φ upon measurement height for plates A and B ($c_1 = 73$ mm). Note that measurement height is defined via the sectioning numbers given in Fig. 4.3. 80

4.6 Measured temperature T_t as a function of process time t at different locations across the thickness of (a) plates A and B and (b) plates B and C. See Table 4.1 for the y -coordinate corresponding to each measurement location. 80

4.7 Model identification by making use of the measured temperature profiles in plate B: predicted (solid lines) and measured (dashed lines) temperature T_t as a function of process time t at different locations across the thickness of the plate. See Table 4.1 for the y -coordinate corresponding to each measurement location. 83

4.8 Predicted values of k_p , k_t , and f as a function of monomer conversion χ by the calibrated model during the in-situ polymerisation of the MMA-based resin at the bottom of plate B ($y \approx 0.06c_1$). Four conversion regimes are identified. 84

4.9 Predicted (solid lines) and measured (dashed lines) temperature T_t as a function of process time t at different locations across the thickness of (a) plate A and (b) plate C. See Table 4.1 for the y -coordinate corresponding to each measurement location. 85

- 4.10 Predicted degree of monomer conversion χ as a function of process time t for (a) plate A, (b) plate B and (c) plate C. See Table 4.1 for the y -coordinate corresponding to each measurement location. 87
- 4.11 Predicted maximum temperature in the preform during polymerisation, T_{\max} , as a function of (a) mould set temperature T_p for selected values of preform thickness c_1 ($\dot{q} = 0.5 \text{ }^\circ\text{C}\cdot\text{min}^{-1}$ and $T_{\text{ext}} = 25 \text{ }^\circ\text{C}$) (b) heating rate \dot{q} for selected values of c_1 ($T_p = 50 \text{ }^\circ\text{C}$, $T_{\text{ext}} = 25 \text{ }^\circ\text{C}$) and (c) ambient temperature T_{ext} for selected values of c_1 (for $\dot{q} = 0$). Manufacturing conditions corresponding to tests A and B are included. 89
- 4.12 Processing maps for the in-situ polymerisation of an MMA-infused thick glass fibre preform: (a) mould set temperature T_p as a function of preform thickness c_1 with predicted $T_{\max} = 101 \text{ }^\circ\text{C}$ boundaries for selected values of heating rate ($T_{\text{ext}} = 25 \text{ }^\circ\text{C}$) and (b) mould set temperature T_p as a function of c_1 with predicted $T_{\max} = 101 \text{ }^\circ\text{C}$ boundary and contours of equal values of peak time t_{peak} for $\dot{q} = 1 \text{ }^\circ\text{C}\cdot\text{min}^{-1}$ and $T_{\text{ext}} = 25 \text{ }^\circ\text{C}$ 90
- 4.13 Processing map of optimum (minimum) process time t_{opt} versus preform thickness c_1 for selected values of heating rate \dot{q} ($T_{\text{ext}} = 25 \text{ }^\circ\text{C}$). The methods to determine the boundaries between regimes I, II and III are detailed in the text. 92
- 4.14 Predicted value of τ_1/τ_2 as a function of monomer conversion χ by the calibrated thermochemical model during the in-situ polymerisation in the middle of plate B ($y \approx 0.50c_1$). Four conversion regimes are identified, see Fig. 4.8 of the manuscript. The grey area highlights the monomer conversion range for which $\tau_1/\tau_2 < \bar{\tau}_{\text{crit}}$ 98
- 4.15 Sectioning diagram for the characterisation of plates A and B ($L = 60 \text{ cm}$, $W = 40 \text{ cm}$, $c_1 = 73 \text{ mm}$) by μCT 99
- 4.16 3D volume renderings of void patterns obtained from μCT across the thickness of plate A ($c_1 = 73 \text{ mm}$). 100
- 4.17 3D volume renderings of void patterns obtained from μCT across the thickness of plate B ($c_1 = 73 \text{ mm}$). 101

★ | List of Figures

5.1 Design of the miniature infusion setup, inspired from [190, 191]: (a) structure and dimensions in mm, (b) simplified side view of the setup and preform during XCT scanning and (c) 3D view of the setup installed in the CT chamber. The red rectangle indicates preform location. 107

5.2 Front (left picture) and back (right picture) views of the infusion setup after installation in the CT chamber. 108

5.3 Reconstructed xz slices obtained from dynamic scans 1 to 5 at $y = w/2$. Red boxes indicate areas where void patterns noticeably change compared to the same area of the previous scan. 111

5.4 Reconstructed xz slices obtained from dynamic scans 6 to 60 at $y = w/2$. Red boxes indicate areas where void patterns noticeably change compared to the same area of the previous scan. 112

5.5 Sectioning method applied to the FOV for porosity calculation, exemplified on the 3D rendering of the voids obtained from scan 51. The four resulting sub-volumes are depicted with different colours for easier visualisation. 113

5.6 Variation of the average porosity Φ (and corresponding Pearson's standard deviation) over the volume of interest and evolution of the surface temperature T_{surface} as a function of dynamic scan number and scanning time. 3D volume renderings of the void patterns generated from dynamic scans 1 (top left) and 8 (top right) are also presented. 114

5.7 LT analysis of the voids determined from scans 1, 5, 9 and 51. The orange and red boxes respectively correspond to inter-ply voids and inter-tow void populations. Examples of these two categories of voids are shown, using boxes of the same colour, on a 2D xz cross-sectional image. 117

5.8 Projected pixel-by-pixel standard deviation map (right) between the xz cross-sectional images of scans 9 and 51 (left), obtained via the Z project tool of ImageJ. 118

5.9 LT analysis of the voids after cooling, determined from dynamic scanning (scan 51) *versus* static scanning. 119

6.1	Unidirectional composite specimens for in-situ transverse compression testing: (a) glass fibre-reinforced TP and (b) carbon fibre-reinforced TS. Fibre orientation is parallel to the z -axis and compression is performed in the x -direction. All dimensions are in mm.	130
6.2	Thermoplastic composite specimen mounted on microtest compression stage.	133
6.3	Optimisation of the speckle pattern for DIC measurements: SEM images of a (a) 2 nm, (b) 5 nm, (c) 10 nm, (d) 20 nm and (e) 50 nm-thick indium speckle deposited by e-beam evaporation onto Si wafers.	138
6.4	Particle size distribution of indium speckle patterns with target thicknesses of (a) 2 to 50 nm and (b) 2 and 5 nm.	139
6.5	Comparison of particle size distributions obtained for a 5 nm-thick indium speckle pattern deposited onto two different substrates: Si wafer vs. carbon fibre-reinforced TS composite. . . .	139
6.6	ROI for the quantification of the spatial and drift distortion amplitudes.	142
6.7	Horizontal displacement field measured by DIC: (a) without any correction, (b) after spatial correction and (c) after spatial and drift corrections.	143
6.8	Macroscopic load-displacement curves obtained from the in-situ compression testing and SEM micrographs of the corresponding ROIs used for DIC analysis of: (a) and (b) an RTM6/carbon fibre specimen and (c) and (d) an Elium/glass fibre specimen. Coloured arrows indicate the location of failure events observed within or close to the ROIs during testing, and the same colour code is used to show force-displacement values at these moments.	144
6.9	Strain maps and evolution of strain profiles across the carbon fibre-RTM6 matrix interface (white dashed line) obtained by DIC: (a),(c) along the x direction and (b),(d) along the xy direction.	146

6.10 Strain maps obtained by DIC in the Elium/glass fibre specimen along the x direction, (a) before 1st failure event and (c) before 2nd failure event, and along the xy directions (b) before 1st failure event and (d) before 2nd failure event, alongside with corresponding strain profiles across the fibre-matrix interface (white dashed line) in the (e) x and (f) xy directions. The terms '1st and 2nd cracks' refer to the failure events identified in Figure 6.8. 147

6.11 RTM6 – Post-mortem observations of the failed material surface: (a) general overview, (b) main crack, (c) fibre/matrix level interface failure, (d) zoom of the interface failure in (c). . 149

6.12 Elium – Post-mortem observations of the failed material surface: (a) general overview, (b) main cracks, (c) fibre/matrix level diffuse cracks and shear bands, (d) zoom of the cracks in (c). . 150

6.13 Comparison between initial and final (post-failure) images for two ROIs: RTM6 system (a) in initial state versus (b) after failure, and Elium system (c) in initial state versus (d) after failure. Note that the failure regions are highlighted by white ellipses, while the white arrows represent source of imperfection for the DIC analysis. 151

6.14 RTM6 - Horizontal ϵ_{xx} strain map at four different stages during the in-situ compression test until the last moment before failure: (a) at 600 N, (b) at 850 N, (c) at 1000 N and (d) at 1150 N. . 153

6.15 Elium - Horizontal ϵ_{xx} strain map at four different stages during the in-situ compression test until the last moment before failure: (a) at 500 N, (b) at 700 N, (c) at 1000 N and (d) at 1300 N. . 154

6.16 Evolution of the horizontal ϵ_{xx} strain along the three numbered profiles shown in Figures 6.14 and 6.15 at different stages during the in-situ compression test: (a) and (b) profiles 1 and 2 on RTM6, respectively; (c) profile 3 on Elium. An interphase of around 400 nm marked by the shaded area is visible for both systems. 155

6.17 Atomic force microscopy measurements obtained by PeakForce Tapping® on (a), (b) the RTM6/carbon fibre composite, and (c), (d) the Elium/glass fibre composite. DMT modulus maps are presented on Figures (a) and (c), while (b) and (d) show the evolution of the DMT modulus along two profiles extracted from each map. 156

6.18	RTM6 – Horizontal ϵ_{xx} strain field (a) measured by DIC versus (b) predicted by FEA using a continuum model, and (c) comparison of strain evolution along the white dashed profile for both DIC and FEA. (d), (e) and (f) show the equivalent in terms of shear strains ϵ_{xy}	157
6.19	Elium, before 2 nd failure event – Horizontal ϵ_{xx} strain field (a) measured by DIC versus (b) predicted by FEA using a continuum model, and (c) comparison of strain evolution along the white dashed profile for both DIC and FEA. (d), (e) and (f) show the equivalent in terms of shear strains ϵ_{xy}	159
6.20	Horizontal ϵ_{xx} strain field measured by DIC: (a) without any correction, (b) after spatial correction and (c) after spatial and drift correction.	162
6.21	Maximum shear γ_{max} strain fields obtained by DIC (a) in the RTM6/carbon fibre system and (b), (c) in the Elium/glass fibre system before 1 st failure event and before 2 nd failure event, respectively	163
7.1	Scanning electron micrograph of the polished surface of a fibre-reinforced Elium composite specimen after polishing, showing (1) intra-tow and (2) inter-tow matrix pocket morphology. . . .	176
7.2	(a) 2D DMT modulus image obtained by AFM in the intra-tow matrix pocket of the Elium composite with location of 1D profiles A and B, and evolution of (b) topography, (c) DMT modulus and (d) PF error values along profiles A and B.	181
7.3	Box plot distribution of interphase thickness values measured by PFT-QNM AFM in the intra-tow matrix pockets of the Elium composite. Whiskers indicate the minimum and maximum values of the distribution, excluding outliers which are depicted by circles. The box extends between the 25 th and 75 th percentiles, while the central horizontal line indicates the median value. . . .	183
7.4	Typical evolution of (a) E and (b) H values measured by nanoindentation in Elium as a function of the penetration depth h . Each colour represents one indent performed in the bulk polymer (i.e. condition(3)) at t_5	184

7.5 Box plot distributions of (a) E and (b) H values measured by nanoindentation in conditions (1), (2) and (3), for several values of the ageing time. Whiskers indicate the minimum and maximum values of each distribution, excluding outliers which are depicted by circles. Boxes extend between the 25th and 75th percentiles, while the central horizontal line indicates the median value. 186

7.6 Median differences (circles) and 95 % CIs (error bars) in (a) E and (b) H values, obtained from the pairwise comparison of nanoindentation datasets acquired at different aging times for the same measurement condition (i.e. (1), (2) or (3)). The grey dotted lines indicate variations of ± 5 or 10 % with respect to the average values of E , i.e. 5.3 GPa and H , i.e. 280 MPa. . . 188

7.7 Median differences (circles) and 95 % CIs (error bars) in (a) E and (b) H values, obtained from the pairwise comparison of nanoindentation datasets acquired in conditions (1), (2) and (3) at the same ageing time. The grey dotted lines indicate variations of ± 5 or 10 % with respect to the average values of E , i.e. 5.3 GPa and H , i.e. 280 MPa. 189

7.8 Histogram distribution and skew gaussian fit of DMT modulus values measured by AFM in intra-tow (condition (1)) versus inter-tow (condition (2)) composite matrix pockets at (a) t_0 and (b) t_5 191

7.9 Sectioning diagram for the micromechanical characterisation of the composite plate ($L = 60$ cm, $W = 40$ cm, $c = 73$ mm); the first cuboid was extracted close to $z = L/2$ and $x = W/2$. Note that infusion direction and fibre tow orientation were parallel to the z axis, see [4]. 193

7.10 2D axisymmetric FE models of AFM indentation with a spherical tip (left) and nanoindentation with a Berkovich tip (right) with boundary conditions. In this example, the contour plots show the Von Mises stress value at the end of loading. 195

7.11 Meshing parameters exemplified in the case of the nanoindentation model, with associated element size. The same meshing parameters were applied for the AFM indentation model with a 0.01 multiplication factor for element size (i.e. 5 nm become 0.05 nm). The edge seeding meshing method by element size was selected; yellow and red lines indicate uniform seeding while green indicates seeding by bias. 196

7.12	Examples of load P versus penetration depth h_{\max} curves obtained from the FE simulation of nanoindentation experiments for several values of the distance x to the closest fibre.	198
7.13	Nanoindentation response of the Elium polymer predicted by FE modelling: evolution of the (a) E/E_{∞} and (b) H/H_{∞} ratios as a function of x/h_{\max} , for two different values of the tip apex radius R . The blue dotted lines only serve as a guide for the eye. The red dashed lines at $E/E_{\infty} = 1$ and $H/H_{\infty} = 1$, respectively, correspond to completely unconstrained resin properties.	199
7.14	Examples of load P versus penetration depth h_0 curves obtained from the FE simulation of AFM indentation experiments for several values of the distance x to the closest fibre.	201
7.15	AFM indentation response of the Elium polymer predicted by FE modelling: evolution of the E/E_{∞} ratio as function of (a) x/h_0 and (b) x . The blue dotted lines only serves as a guide for the eye. The red dashed lines at $E/E_{\infty} = 1$ corresponds to completely unconstrained resin properties. An example of experimental measurement close to the fibre-matrix interface is depicted in Fig. (b) with a full yellow line.	202
9.1	Sectioning diagram of cylindrical tensile test specimens [268].	211
9.2	Compression tests results obtained for (a) Elium 188 XO and (b) Elium 191 OSA.	213
9.3	Evolution of the mean mechanical properties of Elium 188 XO (left) and 191 OSA (right) as a function of $\dot{\epsilon}$: (a), (b) Young's modulus E , (c), (d) peak yield stress σ_y and (e), (f) yield drop. Error bars represent standard deviation values.	214
9.4	Evolution of the fracture strain ϵ_f of Elium (a) 188 XO and (b) 191 OSA as a function of the true strain rate $\dot{\epsilon}$. Error bars represent standard deviation values.	215
9.5	Infusion setup used for the preliminary in-situ experiments: (a) simplified side-view of the mould with vacuum bag and (b) full rig within the XCT scanner.	219
9.6	Void patterns captured with the TESCAN UniTOM XL in Elium.	220
9.7	Proposed design for the new infusion setup, better suited for synchrotron experiments. Rotation axis along the vertical direction.	221

List of acronyms

AFM	Atomic force microscopy
BC	Boundary conditions
BHT	Butylated hydroxytoluene
BPO	Benzoyl peroxide
CFRP	Carbon fibre reinforced polymer
CI	Confidence interval
CSM	Continuous stiffness measurement
CT	Computed tomography
DCM	Dynamic contact module
DGEBA	Bisphenol A diglycidyl ether
DIC	Digital image correlation
DMA	Dynamic mechanical analysis
DMT	Derjaguin-Muller-Toporov
DSC	Differential scanning calorimetry
FE(A)	Finite element (analysis)
FOV	Field of view
FRP(C)	Fibre-reinforced polymer (composite)
GF	Glass fibre
GFRP	Glass fibre-reinforced polymer
HPLC	High-pressure liquid chromatography
IFSS	Interfacial shear strength
LCM	Liquid composite moulding
LT	Local thickness
MFH	Mean-field homogeneisation
MMA	Methyl methacrylate
MW	Molecular weight
PF	Peak force

★ | List of Figures

PFT-QNM	PeakForce Tapping [®] -Quantitative Nanomechanical Mapping
PID	Proportional-integral-derivative
PMMA	Poly(methyl methacrylate)
PS	Poly(styrene)
PVC	Poly(vinyl chloride)
PVD	Physical vapour deposition
QSSA	Quasi-steady state approximation
ROI	Region of interest
RT	Room temperature
RTM	Resin transfer moulding
SEC	Size exclusion chromatography
SEM	Scanning electron microscope
SLS	Swiss Light Source
TGA	Thermogravimetric analysis
THF	Tetrahydrofuran
TP	Thermoplastic
TS	Thermosetting/thermoset
UD	Unidirectional
UV	Ultraviolet
VARTM	Vacuum-assisted resin transfer moulding
VI	Vacuum infusion
XCT	X-ray computed tomography
ZEBRA	Zero waste blade research project

1

Introduction

Thermoplastic composites have gained growing interest since the 1990s as the limitations of their thermosetting counterparts started to emerge. In addition to their higher toughness, repairability, weldability and recyclability compared to thermosets, thermoplastic composites benefit from the extensive amount of literature published on thermoplastic polymers since the 1930s - constituting what polymer scientist F. Cogswell referred to as a *“quality assurance, because all the polymer chemistry has been done by those people whose business is polymer chemistry”*.

This combination of advantages did not go unnoticed to the wind energy sector, which largely relies on fibre-reinforced polymer composites for the production of wind turbine blades. In the context of the energy transition, blade manufacturers and wind farm operators are faced with two pressing matters: increasing blade length to boost power generation capacity, and improving their sustainability and environmental performances. Both technological challenges, which are illustrated by Figure 1.1, can be addressed - at least partially - by transitioning from thermosetting to thermoplastic composites for wind turbine blade manufacturing.

As turbine blades are getting longer and heavier in order to meet the soaring demand for renewable energy, they must support higher and more complex loads during their service life. The linear speed at blade tips also increases, exacerbating the detrimental impact of raindrop erosion or bird

1 | Introduction

collisions on the structural integrity of the blades. An average of 3,800 blade failure events are currently reported every year, among the 700,000 turbines in operation globally. Whatever the primary origin of the incident may be, e.g. via adhesive debonding of glued parts, buckling of the composite shell, fatigue cracking in regions of high stress concentration (such as the transition region between the blade root and the aerodynamic part, or areas containing manufacturing defects), the propagation of cracks is what ultimately leads to the catastrophic failure of the blade structure. With their superior toughness and damage tolerance properties, thermoplastic composites could be a material of choice for avoiding - or at least delaying - such incidents. The damping properties of thermoplastic polymers are also better than those of thermosets, which could *potentially* have a positive influence on the impact resistance of wind turbine blades during transportation, installation and operation.

Thermoplastic composites are also compatible with the “*reduce, repair, reuse, recycle*” motto of circular design. First, their weldable nature could, in theory, eliminate the need for adhesives in the blade assembly process.

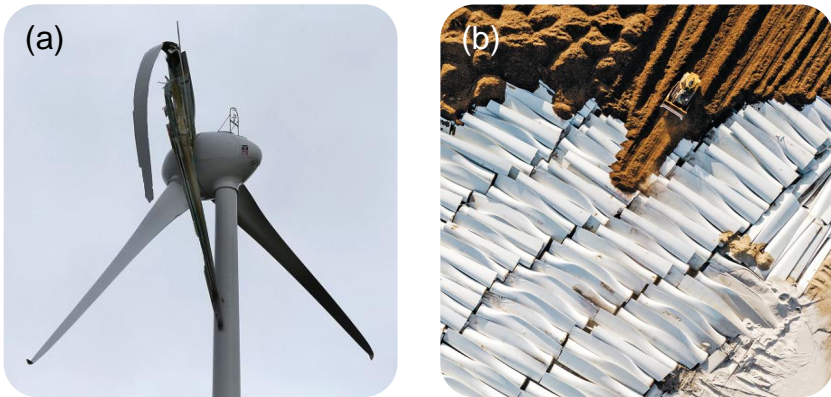


Fig. 1.1 Current obstacles met by the wind energy sector: (a) catastrophic blade failure event near Drumkeen, Ireland and (b) decommissioned blades being buried in a landfill in Wyoming, USA. Photo credit: (a) D. Doherty, 2016 and (b) B. Rasmussen, 2020.

Repairability is another non-negligible advantage of thermoplastic blades, which could contribute to extending their service life significantly. Wind turbine blade repurposing into, e.g., urban furniture, is already applied to thermosetting structures. However, innovative repurposing projects like those shown in Figure 1.2 are still very scarce. We can assume that the thermoformable nature of thermoplastic composites could widen the range of repurposing possibilities in the future. Last but certainly not least, thermoplastic blade structures may be efficiently recycled in a number of ways (see Chapter 2), unlike thermosetting blades which mostly end up in “graveyards” like that shown in Figure 1.1b. Some of the recycling routes envisioned for thermoplastic composites, e.g. solvolysis, could allow recovering nearly 100 % of the matrix and fibre materials without downgrading their properties.



Fig. 1.2 Successful repurposing of wind turbine blades into (a) a bike garage in Denmark and (b) a children playground in the Netherlands. Photo credit: (a) D. Guzzo and (b) C. Yelland.



Turning wind turbine blades into gummy bears

You read right. A research team at Michigan State University developed a novel thermoplastic resin system for wind turbine blade manufacturing...and found a peculiar way to recycle it. In a recent press release from the American Chemical Society, scientist J. Dorgan announced that after alkaline digestion of their new composite material, “[he] recovered food-grade potassium lactate and used it to make gummy bear candies, which [he] ate”. Fortunately or unfortunately, it might take a while before you can get these from your local supermarket.

The reason why the wind industry has not yet taken the leap towards thermoplastic blades is mostly technical. The high viscosity of molten thermoplastic polymers makes them incompatible with liquid moulding processes, among which vacuum infusion - the method of choice for manufacturing large composite structures reinforced with long fibres. On the other hand, asking wind turbine blade manufacturers to rethink their entire production process is not the best way to encourage the transition from thermosetting to thermoplastic matrices. The only viable option is therefore to adapt thermoplastic polymers to liquid moulding processing - not the other way round.

In this context, a low-viscosity monomer formula named Elium® has been developed by the French chemical company Arkema for the processing of continuous fibre-reinforced thermoplastic composites by liquid moulding. The methyl methacrylate-based monomer part is first mixed with a small amount of peroxide initiator, and infused into the composite preform (which usually consists of a glass or carbon fabric layup). After infusion, the monomer polymerises in-situ within the preform, resulting in a polymer close to poly(methyl methacrylate).

The development of Elium has significantly contributed to making thermoplastic wind turbine blades a reality, with the production of the first fully functional prototype in March 2022. The 62 m-long composite structure, which is shown in Figure 1.3, was designed and manufactured as part of the ZEBRA project (Zero wastE Blade ReseArch) launched in 2020 by IRT Jules Verne, France. ZEBRA brings together industrial partners involved in the wind energy sector: a wind farm operator (Engie), a blade manufac-

turer (LM Wind Power), a reinforcing fabric company (Owens Corning), a chemical company (Arkema), a research center specialising in composite materials (CANOE) and a provider of environmental services (Suez).

However, Elium remains a whole new resin system and as such must continue to prove its worth to the wind energy industry - which is used to working with thermosetting resins and trusts their properties as composite matrices. This involves catching up with the level of knowledge acquired on thermosetting composites since the late 1930s, e.g. in terms of thermo-mechanical properties throughout the scales, environmental and chemical resistance, but also formulation, processing and curing behaviour. This has, for the most part, been achieved in the past decade - but there is still work to do.



Fig. 1.3 Thermoplastic blade manufactured as part of the ZEBRA project in 2022. Photo credit: ZEBRA consortium.

Objectives

This thesis lies at the heart of the ongoing research effort directed towards manufacturing Elium-based composites, understanding the mechanisms occurring during processing and how these impact the structural behaviour of the parts under mechanical loading. Emphasis is placed on wind turbine blade shell manufacturing applications, which introduces specific challenges related to the unusually-large thickness of these structures (up to 10 cm in the blade root area).

1 | Introduction

Driven by concrete industrial needs, the thesis follows a dual objective, i.e. solving down-to-earth technological problems while filling some of the gaps remaining in the relevant literature.

From the industrial point of view, the main interest was to mitigate porosity in thick glass fibre-reinforced Elium laminates, which was consistent with an almost complete lack of literature with respect to the void formation mechanisms taking place in Elium composites. The first scientific question was thus easily identified:

Q1 - What are the mechanism(s) leading to void formation during the manufacturing of thick Elium composites by vacuum infusion? At which stage(s) of the process do they take place and what triggers them?

The literature review also revealed an overall lack of information with respect to the specific features of thick (i.e. more than a few mm) Elium composite parts, which gave rise to the second question:

Q2 - Does preform thickness have an influence on the homogeneity of Elium composite parts, during processing and with respect to their final properties?

Two other pending topics, identified in the literature and from discussions with Arkema, led to two additional questions oriented towards the more fundamental side of research, but essential to optimise both the manufacturing process and properties:

Q3 - What is the thermokinetic behaviour of Elium composites during in-situ polymerisation within a fibrous preform? Is it any different from what is already known about the bulk polymerisation kinetics of Elium?

Q4 - What is the mechanical response of Elium composites at the constituent level, i.e. at the micro- and nano-scales, including the fibre-matrix interphase region?

Outline

The thesis is divided into 8 chapters, including the present introduction (Chapter 1) as well as a general conclusion (Chapter 8).

Chapter 2 reviews the state of the art on Elium resins and Elium composites produced via liquid moulding. The focus is intentionally placed on Elium, as each of the following chapters contains a more specific literature review on their topic(s) of interest.

Chapter 3 presents a preliminary top-down study, conducted in the early months of the thesis [1, 2]. Two 7 cm-thick Elium composite plates, manufactured at different temperatures, are subjected to physical and chemical characterisation along the thickness direction. A link is established between preform thickness, processing temperature, thermokinetic behaviour during polymerisation and void formation through monomer boiling. The aforementioned scientific questions are refined accordingly.



The ordering of the four remaining chapters has not been selected randomly. As depicted in Figure 1.4, the lengthscale of interest in this bottom-up part of the thesis keeps going down as one proceeds through the manuscript, spreading from the macroscale in Chapter 4 down to the nanoscale in Chapters 6 and 7.

Chapter 4 follows on the findings from Chapter 3. A thermochemical model is developed for exploring the interaction between heat transfer and heat generation during the in-situ polymerisation of thick Elium laminates [3, 4]. The model, which is validated experimentally, captures the evolution of temperature and monomer conversion across the thickness for a variety of processing conditions. In each case, it allows predicting whether the monomer will boil within the preform, resulting in void formation.

Chapter 5 presents a miniaturised infusion experiment, designed for the in-situ monitoring of void formation in a 2 cm-thick laminate via X-ray computed tomography [5, 6]. Changes in void size, location and morphology are successfully captured during infusion, polymerisation and cooling of the composite. The corresponding void formation mechanisms are identified, and their relative contributions to the final porosity are quantified.

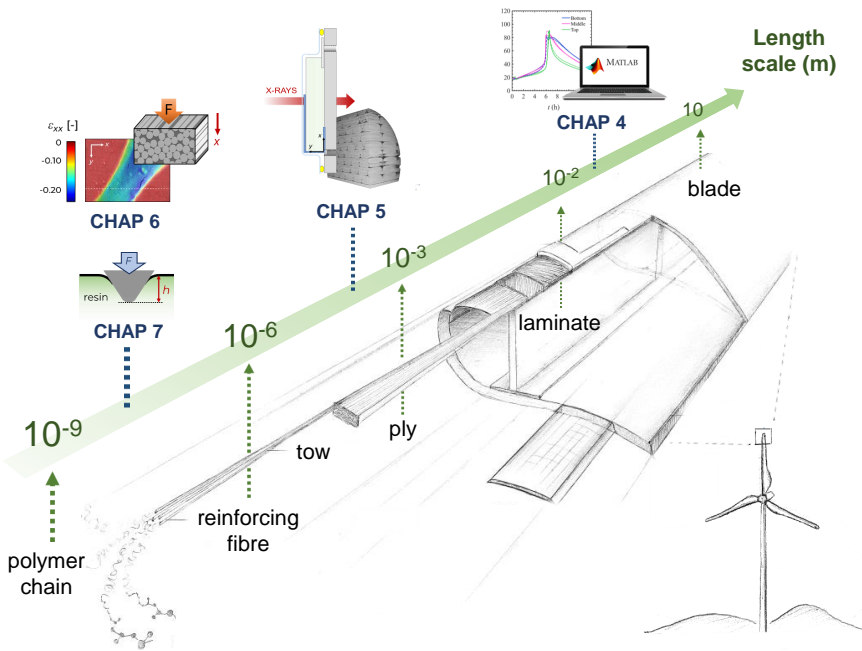


Fig. 1.4 Lengthscales of interest in Chapters 4 to 7, as compared to those of a wind turbine blade composite structure.

Chapter 6 focuses on the development and validation of a nanoscale digital image correlation method dedicated to composites [7]. Using the method, the deformation patterns occurring at the fibre level during transverse compressive loading are characterised in Elium and epoxy composite specimens. The presence of a fibre-matrix interphase is highlighted in both systems and confirmed by finite element simulation and atomic force microscopy. Differences are identified between the thermoplastic and thermosetting matrices in terms of nanoscale deformation and fracture behaviour.

Chapter 7 explores the local mechanical properties of the Elium matrix of a composite material, as compared to those of a bulk resin specimen of the same nature [8]. Small-scale indentation techniques, i.e. nanoindentation and atomic force microscopy, are used to probe matrix pockets as well as

the fibre-matrix interphase region. Finite element models of the two experiments are developed to verify that the measurements are not impacted by the nearby fibre material. The influence of physical ageing and matrix pocket size (i.e. distance to closest fibre) on the indentation response of the resin is assessed via statistical inference.



Different grades of Elium are mentioned throughout the text, namely **Elium 191 OSA** (Chapters 3, 4 and 7), **Elium 151 OSA** (Chapter 5) and **Elium 591** (Chapter 6).

All three formulas contain methyl methacrylate as the main ingredient and only reactive monomer, share the same solid content and give rise to a material close to poly(methyl methacrylate) after polymerisation regardless of the initiating system. They only differ in the formulation of their additive package, which mostly depends on the desired viscosity (0.1 Pa.s for infusion grades like 191 OSA and 151 OSA *versus* 0.5 Pa.s for pulsion grades like 591) and reactivity towards temperature (151 OSA has a much shorter pot life than 191 OSA and 591 under ambient conditions).

2

State of the art

This chapter presents the general state of the art with respect to Elixir resins, and their use as composite matrices in liquid composite moulding processes. Each of the following chapters contains a more specific literature review focusing on different topics of interest.

2.1 A brief history of PMMA

The story of acrylic monomers and polymers started in Central Europe in 1843, when Austrian chemist Josef Redtenbacher first synthesised acrylic acid from acrolein, a natural compound responsible for the acrid smell of burnt fat. Methacrylic acid was obtained from acrylic acid a few years later, and esterified into methyl methacrylate in 1865. Figure 2.1 shows the chemical formulas of acrolein and its derivatives, which all share an α,β -unsaturated carbonyl group. In 1873, German chemist Rudolph Fittig conducted the first lab-scale polymerisation of methyl methacrylate, paving the way for the modern chemistry of acrylic and methacrylic polymers. The industrial production of these compounds only started in the early 1900s, following the discovery of more efficient synthetic routes for acrylate and methacrylate monomers by German scientists Otto Röhm and Walter Bauer. Poly(methyl acrylate) was the first acrylic polymer to be commercialized in Germany, finding applications in the automotive indus-

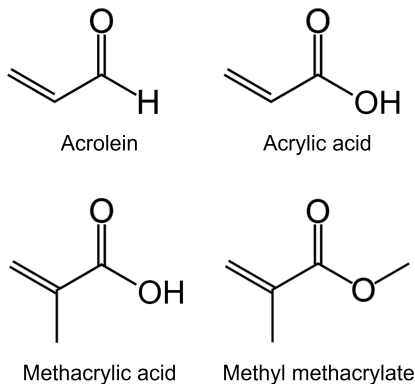


Fig. 2.1 From acrolein to methyl methacrylate.

try for the manufacturing of transparent, flexible and non-yellowing interlayers for safety glass. However, Röhm and Bauer understood that acrylic polymers were unsuitable for structural applications, due to their low glass transition temperature. Methacrylic polymers, on the other hand, were not only transparent but also hard and rigid at room temperature (while remaining easily machinable), and could be easily shaped at temperatures close to 100 °C. In 1933, they produced the first poly(methyl methacrylate) (PMMA) plate, and named this new material “Plexiglas” for its unique combination of physical properties. A decade later, it was also discovered that PMMA was along the very few polymers which could be depolymerised into monomer with a yield higher than 90 %, through a simple pyrolysis process [9, 10].

As the world geared up for war, demand for this new material boomed in the US and Germany as PMMA could be used for manufacturing lightweight military aircraft canopies and windows. By the end of the 1930s, it was already commercialised by several companies and under several tradenames: Plexiglas (Röhm and Haas), Perspex (ICI) and Lucite (DuPont). With the decline of PMMA sales at the end of the war, manufacturers redirected their efforts towards civil applications such as lighting cases for signs, lamp posts and car headlights. Another key asset of PMMA, biocompatibility, was also discovered at that time. During the medical follow-up of injured military pilots, physicians found intact shivers of PMMA coming from shattered aircraft canopies in the

eyes of some of their patients. This opened the door to a wide range of biomedical applications, in particular in the field of dental and bone prosthetics. In 1936, the company Kulzer patented the first mouldable cement for dentistry, made from ground PMMA powder mixed with methyl methacrylate (MMA) monomer. Similar products were used as bone cement in orthopaedics from 1945, e.g. for cranioplasties [11–13].

PMMA is now a widely-used commodity polymer, whose original applications in the transportation, construction, lighting and medical sectors are still relevant today. With the emergence of new information and communication technologies, the use of PMMA was extended to electronics (screen covers, LEDs, optical fibres) and, very recently, to the manufacturing of protective shields during the Covid-19 pandemic. The global PMMA market now reaches a few billion dollars each year and keeps expanding [14, 15].

2.2 Structure-property relationships in PMMA

Figure 2.2 shows how the key physical properties of PMMA mentioned above are direct consequences of the molecular structure of the polymer. Each alternating carbon atom in the polymer backbone bears two large side groups, which results in a high level of steric hindrance and yields the following properties at the macroscale:

- **Transparency to visible light:** Steric hindrance, combined with atacticity, completely prevent chain stacking (i.e. crystallisation), which makes atactic PMMA a 100 % amorphous polymer. Amorphous materials appear transparent as they cannot diffract nor scatter visible light, contrary to crystalline materials which appear opaque. The vast majority of thermoplastic polymers are semi-crystalline (including atactic ones, provided the side groups are small like in poly(propylene) or poly(vinyl chloride)), resulting in various levels of opacity.
- **Rigidity at ambient temperature:** The side groups mentioned above act as “chemical anchors”, making it difficult for polymer chains to slide along each other. More thermal energy is needed to initiate large-scale motion, resulting in a much higher glass transition temperature for methacrylic polymers (close to 100 °C) than for acrylic polymers (< 0 °C), which bears fewer side groups [14].
- **“Unzipping” potential:** PMMA is among the very few polymers whose

depolymerisation reaction occurs preferentially via a chain-end scission mechanism, releasing MMA monomer with a yield up to 98 % [16]. In this case, steric hindrance (especially due to the methyl group) prevents hydrogen abstraction (i.e. capture by a radical) from the polymer backbone, at the expense of hydrogen atoms present at the chain ends.

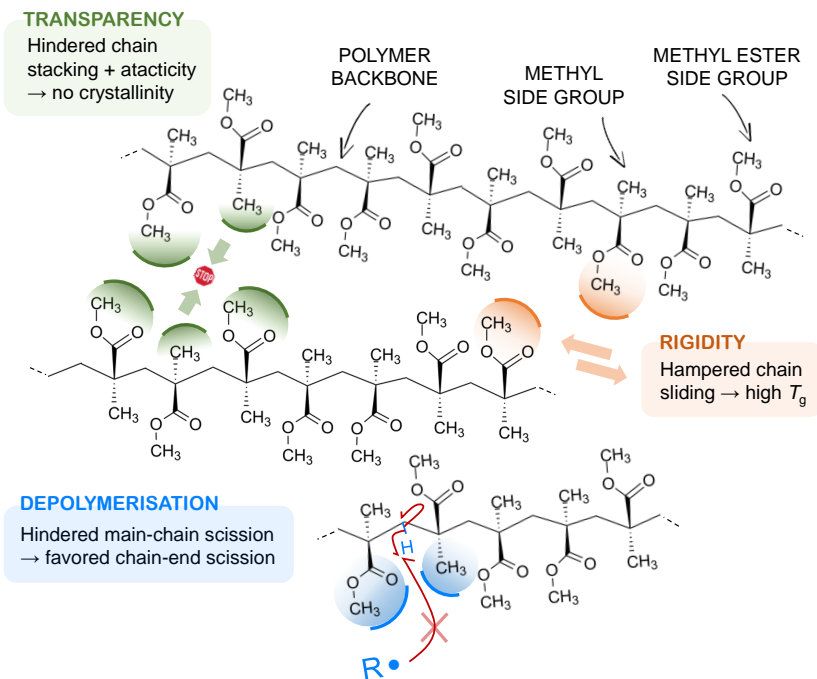


Fig. 2.2 Relationship between the molecular structure of PMMA and its physical properties at the macroscale.

2.3 The peculiar thermokinetics of MMA polymerisation

The thermokinetics of free-radical MMA polymerisation exhibits a very peculiar behaviour, which was first observed by Norrish and Brookman [17] in 1939:

“During the polymerization of methyl methacrylate it was found that after about 10-20 % polymerization there was a rapid increase in the rate of reaction. (...) This rapid rise in the rate of reaction was correlated with an increase in the temperature

of the reacting medium when the polymerizing methacrylate becomes a thick jelly and the heat of reaction cannot be carried away by convection."

This phenomenon, which is known as the gel effect (or Norrish [18] or Trommsdorff [19] effect), will be detailed in Chapters 3 and especially 4, alongside with the general kinetic development of free-radical polymerisation mechanisms. In short, a brutal drop in the diffusivity of the polymer radicals leads to an auto-acceleration of the polymerisation reaction, which manifests itself by a sharp temperature increase in the reaction medium. A few other vinyl monomers, like styrene, also experience the gel effect during polymerisation; however, the phenomenon is much more pronounced in the case of MMA (see e.g. [20]).

2.4 PMMA in composites: from dentures to wind turbines

The idea of using PMMA as a composite matrix has been around since the late 1980s, owing to the field of dentistry. Several patients were unhappy with the way their dental prostheses felt, due to the mismatch in thermal conductivity between PMMA and actual teeth. In 1989, Sehajpal tried to fill PMMA-based dental prostheses with metallic powders in order to improve their sensory properties [21]. The mechanical properties of PMMA prostheses also started to be questioned, especially in terms of fatigue (chewing) resistance. From the early 2000s, numerous attempts have been made to compound PMMA/MMA dental cements with mineral fillers, in particular ceramic particles, chopped fibres of all sorts and even carbon nanotubes [13, 22]. So far, cements reinforced with silanised glass fibres seem to demonstrate the best mechanical properties with respect to dental applications [22, 23].

Applications of PMMA composites could have remained limited to dentistry if carbon saving and waste management issues had not become increasingly pressing over the composite industry. Today, most structural composite parts are still being made from fibre-reinforced thermosetting polymers such as epoxy resins, which are not (or hardly) recyclable. Specific recycling routes are being explored for these materials, with variable technology readiness levels, efficiencies and costs. Most processes focus on retrieving the reinforcing material (long fibres) at the expense of the matrix part, which gets degraded by e.g. solvolysis or gaseification. Other processes rely on the shredding and full integration of used composites into

a new material, but involve severe downgrading of the composite properties. For these reasons, the vast majority of end-of-life thermosetting composite structures still end up in landfill, which is not acceptable anymore in the current environmental context [24–26].

The wind energy sector is particularly aware of this matter, as thermosetting composites account for more than two thirds of the weight of wind turbine blades [27]. Figure 2.3 provides a schematic view of a typical blade structure. Note that glass fibre reinforced composites (GFRPs) make up most of the outer shell including the blade root, while carbon fibre reinforced composites (CFRPs) are generally used as internal stiffeners. Blades have a service life ranging from 20 to 25 years [26], resulting in around 15,000 turbines worldwide being planned for decommission by 2024 [24]. As the global demand for renewable energy is soaring, these will be replaced by more powerful turbines, i.e. higher turbines equipped with longer blades [28]. Indeed, the power generated by a turbine is proportional to air density, area swept during rotation, as well as to the third power of wind speed. Air density and wind speed being mostly location-dependent (though a marginal increase in local wind speed can be achieved by increasing tower height), the preferred way to boost power generation is to extend the swept area, i.e. the blade length. This is illustrated by Figure 2.4, which shows the parallel evolution of offshore wind turbine rotor dimensions and power generation capacity over the last 30 years.

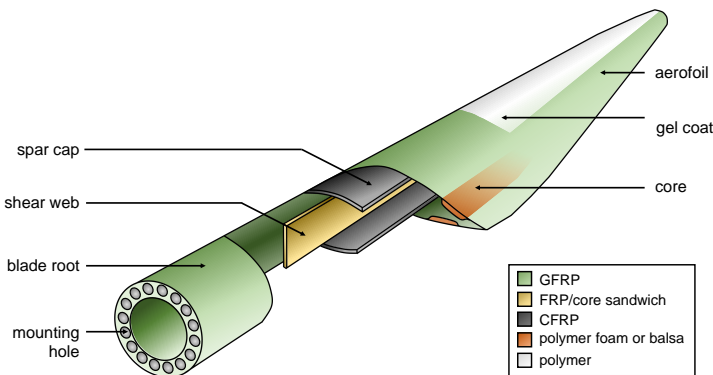


Fig. 2.3 Typical structure of a wind turbine blade. Adapted from [29].

Given this context, a complete change in paradigm is required to enhance the recyclability of future blade structures while maintaining at least the same level of mechanical performances. Additional efforts must be made to improve the overall sustainability of these materials by designing low-energy and low-toxicity manufacturing (and recycling) processes, while increasing repairability to extend service life. One way to achieve these goals is to transition from thermosetting to thermoplastic polymer matrices for the fabrication of wind turbine blades. First, this strategy allows recovering *both* the resin and reinforcing materials through a variety of recycling routes (see section 2.5.2). It also comes with another, non-negligible advantage: thermoplastic polymers can be welded together, potentially limiting the need for adhesive or bolted joints and thus resulting in further weight reduction [30–33].



The peculiar case of vitrimers

Vitrimers, which are reversible covalent polymer networks, have been first synthesised in the 2010s by Ludwik Leibler. This whole new category of polymers combines the processability and repairability of thermoplastics with the high performances of thermosets in terms of chemical resistance and thermomechanical properties. However, the development of vitrimer-based composites is still in its infancy.

Nowadays, around 50 % of polymer composites already consist of thermoplastic matrices [34]. These are mostly obtained through energy-intensive melt processing methods, which are not suitable for producing large parts as they rely on very powerful hydraulic presses [30, 35]. Instead, wind turbine blade manufacturing fully relies on liquid-state processing methods. While internal stiffeners are generally made by pultrusion, the outer shell of the blade (which comprises the aerofoil and blade root parts) is obtained via liquid composite moulding (LCM) methods such as vacuum infusion (VI), also known as vacuum-assisted resin transfer moulding (VARTM). This low-energy and low-cost process, which involves pulling a liquid resin through a fibrous preform using vacuum pressure, is the method of choice for manufacturing the outer shell of wind turbine blades [36].

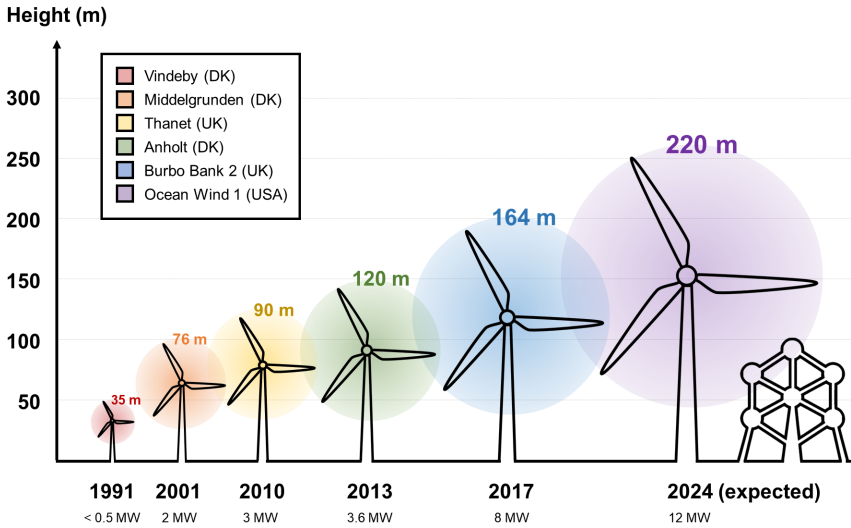


Fig. 2.4 Time evolution of offshore wind power generation capacity and blade rotor dimensions (with Belgian Atomium for scale). Data obtained from [37–42].

Prior to VI, the preform is enclosed in a tightly-sealed flexible bag and connected to the resin and vacuum lines so as to ensure complete impregnation of the fibre mats during infusion. The resin then undergoes a curing step, resulting in the final composite part [36]. Note that VI is preferred over another LCM process known as resin transfer moulding (RTM) for the preparation of large parts. RTM operates at pressures higher than the atmospheric pressure, i.e. the resin is pushed instead of pulled into the preform. This requires placing the preform into a closed mould during processing, resulting in much higher manufacturing and maintenance costs compared to VI.

The viscosity of liquid resin formulations used in LCM must lie between 0.1 and 1 Pa.s [43]. If the resin is too viscous, preform filling is hampered by excessive flow resistance; in the opposite case, proper fibre wetting is compromised [44]. LCM processes have long been dedicated to the processing of thermosetting composites, as various thermosetting monomers or oligomers have a viscosity close to 0.1 Pa.s allowing infusion followed by in-situ crosslinking within the preform. On the other hand, the very high viscosity of molten thermoplastics (which typically lies

in the 500-5,000 Pa.s range [36, 43]) makes them incompatible with LCM methods in their polymer state. However, some thermoplastic monomers or oligomers are fluid enough to enable processing by LCM. In this case, the final composite part is obtained through in-situ polymerisation of the monomer (or oligomer) instead of crosslinking, see e.g. [36, 44–46].

The idea of processing thermoplastic monomers by LCM dates back from the early 2000s [30, 45] but has not been implemented yet at the industrial scale due to a number of technical challenges. Cyclic monomers or oligomers were considered for their ability to polymerise without any by-product via an anionic ring-opening mechanism [36, 45, 46], following the work of Bank [45] on the LCM processing of cyclobutylene terephthalate oligomers. However, these systems have the major disadvantage of requiring high-temperature processing - between 140 and 250 °C - in order to reach a low-enough viscosity for infusion [36]. Note that the same applies to some *linear* thermoplastic polymer precursors, which were also considered though they require even higher processing temperatures (see e.g. the example of Fulcrum, a thermoplastic poly(urethane) precursor from Dow Chemical whose processing temperature reaches 270 °C [36, 47]). In parallel, anionic polymerisation mechanisms are sensitive to the presence of moisture (among other impurities), requiring the use of drastic processing conditions in order to avoid deactivation of initiator molecules [30]. Yet, the pioneering research team of van Rijswijk at TUDelft managed to produce the very first thermoplastic blade structure through VI and in-situ anionic polymerisation of epsilon-caprolactam into polyamide-6 in the early 2000s [30, 48, 49]. Despite the excellent mechanical properties of the obtained part, the scaling-up of the process was strongly hampered by the technical limitations mentioned above.

From the early 2010s, the French chemical company Arkema followed a similar approach as the team of TUDelft, ultimately leading to the development of Elium resins. These consist in a range of methyl methacrylate (MMA)-based monomer formulas, into which a small amount of organic peroxide initiator is added to trigger polymerisation. Elium formulas are fluid enough at ambient temperature to allow processing by LCM. After infusion, they polymerise through a free-radical polymerisation mechanism which is less sensitive to moisture than anionic pathways [44, 46, 50–54]. Among the numerous vinyl monomers able to polymerise via a free-radical mechanism, methyl methacrylate (MMA) was selected as the main constituent of Elium for its nearly-unique depolymerisation potential

(see section 2.2). This is a serious asset when it comes to the recyclability of PMMA-based composites, as depolymerisation should allow separating and recovering both high-purity MMA and full-length reinforcements [55, 56]. Moreover, recycled MMA obtained this way is similar to virgin MMA, meaning that it could – in theory – be polymerised and recycled again an infinite number of times.



Note that two early attempts at producing long-fibre composites from reactive MMA-based formulas had already been made before the creation of Elium in the early 1990s [57] and 2000s [58], as reported in [36]. These studies relied on pultrusion and manual prepregging processes, respectively, but did not result in any industrial application to our knowledge.

2.5 Elium composites for wind energy: current state of the art

The first mention of fibre-reinforced Elium composites in the literature dates back from 2015 [50, 59–62]. Since then, an increasing number of studies have been published on the topic every year, as described in the exhaustive review by Obande [63]. While most of the published work focused on the LCM applications of Elium composites, a few studies successfully explored alternative manufacturing routes such as pultrusion [64] or prepreg consolidation [65]. Unless specified otherwise, the work cited in this section deals with the Elium composites processed by LCM (in particular VI) with an emphasis on wind turbine blade shell applications.

2.5.1 The Elium polymer

Before using Elium as a composite matrix, the formulation of the liquid resin had to be adjusted in order to ensure compatibility with LCM processing in terms of rheology (before and during polymerisation) and reactivity (i.e. thermokinetic behaviour). The mechanical and thermal properties of the polymerised resin have only been marginally studied, as most authors consider Elium to be identical to PMMA after polymerisation.

Formulation of the monomer part and initiating system

Pure MMA has a viscosity close to 0.6 mPa.s at 25 °C [66], i.e. three orders of magnitude below the lower viscosity limit for allowing processing by

LCM. Before using Elium as a composite matrix, the formulation of the monomer part had to be adjusted. The strategy explored by Cousins [44] consisted in dissolving PMMA chains into MMA, which allowed benefiting from existing data on the rheological behaviour of PMMA/MMA syrups [67]. Cousins explored the influence of the concentration and molecular weight of the dissolved PMMA chains on the viscosity of PMMA/MMA syrups in the absence of polymerisation reaction. Several of the tested formulas allowed reaching a viscosity close to 0.15 Pa.s at ambient temperature. However, despite having the same initial viscosity, the selected formulas exhibited different thermokinetic behaviours during polymerisation. Beyond validating the use of PMMA chains as a suitable viscosifying agent for the Elium monomer, the work of Cousins revealed that these could also be used to change the course of the polymerisation reaction by, e.g. limiting and/or delaying exothermicity [44].

Other minor attempts were made at modifying the formulation of the Elium monomer, either for improving the processibility of the resin (e.g. by reducing unwanted MMA evaporation during preparation and handling [51]) or enhancing the thermal, chemical and/or mechanical properties of the Elium polymer (e.g. by adding exotherm control agents [68], co-monomers of a different nature [46] or acrylic block co-polymers [69, 70]).

Finally, various peroxide-based initiating systems were considered for triggering the in-situ polymerisation of MMA. To this end, the influence of initiator content and processing temperature on, e.g., the polymerisation rate, exothermicity pattern and polymer chain length distribution was extensively characterised and/or modelled for several systems [44, 46, 51, 62, 71–73]. Note that beyond relying on common, commercially-available peroxide initiators, some authors like Zoller [62, 71] studied more complex initiating systems, obtained e.g. by adding dedicated catalysts to the MMA monomer formula [74]. The purpose of such studies was to offer a wide range of Elium resins and initiating systems with different levels of reactivity with respect to temperature, which composite manufacturers could choose from depending on the desired application. As an example, Figure 2.5 illustrates how the polymerisation time (at a given temperature, here 105 °C) can be modified by several orders of magnitude by changing the chemical nature and amount of peroxide initiator [71].

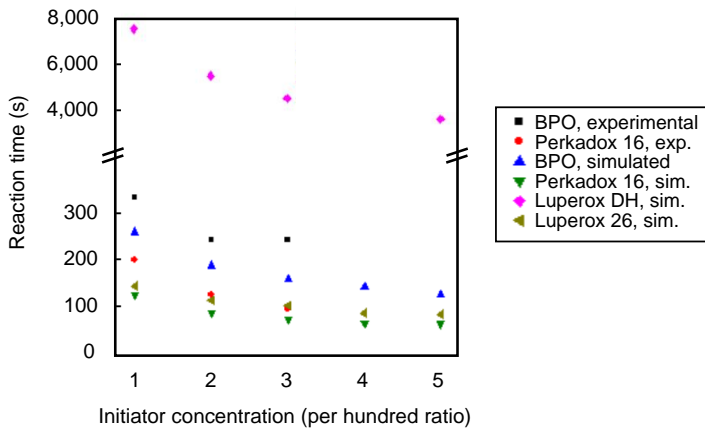


Fig. 2.5 Influence of the chemical nature and amount of peroxide initiator on the polymerisation time of Elium at 105 °C, adapted from Zoller [71]. Both experimental measurements and model predictions are shown.

More importantly, the work of Zoller [62, 71] also helped address an unmet need from the wind industry (and other industry sectors producing large composite parts) by providing the first infusion-grade resin able to polymerise without external heating.

Mechanical and thermal properties of Elium polymers

Whatever the grade of Elium considered for LCM applications, the monomer part consists of approximately 80 wt% MMA, the remaining 20 wt% being additives - in particular dissolved PMMA chains as mentioned above. In theory, the material obtained after polymerisation should be close - if not identical - to PMMA with respect to physical and chemical properties. Hence, in most cases, the authors working with Elium composites implicitly or explicitly assume all Elium matrices to behave like regular PMMA [46, 50, 54], whose mechanical properties are widely available in the literature. To our knowledge, Pini [70] and Obande [63] are the only authors who characterised and compared several grades of Elium in terms of mechanical response. Additional work by Charlier [51] and Murray [68] focused on a single grade of Elium, evaluating instead the influence of minor changes in formulation (amount of peroxide initiator or exotherm control agent, respectively) on the static mechanical response of the resin. These various studies confirm that the mechanical properties of infusion-grade Elium resins are not significantly different from one an-

other nor from PMMA¹. Charlier [51] characterised the thermal properties of Elium via differential scanning calorimetry (DSC) and thermogravimetric analysis (TGA). The obtained glass transition and degradation temperature values were also consistent with those expected for PMMA. Finally, a dynamic mechanical analysis (DMA) study by Fontanier [46] showed that the average value of the mass between chain entanglements in Elium was consistent with values reported in the literature for PMMA. According to the work presented above, it seems safe to conclude that Elium resins, once polymerised, can be regarded as regular PMMA.

Note that a few studies compared the mechanical properties of PMMA to epoxy resins, which are widely used in LCM processes. The term “epoxy resins” covers a variety of different chemical formulas, resulting in a wide range of possible (thermo)mechanical properties. Table 2.1 compares the typical range of mechanical and thermal properties of epoxy resins to those of PMMA, as given by Ashby [75]. There is an overlap between the range of elastic properties of epoxy resins and PMMA, meaning that an epoxy resin may or not outperform PMMA in terms of stiffness and yield strength depending on the case.

Table 2.1 Typical range of mechanical and thermal properties for epoxy resins and PMMA, as described by Ashby [75].

Property	Epoxy resins	PMMA
Young’s modulus E (GPa)	1.5-6	2.5-3.5
Yield strength σ_0 (MPa)	40-80	60-100
Fracture toughness K_{Ic} (MPa.m ^{0.5})	0.3-0.8	0.8-1.1
Maximum service temp. (°C)	≈ 180	≈ 100

¹apart from the particular case of Elium Impact, which contains acrylic block co-polymers as a toughening agent (see section 2.5.1), and will not be further considered in this review.

Tensile tests performed by Charlier [51] and Chilali [76] on Elium versus DGEBA-based epoxy resin specimens revealed a marginal superiority of the epoxy system in terms of elastic properties, but this conclusion should not be generalised for the reason mentioned above and which also applies - to a lesser extent - to Elium resins. However, due to their thermoplastic nature, PMMA and Elium *always* demonstrate slightly higher toughness values than epoxy resins and other thermosetting polymers [75, 76]. Note that Kinvi-Dossou [53] performed Charpy impact tests on both Elium and epoxy polymers, which revealed higher impact performances for Elium (though impact toughness is *not* equal to fracture toughness, there is a positive correlation between these two parameters, see e.g. [77]). Last, Davies [78] compared the tensile properties of Elium to a commonly-used epoxy resin after hygrothermal aging. Elium demonstrated better strength retention than epoxy for the same level of moisture uptake, and fully recovered its initial properties after complete drying.

Figure 2.6 provides an overview of the current state of the art on unreinforced Elium resins, and classifies the contributions mentioned above by topic.

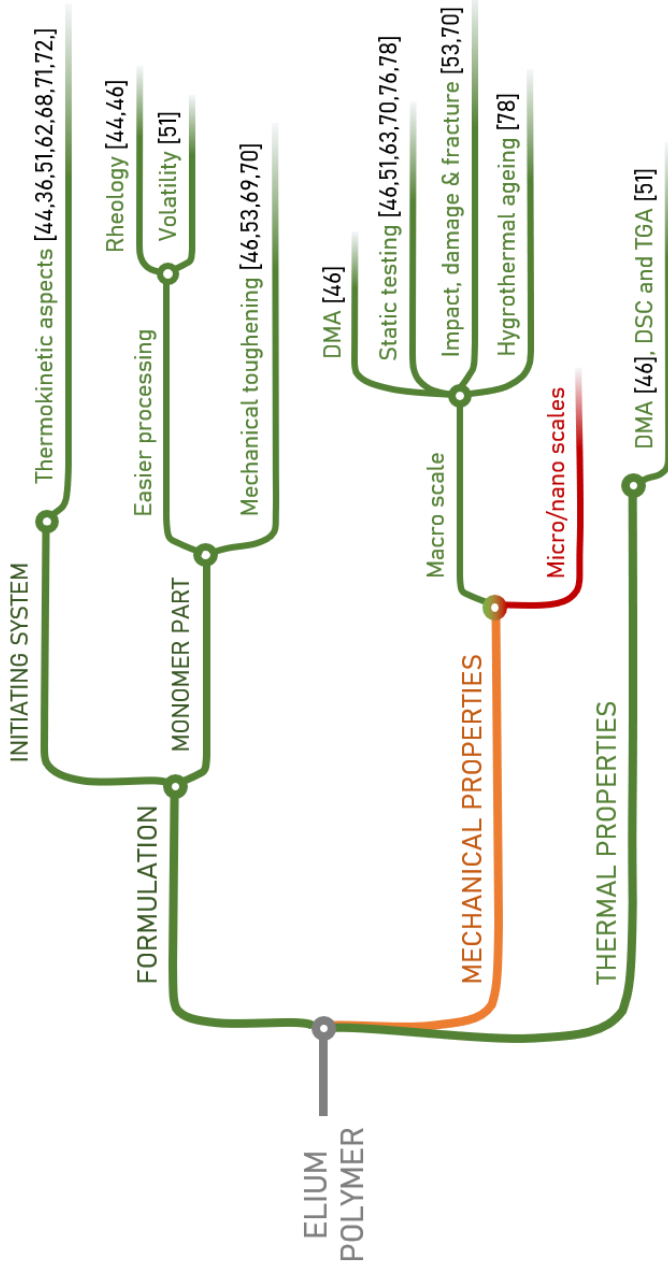


Fig. 2.6 State of the art on unreinforced Elium resins. Colours indicate the level of completeness achieved in each field of study; green: comprehensive studies, orange: partially-investigated topics and red: gaps in the literature.

2.5.2 Elium composites

Recyclability of Elium composites

As mentioned in sections 2.2 and 2.4, the unique macromolecular structure of PMMA provides Elium-based composite materials with an extra recycling option - thermal pyrolysis. This method adds up to the two recycling routes already available for thermoplastic composites: mechanical grinding and solvent dissolution. Starting from an Elium-based wind turbine blade composite spar cap, Cousins [44, 79] compared the three recycling methods in terms of energy consumption, economic relevance and thermomechanical properties of the recovered materials. Despite having the highest energy requirements (4-20 MJ per kg of composite material) and operating costs, dissolution was deemed the most efficient recycling route in the case of Elium composites thanks to the complete preservation of (1) polymer properties, including embedded energy and (2) fibre dimensions, sizing and mechanical properties. Figure 2.7 presents some of the results obtained by Cousins in this respect.

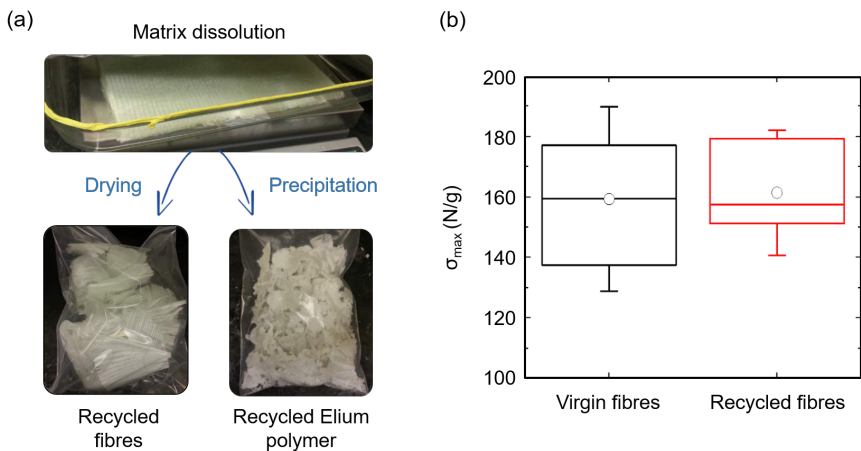


Fig. 2.7 Recycling glass fibre reinforced Elium composites by dissolution: (a) principle of the method and nature of recovered materials, and (b) comparison of ultimate tensile “mass-normalised force σ_{\max} ” values for virgin fibres *versus* fibres recycled by dissolution. Adapted from Cousins [44].

Surprisingly, pyrolysis was considered much less relevant from an economic point of view, despite requiring a fraction of the energy input of dissolution processes (1 MJ per kg). The proposed explanation relied on the downgrading of fibre properties (length, sizing). However, note that Cousins also considered the polymer matrix to be completely lost in the pyrolysis process, which does not reflect reality, see section 2.4. Last, grinding of Elium composites (followed by extrusion or injection-moulding) proved an interesting compromise by combining the lowest processing cost with excellent mechanical properties with respect to short fibre Elium composites made from 100 % virgin materials. Note that a fourth, innovative recycling route was envisioned by Cousins for large parts made of Elium composites: thermoforming [44]. As a proof-of-concept study, a prototype skateboard was obtained by flattening a piece of spar cap, made of thick glass fibre-reinforced Elium composites, sectioning the part parallel to fibre orientation and thermoforming one of the obtained layers into the final shape.

Fibre-matrix interface and interphase characterisation

The mechanical performances of fibre-reinforced composites at the macroscale strongly depend on the quality of interfacial bonding, i.e. on the adhesion between the matrix and individual fibres at the micro- and nanoscales [80]. The interface properties of a composite part build up throughout the manufacturing process. In the case of LCM, final interfacial adhesion results both from a proper wetting of the fibres by the liquid resin during infusion, and from the physical and/or chemical interactions occurring between the fibres and matrix during curing or polymerisation [80]. When a new resin system such as Elium is developed for LCM applications, selecting commercial fibres having the “right” surface properties for ensuring compatibility with the resin is thus of utmost importance. Beguinél [52] characterised the surface energy of various commercial fibres (carbon and glass), as well as their wettability by acrylic latexes having a similar composition as Elium. In parallel, Beguinél [52] and Charlier [51] measured the interfacial shear strength (IFSS) of different fibre-Elium matrix systems after polymerisation by relying on the microbond test [81] (which consists in embedding a single fibre in a droplet of resin and measuring the debonding force after polymerisation). Both studies identified acrylic-based fibre sizings as particularly suitable for the manufacturing of Elium composites [51, 52]. This result was confirmed by Boufaïda [50] via macroscale shear testing. Note that the

values of IFSS reported by Charlier for acrylic-based fibre sizings were close to 40 MPa, i.e. comparable to the IFSS values of most fibre-reinforced epoxy composites.

The term “*interface*” refers to the 2D contact area between the fibre and matrix materials, which may only be defined in terms of surface properties. The concept of *interphase*, on the other hand, defines a 3D transition zone of finite thickness extending from both sides of the interface, whose material properties are distinct from those of the bulk fibre and matrix materials [82]. Just like interface (surface) properties, interphase (material) properties have a significant impact on the macroscale mechanical response of the composite. Many authors have attempted the characterisation of composite interphases at the micro- or nanoscales, as detailed in the introduction of Chapter 7. However, no interphase characterisation results are available for Elium-based systems in the literature apart from a small study by Boufaïda [50]. The latter compared the DMA response of an Elium composite to that of an unreinforced Elium resin. Using numerical homogenisation methods, the author explained the observed differences in storage and loss modulus between the reinforced and unreinforced resin by the presence in the composite of a 0.7- μm thick interphase region 50 % stiffer than the bulk matrix. Boufaïda then performed nanoindentation testing in the composite matrix perpendicular to fibre orientation. From the results, he suggested the presence of an irregular 1- μm thick interphase region around the fibres, characterised again by a higher elastic modulus compared to the bulk Elium matrix. However, the conclusions from these two experiments should be considered with caution as (1) the homogenisation model relied on fitting parameters for improving correlation and (2) the apparent stiffening of the matrix near the interface measured by nanoindentation may only result from the proximity of the fibre material, as explained in Chapter 7.

Mechanical properties of Elium composites

While studies dealing with the mechanical properties of unreinforced Elium resins are scarce (see section 2.5.1), a large number of studies have been published on the macroscale mechanical characterisation of glass [44, 50, 53, 54, 61, 76, 83–85], carbon [83, 86–91] and flax [65, 76, 92–94] fibre-reinforced Elium composites as these are new to the composite industry. The mechanical properties of Elium composites are often described from a comparative point of view, using epoxy composites for benchmarking and

the present section will follow a similar approach. However, differences in fibre material, fibre volume fraction, fabric architecture, ply stacking sequence and/or loading conditions often exist between the two resin systems under comparison in the aforementioned studies. For this reason, it remains difficult to draw definitive conclusions with respect to the relative performances of epoxy and Elium composites, as reported by Obande in a recent review [63]. Still, the following trends seem to emerge:

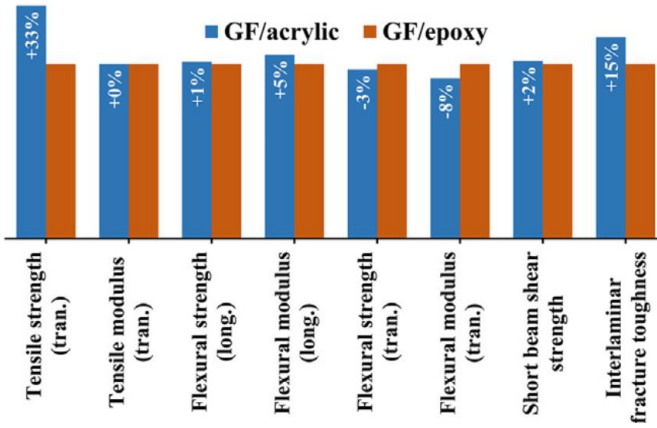
- **Static testing.** The longitudinal, transverse and shear properties of fibre-reinforced Elium composites lie in the same range as their epoxy counterparts, despite a consistent superiority of Elium composites in terms of strength (from a few % to more than 10 % for longitudinal and transverse testing configurations, depending on authors) [44, 61, 65, 76, 83, 84, 90]. As an example, Figure 2.8 (a) summarises the static test results obtained by Obande [84] when comparing glass fibre reinforced Elium *versus* epoxy composites. Note that Davies [83] also reported a better retention of flexural and tensile properties for Elium composites after hydrothermal ageing, especially in terms of strength (e.g. Elium and epoxy composites respectively experienced a 30 and 60 % drop in flexural strength upon immersion).
- **Damage and fracture behaviour, preferred failure modes.** Elium composites exhibit overall higher Mode-I [84, 88] (see Figure 2.8 (a)) and Mode-II [91] interlaminar toughness values due to their ability to resist crack propagation more efficiently. This is visible both from the macroscopic load-displacement behaviour during the tests and from microscale fractography analyses, which reveal clear signs of plastic deformation in the Elium matrix (e.g. crazing or ductile drawing, see Figure 2.8 (b)) and crack arrest mechanisms (e.g. crack deflection) while epoxy fails in a brittle manner [84, 88, 91]. Flexural test results yield similar conclusions with respect to the differences in damage behaviour between both composites before final compressive failure is observed [84, 90].
- **Impact resistance.** As briefly mentioned in section 2.5.1, impact test results should be considered with caution when it comes to comparing fracture toughness and damage behaviour between two systems. Only part of the impactor energy is actually used to create fracture surfaces (absorbed energy), while the rest is dissipated (e.g. through elastic deflection) [54, 85, 89]. Overall impact performance in composites is thus a complex combination of damping and damage resistance properties,

which not only depends on the nature of the matrix, but also on fibre material and orientation, ply thickness and impact strain rate [54, 85, 89]. For this reason, there is still a lack of consensus with respect to the correct way to compare impact performances between Elium and epoxy composites, see e.g. [53, 63, 85, 87]. We will focus on the conclusions of Bhudolia, who relied exclusively on energy criteria [87] to decouple the individual contributions of damping and damage behaviour for each impact test. Bhudolia's conclusions are the following: (1) Elium composites demonstrate strain rate sensitivity unlike epoxy composites, i.e. they exhibit better impact performance at higher energies (as shown also by [54]), (2) Elium composites can withstand higher-energy impacts before final failure with respect to their epoxy counterparts. This results from a combination of better damping properties [95] and tolerance to ductile damage for Elium composites, (3) contrary to epoxy composites which fail in a catastrophic, brittle manner. Note that these three conclusions could be expected, given the inherent higher toughness of thermoplastic polymers compared to thermosets, see section 2.5.1.

- **Fatigue properties.** The fatigue properties of glass fibre-reinforced Elium and epoxy composites have been compared by Davies [83], as part of the hygrothermal ageing study mentioned above. Both unaged specimens experienced similar evolutions of the maximum allowable fatigue stress up to 10^5 cycles, under tensile and flexural loading. Upon immersion in saltwater until complete saturation, Elium composites systematically presented a lower level of moisture uptake than their epoxy counterparts (up to 3 times lower at 60 °C) as well as significantly better retention of their tensile and flexural fatigue properties (e.g. Elium and epoxy composites respectively experienced a ≈ 27 and ≈ 45 % drop in flexural fatigue strength upon immersion).

Additionally, multiscale mechanical models have been developed by Boufaïda [50] and Kinvi-Dossou [53] for predicting the quasi-static and fracture behaviour of Elium woven laminates at the macroscale. While the modelling approaches were different, relying respectively on Fourier series [96] and classical finite element (FE) algorithms, both studies made use of homogenisation methods to obtain the mesoscopic behaviour of the composite, i.e. the mechanical response of a unidirectional fibre tow, from the constitutive laws of PMMA and fibre materials.

(a)



(b)

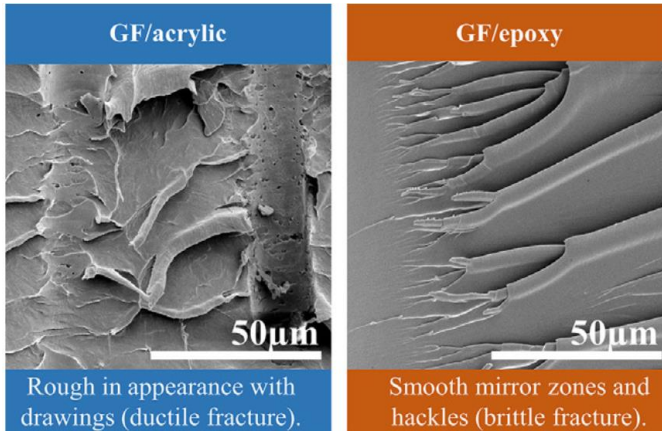


Fig. 2.8 Obande’s [84] work on the mechanical characterisation of glass fibre (GF) reinforced Elium and epoxy composites, including (a) comparison of static properties and (b) fractography images following Mode-I interlaminar fracture testing.

The mesoscopic model was then integrated into a macroscopic model consisting of one or several woven plies. Boufaïda [50] simulated the in-plane shear loading of a single ply, confirmed that the predicted areas of stress concentrations were consistent with experimental failure locations. Kinvi-Dossou [53] simulated the behaviour of a laminate (with intra- and interlaminar damage criteria) subjected to low-velocity impact testing. The model gave reasonably accurate predictions of the damage development patterns, absorbed energy and load values before fracture observed experimentally.

While the macroscale mechanical behaviour of Elium composites has been extensively characterised and modelled as described above, the micro- and nanoscale mechanical response of these materials remains virtually unknown.

Weldability of Elium composites

The outer shell of wind turbine blades is mainly composed of glass fibre-reinforced composites, as illustrated by Fig. 2.3. The final, hollow structure is obtained by bonding together two identical composite halves, which are manufactured separately via infusion. While adhesives have been used so far to assemble the structure, thermoplastic composite shells could - in theory - be simply welded together instead. This possibility is now being explored for Elium-based composites, in particular by Murray [31] and Bhudolia [32, 33]. Several fusion welding techniques were first investigated, namely ultrasonic [32, 33], resistance or induction [31] welding. All composite joints proved superior to classical adhesive joints in terms of static and fatigue lap-shear strength [31–33], although further work is needed before a prototype blade can be assembled this way. These preliminary results are particularly promising as the primary reason for blade failure is the debonding of adhesive joints [31].

Polymerisation thermokinetics in Elium composites

As mentioned in section 2.3, the polymerisation of MMA is prone to self-acceleration leading to a sharp temperature rise in the reaction medium. The thermokinetic behaviour of *bulk* MMA polymerisation is now well understood, as a number of modelling studies have been performed in this regard (see e.g. [62]). Existing models may not, however, apply to MMA polymerisation within a dense fibrous preform and only one attempt has been made so far at modelling the in-situ polymerisation of MMA in thick composite laminates [97]. This matter is crucial for enabling the industrial

scale-up of the Elium technology as (1) composite manufacturers request quantitative information with respect to the resin behaviour during processing (e.g. open time, optimum processing temperature) and (2) thermal runaway may result in the formation of voids in the composite matrix, if the temperature exceeds the boiling point of the remaining MMA monomer (e.g. 101 °C at 1 bar).

Manufacturing defects and preform thickness

Composite materials manufactured by LCM may contain various manufacturing defects, in particular voids, whose consequences on the mechanical properties of the laminates are unpredictable, see Chapter 3. In the case of Elium composites, the main source of void formation is through monomer boiling during the in-situ polymerisation step as explained above. This problem has been mentioned in several studies dedicated to the LCM processing of Elium composites [44, 50, 51, 68, 98], but never addressed except by Murray [68] via the addition of an exotherm control agent to the monomer formula. Other physical mechanisms may trigger cavitation during the manufacturing process, e.g. chemical or thermal shrinkage (cf. Chapter 5), but those have not been explored either for Elium composites. Micrographs of Elium composites containing voids are presented in Figure 2.9. These images were taken by Charlier [51] and Hemmer [98] for highlighting the presence of intra-tow and/or inter-tow porosity in Elium composites processed by LCM. Surprisingly, thick (≥ 1 cm) composite panels (which are used for manufacturing wind turbine blade shells), seem to be especially sensitive to cavitation [68, 98]. Unusual void patterns have even been observed e.g. by Hemmer [98] across the thickness of an Elium laminate, see Figure 2.9 (b). Apart from this small study, the overall influence of preform thickness on the homogeneity of Elium composite parts (in terms of porosity distribution, physical and chemical properties) has not been investigated either.

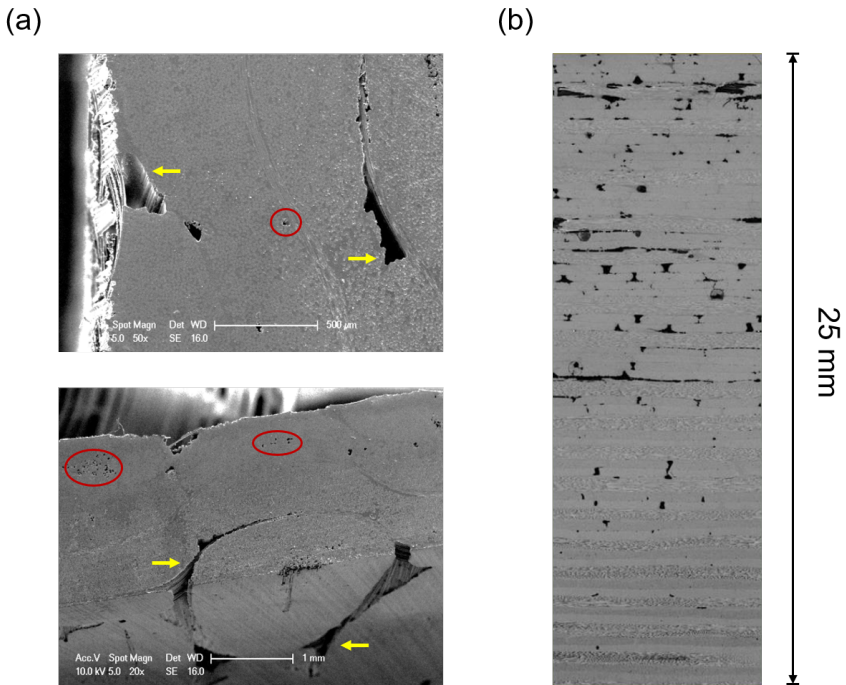


Fig. 2.9 Void patterns observed in glass fibre reinforced Elixir composites produced by infusion (a) at the ply level [51], and (b) through the thickness of a 25 mm laminate [98]. Red circles and yellow arrows have been added to Fig. (a) in order to indicate intra- and inter-tow voids, respectively. Note that only inter-tow voids are visible in Fig. (b).

2.5.3 Conclusions

Similarly to Figure 2.6 dealing with Elium resins, Figure 2.10 provides an overview of the current state of the art on fibre-reinforced Elium composites. The pending research questions - which are depicted in red in both figures - stand out clearly; these are listed below as a reminder.



Pending questions

- **Q1** - *What are the mechanism(s) leading to void formation during the manufacturing of thick Elium composites by vacuum infusion? At which stage(s) of the process do they take place and what triggers them?*
- **Q2** - *Does preform thickness have an influence on the homogeneity of Elium composite parts, during processing and with respect to their final properties?*
- **Q3** - *What is the thermokinetic behaviour of Elium composites during in-situ polymerisation within a fibrous preform? Is it any different from what is already known about the bulk polymerisation kinetics of Elium?*
- **Q4** - *What is the mechanical response of Elium composites at the constituent level, i.e. at the micro- and nano-scales, including the fibre-matrix interphase region?*

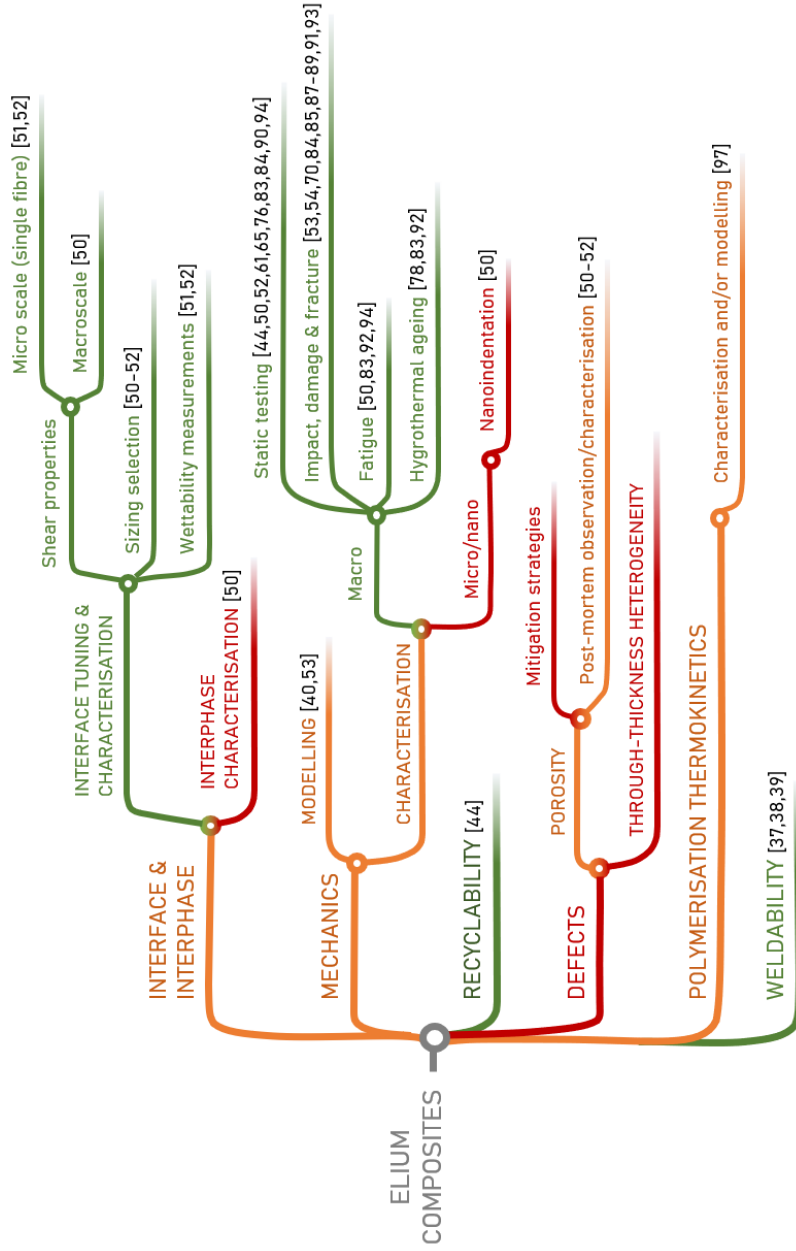


Fig. 2.10 State of the art on Elium composites. Colours indicate the level of completeness achieved in each field of study; green: comprehensive studies, orange: partially-investigated topics and red: gaps in the literature.

3

Top-down preliminary exercise on thick Elium composites

This chapter is an extended version of the conference paper entitled *Relationship between processing parameters and mechanical properties of thick glass fibre reinforced thermoplastic methacrylic composites* by S. F. Gayot, C. Bailly, T. Pardoën and P. Gérard, published in 2019 in the Proceedings of the 7th ECCOMAS Thematic Conference on the Mechanical Response of Composites, Girona, Spain.

Preamble: This phenomenological study has been conducted at the very beginning of the PhD as part of a “top-down” approach, which aimed at better identifying and understanding the key technological challenges met by Arkema, and at quantifying the impact and amplitude of porosity as a function of processing conditions. This work has set the basis for more fundamental developments, which are reported in the next chapters.

3.1 Introduction

Little is known about the behaviour of thick composite parts, whose main application is the manufacturing of wind turbine blades via vacuum infusion. This work explores the relationships existing between the processing conditions, physico-chemical state of the matrix and mechanical properties of 7-cm-thick glass fibre reinforced Elium composite plates at both the micro- and macroscopic scales. Differences in the processing temperature were related to changes in porosity distribution and morphology along the thickness direction. The influence of voids on the mechanical response of the laminate was studied, and chemical and micromechanical characterisation of the matrix was performed in order to provide some insights into the course of the in-situ polymerisation reaction.

3.2 Materials and experimental methods

3.2.1 Materials

Composite preforms were made from quasi-unidirectional non-crimp glass fabric plies (Chomarac, France) with an areal weight of 1.03 kg.m^{-2} (85 % warp and 15 % weft). The resin comprised an infusion-grade monomer formula (Elium 191 OSA of Arkema, France) combined with a ketone peroxide thermal initiator (Luperox K10 of Arkema, France). The Elium 191 OSA mixture contains MMA monomer with 20 to 30 wt % acrylic copolymer chains, which serve as a viscosifying agent. The consumables for bagging and infusion were obtained from Diatex SAS (France).

3.2.2 Preparation of composite specimens

Composite plates were manufactured via vacuum-assisted infusion using the setup illustrated in Figure 3.1. Preforms were produced by laying up 90 glass fabric plies onto a heating mould. Two sets of manufacturing conditions, corresponding to plates A and B, were explored. These conditions differ in heating mould set temperature as detailed in Table 3.1. Each fabric stack was sealed with a vacuum bag and prepared for resin infusion. A thermocouple was placed on top of the bag (close to location $x = w/2$, $y = h$ and $z = L/2$, see Figure 3.1) and secured with sealant tape. Note that for plate B only, a second thermocouple was placed between the mould and

the bottom peel-ply layer (at location $x = w/2$, $y = 0$ and $z = L/2$), and a coupled temperature and viscosity sensor (Optimold sensors by Synthesites [99]) was also inserted within the preform (at $x = w/2$, $y = h/2$ and $z = L/2$), see Figure 3.1.

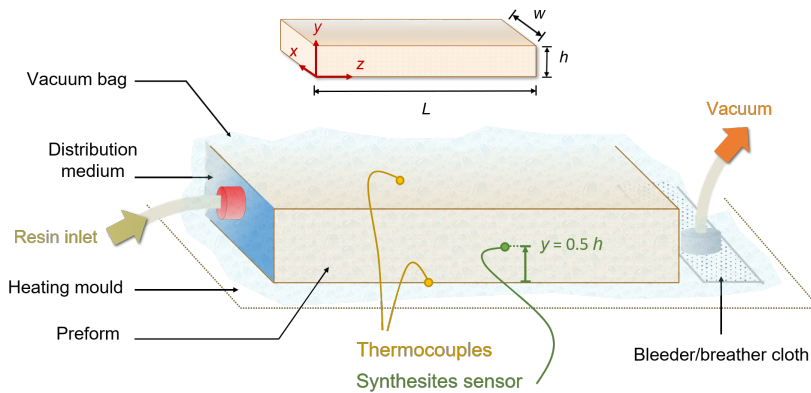


Fig. 3.1 Experimental setup used for the vacuum infusion of plates A and B ($h = 73$ mm, $L = 60$ cm, $W = 40$ cm) with associated coordinate system.

Table 3.1 Additional characteristics of composite plates A and B

Experimental conditions	A	B
Processing temperature	RT	Infusion at RT, then heating at 50 °C (0.5 °C/min ramp + 30-min plateau),
Plate dimensions	$h = 73$ mm, $L = 60$ cm, $W = 40$ cm	
Laminate structure	90 quasi-UD plies, $[(0_{\text{warp}}/90_{\text{weft}})_{45}]_s$	

3 | Top-down preliminary exercise on thick Elium composites

The resin mix was made with three parts initiator per hundred parts resin, mechanically stirred for 5 min, and then degassed for 1 min at a pressure close to 100 mbar. Infusion tests were conducted in the z -direction (i.e. parallel to fibre tow orientation), at a pressure close to 100 mbar and at room temperature (RT). The resin inlet and vacuum line were clamped shut at the end of the infusion process. Then, for condition B, the infused preform was heated via the heating mould from RT to a set temperature equal to 50 °C as described in Table 3.1. The polymerisation of plate A occurred without any external heating. Upon completion of the polymerisation reaction, each plate was left to cool down to RT and demoulded. Final fibre volume fractions were close to 0.5.

Plates A and B were machined using a water-cooled disk milling cutter. Two smaller samples of approximate dimensions $150 \times 25 \times 65 \text{ mm}^3$ were first extracted¹ and named after their respective plates. These were downsized into 5 rectangular pieces as depicted in Figure 3.2 (a), and further divided into smaller specimens when needed. In particular, 5 layers were cut out from subparts a, b and c along the y -axis. The corresponding sectioning diagram and final nomenclature of all specimens are provided in Figure 3.2 (b).

¹with fibre tows oriented perpendicular to plane (yoz) in sample A, and perpendicular to plane (yox) in B

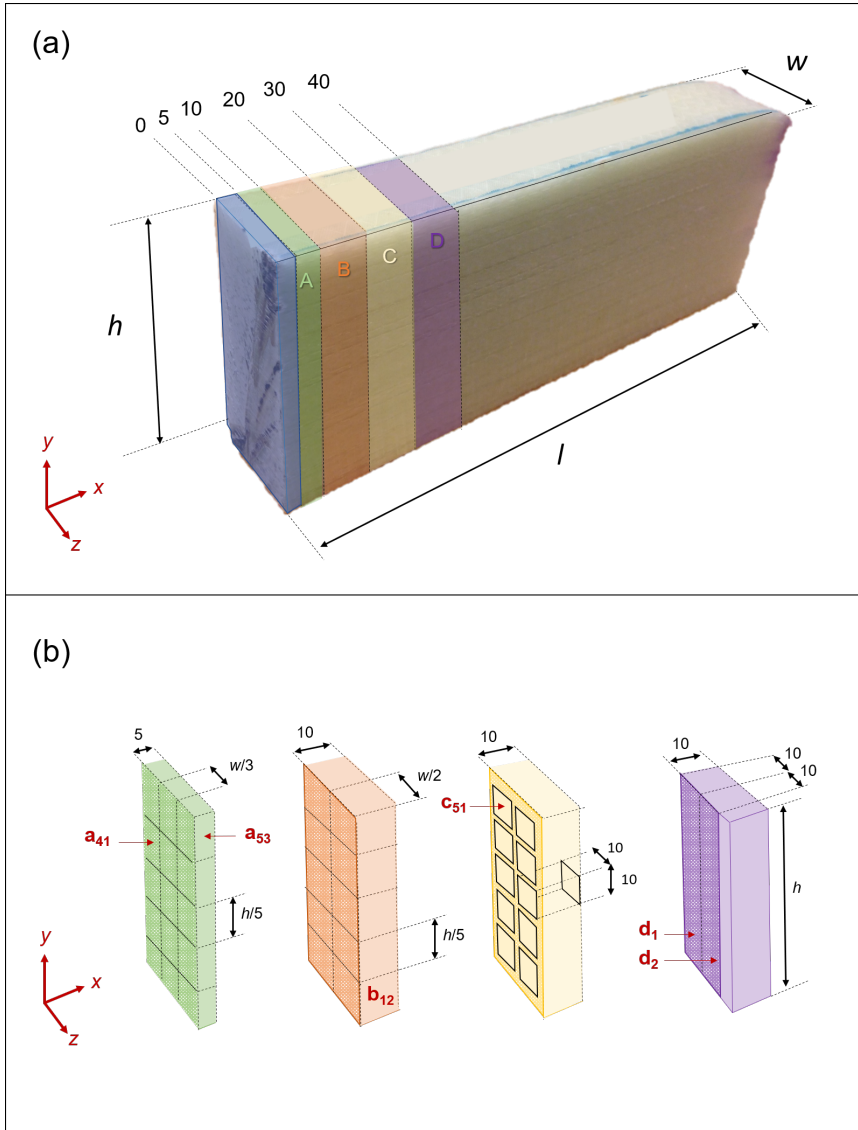


Fig. 3.2 (a) First sectioning diagram of composite plate samples, exemplified in the case of sample A, and (b) final sectioning diagram applied, from left to right, to subparts a to d, and associated nomenclature indicating specimen location with respect to the y and z -axes. Note that only a few specimens were labelled (in red) for the sake of clarity, the logic of numerotation should be self-obvious from the provided examples.

3.2.3 Mechanical characterisation

Specimens b_{11} , b_{21} , b_{31} , b_{41} , and b_{51} were tested by nanoindentation using an Agilent G200 Nanoindenter, equipped with a Berkovich diamond tip and a standard XP head. The composite surfaces perpendicular to fibre tow orientation were roughly polished using resin-bonded diamond discs with successive grit of 1, 200 and 4, 000, and finished using a polishing cloth coated with a 0.3- μm alumina suspension. Indents were performed in Continuous Stiffness Measurement (CSM) mode in the large matrix pockets between fibre tows. The Oliver and Pharr method [100] was used to calculate the indentation modulus and hardness values. For each specimen, about 30 indents were performed with a maximum penetration depth of 2,000 nm. Due to the so-called “indentation size effect”, modulus and hardness values were observed to fluctuate at penetration depths below 1,000 nm, before reaching a plateau. Note that the size effect is often observed in polymeric materials and is thought to have multiple origins (e.g. residual stresses, plastic strain gradient effects, tip blunting, friction, incorrect assessment of the contact area at small depths, etc. [101]). For this reason, the nanoindentation measurements obtained at penetration depths below 1,000 nm were discarded from the study.

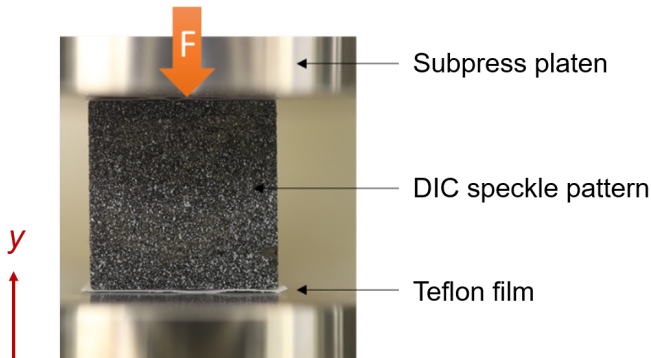


Fig. 3.3 A speckled composite specimen after installation in the compression setup.

Additionally, macroscopic transverse compression tests were carried out on specimens c_{11} , c_{21} , c_{31} , c_{41} , and c_{51} along the y -direction. Prior to mechanical testing, each specimen was polished perpendicular to fibre orientation and imaged by optical microscopy (see section 3.2.6). A black and white speckle pattern was then applied onto the polished surfaces using spray paint, in order to enable digital image correlation (DIC) analysis of the strain fields during compression testing. The speckled specimens were installed on a Zwick-Roell screw-driven universal testing machine equipped with a 250 kN loading cell and a compression subpress (WTF-SP, Wyoming Test Fixtures), as illustrated by Figure 3.3. All compression tests were performed at RT, with a constant crosshead speed equal to $0.1 \text{ mm}\cdot\text{min}^{-1}$. Teflon films were inserted between the specimens and the subpress platens to minimise friction, as advised by Morelle [102], see Figure 3.3. Displacements along the y -direction were measured and further corrected with respect to machine compliance. In parallel, photographs of the speckled surface were taken every 5 seconds during each test to enable DIC analysis.

3.2.4 Chemical analysis

Specimens a_{12} , a_{22} , a_{32} , a_{42} and a_{52} were characterised by size exclusion chromatography (SEC), in order to assess chain length distribution in the Elium matrix across the thickness of the plates. SEC analyses were carried out using a Waters Alliance 2695 device equipped with 2 PLgel Mixed-B columns ($300 \times 7.5 \text{ mm}$, $10 \mu\text{m}$) and the following detectors: a Waters 2487 UV-spectrophotometer (set at 254 nm) and a Waters 2414 refractometer. Polystyrene standards with molecular weights ranging from 580 to $6,870,000 \text{ g}\cdot\text{mol}^{-1}$ (Easivial PS-H by Agilent) were used for calibration. Composite specimens were then prepared for analysis as follows. Each specimen was dissolved in 40 mL spectroscopic grade tetrahydrofuran (THF, HiPerSolv Chromanorm, BHT-stabilised by VWR) for 24 hours, at RT and under magnetic stirring. The obtained solution was diluted 10 times in THF and filtered on a $0.45\text{-}\mu\text{m}$ Teflon membranes. THF was used as the elution solvent and injected at a flow rate of $1 \text{ mL}\cdot\text{min}^{-1}$. The injection volume for each sample was equal to $100 \mu\text{L}$.

The amount of residual methyl methacrylate (MMA) monomer in composite specimens a_{11} , a_{21} , a_{31} , a_{41} , and a_{51} was measured by High-Pressure Liquid Chromatography (HPLC). Measurements were performed at $40 \text{ }^\circ\text{C}$ on a Waters Alliance 2695 equipped with a Waters Sunfire C18 col-

umn (100×4.6 mm, $3.5 \mu\text{m}$), a pre-column and a Waters 2998 PhotoDiode Array detector. Calibration standards of MMA (99 % stabilised, by Acros Organics) were prepared in THF with MMA concentrations ranging from 12.5 to $250 \mu\text{g}\cdot\text{mL}^{-1}$. Composite specimens were then dissolved in 100 mL THF/methanol $20/80$ v/v for 24 hours at RT, under magnetic stirring. All solutions were filtered on $0.45 \mu\text{m}$ Teflon membrane. For the HPLC analysis, the mobile phase consisted of water, acetonitrile and buffer (1 % v/v phosphoric acid in water) using a gradient programme from 25 to 90 % v/v acetonitrile for 5 min and a constant 10 % v/v of buffer solution. The flow rate was equal to $1 \text{ mL}\cdot\text{min}^{-1}$ while the injection volume was $5 \mu\text{L}$. Each MMA solution was analysed twice. Spectroscopic grade THF (Rotisolv, unstabilised, by Roth), methanol, acetonitrile and phosphoric acid were used (HiPerSolv Chromanorm by VWR), while ultrapure water was obtained with a Purity 15UV device (VWR).

3.2.5 Thermal analysis

The glass transition temperature T_g of the Elium matrix was measured by Differential Scanning Calorimetry (DSC) in specimens a_{13} , a_{23} , a_{33} , a_{43} and a_{53} . A hammer was used to delaminate each composite platelet into 15 to 20-mg flakes, two of which were placed into sealed crucibles. A heating ramp from 30 to 150 °C was applied, followed by a cooling ramp from 150 to 30 °C. The heating and cooling rates were equal to 10 °C $\cdot\text{min}^{-1}$. This temperature cycle was performed twice, under a nitrogen flow ($50 \text{ mL}\cdot\text{min}^{-1}$). T_g values were measured by applying the peak differential heat flow method during the second heating ramp.

3.2.6 2D and 3D imaging

Porosity patterns in plates A and B were first studied by microscopy. Optical images of specimens c_{11} , c_{21} , c_{31} , c_{41} , and c_{51} were taken before compression testing (see section 3.2.3) and the void surface fraction was determined through image processing with the open-source software ImageJ.

Specimens d_1 were subjected to X-ray Computed Tomography (XCT) analysis on a Phoenix Nanotom S XCT system (GE Inspection Technologies). The specimens were mounted on a holder, with the y -axis aligned along the rotation axis of the rotation stage. 360° -tomographic projections were acquired with a 0.15° step, and the X-ray source voltage and current values were respectively set at 110 kV and $270 \mu\text{A}$. The target material con-

sisted of tungsten-coated synthetic diamond, and 0.2 mm-thick copper and aluminium filters were installed to harden the beam. Scans were acquired at different positions along the y -direction, respectively near the bottom, middle and top parts of the specimens. The isotropic voxel resolution was equal to $7.5\ \mu\text{m}$, i.e. smaller than the diameter of the elemental glass fibres ($\approx 15\ \mu\text{m}$). The exposure time was set to 500 ms and the fast scan mode was activated, leading to a total scan time of 20 minutes. The Datos|x software was used for reconstructing the 3D scans and exporting the 2D cross-sectional images of each specimen, while further image processing was performed with MATLAB (R2016b) and Avizo (2019.1). More precisely, a double threshold hysteresis function was first applied with MATLAB to isolate the voids, and 3D renderings of specimen microstructure and porosity patterns were generated in Avizo.

3.3 Results and discussion

3.3.1 Thermal behaviour of the laminate during in-situ polymerisation

Figure 3.4 shows the temperature profiles recorded during the in-situ polymerisation of plates A and B. As mentioned previously, plate A only had one surface thermocouple, while plate B was equipped with two additional sensors located underneath the preform (at $y = 0$) and at mid-thickness (at $y = h/2$), see Fig. 3.1. All curves exhibit a sharp temperature peak which is characteristic of the gel effect occurring during MMA polymerisation, see Chapter 2. Note that the polymerisation reaction is considered complete as soon as the maximum temperature has been reached. Comparing the surface temperature plots of A and B, which are depicted in green in Figure 3.4, it appears that plate B experienced the gel effect first (at $t \approx 4\ \text{h}$, versus $t \approx 7\ \text{h}$ for plate A). The maximum surface temperature was also higher for plate B, reaching $115\ ^\circ\text{C}$ at the peak while that of plate A was close to $90\ ^\circ\text{C}$. The core and mould temperature profiles of plate B, which are respectively depicted in pink and blue in Figure 3.4, provide insight into the timeline of events across the thickness of plate B. The sharp temperature rise, which is symptomatic of the gel effect, occurred first near the mould (at $y = 0$), then in the middle of the laminate (at $y = h/2$), and finally in the top part. Additionally, the three temperature profiles of plate B have different shapes: they become sharper as y increases. The temperature values at the maximum are also higher as the sensors are located closer to the surface of the plate. Recall that the boiling point of MMA is equal

3 | Top-down preliminary exercise on thick Elium composites

to 101 °C at atmospheric pressure, cf. section 2.5.2. The pressure within the vacuum bag is below 1 bar, i.e. the locations at which temperature values above (or equal to) 101 °C were recorded have definitely experienced monomer boiling. This is the case for the middle and top parts of plate B, and probably also for the bottom part (whose maximum temperature is exactly equal to 101 °C). It is more difficult to draw definitive conclusions for plate A, whose only sensor was placed outside of the laminate. The poor thermal conductivity of the bagging material could lead to a slight underestimation of the surface temperature value with respect to reality.

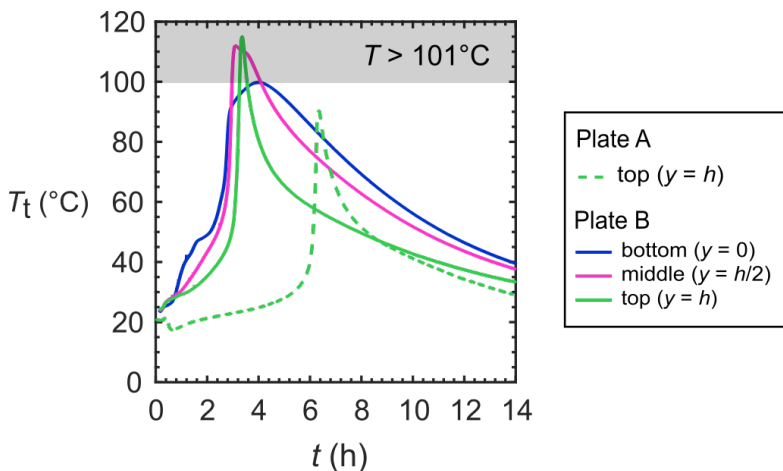


Fig. 3.4 Temperature profiles recorded in plates A (dashed line) and B (full lines) during the in-situ polymerisation of Elium, at different locations along the y -axis. The grey-shaded area corresponds to temperature values equal to or exceeding the boiling point of MMA at atmospheric pressure, i.e. 101 °C.

As plates A and B share the exact same features in terms of preform properties, resin formulation and processing conditions, except for the temperature programme applied to the mould (see Table 3.1), it seems clear that the latter is responsible for the differences in thermal behaviour mentioned in the previous paragraph. While A was infused and left to polymerise at RT, B was also infused at RT but then slowly heated up to 50 °C during polymerisation. It is not surprising that the onset of the gel effect was observed sooner in B, as heating is known to accelerate most chemical reactions (their rate constant depends on temperature via the Arrhenius equation [103]). What we could not predict, however, is the 35-°C difference in peak surface temperature between plates A and B, which implies that the overall intensity of the gel effect also depends on the processing temperature. For plate B, the increase in peak sharpness and maximum temperature value as y increases suggests that the gel effect also became more and more intense as it occurred closer to the surface - but this remains to be confirmed.

3.3.2 Characterisation of porosity patterns in the composite

A first assessment of void content along the thickness direction of plates A and B was made from the optical micrographs of specimens c_{11} , c_{21} , c_{31} , c_{41} , and c_{51} (see section 3.2.3), some of which are displayed in Figure 3.5. While the porosity seems to be close to zero in plate A, plate B displays a gradient of void size and distribution along the y -axis. More precisely, more and larger voids are observed as y increases. Through image processing, the approximate areal fraction of the voids in plate B was estimated to be around 2.7 % for specimen c_{11} , 5.4 % for c_{31} and 10.1 % for c_{51} . These values include both macrovoids (which we define here as voids whose smallest dimension exceeds 100 μm) and microvoids (i.e. the others), though only macrovoids are visible in Fig. 3.5 given the limited picture size.

The XCT analysis of A and B confirmed the results obtained by optical microscopy. As illustrated by Figure 3.6, a gradient of porosity is also observed along the y -axis of plate B, and the calculated void volume fractions Φ are in the same order of magnitude as the areal fractions obtained from optical micrographs. Concerning plate A, XCT scans reveal the presence of a very small ($\Phi \approx 0.15$ vol %) amount of randomly-distributed porosity. Last, the XCT analysis indicates that the vast majority of the observed voids are macrovoids in both plates. These are exclusively located in matrix pockets, i.e. in the spaces in between two fibre tows from the same ply

3 | Top-down preliminary exercise on thick Elium composites

or in the narrower inter-ply area. In plate B, the longest dimension of the voids ranges from 500 μm to 3 mm. Their shape changes from discontinuous, ellipsoidal cavities to continuous channels running in between fibre tows as y increases, see Fig. 3.6. This observation leads to the assumption that 3D porosity (Φ) values are reasonably close to the 2D areal fractions measured via optical microscopy, especially as porosity increases.

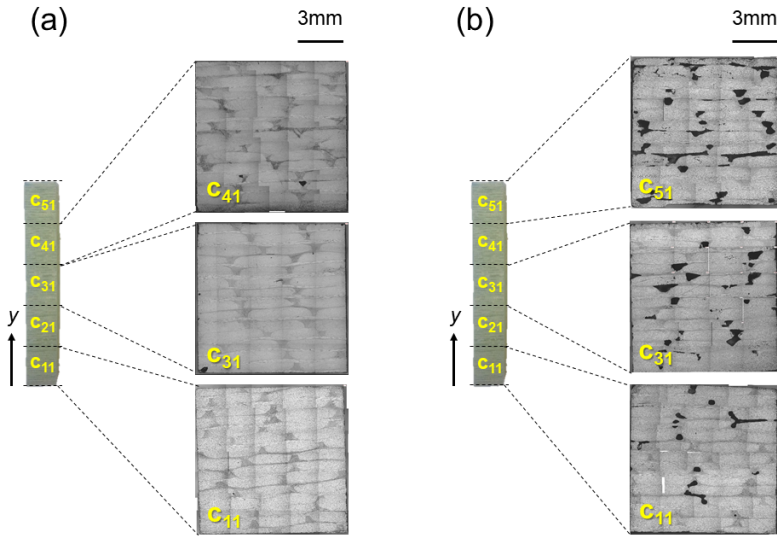


Fig. 3.5 Optical micrographs of (a) plate A and (b) plate B cross-sectional specimens extracted at various locations along the y -axis.

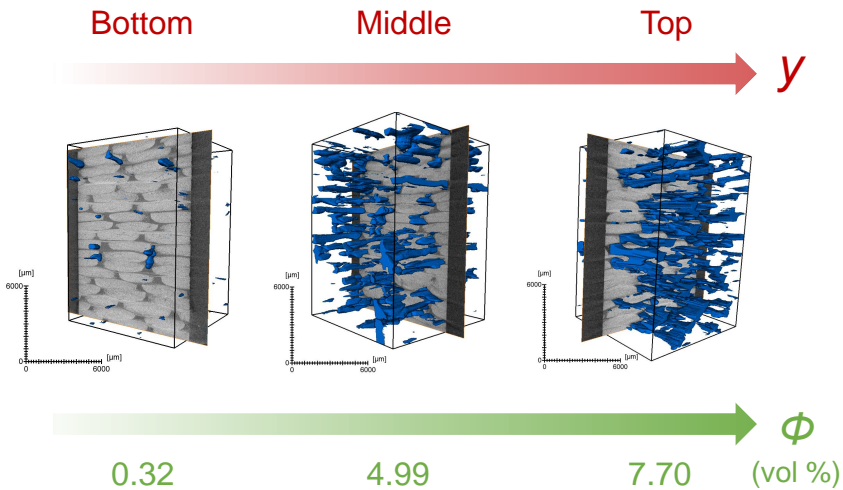


Fig. 3.6 3D volume rendering of void patterns across the thickness of plate B in (from left to right) the bottom, middle and top third of the laminate, with associated porosity Φ .

3.3.3 Chain length distribution and residual monomer content in Elium

The molecular weight (MW) distributions of PMMA chains along the y -axis of plates A and B are displayed in Figure 3.7. Peak heights, which are related to the amount of matrix in the specimens analysed by SEC, have been normalised. In both plates, a unimodal distribution of molecular weights is observed. Number- and weight-average molecular weight values \overline{M}_n and \overline{M}_w range between 1.5-2 and $2-3.5 \times 10^5$ g.mol⁻¹, respectively, i.e. more than ten times the critical mass between entanglements of PMMA (10^4 g.mol⁻¹). This is enough to reach the expected level of mechanical properties for the Elium matrix in both plates [104]. The polydispersity index I_p is close to 4 for all specimens. Note that I_p values significantly higher than 2 are characteristic of uncontrolled free-radical polymerisation reactions prone to the gel effect (see e.g. [105]). The values of \overline{M}_n , \overline{M}_w and I_p mentioned above are consistent with previous work on the bulk free-radical polymerisation of MMA in Elium resins [51].

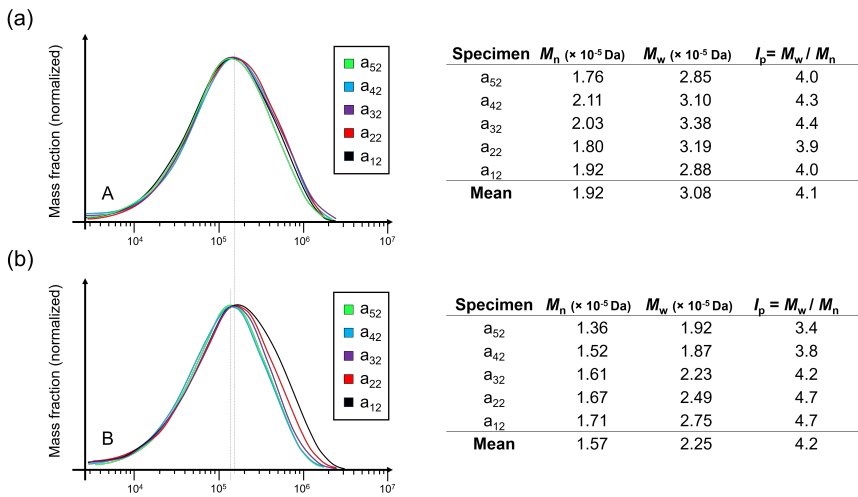


Fig. 3.7 Molecular weight distributions determined by SEC for plates (a) A and (b) B at different locations across the thickness direction, alongside with the calculated values of \overline{M}_n , \overline{M}_w and I_p for each specimen.

However, subtle differences can be observed in Figure 3.7 between the MW distributions of plates A and B. While MW distributions seem quite homogeneous across the thickness of plate A, see Figure 3.7 (a), those of plate B get narrower and shift towards lower \overline{M}_w values as y increases, see Figure 3.7 (b). The mean values of \overline{M}_n and \overline{M}_w are also significantly lower in B, compared to A. In his work on Elium resins, Charlier [51] related variations in gel effect intensity to changes in final MW distributions. He concluded that (1) a more acute gel effect leads to shorter PMMA chains and (2) heating the polymerisation medium has an impact on gel effect intensity. These statements are not only consistent with the SEC results presented above for plates A and B, but also with the assumptions made from the temperature profiles in section 3.3.1. These suggested a more intense gel effect in plate B than in plate A and, in the case of B, an increase in gel effect intensity as y increases.

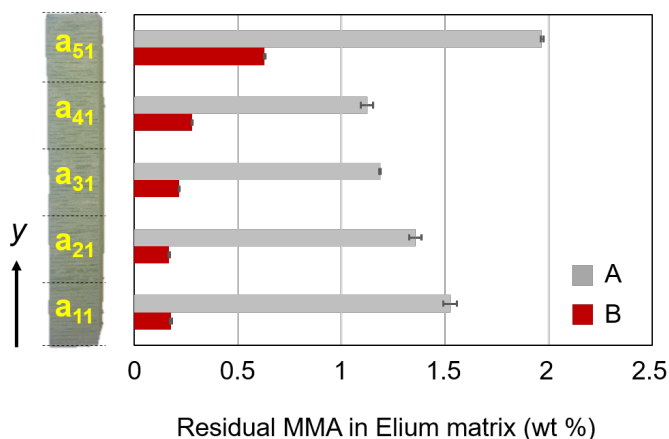


Fig. 3.8 Weight percentage of residual MMA in Elium along the y -axis of plates A (grey) and B (red). Each bar plot is obtained by averaging the results of two analyses, whose values are displayed via the error bars.

Figure 3.8 shows the amount of residual MMA found in the Elium matrix along the y -axis of plates A and B. Both parts contain a non-zero proportion of MMA, which is expected for a free-radical polymerisation reaction experiencing the gel effect. The latter is not *per se* responsible for the incomplete monomer conversion, but triggers the onset of another diffusion-controlled regime known as the glass effect: monomer diffusion towards macroradicals progressively stops before full conversion is reached, see Chapter 4. The extent of the temperature surge during MMA polymerisation *partially* dictates the final monomer content: the higher the peak temperature, the more delayed the glass effect (as high temperatures promote molecular motion) and thus the lower the amount of residual MMA in the material. This explains why plate B, which experienced higher temperatures than A during in-situ polymerisation, contains between 3 and 8 times less residual MMA than plate A depending on the location along the y -axis. On the other hand, the smaller variations observed within each plate do not have a straightforward interpretation. While the maximum temperature value does have a significant effect on residual monomer content, it cannot explain everything, e.g., why more residual monomer is found in plate B as y increases although the evolution of peak temperature values along y should yield the opposite trend.

3.3.4 Thermal properties

The glass transition temperature T_g values measured by DSC across the thickness of plates A and B are presented in Table 3.2. Recall that each composite specimen was crushed into flakes, two of which were subjected to DSC analysis separately. The corresponding T_g measurements are referred to as $T_{g,\text{test1}}$ and $T_{g,\text{test2}}$ in Table 3.2. The mean values of T_g in plates A and B are very close, both around 97 °C. The variations in T_g values along the y -axis of each plate are not considered significant for three reasons. First, they do not exceed plus or minus 2 °C with respect to the mean T_g value of the plates. Second, T_g values seem to have a random evolution along the y -axis (i.e. they do not constantly increase or decrease along y). Finally - and perhaps more importantly -, the fluctuations observed along y in both plates are of the same order of magnitude as those observed between tests 1 and 2 for a single specimen, see e.g. the case of a_{23} in plate A. This lack of precision in DSC measurements is attributed to the poor thermal contact between DSC crucibles and glass fibre composite flakes, which are not perfectly flat and have a low thermal conductivity (close to $0.5 \text{ W}\cdot\text{m}^{-1}\cdot\text{K}^{-1}$

[75]). The resulting thermal inertia makes it impossible to capture small changes (less than a few °C) in the glass transition temperature of the analysed composite specimens, but would still allow highlighting large variations (e.g. greater than 5 °C). Hence, we can conclude that the differences in thermal behaviour *within* and *between* plates A and B, if they exist, are small. This is consistent with the fact that all tested specimens contain almost fully-polymerised PMMA with high MW values (above $10^5 \text{ g}\cdot\text{mol}^{-1}$).

Table 3.2 Glass transition temperature T_g values measured by DSC along the y -axis of plates A and B. Tests 1 and 2 correspond to two different samples from the same specimen (e.g. a₁₃).

	PLATE A		PLATE B	
	T_g , test 1 (°C)	T_g , test 2 (°C)	T_g , test 1 (°C)	T_g , test 2 (°C)
a ₅₃	97.3	97.4	95.4	96.6
a ₄₃	98.0	96.1	98.8	97.6
a ₃₃	96.1	98.0	99.8	97.3
a ₂₃	97.9	94.5	98.9	96.9
a ₁₃	97.6	96.8	98.4	97.4
Mean plate	97.0		97.7	

3 | Top-down preliminary exercise on thick Elium composites

Note that the measured T_g values, which are close to 97 °C, are surprisingly low compared that the expected value for PMMA containing 1-2 wt% residual MMA. Looking at Figure 3.9, which shows the evolution of the glass transition temperature of PMMA as a function of residual monomer content, one could have expected T_g values at least equal to 100 °C for plates A and B. However, several authors [106, 107] have already reported a 3-to-5 °C drop in the T_g values of fibre-reinforced composite matrices, compared to those obtained from bulk polymers. They attributed this observation to the presence of a sizing at the surface of the fibres, which in the case of Elium could act as a second plasticiser in addition to residual MMA. The main components of glass fibre sizings, in particular, are low molecular weight film-forming polymers, which may diffuse into the composite matrix during liquid moulding processing [108]. These sizings generally account for 0.5 to 1.5 % of the total weight of glass fibre rovings, which may not be negligible for composites with high fibre volume fractions like plates A and B (see section 3.2.2).

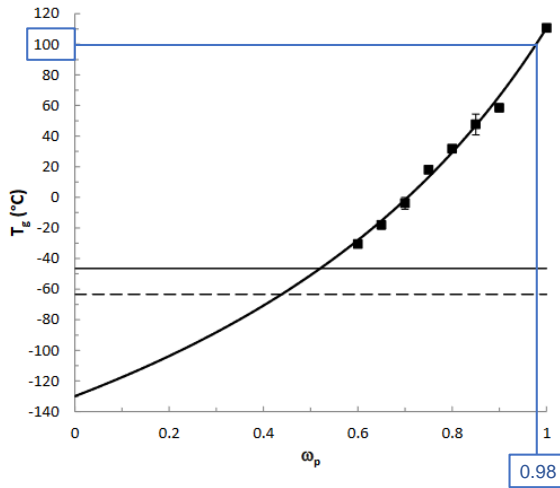


Fig. 3.9 Variation of the glass transition temperature T_g of a PMMA/MMA mixture as a function of the mass fraction ω_p of PMMA, adapted from Fontanier [46]. The dashed and full black lines respectively indicate the crystallisation and melting temperatures of MMA.

3.3.5 Micromechanical response of the composite matrix

The results of nanoindentation testing performed in the Elium matrix pockets along the thickness of plates A and B are presented in Figure 3.10. The distributions of modulus and hardness values obtained for each specimen (from approximately 30 indents, see section 3.2.3) are displayed as box plots. Both plates exhibit overall similar hardness (≈ 300 MPa) and modulus² (≈ 5.5 GPa) values, meaning that the mechanical properties of the composite matrix do not depend much on the processing temperature.

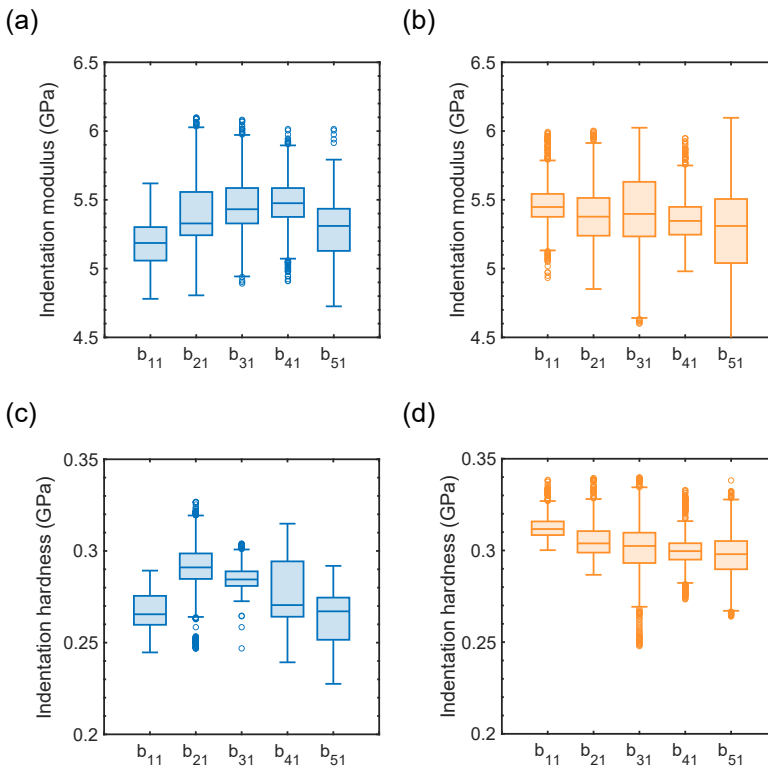


Fig. 3.10 Elastic modulus and hardness of the Elium matrix measured by nanoindentation along the y -axis of (a), (c) plate A and (b), (d) plate B, respectively.)

²Note that the indentation modulus of Elium is higher than the Young's modulus of Elium obtained from static testing (≈ 3 GPa [70]). These two parameters are not calculated the same way, although they are often used interchangeably.

Looking at the results in more details, slight variations are still noticeable between A and B, as well as along the y -axis of both plates. First, plate B exhibits hardness values 10 to 15 % higher than plate A, see Figures 3.10 (c) and (d). Second, the properties of plate A significantly vary across the thickness, with lower modulus and hardness values obtained in specimens b_{11} (i.e. close to the mould) and b_{51} (i.e. close to the vacuum bag), see Figures 3.10 (a) and (c). These two observations may be related to the differences in residual MMA content presented in section 3.3.3. As mentioned above, residual MMA acts as a plasticiser for PMMA. Recall that the overall amount of residual monomer in B is much lower than in A, which could explain why hardness values are higher in B. The same reasoning applies to the variations in nanoindentation results along the y -axis of plate A; more residual MMA was found near the mould (in specimen a_{11}) and close to the surface (in a_{51}), which also corresponds to the locations where lower hardness and modulus values were measured.

3.3.6 Influence of porosity on transverse compression response

The results of macroscopic compressive tests are presented in Figure 3.11 as well as Table 3.3. As described in sections 3.3.3 to 3.3.5, the chemical and physical properties of the Elium matrix are broadly similar in plates A and B, and relatively homogenous along the y -axis in both cases. Hence, any difference in the compressive behaviour of the composite specimens likely results from differences in porosity. The comparison of Figures 3.11 (a) and (b) highlights the detrimental impact of voids on the mechanical response of the composite material. Plate A, which is virtually free of voids, exhibits overall higher Young's modulus E and first fracture stress σ_f values than plate B, which contains a significant proportion of voids. The calculated values of E and σ_f are presented in Table 3.3, alongside with the corresponding void surface fractions estimated from optical micrographs in section 3.3.2. In plate A, the E and σ_f values of specimens c_{11} and c_{41} are close to 7 GPa and 250 MPa, respectively (c_{51} exhibits slightly inferior properties as a result of a sectioning defect: the specimen is not exactly cubic). On the other hand, the compressive properties of plate B degrade significantly as the void fraction increases. Note that the E and σ_f values of specimen c_{51} , which contains 10 % porosity, are twice lower than those of plate A specimens. These observations lead to the (unsurprising) conclusion that the higher the porosity in the composite specimens, the stronger

the drop in their mechanical properties compared to a void-free specimen - except for the fracture strain ϵ_f value, which does not seem to be affected by porosity and ranges between 0.05 and 0.07 in all A and B specimens.

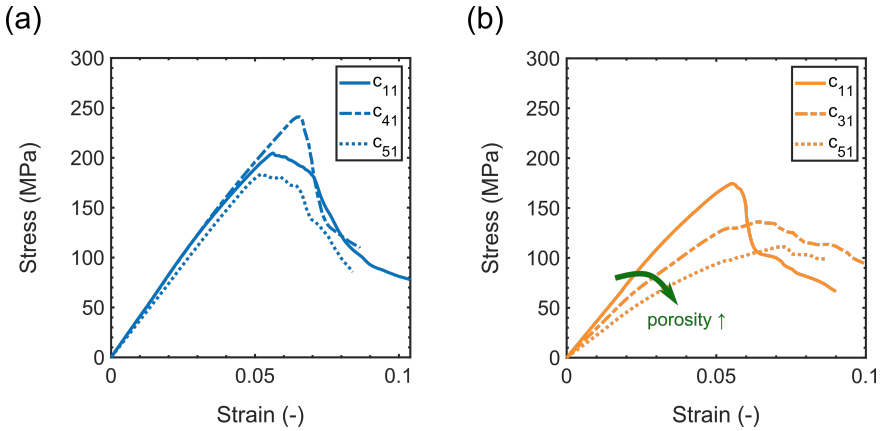


Fig. 3.11 Stress-strain curves obtained from the transverse compression testing of composite specimens extracted from plates (a) A and (b) B.

Table 3.3 Young's modulus E , fracture stress σ_f and void surface fraction of Elium composite specimens subjected to transverse compression parallel to the y -axis. For specimen c_{51} of plate A, the values of E and σ_f are not considered representative.

Plate	Specimen	E (GPa)	σ_f (MPa)	Void fraction (%)
A	c_{11}	6.7	286	< 0.1
	c_{41}	6.9	244	< 0.1
	(c_{51})	5.6	215	< 0.1
B	c_{11}	6.1	207	2.7
	c_{31}	5.1	162	5.4
	c_{51}	3.5	132	10.1

DIC analysis and mean-field homogenisation (MFH) models were used to better understand the influence of voids on the respective values of σ_f and E for Elium composites subjected to transverse compression. Figure 3.12 shows the vertical strain ε_y maps obtained from the DIC analysis of plate B specimens c_{11} , c_{31} and c_{51} just before the first failure event was observed. Strain fields have been superimposed onto the corresponding optical micrographs for easier interpretation. The latter allow observing the evolution of void morphology along the y -axis of plate B in more details compared to Figure 3.6 (b). As porosity increases along the y -axis, inter-tow macrovoids adapt to the shape of the matrix pockets, which are elongated in the direction perpendicular to compressive loading. As a result, macrovoids display sharper, narrower “tips” as y increases. DIC strain maps reveal that the sharper the void “tips”, the stronger the strain localisation in the y -direction. This explains why the macroscopic fracture stress σ_f of plate B specimens decreases as y increases. Note that a few examples of sharp *versus* blunt void tips are depicted with yellow and blue ellipses in Figure 3.12, also highlighting the resulting difference in terms of strain concentration.

Two additional observations can be made from the micrographs and DIC results shown in 3.12. First, in addition to inter-tow macrovoids (which account for most of the measured porosity in plate B), note that a few clusters of smaller, intra-tow voids are present. These also induce significant strain localisation, as depicted by the white arrows in Figure 3.12. Second, the average value of ε_y calculated from DIC results is close to 0.02 for all three specimens, which is below the macroscopic value of fracture strain obtained from stress-strain curves (i.e. around 0.06). This discrepancy is attributed to the fact that voids, which undergo extensive deformation during transverse compression, have been excluded from the DIC analysis. This logically results in a systematic underestimation of the mean value of ε_y , with respect to that of the macroscopic failure strain.

The influence of void shape and volume fraction on the Young’s modulus of Elium composites subjected to transverse compression was assessed qualitatively via simple mean-field homogenisation (MFH) models. MFH assumes the existence of relationships between the volume averages of stress and strain fields in each phase of a two-phase material. Most MFH models derive from the early work of Eshelby [109], who determined the stress level inside a single ellipsoidal inclusion embedded in an infinite solid body.

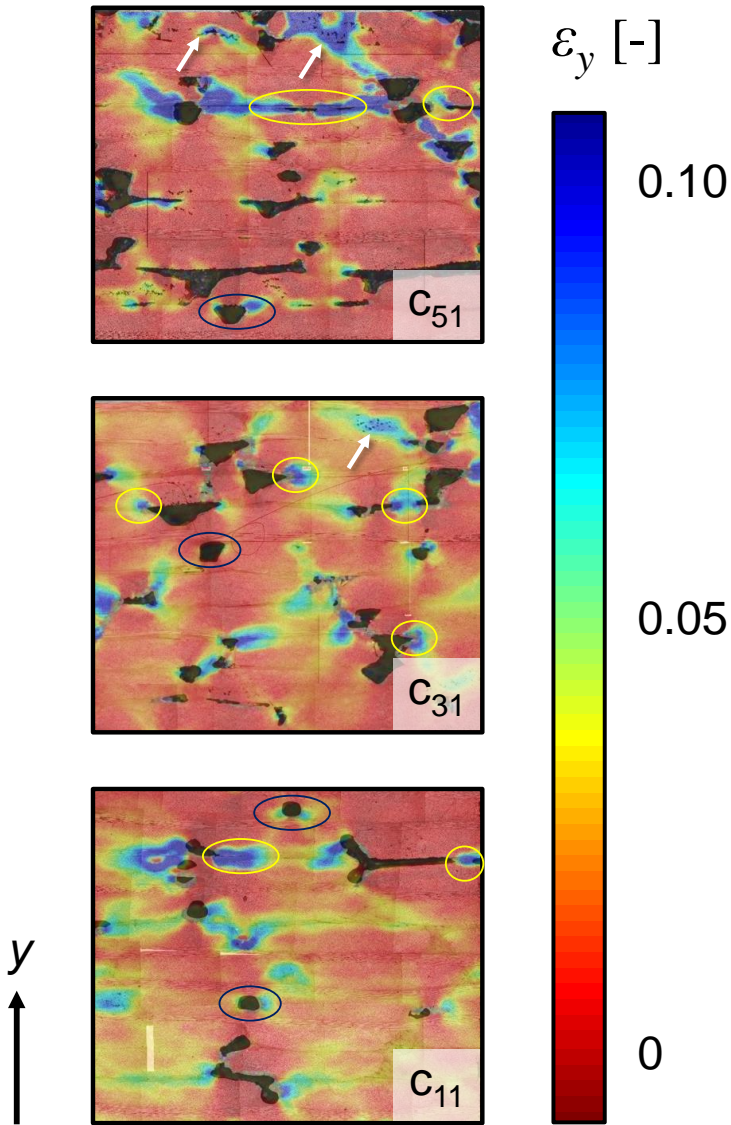


Fig. 3.12 Vertical strain ε_y fields obtained from the DIC analysis of plate B specimens c_{11} , c_{31} and c_{51} , from bottom to top. Arrows and ellipses respectively indicate areas of high strain concentration within and between fibre tows. Yellow and blue ellipses are used to distinguish acute ($\varepsilon_y \geq 0.1$) from more diffuse ($0.05 \leq \varepsilon_y < 0.1$) strain localisation phenomena.

3 | Top-down preliminary exercise on thick Elium composites

In the case of interest, the isolated phase consists of voids, while the second phase is the (void-free) Elium composite. Figure 3.14 compares the evolution of E as a function of porosity Φ (i.e. void volume fraction) measured experimentally in plates A and B *versus* predicted by the following MFH models. Note that we assume Φ values to be equal to the areal void fractions obtained from optical micrographs in section 3.3.2.

- **Voigt model.** The Voigt model provides an upper bound [110] for the evolution of E as a function of Φ by considering a weighted mean of the two phases' moduli:

$$E_{\text{Voigt}} = \Phi E_{\text{void}} + (1 - \Phi) E_{\text{comp}}, \quad (3.1)$$

where E_{comp} is the Young's modulus of a void-free Elium composite under transverse compressive loading. In this work, the value of E_{comp} is assumed to be equal to 6.8 GPa, i.e. the average modulus value measured in plate A specimens c_{11} and c_{41} .

- **Becker and Hopmann's model [111].** This approach, which is derived from the work of Eshelby [109], and Mori and Tanaka [112], is especially adapted to the case of unidirectional fibre-reinforced composites containing voids. As illustrated by Figure 3.13, the latter are assumed to have an infinite length parallel to fibre orientation, as well as an elliptic base characterised by the aspect ratio α . Though the Elium composites are not perfectly unidirectional, this model (referred to as the B-H model) should provide a reasonably accurate estimation of the transverse compression modulus E as a function of porosity Φ via the following equation (cf. equation (45) in [111]):

$$E_{\text{B-H}} = E_{\text{comp}} \alpha \frac{1 - \Phi}{\alpha + 2\Phi}, \quad (3.2)$$

where α is the aspect ratio of the voids, as described in Figure 3.13.

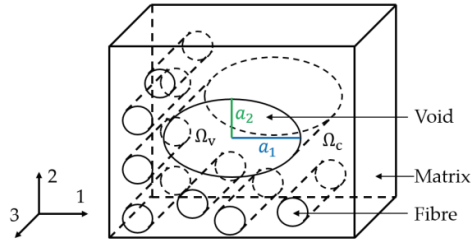


Fig. 3.13 Definition of fibre and void orientation in the work of Becker and Hopmann [111]. Aspect ratio α is defined as a_2/a_1 . Directions 2 and 1 respectively correspond to the y - and z -axes for plate A and the y - and x -axes for B, see section 3.2.2.

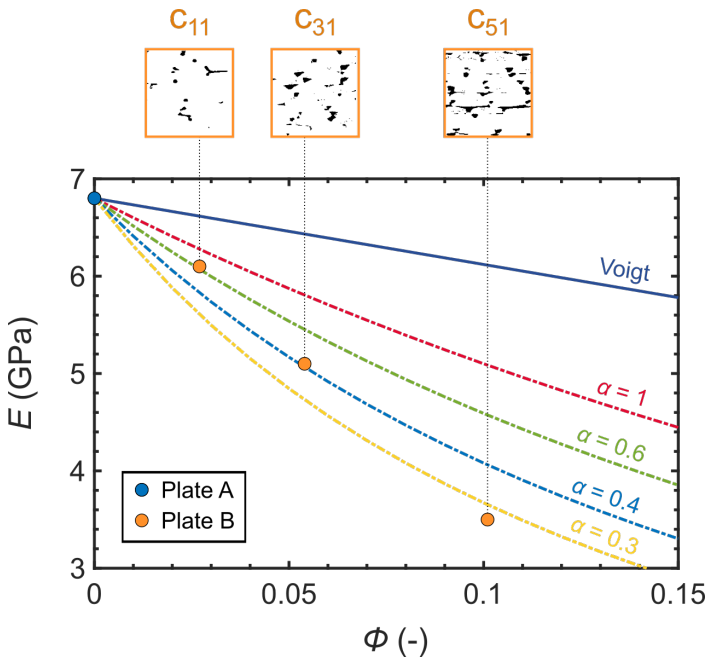


Fig. 3.14 Evolution of the Young's modulus E of the Elium composite in transverse compression with porosity Φ , as measured experimentally *versus* as predicted from Voigt (full line) and B-H models (dashed lines) for several values of void aspect ratio α .

As expected, the measured drop of Young's modulus with increasing porosity is largely underestimated by the Voigt model. The phenomenon is not captured either by a single B-H equation, see Figure 3.14. However, the modulus value obtained experimentally for plate B specimen c_{11} (which contains around 3 % voids), seems to be accurately predicted by the B-H equation corresponding to $\alpha = 0.6$. The measured modulus values for specimens c_{31} and c_{51} , whose void fractions are close to 5 and 10 %, are best predicted by the B-H equations corresponding to $\alpha = 0.4$ and $\alpha = 0.3$, respectively. From a qualitative point of view, this suggests that the aspect ratio of the voids decreases as y increases in plate B. This assumption is consistent with the observation made previously with respect to the void "tips" becoming sharper as y increases (see Figure 3.12). Hence, the aspect ratio of these void "tips" seems to have a dramatic impact on the mechanical response of the composite, at least in transverse compression.

3.4 Conclusions

This preliminary phenomenological study aimed at exploring the effect of external heating on the chemical and mechanical properties of two identical 7 cm-thick Elium composite plates produced by vacuum infusion and in-situ polymerisation. While plate A was left to polymerise at room temperature, plate B was subjected to a heating ramp up to 50 °C to shorten the processing time. The key findings of the study are the following:

- External heating may have a significant impact on the thermokinetic behaviour of Elium laminates during in-situ polymerisation, by triggering an overall more intense gel effect (compared to a similar laminate processed at room temperature).
- The resulting exotherm leads to local monomer boiling and subsequent void formation wherever the maximum temperature reaches or exceeds 101 °C during polymerisation. As observed in plate B, the maximum temperature value seems to govern the extent of void formation: the higher it is, the greater the local porosity in the final part. The total amount of time spent at (or above) 101 °C does not seem to have a first-order effect on void formation.
- Heating a thick Elium laminate locally (e.g. from the bottom, via a heating mould) seems to induce a "snowballing" gel effect, starting from the plies in contact with the heat source and propagating to the other plies

with increasing intensity. In the case of plate B, higher temperatures are reached as we move away from the heating mould, i.e. as we get closer to the surface of the laminate. The observation of a gradient in void size and volume fraction across the thickness of B is a direct consequence of this phenomenon. The intrinsic physical properties of the matrix, however, do not seem to be significantly affected by changes in the processing temperature. They remain relatively homogenous across the thickness of plate B, and are overall very close to those measured in plate A. This is not surprising, as some³ physical properties of thermoplastic polymers, including the glass transition temperature, yield stress (which is related to hardness) and elastic modulus [113] are known to plateau as the molecular weight of the polymer chains keeps increasing much beyond the critical entanglement molecular weight.

- Heterogenous void patterns across the thickness of Elium composites can have an unpredictable effect on the mechanical response. In plate B, void shape and volume fraction both vary significantly along the thickness direction. As voids get larger, they become more and more elongated as their growth is constrained by the shape of inter-tow matrix pockets. Elongated void “tips” act as pre-cracks by inducing intense strain localisation in the surrounding material, ultimately leading to the macroscopic failure of the laminate during loading. Existing MFH models allow predicting the impact of porosity on the mechanical properties of fibre-reinforced composite materials, provided the average aspect ratio of the voids remains relatively constant throughout the part - which is not the case here.

³Other physical properties - in particular mechanical properties - keep increasing as the molecular weight increases, e.g. the impact strength, fracture toughness and creep resistance [113].



What is next ?

The questions raised by this preliminary study are consistent with the identified gaps in the literature and allow refining the scientific questions outlined previously. In particular, there seems to be a link between void formation through monomer boiling (Q1) and the occurrence of thermokinetic coupling effects during the polymerisation of Elium (Q3) within thick preforms (Q2). More precisely, the existence of non-trivial interactions between heat transport and heat generation mechanisms during the in-situ polymerisation of Elium within thick laminates was highlighted. At this stage, multi-physics modelling emerged as an essential tool for capturing the peculiar thermokinetic behaviour of thick Elium composites, and ultimately predicting the impact of processing temperature and preform thickness on monomer boiling and subsequent void formation.

4

Thermokinetic behaviour of thick Elium laminates during in-situ polymerisation

This chapter is based on the published article *Processing maps based on polymerisation modelling of thick methacrylic laminates*, S. F. Gayot, C. Bailly, T. Pardoën, P. Gérard and F. Van Loock, *Materials and Design* 196 (2020), 109170 [4].

4.1 Introduction

The recyclability of lightweight materials with high specific strength and stiffness is an ongoing challenge in the composite manufacturing industry. This challenge is driving the transition from thermoset to recyclable thermoplastic matrices for fibre-reinforced polymer composites [79, 114]. Dedicated thermoplastic resin formulations have been developed to ensure compatibility with existing liquid composite moulding (LCM) manufacturing techniques. For instance, a range of methyl methacrylate (MMA)-based resins has been designed for the production of thermoplastic fibre-reinforced polymer composites via resin transfer moulding or vacuum infusion [44, 115–117]. During composite manufacturing via LCM, the monomer-based resin is infused through a preform, consisting of layers of glass or carbon fibre mats, before undergoing in-situ polymerisation.

Composites produced by LCM techniques contain defects such as micro- and macro-sized voids. Porosity may have a significant and unpredictable impact on the mechanical behavior [118–122]. Voids nucleate and grow during the manufacturing process of epoxy-based composites due to a number of phenomena including incomplete resin degassing, air entrapment during mould filling, volatilisation of resin components (or polymerisation by-products) during in-situ curing, and/or matrix shrinkage upon curing and cooling [123–127]. Several process control strategies have been developed to reduce void nucleation and growth during LCM with epoxy resin [44, 124, 128–130].

The main source of cavitation during the manufacturing of MMA-based composites is through monomer boiling during in-situ polymerisation [44, 51, 97]. As discussed by Murray et al. [114], a practical challenge arises when producing thick laminates (in the order of 1 cm and above). The free-radical polymerisation kinetics of MMA exhibits a gel effect (also known as Trommsdorff effect [19]): when the degree of monomer conversion exceeds a critical value, the exothermic reaction self-accelerates and the temperature increases. Voids nucleate and grow within the polymerising matrix when the boiling temperature of the residual monomer is locally exceeded [51, 97].

An external heat source is often used to reduce the polymerisation time [84]. The external heating program can be adapted in order to control

the maximum temperature within the preform and, therefore, void nucleation due to monomer boiling. The compromise between a short cycle time and the absence of porosity can be found via a trial-and-error approach, as is common practice in the industry. Alternatively, a thermochemical model, informed by in-situ process monitoring data, can guide this process design exercise by predicting the (maximum) temperature within the matrix as a function of processing parameters such as preform thickness and external heating rate. Such a model needs to account for (1) heat transfer within the moulded preform and to the environment and (2) the release of heat due to the auto-accelerating exothermic reaction of MMA.

A large number of studies focus on the auto-accelerating nature of the polymerisation of MMA. Trommsdorff [19] and Norrish and Smith [18] related the gel effect to a decrease of the coefficient quantifying the rate of radical termination k_t . The decrease of k_t occurs at a critical value of monomer conversion χ at which the diffusivity of the polymer radicals is significantly reduced. Analytical frameworks have been developed to predict the dependence of k_t upon χ , often based on the concept of free volume, see, for example, the work of Hamielec [105, 131, 132] and of Achilias [74, 133, 134]. Empirical models relating the sensitivity of k_t to also exist [62, 135–137].

Many numerical thermochemical models have been developed to predict the curing temperature and the degree of monomer conversion during vacuum infusion of fibre-reinforced thermoset composites. Most of these make use of the approach of Loos and Springer [138] who constructed an experimentally validated one-dimensional (1D) framework coupling a heat equation with the curing kinetics of an epoxy matrix. Curing tests were conducted on relatively thick (up to 1.5 cm) carbon prepreg lay-ups in an autoclave and good agreement between the predicted and measured temperature profiles was observed. While many similar one- to three-dimensional models have been reported for the curing of thermoset composites [139–145], only a limited number of them are adapted to the polymerisation of thermoplastic composites [49, 97, 146]. Borzacchiello et al. [146] and Suzuki et al. [97] have constructed 1D models to study the polymerisation of methacrylate-based resins in composites. Borzacchiello et al. [146] combined the heat equation with a calibrated empirical model for the polymerisation kinetics, and gave predictions for the temperature profiles measured during the polymerisation of a methacrylic dental cement. Suzuki et al. [97] also solved the heat equation to predict the tempera-

ture and degree of monomer conversion during the in-situ polymerisation of an MMA-infused glass fabric preform of thickness ranging from 10 cm to 50 cm. Suzuki and co-workers considered a preform sandwiched between two glass plates at constant temperature ($\approx 20\text{ }^\circ\text{C}$) and assumed the preform to be equivalent to a homogeneous slab of variable thickness. To reduce the computational cost, Suzuki et al. assumed the value of the termination coefficient k_t to be independent of temperature and monomer conversion. Hence, their model does not account for the gel effect, and the predicted profiles are of qualitative nature.

The objective of the work is twofold. The first goal is to develop a thermochemical model for the in-situ polymerisation of MMA in fibre-reinforced composites, which takes the auto-accelerating polymerisation kinetics of MMA into account while being computationally efficient. Computationally efficient means that a parametric study can be performed at a reasonable computational cost (e.g. a few hours on a standard personal computer). The second goal is to apply the model to predict the temperature and the degree of monomer conversion across the thickness of an MMA-infused glass fibre layup as a function of key processing variables such as preform thickness and external heating rate. This allows the construction of processing diagrams based on the maximum temperature attained in the composite, which dictates the occurrence of monomer boiling (and thermally-induced cavitation).

4.2 Materials and experimental methods

4.2.1 Materials

Composite preforms were made from quasi-unidirectional non-crimp glass fabric plies (Chomarat, France) with an areal weight of $1.03\text{ kg}\cdot\text{m}^{-2}$ (85 % warp and 15 % weft). The resin comprised an infusion-grade monomer formula (Elium 191 OSA of Arkema, France) and a ketone peroxide thermal initiator (Luperox K10 of Arkema, France). The Elium 191 OSA mixture contains MMA monomers with 20 to 30 wt% acrylic copolymer chains, which serve as a viscosifying agent. The consumables for bagging and infusion were obtained from Diatex SAS (France). The temperature within the preforms was measured during the infusion experiments using J-type thermocouples (TC S.A., France).

4.2.2 Composite manufacturing

Composite plates were manufactured via vacuum-assisted infusion using the setup illustrated in Figure 4.1. Preforms were produced by laying up glass fabric plies onto a heating mould. Three sets of manufacturing conditions, corresponding to plates A, B, and C, were explored. These conditions differ in preform thickness and heating mould set temperature as detailed in Table 4.1. The preforms consisted of 90 fabric plies for conditions A and B, and of 60 plies for condition C. Thermocouples were placed in the middle of the preform (at $x = W/2, z = L/2$, see Figure 4.1.) at three locations along the y -axis, see Table 4.1.

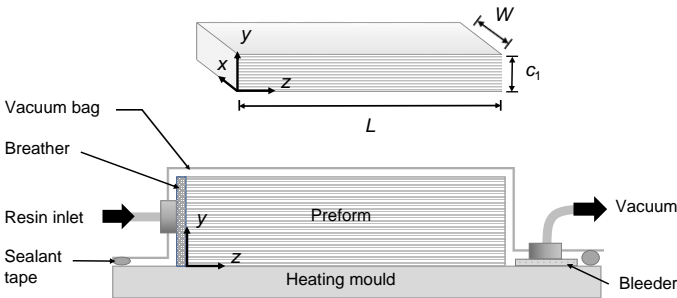


Fig. 4.1 Experimental setup for the vacuum infusion of laminates of variable thickness c_1 ($L = 60$ cm, $W = 40$ cm).

Table 4.1 Summary of the processing conditions for tests A, B and C.

Experimental condition	A	B	C
Ambient temperature during experiment T_{ext}	$\approx 17^\circ\text{C}$	$\approx 25^\circ\text{C}$	$\approx 21^\circ\text{C}$
Laminate structure	90 plies [[0 _{warp} /90 _{weft}] ₄₅] _s		60 plies [[0 _{warp} /90 _{weft}] ₃₀] _s
Final part thickness	$c_1 = 73$ mm		$c_1 = 49$ mm
Location of thermocouples	Bottom: ply 5/90 ($y \approx 0.06c_1$) Middle: ply 45/90 ($y = 0.50c_1$) Top: ply 85/90 ($y \approx 0.94c_1$)		Bottom: ply 5/60 ($y \approx 0.08c_1$) Middle: ply 30/60 ($y = 0.50c_1$) Top: ply 55/60 ($y \approx 0.92c_1$)

Note that an additional test for conditions A and B was conducted. The measured temperature profiles at the top of the plate during the nominal and repeat tests for conditions A and B were close to identical. Each fibre stack was sealed with a vacuum bag and prepared for resin infusion. The resin mix was made with three parts initiator per hundred parts resin, mechanically stirred for 5 min, and then degassed for 1 min at a pressure close to 100 mbar. Infusion tests were conducted at a pressure close to 100 mbar at room temperature; the resin flows in the direction of the z -axis (i.e. aligned with the fibre tows). For all test conditions, the resin front reached the section instrumented with thermocouples (at $z = L/2$) when the process time t was close to 5 min (where $t = 0$ corresponds to the start of the infusion process). The resin inlet and vacuum outlet were clamped shut at the end of the infusion process. Then, for conditions B and C, the infused preform was heated via the heating mould from room temperature to a set temperature T_p equal to 50 °C (with a controlled heating rate close to 0.5 °C.min⁻¹), see Figure 4.2. The mould set temperature was maintained for 30 min, before the external heating was ceased. The polymerisation of plate A occurred without any external heating. Upon completion of the polymerisation reaction, at process time $t \gg t_3$ (see Figure 4.2), the plate was left to cool down to room temperature and the composite was removed from the mould. Final fibre volume fractions were close to 0.5.

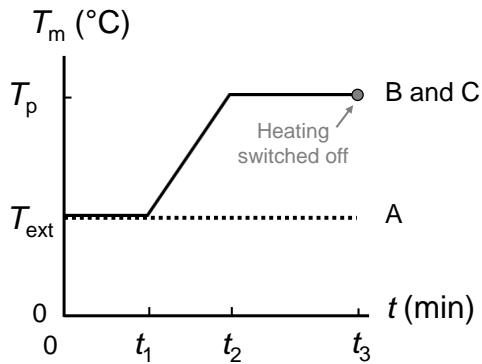


Fig. 4.2 Heating mould temperature T_m versus process time t for test conditions A, B and C, where T_{ext} denotes the ambient temperature, T_p (= 50 °C) the mould set temperature, t_1 (\approx 25 min) the end of the infusion stage, t_2 (\approx 75 min) the end of the heating ramp, and t_3 (\approx 105 min) the end of the temperature plateau at $T_m = T_p$.

4.2.3 Composite characterisation

Cuboids of dimensions $10 \times 13 \times 10 \text{ mm}^3$ were machined from composite plates A and B using a water-cooled disk-milling cutter, according to the sectioning diagram shown in Figure 4.3. A surface perpendicular to the fibre tow orientation was polished each side using resin-bonded diamond discs (successive grit of P1200 and P4000) and an alumina suspension (de-agglomerated 0.05 micron alumina suspension of Allied, USA) for the finishing step. Micrographs of the polished surfaces were taken with an optical microscope (AX70 Provis, Olympus, Japan). The porosity Φ of the samples was measured by analysing micrographs with the ImageJ [147] software. A computed tomography (CT) machine was used to confirm the accuracy of these measurements, see section 4.6.3.

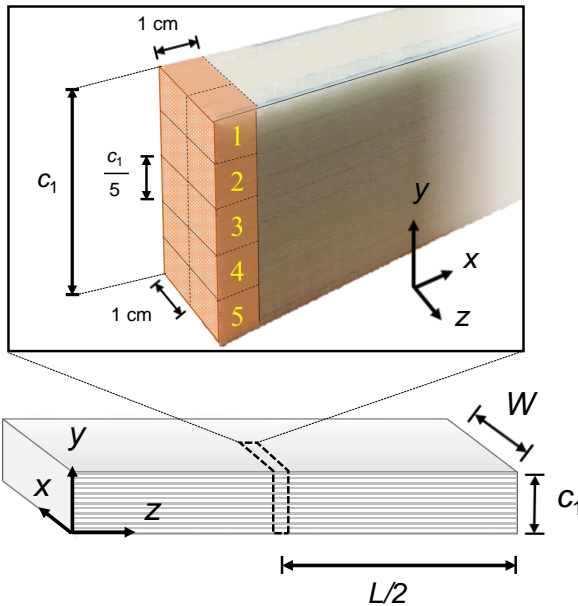


Fig. 4.3 Sectioning diagram for the characterisation of plates A and B ($L = 60 \text{ cm}$, $W = 40 \text{ cm}$, $c_1 = 73 \text{ mm}$).

4.3 Thermochemical model

4.3.1 Theory

A one-dimensional thermochemical model is developed to predict the temperature T , the concentration of monomer M and the degree of monomer conversion χ as a function of time t across the preform thickness. We assume the simulation time and the polymerisation reaction to start when the resin front is at the simulation section of interest ($t = t_s$). In this work, predictions will be given at the laminate's half-length (at $z = L/2$) where the thermocouples are placed during the infusion tests. As detailed in section 4.2.2, $t_s = 300$ s. The infused composite preform is idealised as a slab of homogeneous material with a uniform thermal diffusivity. It is recognised that the thermal diffusivity in the composite is of a heterogeneous nature and that the assumption of a uniform and time-independent value for the diffusivity, based on a rule of mixture, has a limited range of validity at the microscale. An extension of the model could include a time- and space-dependent thermal diffusivity. However, this extension is considered to lie beyond the scope of the present study.

The values of T , M and χ are assumed to be independent of the transverse x and z coordinates, see Figure 4.1 (i.e. edge effects are neglected close to the preform surfaces at the planes $x = 0, x = W, z = 0$, and $z = L$). The dependence of T upon position coordinate y and time t is calculated by solving the following heat equation:

$$\frac{dT}{dt} = \alpha_1 \frac{d^2T}{dy^2} - \frac{\Delta H}{C_p M_w^0} \frac{dM}{M_0 dt}. \quad (4.1)$$

The heat source term on the right-hand side of Eq. 4.1 accounts for the exothermic nature of the free-radical bulk polymerisation reaction [49, 97, 138, 146], where C_p is the specific heat capacity of the composite, ΔH is the enthalpy of polymerisation, M_w^0 is the molecular weight of MMA, M_0 is the initial molar concentration of MMA in the preform, and $\frac{dM}{dt}$ is the rate of change of monomer concentration. Both C_p and $\frac{dM}{dt}$ are a function of y and t as detailed below. The value of C_p is based on the temperature-dependent specific heat capacity of the MMA monomer $C_{p,m}$, of the poly(methyl methacrylate) (PMMA) polymer $C_{p,p}$, and of the fibre

$C_{p,f}$ via a rule of mixtures:

$$C_p = (1 - w_f) \underbrace{((1 - \chi) C_{p,m} + \chi C_{p,p})}_{C_p \text{ of resin matrix}} + w_f C_{p,f}, \quad (4.2)$$

where w_f is the mass fraction of the glass fibres.

Next, the value of $\frac{dM}{dt}$ is calculated based on five coupled kinetic equations governing the polymerisation of MMA. These kinetic equations are summarised in Table 4.2; the dependence of the kinetic constants upon T and χ is detailed in section 4.6.1. Several assumptions can be made to reduce the computing time. First, the long-chain hypothesis is invoked: polymer chains consist of a large number of monomer units (and this is experimentally validated for our system [1]), therefore the rate of propagation is much higher than the initiation rate r_i and the chain transfer rate $r_{tr,x}$. Flory's hypothesis is also used, i.e. the chemical reactivity of all propagating radicals is assumed to be equal. In addition, we apply the quasi-steady state approximation (QSSA) for the initiating and propagating radicals [148]. The QSSA is essential to reduce the computational cost of the model. This assumption is generally accepted to be valid for a free-radical polymerisation without diffusional limitations [148]. However, the significant reduction of the termination constant k_t at the end of the polymerisation reaction due to the gel effect may invalidate the use of the QSSA. This issue is discussed in detail in section 4.6.2. The conclusion of the analysis is that the QSSA for the MMA material system of interest remains valid up to a critical value of monomer conversion ranging from $\chi = 0.85$ to $\chi = 0.90$. Consequently, the effect of the QSSA on the predicted time-temperature profiles up to, and including, the peak temperature due to the thermal excursion is considered to be small. Finally, only chain transfer reactions from the propagating radicals to the monomer and initiator molecules are considered. The rate of change of monomer concentration $\frac{dM}{dt}$ then reads

$$\frac{dM}{dt} = -k_p M \sqrt{\frac{r_i}{k_t}} = -k_p M \sqrt{\frac{2fk_d I}{k_t}}, \quad (4.3)$$

where k_p , k_t and k_d are the rate coefficients of the radical propagation, radical termination and initiator decomposition steps, respectively, I is the initiator concentration and f is the efficiency factor of the initiator (equal

to the fraction of initiating radicals that lead to the formation of polymer chains). In the case of MMA, polymerisation is subject to various diffusional limitations: the values of k_t , k_p and f decrease with increasing conversion χ . The associated phenomena are known as the gel effect (as discussed above), the glass effect, and the cage effect, respectively [148]. The glass effect is related to a decrease in the mobility of monomer molecules (hence a decrease in k_p) as χ increases. The cage effect is related to a reduction of the mobility of newly-formed initiating radicals with increasing χ .

The free volume-based analytical model of Achilias et al. [74, 134] is used to calculate the dependence of k_p , k_t and f upon monomer conversion χ via the free volume V_f . The free volume of a polymer-solvent system is idealised as the ratio of the volume which is not occupied by the polymer chains nor the solvent molecules to the total volume of the polymer-solvent system [149, 150]. The equations for the dependence of k_p , k_t and f upon T and χ are given in section 4.6.1. The modification of Achilias's theory [74, 134] is a correction of the macroradicals diffusion constant in the entangled regime in order to account for the effective entanglement density. The values of the kinetic and physical parameters of the theory above are summarised in Tables 4.3 and 4.4.

Table 4.2 Overview of the free-radical polymerisation mechanism ($M =$ MMA monomer, $I =$ initiator, $R_n^\bullet =$ macroradical with n monomer units, $R^\bullet =$ all macroradicals, $P =$ dead polymer, $X =$ transfer agent, i.e. M, P, I or other molecule, $f =$ initiator efficiency, $C_x =$ transfer constant for chain transfer to transfer agent X).

Step	Equation	Kinetic coefficient	Reaction rate equation
Initiator decomposition	$R_2 \rightarrow 2I^\bullet$	k_d	$r_d = 2fk_d[I_2]$
Initiation	$I^\bullet + M \rightarrow IM^\bullet$	k_i	$r_i = k_i[R^\bullet][M]$
Propagation	$R_n^\bullet + M \rightarrow P_n^\bullet$	k_p	$r_p = k_p[R^\bullet][M]$
Termination by recombination by dismutation	$R_n^\bullet + R_m^\bullet \rightarrow P_{n+m+2}$ $R_n^\bullet + R_m^\bullet \rightarrow P_{n+1} + P_{m+1}$	k_t (accounts for both mechanisms)	$r_t = k_t[R^\bullet]^2$ (accounts for both mechanisms)
Chain transfer	$R_n^\bullet + X \rightarrow P_n + X^\bullet$	$k_{tr,X}$	$r_{tr,X} = C_x k_p [R^\bullet][X]$

Table 4.3 Kinetic parameters and material properties for the infusion of a glass fibre preform with MMA.

Parameter	Symbol	Value	Unit	Reference
Weight fraction of glass fibres	w_f	≈ 0.73		this work
Preform diffusivity	a_1	2.4×10^{-7}	$\text{m}^2 \cdot \text{s}^{-1}$	[75]
Mould diffusivity	a_2	3×10^{-7}	$\text{m}^2 \cdot \text{s}^{-1}$	[75]
Thermal conductivity of vacuum bag	λ_1	0.2	$\text{W} \cdot \text{m}^{-1} \cdot \text{K}^{-1}$	[75]
Thermal conductivity of mould	λ_2	0.4	$\text{W} \cdot \text{m}^{-1} \cdot \text{K}^{-1}$	[75]
Thermal expansion coefficient of MMA	β_m	1.2×10^{-3}	K^{-1}	[151]
Thermal expansion coefficient of PMMA	β_p	2.1×10^{-4}	K^{-1}	[152]
Specific heat capacity of MMA	$C_{p,m}$	$114.1 + 6.83T$	$\text{J} \cdot \text{kg}^{-1} \cdot \text{K}^{-1}$	[153]
Specific heat capacity of PMMA	$C_{p,p}$	$-14.45 + 4.65T$	$\text{J} \cdot \text{kg}^{-1} \cdot \text{K}^{-1}$	[154]
Specific heat capacity of glass fibre	$C_{p,f}$	$442.1 + 1.24T$	$\text{J} \cdot \text{kg}^{-1} \cdot \text{K}^{-1}$	[155]
Specific volume of MMA	v_m	1.6×10^{-3}	$\text{m}^3 \cdot \text{kg}^{-1}$	[154]
Specific volume of PMMA	v_p	8.55×10^{-4}	$\text{m}^3 \cdot \text{kg}^{-1}$	[154]
Glass transition of MMA	$T_{g,m}$	-126		[156]
Glass transition of PMMA	$T_{g,p}$	114		[156]
Free volume of MMA at glass transition temperature	$V_{g,p}$	0.025		[74]
Free volume of PMMA at glass transition temperature	$V_{g,m}$	0.025		[74]
Pre-exponential factor of the MMA diffusion coefficient	D_m^0	3.0×10^{-8}	$\text{m}^2 \cdot \text{s}^{-1}$	[62]
Interaction radius of propagation	R_p	2.93×10^{-10}	m	[62, 74, 157]
Average entanglement spacing in PMMA	j_c	70		[154]
End-to-end distance per square root of number of monomer units in chain	δ	6.9×10^{-10}	m	[157]
Molecular weight of MMA	M_w^0	100.12	$\text{g} \cdot \text{mol}^{-1}$	[158]
Molecular weight between entanglements of PMMA	M_e	7,000	$\text{g} \cdot \text{mol}^{-1}$	[154]
Initial monomer concentration of MMA	M_0	3,700	$\text{mol} \cdot \text{m}^{-3}$	N/A
Initial initiator concentration	I	14	$\text{mol} \cdot \text{m}^{-3}$	N/A
Polymerisation enthalpy of MMA	δH	57.8	$\text{kJ} \cdot \text{mol}^{-1}$	[154]
Pre-exponential factor for propagation	A_p	2.67×10^3	$\text{m}^3 \cdot \text{mol}^{-1} \cdot \text{s}^{-1}$	[159]
Activation energy for propagation	E_p	22.36	$\text{kJ} \cdot \text{mol}^{-1}$	[159]
Pre-exponential factor for the termination rate coefficient	A_t	1.984×10^5	$\text{m}^3 \cdot \text{mol}^{-1} \cdot \text{s}^{-1}$	[160]
Activation energy for termination	E_t	5.89	$\text{kJ} \cdot \text{mol}^{-1}$	[160]
Pre-exponential factor for initiator decomposition rate	A_d	4.017×10^5	s^{-1}	[161]
Monomer transfer coefficient	C_m	5×10^{-5}		[154]
Initiator transfer coefficient	C_i	6×10^{-2}		[154]

Table 4.4 Fitting parameters of the thermochemical model, including their selected values and imposed range of acceptability.

Parameter	Symbol	Fitted value	Unit	Accepted range	References
Convection coefficient of air (bag side)	h_1	6	$\text{W}\cdot\text{m}^{-2}\cdot\text{K}^{-1}$	0.5 – 50	[162]
Convection coefficient of air (mould side)	h_2	0.5	$\text{W}\cdot\text{m}^{-2}\cdot\text{K}^{-1}$	0.5 – 50	[162]
Initial initiator efficiency	f_0	0.5		0.3 – 0.8	[14]
Activation energy for initiator decomposition	E_d	63.25	$\text{kJ}\cdot\text{mol}^{-1}$	50 – 100	[163]
Normalised initiator diffusion coefficient	D_i^0/C	12.5		$10^{-4} - 10^4$	[62, 74]
Overlap factor of monomer	γ_m	0.8		0 – 2	[62, 74, 133, 164]
Overlap factor of macroradical	γ_t	1.8		0 – 2	[62, 74, 133, 164]
Overlap factor of initiator	γ_i	0.05		0 – 2	[62, 74, 133, 164]
Pre-exponential factor of PMMA diffusion coefficient	D'_p	3×10^{-6}	$\text{m}^2\cdot\text{s}^{-1}$	$10^{-7} - 10^{-5}$	[74, 133]

4.3.2 Numerical implementation of the model

The thickness of the preform is discretised into N_y intervals δy ($= c_1/N_y$, see Fig. 4.4). Likewise, the simulation time, which starts when the process time t is equal to t_s , is discretised into N_t time increments δt ($= t_{\text{tot}}/N_t$), where t_{tot} is the total reaction time. In this study, we take $\delta y = 1$ mm, $t_{\text{tot}} = 6 \times 10^4$ s and $\delta t = 7$ s. Note that the selected value for t_{tot} includes the polymerisation time of the resin and the cooling time of the plate.

Convective boundary conditions are considered at the top surface of the preform (i.e. at $y = c_1$, see Fig. 4.4):

$$\left(\frac{dT}{dy}\right)_{y=c_1} = \frac{h_1}{\lambda_1} (T_{y=c_1} - T_{\text{ext}}), \quad (4.4)$$

where h_1 is the convective heat transfer coefficient for the preform/air interface, λ_1 is the thermal conductivity of the polymer-based vacuum bag material, and T_{ext} is the ambient temperature outside the bag. A more sophisticated boundary condition is applied at the bottom and accounts for the transfer of heat from the preform to the infusion mould via conduction as follows. The mould consists of a homogeneous plate of thickness c_2 made of glass fibre reinforced polymer with a thermal diffusivity α_2 , and covered with a polymeric heating film of thickness close to 0.1 mm. Therefore, the spatial mesh extends from $y = 0$ to $y = -c_2$ with nodes equally spaced by intervals δy , see Fig 4.4. The temperature T on the nodes of the extended mesh is calculated as a function of time by solving the heat equation:

$$\frac{dT}{dt} = \alpha_2 \frac{d^2T}{dy^2}. \quad (4.5)$$

A convective boundary condition is considered at the bottom of the mould (i.e. at $y = -c_2$):

$$\left(\frac{dT}{dy}\right)_{y=-c_2} = \frac{h_2}{\lambda_2} (T_{y=-c_2} - T_{\text{ext}}), \quad (4.6)$$

where h_2 is the convective heat transfer coefficient for the mould/air interface and λ_2 is the thermal conductivity of the mould material. Note that, for processing conditions B and C, we impose the time-dependent temperature profile presented in Fig. 4.2 at node $y = -\delta y$ to account for controlled external heating via the heating film.

The MATLAB (R2018a) computing environment is used for the implementation of the 1D thermochemical model detailed in section 4.3. The set of coupled equations is solved with the semi-implicit Crank-Nicolson finite difference method. The computing times for all predictions given in this article do not exceed 60 s on a standard personal computer (equipped with an Intel®Core™ i7 – 4600U 2.10 GHz processor and with 16 Gb of RAM).

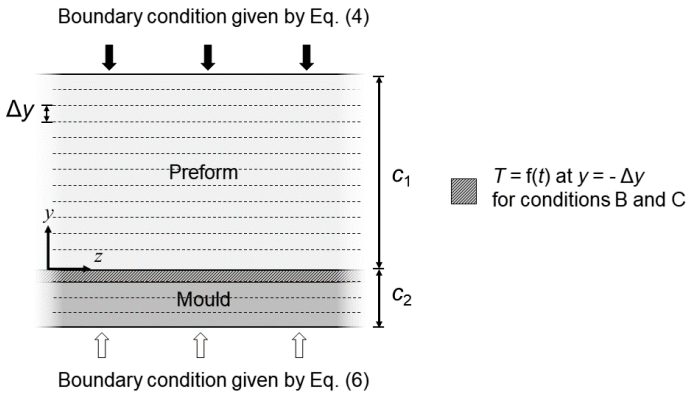


Fig. 4.4 Boundary conditions used in the 1D thermochemical model. Note that c_1 refers to preform thickness ($c_1 = 49$ mm for condition C and $c_1 = 73$ mm for conditions A and B) and c_2 is the thickness of the mould ($c_2 = 15$ mm). The time-dependent temperature profile applied at node $y = -\delta y$ for testing conditions B and C is given in Fig. 4.2).

4.4 Results and discussion

4.4.1 Infusion test results

Optical micrographs of samples extracted from plates A and B are shown in Fig. 4.5. The measured void content is sensitive to the heating program: the porosity of plate A is close to zero across the entire thickness, while the measured porosity in plate B increases from the bottom ($\Phi \approx 0$) to the top ($\Phi \approx 0.1$) of the plate. The measured temperature T_t at three locations along the thickness of plates A, B and C is plotted as a function of process time t in Fig. 4.6.

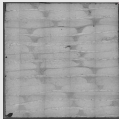
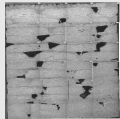
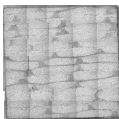
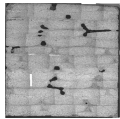
PLATE A No heating			PLATE B Heating to 50 °C (see Fig. 2)		
Specimen	3mm	Φ (%)	Specimen	3mm	Φ (%)
2		< 0.1	1		10
3		< 0.1	3		5.4
5		< 0.1	5		2.7

Fig. 4.5 Dependence of the measured porosity Φ upon measurement height for plates A and B ($c_1 = 73$ mm). Note that measurement height is defined via the sectioning numbers given in Fig. 4.3.

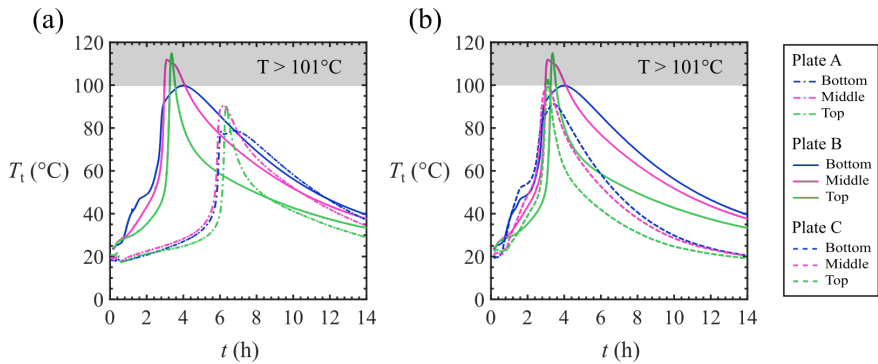


Fig. 4.6 Measured temperature T_t as a function of process time t at different locations across the thickness of (a) plates A and B and (b) plates B and C. See Table 4.1 for the y -coordinate corresponding to each measurement location.

A peak is observed on all time-temperature profiles; this is a signature of the gel effect. The measured temperature profiles are found to be sensitive to the measurement location along the y -axis of the preform: the maximum temperature increases from the bottom to the top of plates A and B, whereas the width of the peak decreases, see Fig. 4.6a. The peak temperature T_{\max} on the measured profile of plate B is almost 20 °C higher than the peak temperature on the corresponding profile of plate A.

The contrast in void content between plates A and B can be related to the difference in the time-temperature profiles. The boiling temperature T_b of the MMA monomer is close to 101 °C at a pressure equal to 1 bar [158]. Note that the pressure inside the vacuum bag rises back to a value close to, but below, atmospheric pressure upon impregnation of the preform¹. The value of T_b may therefore be lower than 101 °C (e.g. $T_b = 94$ °C at a pressure equal to 0.8 bar [44]), but in the remainder of this text we will assume $T_b = 101$ °C as a first-order approximation. The measured temperature T_t exceeds T_b at the mid-height and top of plate B, see Fig. 4.6a. This results in the observed void content in plate B at these locations. In contrast, the measured value of T_t remains below T_b throughout the infusion test for plate A, leading to a porosity close to zero across the thickness of the plate. In passing, we note that voids nucleated due to monomer boiling are unlikely to move due to buoyancy: the shear viscosity of infusion-grade MMA-based resins at the onset of the gel effect is close to 10 Pa.s, i.e. 100 times larger than the shear viscosity at the start of the polymerisation [46, 51]. The presence of the fibre tows is an additional obstacle to any movement across the thickness of the plate. Therefore, we expect the observed gradient in porosity in plate B to correspond to the observed increase in peak temperature across the thickness, see Fig. 4.6a. The difference in porosity between plates A and B demonstrates how external heating during vacuum infusion of an MMA-based resin may influence the microstructure of the polymerised composite part. Heating programs are typically used to shorten the manufacturing time. This is also illustrated in Fig. 4.6a: the end of the reaction (when the peak temperature, T_{\max} , is reached) occurs three hours earlier in plate B compared to plate A which has an identical

¹Grimsley et al. [165] and Moghaddam [166] conducted infusion tests with an epoxy resin on a glass fibre preform with dimensions similar to plates A, B and C in this study. They measured the resin pressure inside the bag throughout the curing process and found that the pressure ranged between 0.7 and 1 bar when the resin inlet and vacuum outlet were clamped shut after infusion.

thickness.

We now explore the effect of preform thickness on the measured temperature profile. The measured temperature T_t in plates B ($c_1 = 73$ mm) and C ($c_1 = 49$ mm) at three locations across the thickness is plotted as a function of process time t in Fig. 4.6b. Note that both plates are subjected to the heating program summarised in Fig. 4.2. The peak temperature values in plate B are close to 10 °C higher than in plate C. This result illustrates how the peak temperature (and, therefore, the possibility of cavitation due to monomer boiling) depends upon preform thickness c_1 .

4.4.2 Model calibration

The calibration parameters of the model presented in section 4.3 have been identified by using the measured temperature profiles of a single infusion test (plate B). These fitting parameters are summarised in Table 4.4 and have been adjusted in order to match the predicted T_t versus t profiles with the measured ones for the three measurement locations across the thickness of plate B. Note that a physically acceptable range for each calibration parameter is defined in Table 4.4 and imposed to the fitted value of each parameter. The temperature profiles predicted by the calibrated model are included in Fig. 4.7: good agreement is observed between the model predictions and the measurements after identification, but this is not a sufficient validation of the model yet. We note in passing that, without the calibration step, the structural response of the predicted T versus t response is close to the measured ones. For instance, the model predicts the typical observed shape of the temperature-time response close to the peak in temperature. The thermochemical framework also predicts a dependence of peak time t_{peak} upon preform thickness and a sensitivity of peak width to the measurement location across the thickness of the preform.

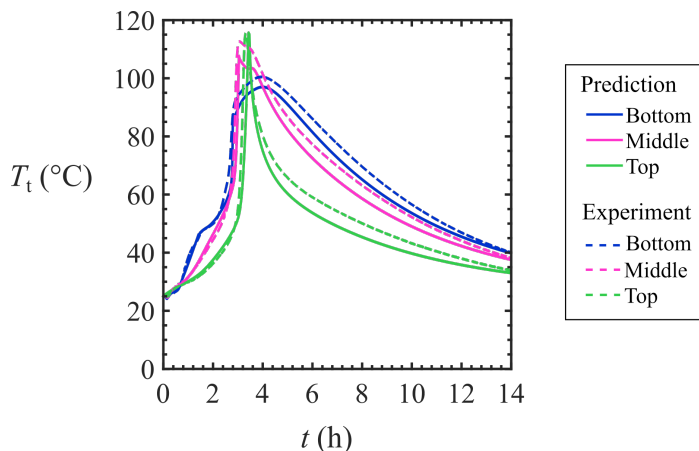


Fig. 4.7 Model identification by making use of the measured temperature profiles in plate B: predicted (solid lines) and measured (dashed lines) temperature T_t as a function of process time t at different locations across the thickness of the plate. See Table 4.1 for the y -coordinate corresponding to each measurement location.

The predicted values for the termination rate coefficient k_t , the propagation rate coefficient k_p and initiator efficiency f are plotted as a function of monomer conversion χ in Fig. 4.8, for a selected measurement location across the thickness of plate B. The curves obtained with the calibrated model are consistent with experimental data found in the literature for the bulk polymerisation of methacrylic monomers [167, 168]. The moderate increase of the value of k_p from $\chi = 0$ to $\chi = 0.8$ is due to the temperature increase in the preform. Four successive regimes are identified in Fig. 4.8, these correspond to the conversion regions defined by Achilias and co-workers [74, 133, 134]. The first regime corresponds to a free-radical polymerisation mechanism in the absence of any diffusional limit. At the onset of the second regime, the value of k_t decreases with increasing χ due to the gel effect: the macroradicals lose translational mobility. When the reaction proceeds and χ further increases, the propagation-related radical mobility starts to dominate and the value of k_t plateaus. This plateau corresponds to regime 3. When χ continues to increase, both radical propagation and termination rates abruptly decrease, indicating the onset of regime 4. The initiator efficiency factor f also decreases with increasing monomer conversion in regime 4 due to the cage effect.

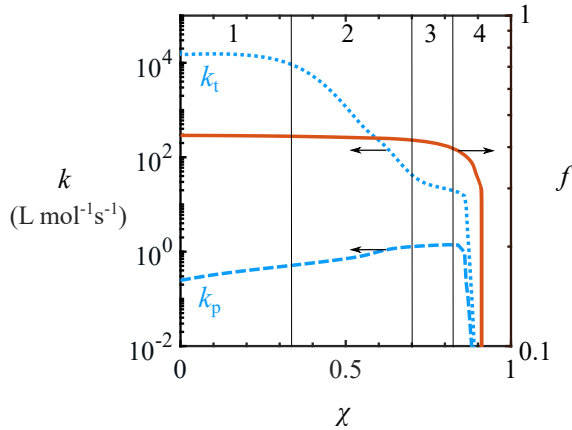


Fig. 4.8 Predicted values of k_p , k_t , and f as a function of monomer conversion χ by the calibrated model during the in-situ polymerisation of the MMA-based resin at the bottom of plate B ($y \approx 0.06c_1$). Four conversion regimes are identified.

4.4.3 Model validation based on temperature profile predictions

The calibrated model is now validated based on the experimental temperature profiles measured for plates A and C. The predicted and measured T_t versus t response at three locations across the thickness of preforms A and C is plotted in Figs. 4.9a and 4.9b, respectively. Recall the differences in processing conditions for plates A, B and C: plate A is polymerised without an external heating program, while plate C is thinner ($c_1 = 49$ mm) than plate B ($c_1 = 73$ mm), see Table 4.1. There is an excellent agreement between the predicted and measured temperature profiles for both testing conditions A and C. The peak temperature, peak time and the shape of the temperature profiles are accurately captured. In addition, the predicted sensitivity of the T_t versus t response to the measurement position across the thickness of the preform is in line with the measurement data.

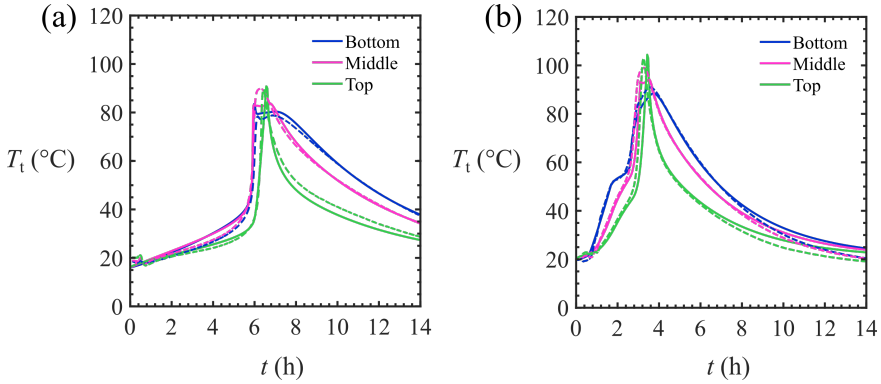


Fig. 4.9 Predicted (solid lines) and measured (dashed lines) temperature T_t as a function of process time t at different locations across the thickness of (a) plate A and (b) plate C. See Table 4.1 for the y -coordinate corresponding to each measurement location.

4.4.4 Conversion predictions

The predicted degree of monomer conversion χ is plotted as a function of process time t for tests A, B, and C in Figs. 4.10a, 4.10b and 4.10c, respectively. The shape of the χ versus t curves in Fig. 4.10 is close to identical for the three test conditions. First, the rate of monomer conversion is slow, and the slope of the χ versus t curve only moderately increases as the reaction proceeds. This corresponds to the first conversion regime identified in Fig. 4.8, during which there is no diffusional constraint on the reaction. Then, at a critical value of χ between 0.2 and 0.4, the reaction auto-accelerates. The gel effect results in a steep rise of the χ versus t curves, corresponding to regimes 2 and 3 shown in Fig. 4.8. Finally, a plateau value of χ close to 0.9 is reached, which marks the end of the reaction. This conversion plateau is consistent with the final drop in the values of k_p , k_t , and f observed in regime 4, see Fig. 4.8. The predicted plateau value of χ_{\max} ranges between 0.9 and 0.95 for the explored range of processing conditions, with a negligible dependence upon measurement location across the thickness. This value of χ_{\max} is slightly lower than the measured values (between 0.95 and 0.99 [1, 46, 51]) for the resin under consideration when subjected to similar processing conditions. This small discrepancy can be attributed to the use of the QSSA (see section 4.6.2), and the assumption that the initial value of conversion χ is equal to zero. In practice, some chains are present in the resin before polymerisation. These are added as

a viscosifying agent but have an influence on the polymerisation kinetics [44, 62, 97, 169]. One may account for the presence of the PMMA chains by assuming a non-zero initial value for conversion [97]. However, it is unlikely that their rheological behavior is identical to that of a 'pure MMA system' at a non-zero conversion value. The treatment of this complex behavior is beyond the scope of the present study. We therefore follow Zoller [62], assume the initial value of χ to be zero, and realise that the predicted value of χ_{\max} may be slightly below the typically measured value for χ_{\max} as a consequence of this assumption.

The predicted conversion profiles shown in Fig. 4.10 demonstrate that the auto-acceleration of the reaction starts in the lower part of preforms A, B and C, and the time at which the gel effect takes place increases with increasing height. Recall from Fig. 4.7 (test B) and Fig. 4.9 (tests A and C) that the predicted and measured T_t versus t response at the top of the plates exhibits a sharper temperature rise and a higher peak temperature compared to the temperature profile at the bottom of the plate. This is attributed to the excess heat coming from the lower part of the plate, where the auto-acceleration of the reaction first takes place. This effect is more pronounced for the infusion of a thick plate with external heating, as shown in Fig. 4.7 via the temperature profiles for test B.

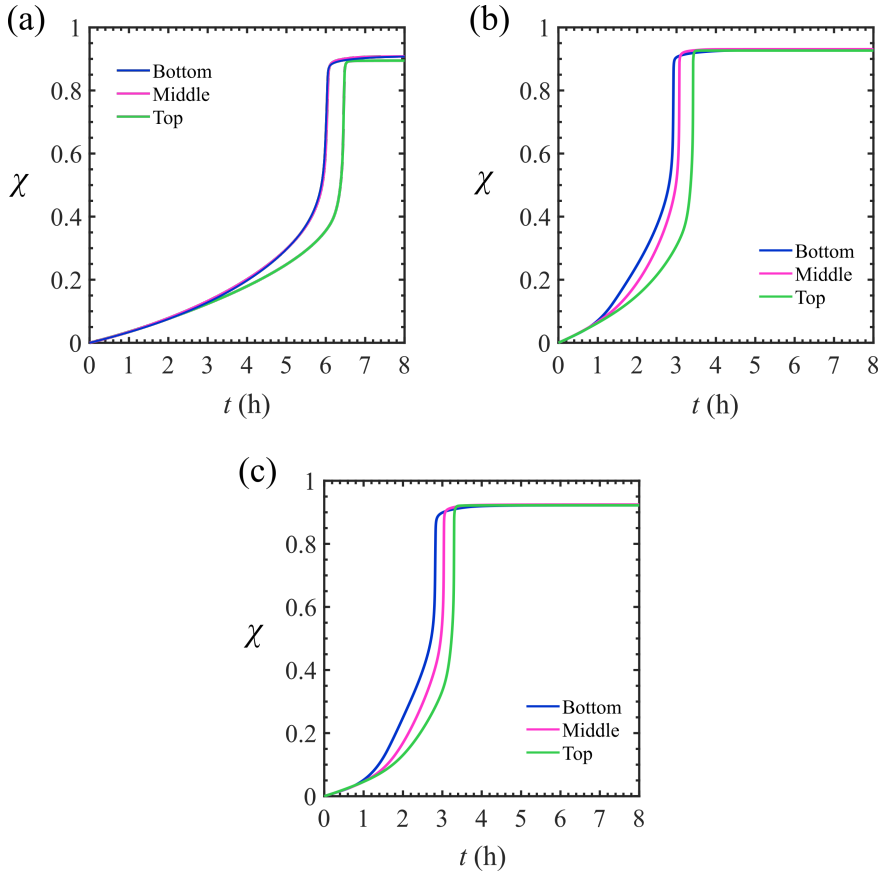


Fig. 4.10 Predicted degree of monomer conversion χ as a function of process time t for (a) plate A, (b) plate B and (c) plate C. See Table 4.1 for the y -coordinate corresponding to each measurement location.

4.4.5 Processing maps

Optimal processing conditions for vacuum infusion with an MMA-based resin should lead to short polymerisation times and laminates without thermally-induced voids. We assume that thermally-induced void nucleation (and growth) occurs when T_{\max} at any location exceeds the boiling temperature of the monomer ($T_b = 101\text{ }^\circ\text{C}$). We make use of the calibrated thermochemical model to illustrate how preform geometry, external heating conditions and the ambient temperature govern both T_{\max} (and, therefore, the possibility of monomer boiling) and the (minimum) polymerisation time. The simulations conducted for the predictions in this section are based on the values of the material and processing parameters given in Tables 4.3 and 4.4, unless stated otherwise.

The predicted value for T_{\max} is plotted in Fig. 4.11a as a function of mould set temperature T_p , for selected values of preform thickness and for a heating rate $\dot{q} = 0.5\text{ }^\circ\text{C}\cdot\text{min}^{-1}$ (and $T_{\text{ext}} = 25\text{ }^\circ\text{C}$). The value of T_{\max} increases with increasing T_p within the range $30 < T_p < 70\text{ }^\circ\text{C}$ for the explored range of preform thicknesses. In contrast, the value of T_{\max} is almost insensitive to T_p for $T_p < 30\text{ }^\circ\text{C}$ and $T_p > 70\text{ }^\circ\text{C}$. The predicted value of T_{\max} is plotted in Fig. 4.11b as a function of mould heating rate \dot{q} , for selected values of preform thickness and for $T_p = 50\text{ }^\circ\text{C}$ (and $T_{\text{ext}} = 25\text{ }^\circ\text{C}$). The value of T_{\max} is sensitive to \dot{q} within the narrow range $0.12 < \dot{q} < 0.5\text{ }^\circ\text{C}\cdot\text{min}^{-1}$. In addition, the predictions shown in Figs. 4.11a and 4.11b indicate that the processing window requiring $T_{\max} < 101\text{ }^\circ\text{C}$ shrinks as the preform thickness increases. Note that the location for test B in Figs. 4.11a and 4.11b is included.

We proceed by exploring the sensitivity of the calculated peak temperature T_{\max} to the ambient temperature T_{ext} . Fig. 4.11c shows the variation of T_{\max} as a function of T_{ext} for three different preform thicknesses and in the absence of external heating (i.e. $\dot{q} = 0$). The value of T_{\max} monotonously increases with increasing T_{ext} . The location of test A is included in Fig. 4.11c. The predictions shown in Fig. 4.11c also indicate that increasing the preform thickness leads to a reduction of the ambient temperature processing window. The processing conditions selected for Fig. 4.11c indicate that the boiling of the monomer occurs when T_{ext} exceeds $35\text{ }^\circ\text{C}$ for a preform thickness c_1 equal to 3 cm , while, for $c_1 = 7\text{ cm}$, monomer boiling already takes place when the infusion is conducted at an ambient temperature above $22\text{ }^\circ\text{C}$.

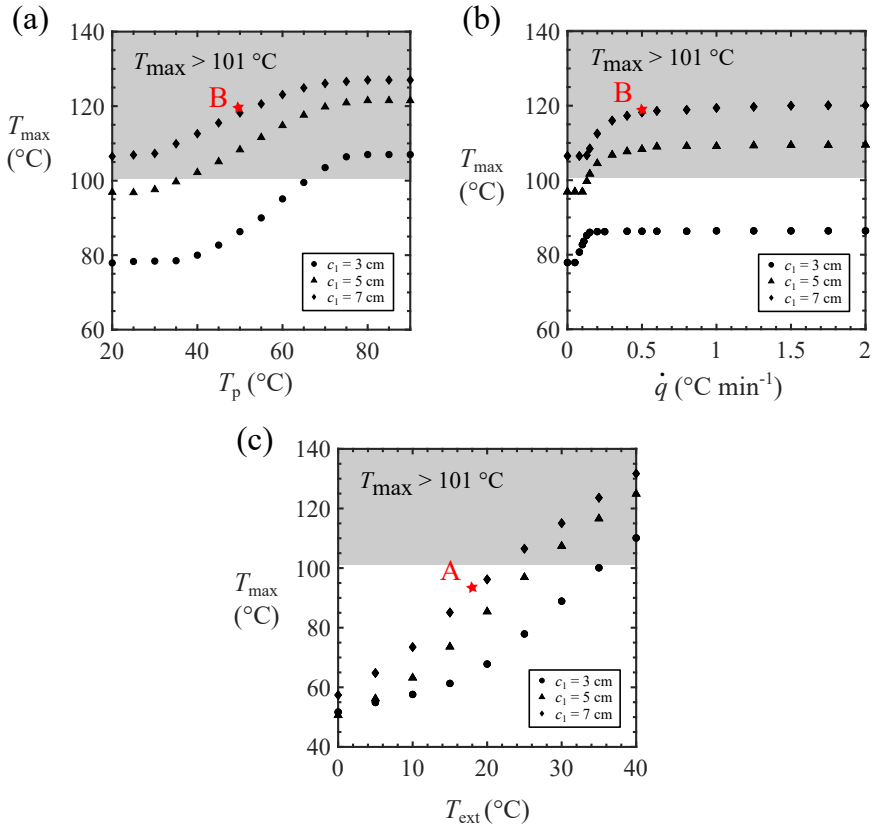


Fig. 4.11 Predicted maximum temperature in the preform during polymerisation, T_{\max} , as a function of (a) mould set temperature T_p for selected values of preform thickness c_1 ($\dot{q} = 0.5$ °C.min⁻¹ and $T_{\text{ext}} = 25$ °C) (b) heating rate \dot{q} for selected values of c_1 ($T_p = 50$ °C, $T_{\text{ext}} = 25$ °C) and (c) ambient temperature T_{ext} for selected values of c_1 (for $\dot{q} = 0$). Manufacturing conditions corresponding to tests A and B are included.

Structural and other functional requirements often dictate the thickness of the laminate. Wind turbine blades, for instance, comprise composite parts produced via vacuum infusion of thickness in the range 1 cm to 10 cm [44, 48, 170]. It is therefore convenient to construct a processing map with axes c_1 and T_p , and to plot the predicted boundary at which T_{\max} is equal to 101 °C for selected values of heating rate, see Fig. 4.12a. For a given value of \dot{q} the $T_{\max} = 101$ °C boundary divides the map into two regimes: a $T_{\max} < 101$ °C window where no cavitation due to monomer boiling is expected, and a $T_{\max} > 101$ °C regime where monomer boiling is expected (this regime corresponds to the grey-shaded area in Fig. 4.12a for $\dot{q} = 0.2$ °C.min⁻¹). The $T_{\max} = 101$ °C boundary is close to independent of the heating rate when the value of \dot{q} is lower than 0.12 °C.min⁻¹ or exceeds 0.5 °C.min⁻¹. The map shown in Fig. 4.12a is re-drawn in Fig. 4.12b for $\dot{q} = 1$ °C.min⁻¹. In addition, contours of equal values for the time at peak temperature t_{peak} for $\dot{q} = 1$ °C.min⁻¹ are superimposed on the map. Recall that we assume the polymerisation reaction ends at t close to t_{peak} . Three regimes are identified on the map shown in Fig. 4.12b.

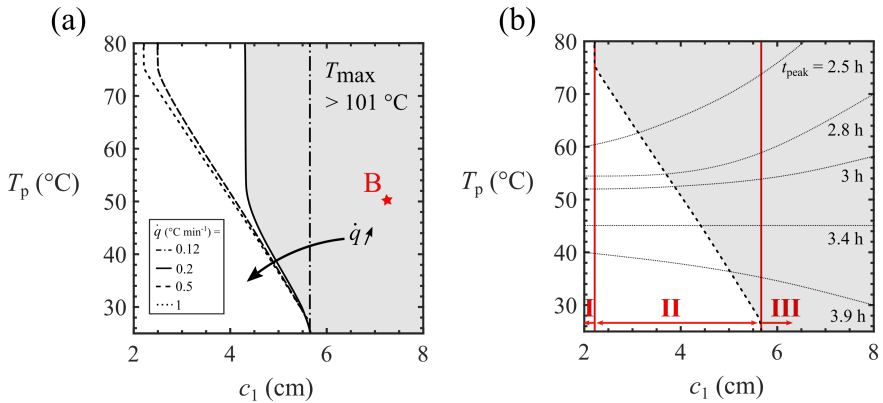


Fig. 4.12 Processing maps for the in-situ polymerisation of an MMA-infused thick glass fibre preform: (a) mould set temperature T_p as a function of preform thickness c_1 with predicted $T_{\max} = 101$ °C boundaries for selected values of heating rate ($T_{\text{ext}} = 25$ °C) and (b) mould set temperature T_p as a function of c_1 with predicted $T_{\max} = 101$ °C boundary and contours of equal values of peak time t_{peak} for $\dot{q} = 1$ °C.min⁻¹ and $T_{\text{ext}} = 25$ °C.

For a small preform thickness ($c_1 < 2.3$ cm), in regime I, the condition $T_{\max} = 101$ °C can only occur when the mould set temperature is close to 101 °C. For an intermediate value of preform thickness ($2.3 < c_1 < 5.6$ cm), in regime II, the maximum mould set temperature T_p to prevent monomer boiling is a function of c_1 . In addition, the optimum (minimum) process time t_{opt} for a thickness value of interest in regime II is obtained by finding the t_{peak} contour intersecting the $T_{\max} = 101$ °C boundary at the selected value of preform thickness. For a large value of preform thickness ($c_1 > 5.6$ cm), monomer boiling occurs irrespective of the selected value of \dot{q} and T_p and regime III is entered.

The three regimes (I, II and III) are plotted on a final processing map with axes c_1 and t_{opt} , see Fig. 4.13. Contours of equal values of the heating rate \dot{q} in regimes I and II are included via the following method. The map shown in Fig. 4.12b is re-constructed for selected heating rates. For intermediate values of preform thickness (regime II), the value of t_{opt} is obtained as a function of c_1 by the intersection loci of the superimposed t_{peak} contours and the $T_{\max} = 101$ °C boundary as explained above. For lower values of preform thickness, the slope of the $T_{\max} = 101$ °C boundary becomes infinite, corresponding to the onset of regime I. In regime I, the value of t_{opt} corresponds to the peak time for a mould set temperature equal to 101 °C. The map shown in Fig. 4.13 yields the following useful insights. The minimum process time is almost independent of preform thickness in regime I. For low heating rates (i.e. $\dot{q} \leq 0.1$ °C.min⁻¹) regime I encompasses the entire thickness range for which monomer boiling may be prevented (i.e. $c_1 < 5.6$ cm). There is a strong dependence of t_{opt} upon the selected value of \dot{q} in regime I. In contrast, the sensitivity of t_{opt} to \dot{q} is low in regime II. For \dot{q} exceeding 1 °C.min⁻¹ in regime II, the value of t_{opt} is a linear function of the preform thickness and is insensitive to \dot{q} (i.e. increasing \dot{q} does not result in a shorter process time). In addition, for the MMA-based resin of interest, the regime II to regime III boundary at c_1 close to 5.6 cm is found to be independent of the selected heating conditions.

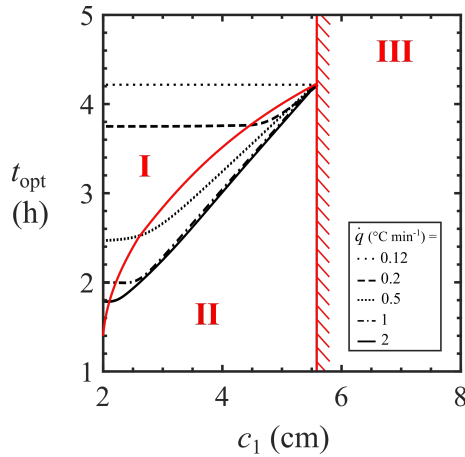


Fig. 4.13 Processing map of optimum (minimum) process time t_{opt} versus preform thickness c_1 for selected values of heating rate \dot{q} ($T_{ext} = 25$ °C). The methods to determine the boundaries between regimes I, II and III are detailed in the text.

4.5 Concluding remarks

A thermochemical model is developed to predict the temperature field across the thickness of a composite laminate processed by infusion and in-situ polymerisation of a methyl methacrylate (MMA)-based resin. The main challenge is to limit void formation due to local monomer boiling which is the result of the auto-accelerating, exothermic polymerisation reaction. The main findings of the present study are the following:

- The quasi-steady state approximation (QSSA) can be used to describe the self-accelerating polymerisation reaction of MMA in a finite difference thermochemical model. The QSSA significantly reduces the computing cost of the model, yet it leads to accurate temperature and monomer conversion predictions up to a critical monomer conversion value close to 0.9.
- The occurrence of cavitation due to monomer boiling is highly sensitive to the selected mould heating program and to the thickness of the preform.
- The computationally efficient thermochemical model enables the construction of comprehensive processing maps, which can be used

to reveal optimum mould heating conditions for the fast production of thick MMA-based preforms of a given thickness range without thermally-induced voids. There is, however, an upper bound on the preform thickness above which monomer boiling takes place irrespective of the selected heating program.

4.6 Supplementary information

4.6.1 Influence of diffusional effects on kinetic coefficients

The free volume-based analytical model of Achilias [74, 134] is used to calculate the dependence of k_p , k_t , and f upon monomer conversion χ and temperature T via the free volume V_f .

Dependence of free volume V_f upon T and χ

Consider two contributions to the value of the free volume fraction V_f : (1) the free volume related to the monomer $V_{f,m}$ and (2) the free volume related to the polymer chain $V_{f,p}$. The value of $V_{f,m}$ is calculated as

$$V_{f,m} = V_{g,m} + \beta_m (T - T_{g,m}), \quad (4.7)$$

where $T_{g,m}$ is the glass transition temperature of the monomer, $V_{g,m}$ is the free volume of the monomer at $T = T_{g,m}$ and β_m is the thermal expansion coefficient of the monomer. Likewise, the value of $V_{f,p}$ is obtained via

$$V_{f,p} = V_{g,p} + \beta_p (T - T_{g,p}), \quad (4.8)$$

where $T_{g,p}$ is the glass transition temperature of the PMMA polymer, $V_{g,p}$ is the free volume of the polymer at $T = T_{g,p}$ and β_p is the thermal expansion coefficient of the polymer. Then, the free volume fraction V_f reads

$$V_f = V_{f,m} (1 - \varphi_p) + V_{f,p} \varphi_p, \quad (4.9)$$

where the volume fraction of entangled polymer φ_p depends upon the degree of monomer conversion χ via:

$$\varphi_p = \chi \left(1 - \frac{v_m - v_p}{v_m} \right) \left(1 - \chi \frac{v_m - v_p}{v_m} \right)^{-1}, \quad (4.10)$$

4 | Thermokinetic behaviour of thick Elium laminates

where v_m and v_p are the specific volumes of the monomer and the polymer, respectively.

Dependence of propagation rate coefficient k_p upon χ and T

The value of k_p depends upon the diffusion coefficient D_m of the MMA monomer molecule via

$$k_p^{-1} = \left(k_p^0\right)^{-1} + (4\pi N_A R_p D_m)^{-1}, \quad (4.11)$$

where N_A is Avogadro's number, R_p is the radius of interaction for the propagation reaction and k_p^0 a temperature-dependent coefficient:

$$k_p^0 = A_p \exp\left(-\frac{E_p}{RT}\right), \quad (4.12)$$

where A_p is a pre-exponential factor, E_p is the activation energy of propagation, and R is the ideal gas constant. In addition, the value of D_m is sensitive to the free volume of the polymerising medium V_f via

$$D_m = D_m^0 \exp\left(-\frac{\gamma_m}{V_f}\right), \quad (4.13)$$

where D_m^0 is a pre-exponential factor and γ_m is an overlap factor, accounting for shared free volume between multiple neighbouring molecules [149, 150].

Dependence of termination rate coefficient k_t upon χ and T

The value of k_t depends upon the diffusion coefficient of the macroradicals D_p via

$$k_t^{-1} = \left(k_t^0\right)^{-1} + (4\pi N_A R_t D_p)^{-1}, \quad (4.14)$$

where R_t is the radius of interaction for the termination reaction; we assume $R_t = \delta$, where δ is the root-mean-square end-to-end distance per square root of the number of monomer units in the chain [171] and j_c is the entanglement distance for PMMA. In addition, k_t^0 is a temperature-dependent coefficient:

$$k_t^0 = A_t \exp\left(-\frac{E_t}{RT}\right), \quad (4.15)$$

where A_t is a pre-exponential factor and E_t is the activation energy of termination.

We proceed by modifying the theory of Achilias and co-workers [74, 134] and calculate the value of D_p via

$$D_p = D'_p \left(\frac{\varphi_p \bar{M}_w}{M_e} \right)^{-2} \exp \left(-\frac{\gamma_t}{V_f} \right) + \frac{2}{3} \delta^2 k_p M, \quad (4.16)$$

where D'_p is a pre-exponential factor, γ_t is an overlap factor, M_e is the molecular weight between entanglements of PMMA and \bar{M}_w is the cumulated weight-average molecular weight of the PMMA chains calculated via the method detailed below. The first term on the right-hand side of Eq. 4.16 accounts for the free volume corrected radical diffusion due to the motion of the center of mass of the entangled macroradicals and the second term accounts for the contribution of chain propagation to radical mobility [74]. Note that the first term of Eq. 4.16 is a modified version of Eq. (19) in the work of Achilias [74], where we include φ_p to calculate the effective number of entanglements, $\varphi_p \bar{M}_w (M_e)^{-1}$, in accordance with the concept of effective entanglement density for ideal polymer solutions [172]. Note that, in the present study, Equation 4.16 is assumed to be valid within the whole conversion range from $\chi = 0$ to $\chi = 1$, though the onset of entanglement occurs around $\chi = 0.1$.

The value of \bar{M}_w is calculated based on the value of the weight-average degree of polymerisation \overline{DP}_w and the molecular weight M_w^0 of the MMA monomer:

$$\bar{M}_w = \overline{DP}_w M_w^0, \quad (4.17)$$

where the value of \overline{DP}_w is calculated via

$$\overline{DP}_w = \frac{\sum_j \left(\frac{dM}{dt} \right)_{t_j} \left(\frac{2}{1-\omega_j} - 1 \right)}{\sum_j \left(\frac{dM}{dt} \right)_{t_j}}, \quad (4.18)$$

where ω_j is the probability of propagation of the macroradicals at time $t = t_j$ and we made the following three assumptions: (1) the instantaneous molecular weight distribution at $t = t_j$ is a Flory distribution, (2) the radical termination occurs through disproportionation only [148], and (3) the values of $(dM/dt)_{t_j}$ and ω_j remain constant during the time interval

ranging from t_j to t_{j+1} . The value of ω_j reads [148]:

$$\omega_j = \frac{r_p}{r_p + r_t + r_{tr,M} + r_{tr,I}} = \frac{k_p M}{(k_p + k_{tr,M})M + \sqrt{2fk_d k_t I_0} + k_{tr,I} I_0}, \quad (4.19)$$

where r_p , r_t , $r_{tr,M}$ and $r_{tr,I}$ are the reaction rates of propagation, termination, transfer to monomer and transfer to initiator, respectively, see Table 4.2 of the manuscript.

Dependence of initiator efficiency f upon χ and T

The concentration of the initiating radicals decreases as the reaction proceeds due to the depletion of the initiator molecules as they thermally decompose. Hence, two different mechanisms contribute to the reduction of the activity of initiating radicals upon increasing χ . In this study, we assume that the (apparent) efficiency factor f accounts for the contributions of both the cage effect and the initiator depletion effect. The value of the initiator concentration I is assumed to remain constant.

The apparent initiator efficiency factor f depends upon the diffusion coefficient of the initiator radicals D_i :

$$f = \frac{f_0}{1 + \frac{C}{D_i}}, \quad (4.20)$$

where f_0 is the initial efficiency value, C is a fitting parameter, and D_i is the diffusion coefficient of the initiating radical:

$$D_i = D_i^0 \exp\left(-\frac{\gamma_i}{V_f}\right). \quad (4.21)$$

Here, D_i^0 is a pre-exponential factor and γ_i an overlap factor.

Dependence of initiator decomposition rate coefficient k_d upon T

The rate coefficient of peroxide decomposition k_d is assumed to depend on temperature only:

$$k_d = k_d^0 = A_d \exp\left(-\frac{E_d}{RT}\right), \quad (4.22)$$

where A_d is a pre-exponential factor and E_d is the activation energy of peroxide decomposition.

4.6.2 Validity of the quasi-steady state approximation (QSSA) in the presence of diffusional effects

The quasi-steady state approximation (QSSA) is commonly used to simplify the kinetic treatment of chemical reactions involving highly reactive intermediate species. The QSSA may be applied to all radical species R^\bullet involved in the free-radical polymerisation mechanism. It states that the overall rate of change in radical concentration is negligible, as the rate of radical production is approximately equal to the rate at which they are destroyed:

$$\frac{d[R^\bullet]}{dt} \approx 0. \quad (4.23)$$

This is only valid if the characteristic time τ_1 required for the production of radical species is significantly longer than the characteristic time τ_2 required for their consumption [148]. The values of τ_1 and τ_2 read

$$\tau_1 = \frac{1}{2fk_d} \quad (4.24)$$

and

$$\tau_2 = \frac{1}{k_t [R^\bullet]}, \quad (4.25)$$

respectively. During the polymerisation of MMA, the gel effect leads to an accumulation of radicals in the reaction medium. Hence, the QSSA is generally considered invalid in this case [148]. However, it is still possible to use this assumption in the conversion range where $\tau_1 \gg \tau_2$.

The calculated value of the ratio τ_1/τ_2 is plotted as a function of MMA conversion χ for plate B in Fig. 4.14. Consider a conservatively chosen critical value of $\bar{\tau}_{\text{crit}} = \tau_1/\tau_2 = 100$ below which the QSSA ceases to be valid. The value for τ_1/τ_2 ratio remains above $\bar{\tau}_{\text{crit}}$ in conversion regimes 1 to 3 for the three experimental testing conditions considered in the present study (predictions for τ_1/τ_2 for tests A and C are not shown). We therefore conclude that the QSSA holds in the monomer conversion range from $\chi = 0$ to $\chi = 0.9$. The predicted value of τ_1/τ_2 is below $\bar{\tau}_{\text{crit}}$ in domain 4 at a degree of monomer conversion above 0.9. In addition, our predictions show that for any location across the thickness of the preform, the value of τ_1/τ_2 is below $\bar{\tau}_{\text{crit}}$ after reaching the peak in temperature T_{max} , see Fig. 4.8 of the manuscript.

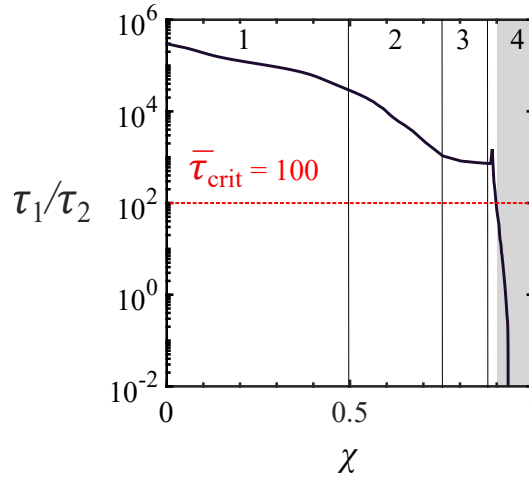


Fig. 4.14 Predicted value of τ_1/τ_2 as a function of monomer conversion χ by the calibrated thermochemical model during the in-situ polymerisation in the middle of plate B ($y \approx 0.50c_1$). Four conversion regimes are identified, see Fig. 4.8 of the manuscript. The grey area highlights the monomer conversion range for which $\tau_1/\tau_2 < \bar{\tau}_{crit}$.

Hence, the loss of validity of the QSSA at a conversion degree above 0.9 is expected to have only a small influence on the predicted values of the peak time and peak temperature.

4.6.3 Characterisation of plate microstructure by X-ray tomography [1]

Materials and methods

Cuboids of dimensions $10 \times 10 \times 73 \text{ mm}^3$ were machined from composite plates A and B using a water-cooled disk-milling cutter, according to the sectioning diagram shown in Fig. 4.15. Micro-Computed Tomography (μ CT) was performed on a Phoenix Nanotom S X-ray computed tomography system (GE Inspection Technologies), according to the protocol described in the work of Gayot [1]. The composite samples were mounted on a holder, with y -axis aligned along the rotation axis of the rotation stage, and were scanned at three positions along the y -direction, respectively near the bottom, middle and top parts of each plate.

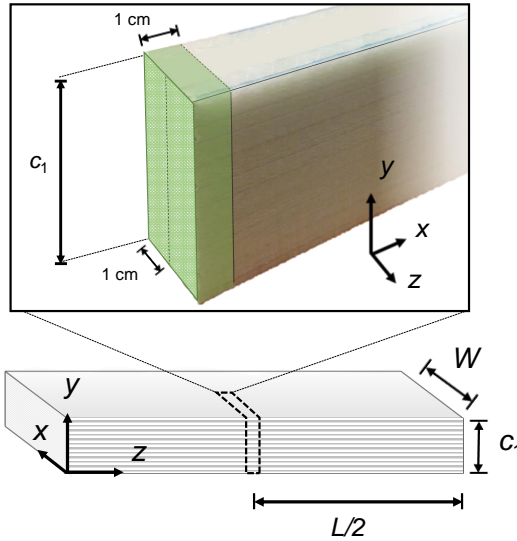


Fig. 4.15 Sectioning diagram for the characterisation of plates A and B ($L = 60$ cm, $W = 40$ cm, $c_1 = 73$ mm) by μ CT.

The isotropic voxel resolution was set to $7.5 \mu\text{m}$, i.e. smaller than the diameter of the glass fibres ($15 \mu\text{m}$). The scans were reconstructed and processed using the method presented in the work of Gayot [1].

Characterisation of plate microstructure

The 3D volume renderings of the void patterns in plates A and B are presented in Figs. 4.16 and 4.17, respectively. The results obtained with μ CT are consistent with those obtained from optical microscopy in terms of void volume fractions Φ , see Fig. 4.5 of the manuscript. In particular, the close-to-zero porosity in plate A and the presence of a porosity gradient along the y -axis of plate B are confirmed. For both conditions A and B, μ CT also confirms that the fibrous preform is comparable to a dual-scale porous medium with millimetre-sized inter-tow channels and micrometre-sized intra-tow channels. As observed with optical microscopy, cavitation seems to occur almost exclusively in the inter-tow area, giving rise to millimetre-sized ‘macropores’. In low-porosity parts like plate A ($\Phi \approx 0.1\%$) or the bottom third of B ($\Phi \approx 0.3\%$), voids are spheroidal. They form preferentially in the largest resin pockets available, i.e. where several inter-tow channels are connected along the y -axis, see Figs. 4.16 and 4.17. As the

4 | Thermokinetic behaviour of thick Elium laminates

value for Φ increases along the thickness of plate B, the shape of the pores changes from spheroidal to ellipsoidal due to the confining presence of the inter-tow area, see Fig. 4.17. In the top part of plate B, where Φ is close to 10%, these ellipsoidal cavities merge into a continuous 3D network running across the inter-tow channels.

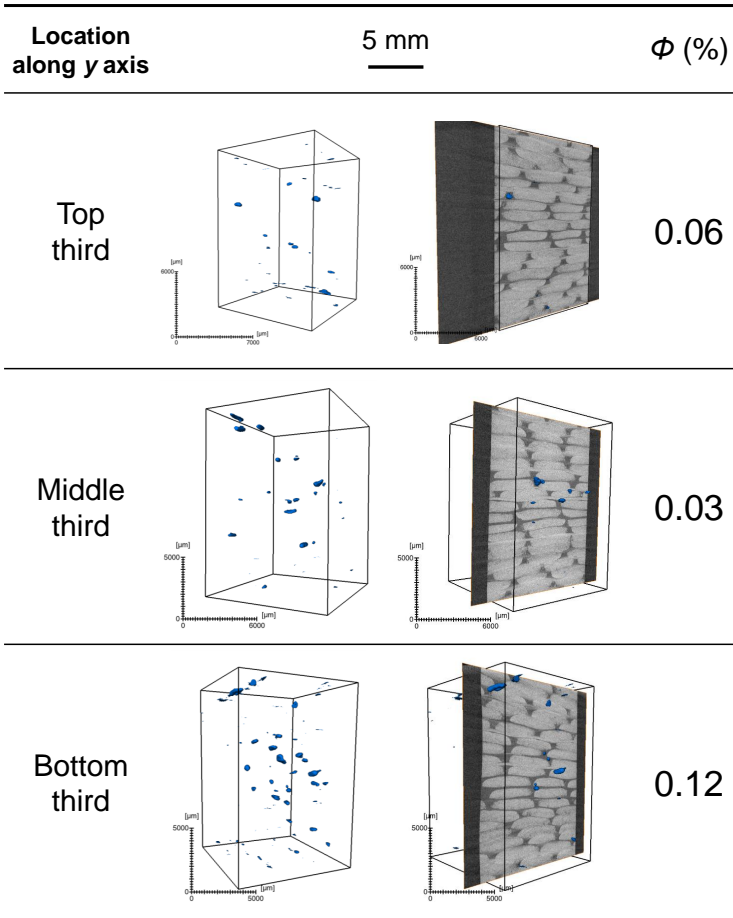


Fig. 4.16 3D volume renderings of void patterns obtained from μ CT across the thickness of plate A ($c_1 = 73$ mm).

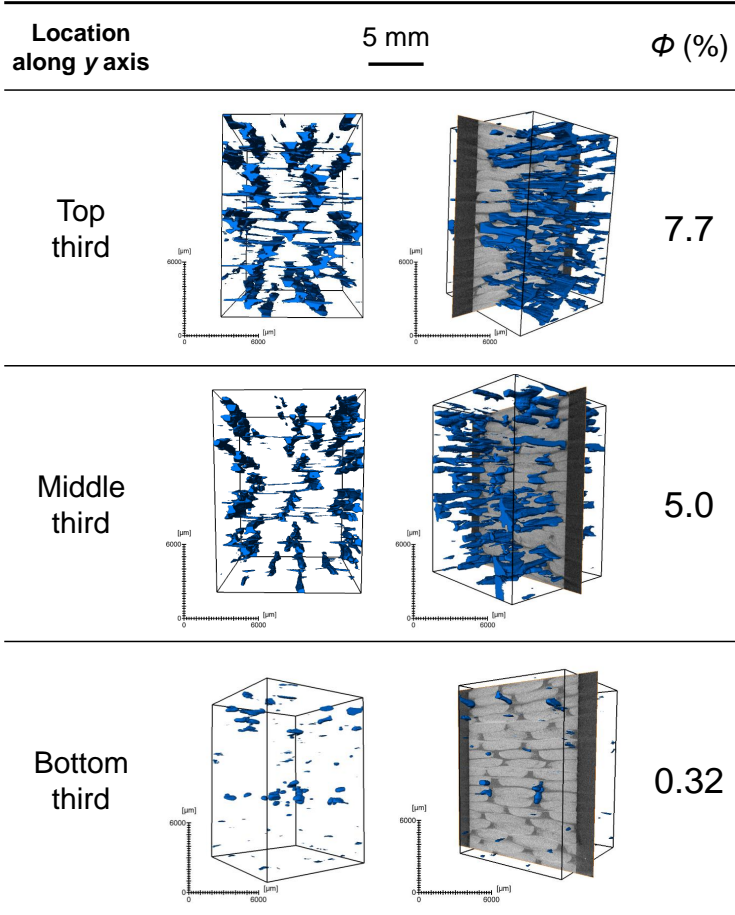


Fig. 4.17 3D volume renderings of void patterns obtained from μ CT across the thickness of plate B ($c_1 = 73$ mm).

5

4D-XCT monitoring of void formation in thick Elium composites produced by infusion

This chapter is an extended version of the conference paper entitled *Monitoring void formation during liquid composite moulding by in-situ X-ray computed tomography* by S. F. Gayot, J. Soete, J. Vanhulst, C. Bailly, P. Gérard and T. Pardoën, published in 2022 in the Proceedings of the 37th American Society for Composites (ASC) Annual Technical Conference in Tucson, AZ, USA [5].

J. Soete designed the XCT scanning method, performed and processed the scans. J. Vanhulst designed, manufactured and installed the miniature infusion setup and mount in the CT scanner (including connections to the vacuum and heating systems). S. F. Gayot was in charge of the conceptualisation and coordination of the project and took care of the tasks related to composite processing.

5.1 Introduction

Fibre-reinforced polymer composites produced by liquid moulding techniques contain voids, which can be detrimental to the mechanical properties of the structural components. While the formation of porosity cannot be avoided entirely, mitigation actions can be applied to control the main sources of void formation. These sources include incomplete resin degassing and void entrapment during mold filling, volatilisation of resin components (or polymerisation by-products) and chemical shrinkage during in-situ curing, and thermal shrinkage upon cooling [123–127]. This implies building up a good level of understanding of the mechanisms involved in void formation for a given manufacturing process. Various characterisation methods exist for the post-mortem analysis of porosity in composite materials, e.g. X-ray computed tomography (XCT), microscopy of polished cross-sections, thermography, or ultrasonic inspection. However, the identification of the origins/sources of porosity remains elusive. When several mechanisms are involved in the process of void nucleation, growth and transport, post-mortem methods are unable to decorrelate them and reconstruct the timeline of events.

Over the past decade, novel characterisation techniques have been designed for monitoring void formation during composite manufacturing. Though a few studies mention the use of transparent tooling for the direct observation of surface porosity [173–175], most of them rely on XCT. This non-destructive characterisation technique allows 3D imaging of a specimen, obtained by reconstructing a series of planar X-ray projections equispaced along a 360° sample rotation. XCT can be used to monitor void formation in composite materials either via ‘in-situ’ or ‘ex-situ’ protocols. In ex-situ methods, composite specimens are produced outside of the scanner. The manufacturing process must be interrupted at a given step in order to extract the sample and perform subsequent CT characterisation [176, 177]. Several authors relied on ex-situ methods to study void formation during the out-of-autoclave consolidation of epoxy-based carbon prepregs [178–180]. Laminates were prepared outside of the scanner, partially cured, cooled down to prevent further resin crosslinking, downsized, and finally subjected to CT scanning. The disadvantage of an ex-situ approach is that information can only be obtained for the steps at which the experiment was interrupted and a CT scan was taken [176, 177]. The timing and order of the changes that take place in between consecutive steps

are lost. There is also an uncertainty related to the cooling rate in case the voiding process is very fast.

On the other hand, dynamic in-situ methods, i.e. an uninterrupted experiment and continuous data acquisition, can lead real-time observation of void formation in composites directly within the CT scanner [176, 177, 181]. A miniature version of the process must be designed: the setup must fit and rotate 360° inside the tomograph and should be made of thin, relatively low-atomic-number and low-density materials in order to minimise unwanted X-ray attenuation during scanning. More importantly, there is always a trade-off between scan speed and image quality, which makes the observation of small-scale dynamic phenomena, e.g., void growth, particularly difficult. Synchrotron X-ray sources may be used to circumvent this problem, but they are less accessible than lab-based CT scanners. For these reasons, the first in-situ XCT experiments dedicated to void monitoring during composite manufacturing were developed only very recently. Apart from Kratz et al. [182], who made use of a lab-based CT scanner, all other studies relied on synchrotron X-ray facilities [183–189]. Some authors studied the (de)consolidation of semi-finished products, i.e., prepreg or sheet moulding compounds, under heat and/or pressure [182, 185, 187, 188]. Other researches focused on liquid moulding (LM) techniques [184, 186, 189] but the in-situ analysis only covered the impregnation step and the setup consisted of a single fibre tow, providing limited insights into the void formation mechanisms involved in real-scale LM processes.

The objective of this study is twofold. First, a new lab-based XCT method is developed for the in-situ dynamic monitoring of void formation during the vacuum infusion and curing of a thick (> 2 cm) glass fibre-reinforced polymer composite. The principle of the experimental setup used for in-situ infusion is inspired from the work by Hemmer et al., who studied the evolution of the fibrous preform microstructure upon infusion of a non-reactive model fluid [190, 191]. The mechanisms leading to void formation and transport are then investigated for the particular case of a 2.3 cm-thick methyl methacrylate (MMA)-based thermoplastic composite, produced by vacuum infusion of a dedicated monomer-based formula into a glass fabric layup and polymerisation within the preform. This system can be subjected to monomer boiling due to the exothermic and self-accelerating nature of the polymerisation reaction [4, 44, 51, 192]. It can also be prone to void formation through common mechanisms including flow-related void entrapment during the impregnation step.

5.2 Materials and experimental methods

5.2.1 Materials

Composite preforms were made of quasi-unidirectional HiMax™ XGE190 bi-axial non-crimp glass fabric (Hexcel, CT, USA) with an areal weight of $3.791 \text{ kg}\cdot\text{m}^{-2}$. The thermoplastic resin, which has been formulated to ensure compatibility with liquid composite moulding technologies, comprised an infusion-grade monomer formula (Elium® 151 OSA of Arkema, France) and a ketone peroxide thermal initiator (Butanox® M-50 of Nouryon, Netherlands). The consumables for bagging were obtained from Diatex SAS (France). The materials used for manufacturing and operating the setup are detailed in Table 5.1 of the Appendix. Aluminium was used as the main constituent of the setup for its combination of high thermal conductivity and relatively low density, compared to other metals.

5.2.2 Miniature infusion setup

The downsized infusion setup was designed based on the work of Hemmer et al. [190, 191], who studied the microstructural evolution of a glass fabric preform upon in-situ infusion with a non-reactive fluid using XCT. The original setup of Hemmer consisted of a PVC plate pierced with holes for connecting the resin and vacuum lines, and was used for the infusion of a 9 mm-thick glass fabric stack. The setup manufactured in this work is shown in Figure 5.1, alongside with the associated coordinate system. Note that the following alterations were made with respect to Hemmer's setup: (1) addition of a heating system, (2) use of thermally conductive materials and (3) addition of a dedicated rotating mount shown in Figure 5.1c.

5.2.3 In-situ infusion experiment

Preparation

Composite specimens were manufactured using the miniature infusion setup illustrated in Figure 5.1. Preforms were produced by laying up 10 glass fabric plies of dimensions $L = 9 \text{ cm}$ and $w = 4 \text{ cm}$ onto the heating plate. The final preform thickness h was close to 2.3 cm. Tow orientation was aligned along the x -axis (i.e. infusion direction).

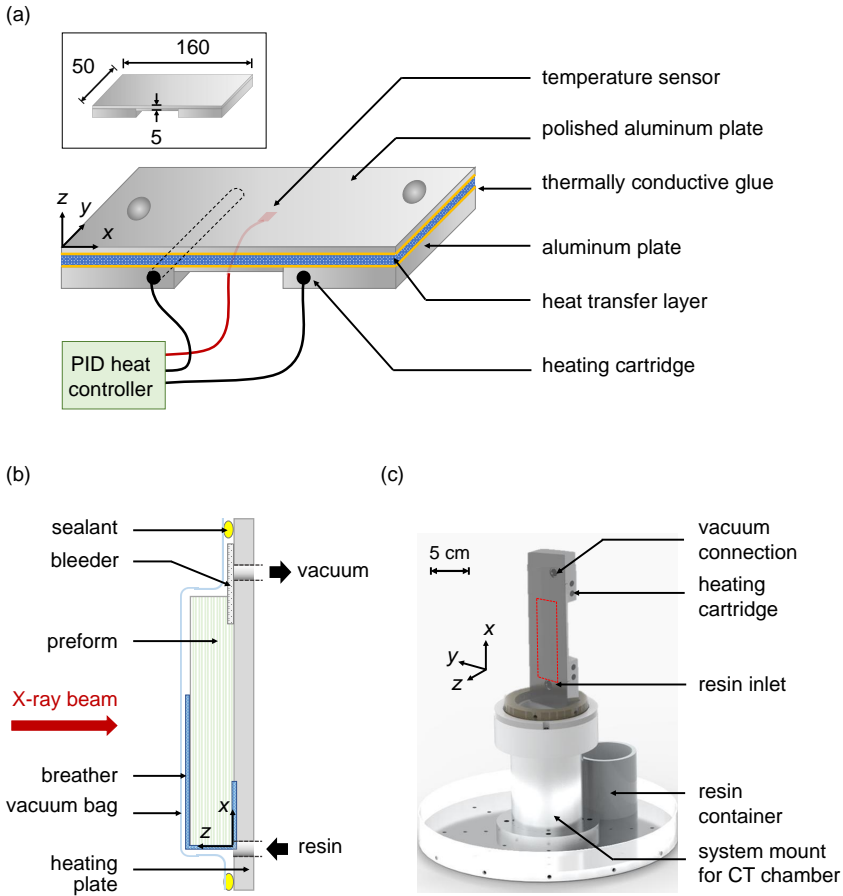


Fig. 5.1 Design of the miniature infusion setup, inspired from [190, 191]: (a) structure and dimensions in mm, (b) simplified side view of the setup and preform during XCT scanning and (c) 3D view of the setup installed in the CT chamber. The red rectangle indicates preform location.

5 | 4D-XCT monitoring of void formation in Elium composites

The layup was wrapped in peel ply in order to prevent any stray glass filaments from compromising the bagging step. As described in Figure 5.1b, strips of breather and bleeder materials were placed onto and underneath the preform to improve resin flow and vacuum distribution, respectively. The vacuum bag was installed onto the edges of the heating plate using 6 mm-wide strips of mastic sealant, and pleated according to standard bagging practices. Tubing for resin inlet and vacuum line was connected to the back of the setup using pneumatic elbows. The setup was screwed onto a dedicated rotating mount in the CT chamber, see Figure 5.1c. Connections to an external vacuum pump and heating controller were achieved via slip ring connectors (to enable setup rotation during scanning) and vacuum-tight gate valves. Any loose tube or cable was secured out of the field of view of the detector using adhesive tape. Photographs of the installed setup are presented in Figure 5.2. The composite preform was subjected to 200 mbar vacuum conditions and left to degas and stabilise for one hour, as described by Hemmer [190, 191].

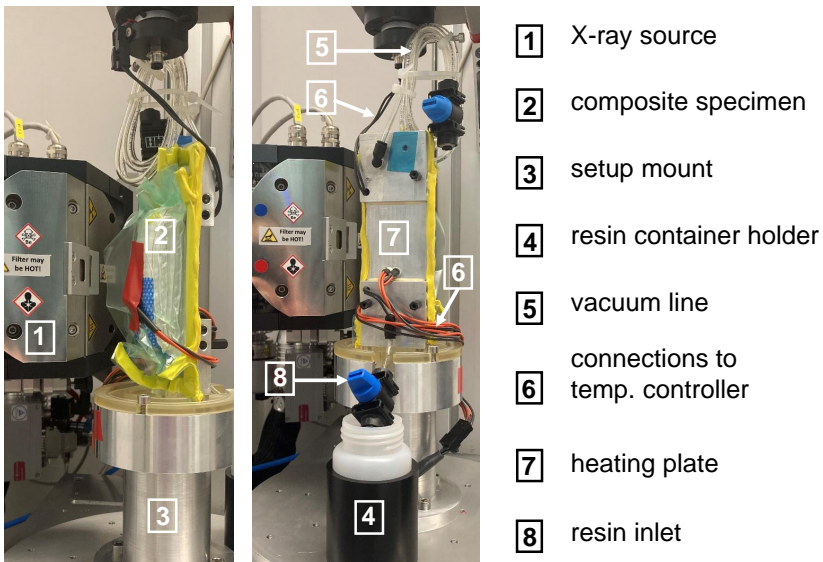


Fig. 5.2 Front (left picture) and back (right picture) views of the infusion setup after installation in the CT chamber.

In-situ infusion experiment

The resin mix was prepared with 1.5 parts initiator per hundred parts monomer formula, mechanically stirred for 5 min, and then degassed for 1 min at 100 mbar. The time at which the initiator was added is referred to as t_0 . Between t_0 and $t_0 + 8$ min, the resin container was secured inside the CT chamber using the dedicated holder shown in Figures 5.1c and 5.2. Resin infusion was then carried out under 200 mbar vacuum and at room temperature. Complete filling of the preform was achieved within 2 minutes of infusion (i.e. around $t_0 + 10$ min), after which the valves connecting the setup to the resin inlet and vacuum line were closed. In-situ dynamic scanning was started around $t_0 + 12$ min, and the temperature controller was switched on. The infused preform was heated from the initial chamber temperature (i.e. 30 °C) to 80 °C, with a heating rate close to 7 °C.min⁻¹. The setup temperature was maintained at 80 °C until a sharp temperature peak was reached at the surface of the preform, indicating the completion of polymerisation reaction [1, 4]. The setup was then left to cool down to room temperature, which had raised to approximately 40 °C inside the CT chamber due to X-ray irradiation. Dynamic scanning was interrupted, after which a final static scan of the composite specimen was taken.

5.2.4 XCT scanning parameters

3D imaging of the composite specimens was performed on a 230 kV/300 W TESCAN Unitom XL computed tomography system, with the setup mount rotating 360° around the x -axis of the composite sample. A tungsten target was installed on the reflection source together with a 0.1 mm thick CuZn filter to harden the X-ray beam. Two different sets of acquisition methods, referred to as 'dynamic' and 'static', were applied during the experiment. Both acquisition methods applied a tube voltage of 150 kV and a tube power of 15 W. The dimensions of the field of view (FOV) were set to 25, 30 and 20 mm in the x , y and z -directions, respectively, meaning that neither the uppermost glass fabric ply nor the lateral edges of the preform (along the y -axis) were observed. However, a compromise had to be found between enlarging the field of view and moving the setup closer to the source for achieving better spatial resolution.

Dynamic scanning was initiated after infusion and covered the whole duration of the polymerisation and cooling steps. Static scanning was used to image the specimen in its final state, i.e., after complete cooling of the setup. The purpose of the static scan was to obtain the smallest possible

voxel size with the in-situ setup installed. The associated scan time did not matter in this case, as no time-dependent phenomena were expected to occur. A voxel size of $11.25\ \mu\text{m}$ was obtained in static acquisition mode. 2400 radiographic projections were acquired at an exposure time of 275 ms, resulting in a scan time of 23 minutes. On the other hand, in dynamic acquisition mode, the scan time had to be short enough to capture subtle changes in void pattern over time. The scan speed was gained by sacrificing image quality through larger rotation steps, and detector binning. In this specific case, a 2×2 binning of the detector was applied (i.e. each 2×2 matrix of pixels was combined into one larger pixel). This doubles the voxel size (i.e. $22.5\ \mu\text{m}$) compared to the static experiment, but at the same time provides a better signal to noise ratio and shorter exposure time (150 ms), which allowed working with a reduced number of radiographic projections (900). 60 continuous 360° acquisitions at a temporal resolution of 135 seconds resulted in a duration of 135 minutes for the dynamic experiment.

5.2.5 Processing of XCT results

The software Panthera (V. 1.3b1, TESCAN XRE NV) was used to reconstruct the XCT scans and export cross-sectional images. The open-source software ImageJ [147] was used to further analyse some of the 2D cross-sectional images, while post-processing of the 3D data and was performed in Avizo 2021.2 (ThermoFisher). Prior to the quantitative analysis, noise filtering was applied, using a median filter with the neighborhood connectivity set to 26 and 3 iterations. The median filter reduces the photon noise in the scanned volume. Next, a greyscale thresholding was performed to segment the images into three phases, i.e., voids, matrix and glass fibre tows.

5.3 Results and discussion

5.3.1 Cross-sectional images of the composite specimen

2D cross-sectional images were extracted from each of the 60 reconstructed dynamic scans at a fixed location, i.e. in the (xoz) plane intercepting the y -axis at $y = w/2$. The corresponding images are displayed in Figures 5.3 and 5.4. Each phase of the material (i.e. fibres, resin and voids) is characterised by a different shade of grey: glass fibre tows appear light grey,

while the resin looks darker and the voids are black. The red rectangles in Figures 5.3 and 5.4 serve as a guide for the eye, by indicating regions where a significant change in void morphology is observable as compared to the scan taken immediately before. Note that only one image is presented for scans 1 and 2 in Figure 5.3, and for scans 8 to 60 in 5.4, as no significant change in void pattern was observed within these two series of images.

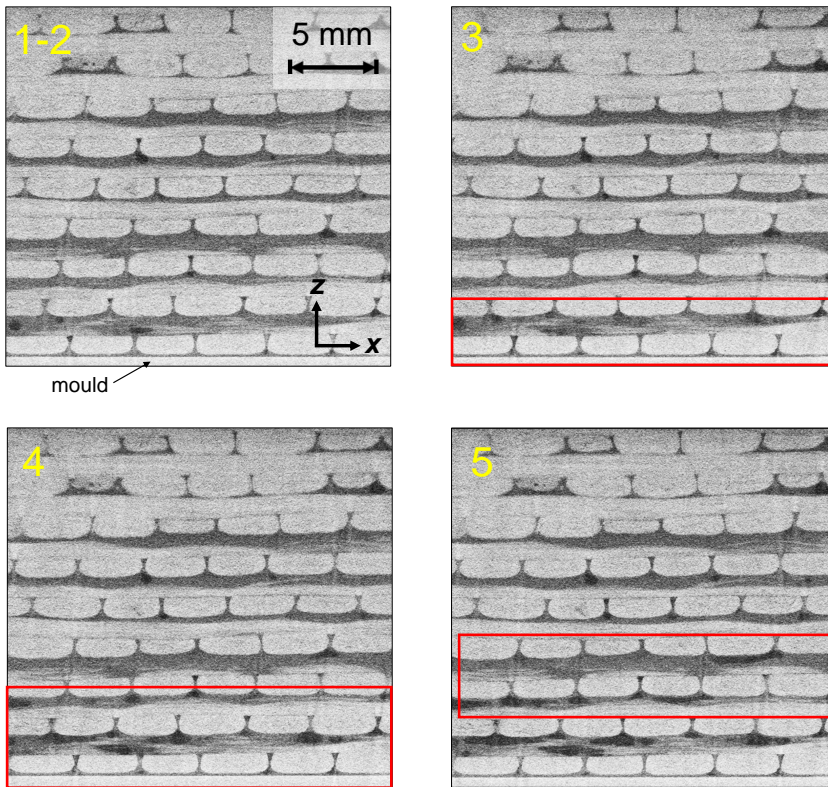


Fig. 5.3 Reconstructed xz slices obtained from dynamic scans 1 to 5 at $y = w/2$. Red boxes indicate areas where void patterns noticeably change compared to the same area of the previous scan.

5 | 4D-XCT monitoring of void formation in Elium composites

The cross-sectional images presented in Figures 5.3 and 5.4 reveal that the vast majority of void formation events occurs between scans 2 and 8, i.e. within the first 30 minutes following peroxide introduction, though a few randomly distributed voids are already present in scans 1-2.

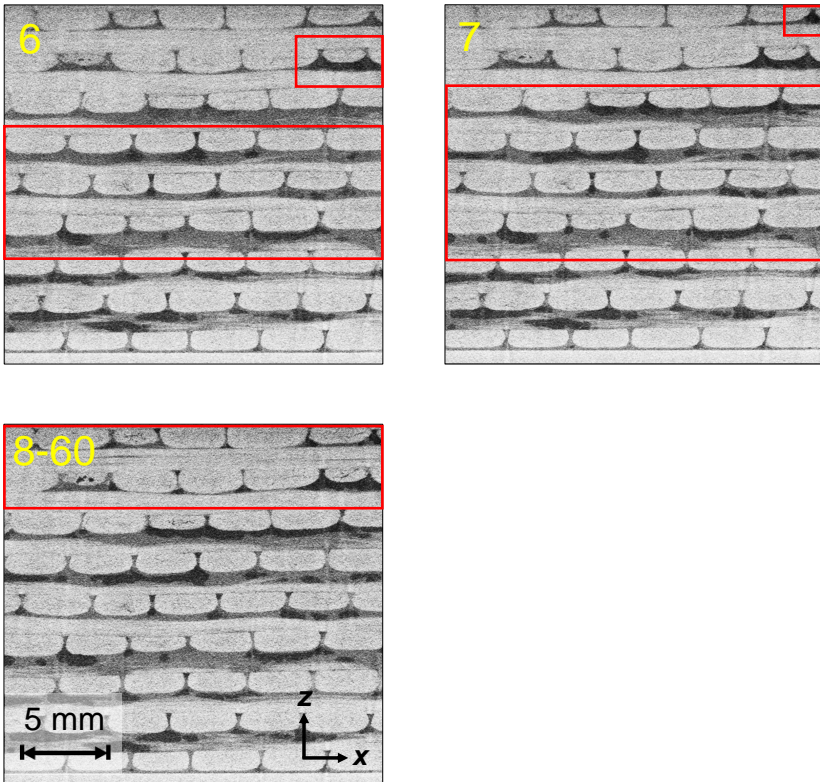


Fig. 5.4 Reconstructed xz slices obtained from dynamic scans 6 to 60 at $y = w/2$. Red boxes indicate areas where void patterns noticeably change compared to the same area of the previous scan.

Second, voids are exclusively observed in between two subsequent fabric plies and/or in between fibre tows of the same ply. Their smallest dimension is on the order of a few hundred microns. Third, void growth events take place gradually along the z -axis between scans 2 and 8, i.e. voids form first in the region near the mould (see scans 3 and 4 of Figure 5.3). Once these have attained their final size, other voids start to grow in the upper plies (see scans 5 to 8). This continues until the surface of the preform is reached (scan 8), after which the void pattern does not evolve anymore.

5.3.2 Evolution of porosity

The average volume fraction of voids in the composite specimen, which will be referred to as the porosity Φ , was estimated for each of the 60 dynamic scans as follows. First, the heating plate was cropped out of the FOV as it would interfere with the determination of the porosity. The cropped FOV was further divided into 4 identical cuboid sub-volumes perpendicularly to the z - and x -axes, as illustrated by Figure 5.5. The volume fraction of voids in each cuboid - referred to as φ - was estimated, resulting in a set of 4 measurements per scan from which the average value Φ was calculated alongside with the associated standard deviation.

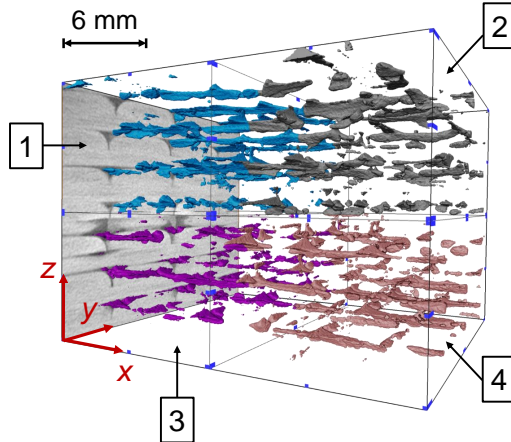


Fig. 5.5 Sectioning method applied to the FOV for porosity calculation, exemplified on the 3D rendering of the voids obtained from scan 51. The four resulting sub-volumes are depicted with different colours for easier visualisation.

The evolution of Φ is presented in Figure 5.6 as a function of scan number and corresponding time of the experiment (whose origin is defined as t_0 , i.e. peroxide introduction). The value of Pearson's standard deviation associated to each value of Φ is depicted with error bars.

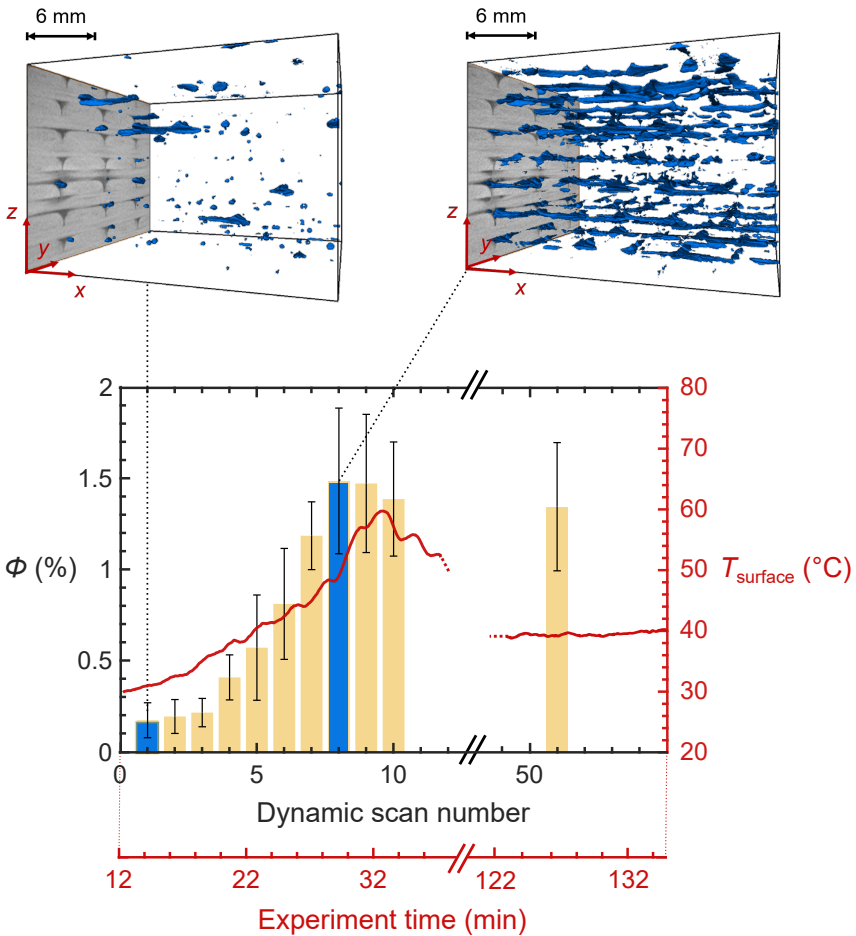


Fig. 5.6 Variation of the average porosity Φ (and corresponding Pearson's standard deviation) over the volume of interest and evolution of the surface temperature T_{surface} as a function of dynamic scan number and scanning time. 3D volume renderings of the void patterns generated from dynamic scans 1 (top left) and 8 (top right) are also presented.

The evolution of the specimen's surface temperature T_{surface} is also included, alongside with two examples of 3D void pattern renderings obtained from scans 1 and 8. As no significant evolution in porosity was observed beyond scan 10, only one Φ value is represented for scans 11 to 60. It was obtained from scan 51, which was acquired after the preform had cooled down to CT chamber temperature and is thus considered representative of the final state of the system.

The information displayed in Figure 5.6 consolidates the assumptions made from the cross-sectional images. In particular, the value of Φ for scan 1 is not equal to zero but close to 0.2 %, which confirms the presence of voids in the composite before the start of dynamic scanning. These likely arise from the infusion step *per se*, i.e. preform filling. The 3D rendering of scan 1 reveals a homogenous, random-looking distribution of these voids throughout the scanned volume, which was also inferred from the 2D images. Secondly, Figure 5.6 allows verifying that void formation/evolution events exclusively occurred between dynamic scans 1 and 8, as shown by the continuous increase of Φ from ≈ 0.2 % at scan 1 up to the maximum value of ≈ 1.5 % at scan 8. As concerns the slight apparent drop in the calculated value of Φ between scans 8 ($\Phi \approx 1.5$ %) and 51 ($\Phi \approx 1.3$ %), it is too small to be directly related to an actual change in void pattern, as detailed in the next section.

The results shown in Figure 5.6 also allow correlating the evolution of porosity Φ with the timeline of the polymerisation reaction, through the temperature plot. As mentioned in the introduction, MMA polymerisation exhibits a characteristic thermokinetic behaviour. In the early stages of monomer conversion, the temperature of the reaction medium increases slowly and steadily. Then, self-acceleration occurs: the temperature increases more and more sharply until reaching a peak, which corresponds to the completion of the reaction. Finally, the polymerisation medium cools down back to room temperature. Here, the surface temperature of the preform reaches its maximum value (i.e. 60 °C) around 30 min after the peroxide introduction, which corresponds to the end of scan 9. Therefore, the first 9 scans cover the polymerisation step, while the rest of the scans cover the cooling step. The rates at which T_{surface} and Φ values increase during polymerisation follow a similar evolution, i.e. both parameters increase faster as time passes by, until the maximum value is reached. This further highlights the direct link existing between the polymerisation reaction and void formation/evolution in the composite specimen.

Note that the standard deviation of Φ also varies over the course of the experiment, starting from a value below 0.1 % at scan 1 and rising up to 0.3-0.35 % from scan 5 onwards, see Figure 5.6. This apparent increase in the dispersion of Φ values arises from the choice of sectioning method applied to the FOV for studying porosity. Recall from Figure 5.5 that the FOV was divided into two equal parts along the x -axis and two equal parts along the z -axis, giving rise to 4 cuboid sub-volumes. As already known from section 5.3.1, sub-volumes no. 1 and 2 - which comprise the upper plies of the preform (see Figure 5.5) - experience delayed void growth compared to the lowermost plies, i.e. to sub-volumes no. 3 and 4. More precisely, sub-volumes no. 3 and 4 experience void formation events between scans 3 and 6, while sub-volumes 1 and 2 only do so between scans 5 and 8, which causes the dispersion of Φ values to increase during polymerisation.

5.3.3 Evolution of void size

The size of the voids can be characterised for each of the dynamic scans via a 3D local thickness (LT) analysis. This operation consists in automatically fitting spheres inside each void, starting from the largest possible diameter values. For each scan, a distribution of the cumulated volume of the inscribed spheres as a function of their diameter can be plotted, which is one way of determining void 'size'. Compared to other procedures aiming at characterising void shapes and dimensions, e.g. in terms of their Feret diameter, the LT analysis has the advantage of limiting the influence of noise (which can give rise, e.g. to spurious connectivity between adjacent voids), on the results.

The results of the LT analysis of the voids captured by scans 1, 5, 9 and 51 are displayed in Figure 5.7. The amplitude of the distributions evolves in a similar way as the porosity Φ , i.e. it increases between scans 1 and 9 and then slightly decreases between scans 9 to 51. The range of LT values obtained from the scans remains relatively unchanged, extending from 50 to $\approx 800 \mu\text{m}$ in all cases. As Φ increases, two distinct populations appear within the void size distributions, as depicted by the orange and red boxes in Figure 5.7. The orange and red boxes contain LT values below and above $\approx 500 \mu\text{m}$, respectively. The former can be attributed to inter-ply voids, while the latter are characteristic of inter-tow voids forming in the V-shaped space between two adjacent fibre tows belonging to the same ply. As illustrated by Figure 5.7, these two categories can co-exist within a single, large void.

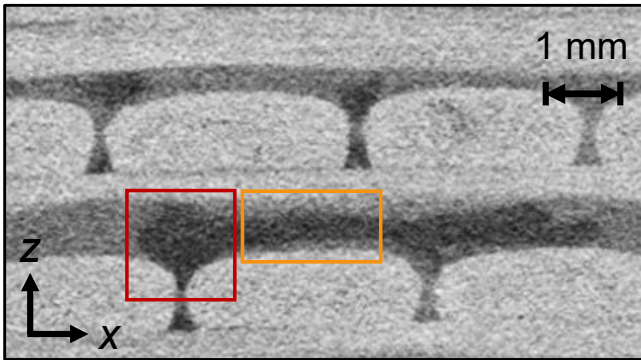
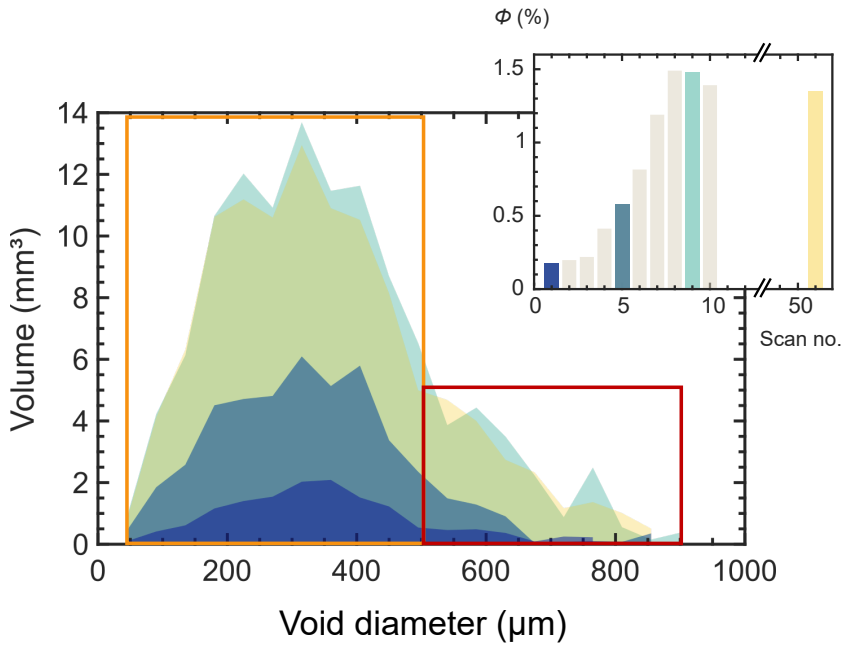


Fig. 5.7 LT analysis of the voids determined from scans 1, 5, 9 and 51. The orange and red boxes respectively correspond to inter-ply voids and inter-tow void populations. Examples of these two categories of voids are shown, using boxes of the same colour, on a 2D xz cross-sectional image.

The architecture of the fibrous preform constrains the expansion of the voids in the z -direction, resulting in more and more elongated cavities in the x and y -directions as Φ increases. As shown by the 3D volume rendering of scan 8 in Figure 5.6, this results in a partial or full coalescence of the voids in planes perpendicular to the z -direction.

Last, comparing the size distributions of the voids captured by scans 9 and 51 reveals a very slight and homogenous decrease in the volume of the voids, regardless of their size. More precisely, the *total* volume of the voids in the region of interest drops by 1.3 % between scans 9 and 51, i.e. during cooling of the composite preform. This is nowhere near sufficient, however, to explain the measured drop in Φ values mentioned previously. Indeed, a 1.3 % decrease in the total volume of the voids should have led to a negligible drop of around 0.02 % in the calculated value of Φ . The observed discrepancy between the LT analysis and calculated porosity values can be easily explained by superimposing xz cross-sectional images of scan 9 and 51 (taken at the $y = w/2$ location) and projecting the measured standard deviation in grey level for each pixel via the 'Z project' tool of ImageJ. The standard deviation map is presented in Figure 5.8. The white areas indicate the locations where significant differences have been detected between the two images. There is a clear vertical shift (i.e. along the z -axis) between the two images, which becomes larger as the z coordinate increases.

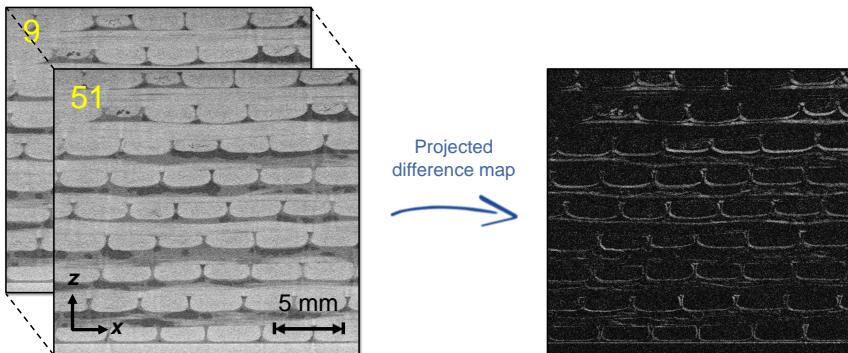


Fig. 5.8 Projected pixel-by-pixel standard deviation map (right) between the xz cross-sectional images of scans 9 and 51 (left), obtained via the Z project tool of ImageJ.

This vertical contraction of the material results from the thermal shrinkage experienced by the composite during cooling. We note in passing that the heterogeneous contraction in the z -direction is likely due to the fact that the surface plies, which are closer to the bag, cool down faster through air convection than the bottom plies, which are in contact with a thick layer of metal. Coming back to the matter of interest, thermal shrinkage thus affects the relative proportions of voids, matrix and fibre tows within the fixed field of view used for calculating porosity. This explains the discrepancy between the calculated drop in porosity and the expected value of this drop, as estimated from the LT analysis of the voids.

5.3.4 Assessment of dynamic scan uncertainty

The static scan and one of the last dynamic scans, i.e. scan 51, were compared to verify the representativeness of the dynamic scanning method in terms of void size. As mentioned previously, the two datasets were both acquired once the system had completely cooled down and was no longer expected to evolve. The distributions of LT values obtained via both scanning methods are presented in Figure 5.9.

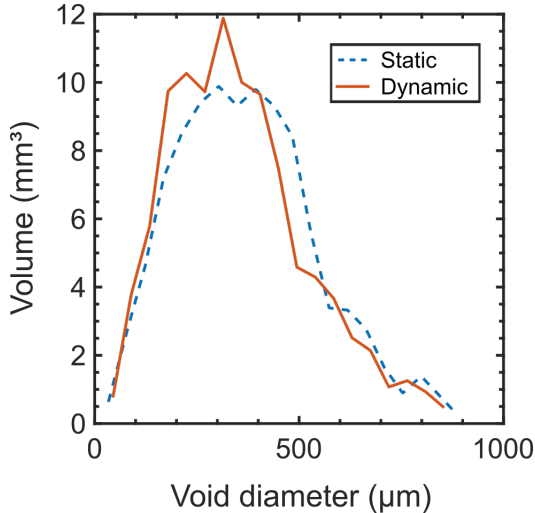


Fig. 5.9 LT analysis of the voids after cooling, determined from dynamic scanning (scan 51) *versus* static scanning.

The plots have overall similar shapes, which confirms the ability of the dynamic scanning method to capture voids with reasonable accuracy. However, the LT values of the voids captured by the dynamic scan are systematically higher than those obtained from the static scan in the 150-400 μm range, while the opposite trend is observed in the 400-550 μm range. This results in a significantly higher Φ value for the static scan ($\approx 1.9\%$) compared to the dynamic scan ($\approx 1.3\%$). In this case, the mismatch is probably due to a more precise detection of the edges of the voids via higher-resolution static scanning. However, both porosity values remain in the same order of magnitude, which is deemed sufficient with respect to the purpose of the study (i.e. identifying void formation mechanisms).

5.3.5 Identification of void formation mechanisms

In light of the results presented in Figures 5.3 to 5.7 and the main sources of porosity identified from the literature, the following timeline and explanations are proposed with respect to the void formation events occurring in the Elium composite specimen. First, a small amount ($\approx 15\%$) of the final volume of the voids arises from the infusion step, during which voids may form through the degassing of the resin and/or through the flow-related entrapment of voids during preform filling. In this work, the resin was degassed prior to infusion at a pressure lower than the infusion pressure. Therefore, it is assumed that the few voids observed within the preform after infusion result from flow-induced entrapment upon preform filling.

The majority of void growth events in the Elium composite are clearly attributed to the in-situ polymerisation step, during which they occurred gradually along the thickness direction of the preform. The two possible causes for cavitation during polymerisation are through the boiling of one or several resin component(s) (or by-product(s)) and/or the chemical shrinkage of the resin. The boiling of the Elium monomer MMA within thick composite parts produced by vacuum infusion has been thoroughly studied in references [1, 4]. Assuming the pressure inside the bag raises back to around 1 atm after infusion (which should be the case after closing the resin inlet and vacuum lines [165, 166]), the boiling temperature of MMA should be close to 101 $^{\circ}\text{C}$ within the bag. The Elium composite specimen reached a maximum surface temperature of 60 $^{\circ}\text{C}$ during polymerisation (as recorded by the thermocouple), and a maximum mould temperature of 80 $^{\circ}\text{C}$ (as measured by the PID heating system). Therefore, it seems unlikely that MMA could boil within the preform. Besides, the homoge-

nous void pattern observed along the z-axis after polymerisation does not resemble the characteristic gradient pattern resulting from monomer boiling issues [1, 4, 98]. By elimination, chemical shrinkage appears as the most probable source of void formation in the Elium composite of interest. This hypothesis is supported by the fact that poly(methyl methacrylate) (PMMA), which is the main constituent of Elium after polymerisation, is known to be around 20 % denser than the MMA monomer [14].

Finally, there is a very slight reduction in void size upon cooling of the composite specimen as a consequence of thermal shrinkage. However, the resulting change in the overall void pattern of the composite material can be considered negligible.

5.4 Conclusions and perspectives

This study provides a proof of concept for a novel 4D-XCT lab-based experiment aimed at monitoring the processing of composites by vacuum infusion and in-situ polymerisation. The key focus was placed on void formation. The main outcomes of the study are the following: (1) the design, manufacturing and successful testing of a miniature heating infusion setup, (2) the characterisation of void formation and growth events in a composite preform during matrix polymerisation and (3) a semi-quantitative assessment of the nucleation, growth and coalescence process in terms of shape, size, and location of the voids.

Obviously, laboratory-based X-ray scanners are subjected to technical limitations which make it difficult to perform dynamic experiments with both a high spatial resolution and a high scanning rate. In this work, the best possible trade-off we could find led to a scan time of 2 min 15 and a voxel size of 22 μm . The scan time is too long for fully capturing void nucleation and growth events in a viscous liquid [193], while the voxel size is too large for distinguishing individual fibres within the tows and detecting voids smaller than 50-60 μm . Using a synchrotron X-ray light source would certainly help to overcome these limitations, as described in Annex 2 (see section 9.2). However, this would bring in turn a number of new challenges [194]. First, the field of view would be drastically reduced, decreasing the probability of capturing several void formation events. Second, the high luminosity of synchrotron sources would certainly cause self-heating of the setup, which - in the case of Elium - could cause monomer boiling and subsequent void formation. Finally, the enormous amount of data gener-

ated by synchrotron XCT scanning would make it impossible to monitor the entire polymerisation of Elium in a continuous manner.

5.5 Acknowledgements

Financial support from Arkema and from the KU Leuven project no. C24/17/052, (regarding in-situ X-ray CT characterisation of composite materials and tissues during mechanical testing) is gratefully acknowledged. The FWO large infrastructure I013518N project is also acknowledged for their financial support of the X-ray infrastructure, as well as the KU Leuven XCT Core facility is for the 3D image acquisition and quantitative post-processing tools (<https://xct.kuleuven.be/>). The authors would also like to thank the Elium team at Groupement de Recherche de Lacq (Lacq, France) for helping design the bagging protocol for the miniature setup. Finally, the authors wish to address their warm thanks to Dr. Florent Hannard, for his guidance and assistance with image processing.

5.6 Appendix

Table 5.1 Material used for assembling and operating the infusion setup.

Description of the part	Reference or characteristics	Manufacturer
Polished aluminium plate	160 × 50 × 1 mm ³	-
Heat transfer layer	MHP-2550A100A	AMEC Thermasol
Ceramic cartridge heaters	12V 40W, ∅ 6 × 20 mm ³	Reprap
Temperature sensors	LM35CAH	Texas Instruments
Wire connectors	Micro Mate-N-Lock	TE Connectivity
Thermally conductive glue	TC-2810	3M
Elbow pneumatic connectors	3199 04 19, 4 mm	Legris
Heating controller	Love 32B-22-LV	Dwyer Controls
Power supply	24V/5A	-
Slip ring	SRH 1254	Gileon
Vacuum pump	XL 20	PIAB
Resin/vacuum PUER tubing	1025U04R08, 4mm	Legris
Manual pneumatic valve	7910 04 00	Legris
Remote pneumatic valve	VX220AGA	SMC
Vacuum gauge	GZ46-K-02	SMC

6

Nanoscale digital image correlation at elementary fibre/matrix level in polymer-based composites

This chapter is based on the published article *Nanoscale digital image correlation at elementary fibre/matrix level in polymer-based composites*, N. Klavzer and S. F. Gayot, M. Coulombier, B. Nysten, T. Pardoën, *Composites Part A: Applied Science and Manufacturing* 168 (2023), 107455 [7].

N. Klavzer and S. F. Gayot designed and performed the in-situ compression experiments and DIC analyses. M. Coulombier took care of PVD-related tasks. N. Klavzer was in charge of distortion correction aspects and S. F. Gayot performed the particle size and strain deviation analyses.

6.1 Introduction

Quantitative submicron scale experimental data about the deformation and failure of fibre-reinforced polymer composites (FRP) at the matrix/interface/fibre level is currently missing, preventing a full understanding of the local mechanics and impeding the development of enriched micromechanical models. Bottom-up multiscale mechanics approaches are indeed at the core of the advanced design strategy of fail-safe composite structures [195]. Available finite element (FE) numerical frameworks rely on experimental results for modelling the behaviour of FRPs at the micro- (ply level), meso- (laminate level) and macro- (part level) scales [196]. While macro- and mesoscale properties are relatively straightforward to extract using classical mechanical tests, the response at the microscale has yet to be fully explored especially in terms of quantitative mechanical behaviour data. Evidence shows that neglecting the local fibre/matrix behaviour, such as possible size effects, the presence of an interphase of different nature, local variations in polymer structure and/or constraint effects on local shear banding, significantly limits the accuracy of numerical predictions, particularly in loading conditions where the matrix is the main carrier of deformation (i.e. transverse compression or shear) [197]. In other words, one cannot ‘simply’ rely on the bulk polymer mechanical response and known fibre behaviour to model the microlevel.

A number of experimental approaches are available to address the local matrix, fibre-matrix interface and interphase characterisation, see recent review [198]. Nanoindentation has been widely used to characterise both bulk polymer glasses and ‘confined’ matrices within FRPs [199–205]. Although the interpretation of experimental load-penetration curves in small matrix pockets remains controversial, the properties determined by nanoindentation very often differ from those extracted from macroscale tests. The local strength in FRPs tends to be 15–20 % higher compared to bulk samples, while stiffness is also often found to be larger within inter-fibre matrix regions. Nanoindentation data have been used to either determine the underlying deformation mechanisms or to feed FE models [206]. Atomic force microscopy (AFM) has been applied to FRPs to determine local heterogeneities and to map the size of the interphase region around the fibres. The local property landscape in polymer glasses is systematically heterogeneous and the size of the interphase is found to be ranging from a few tens of nanometres up to a few microns [207–210].

However, nanoindentation and AFM do not provide information on the stress and strain fields during loading.

Recently, micro digital image correlation (DIC) has been adapted to the study of FRPs, aiming at characterising the local deformation processes [211, 212]. DIC is a non-contact method, which tracks the relative displacement of material points between two images. The strain field is then extracted from the displacement field [213, 214]. DIC can, in theory, be applied at any scale as long as a suitable speckle pattern (i.e. used for the tracking) can be created or by using inherent material surface features. Although macro DIC is widely used by the composite community [215–217], the use of micro DIC remains scarce and nano DIC has, to the authors' knowledge, not been applied to FRPs yet.

Micro DIC on FRPs was first introduced by Canal et al. [211]. In-situ transverse compression tests were performed within a scanning electron microscope (SEM) on unidirectional (UD) composite samples to favour matrix plasticity. A fine alumina dispersion was used to track displacements. The potential of micro DIC was demonstrated by qualitatively mapping the strain fields over the region of interest (ROI), in accordance with FEA predictions. Inter-fibre strain localisation was also detected, however the overall strain measurements for each phase were inaccurate due to averaging by the correlation algorithm linked to speckle coarseness. Subsequent studies by Mehdikhani et al. [212, 218] showed that micro DIC is also capable of clearly identifying regions of strain concentration or even the presence of carbon nanotube clusters. Yet, the authors pointed out the importance of evaluating the error resulting from the speckle pattern quality, DIC analysis parameters and SEM-related effects (e.g. charging, spatial and drift distortion, etc.). Hence, the speckle pattern quality is the primary factor limiting the quantitative use of micro DIC at the fibre/matrix level. More recently, Chevalier et al. [197] performed an extensive experimental and numerical study on the transverse compression of UD specimens. The DIC maps did not match the FE predictions obtained with a classical continuum model in confined regions between fibres, where the FEA largely overestimates the strain amplitude. The key conclusions from these studies are, on the one hand, that the accuracy of micro DIC is mainly limited by the speckle pattern quality and SEM artefacts and, on the other hand, that macroscale continuum models are unable to quantitatively capture microscale deformation behaviours in confined volumes.

In order to extract quantitative information from micro DIC, issues related to the speckle pattern and SEM have to be addressed. Improving the speckle pattern quality has been a point of interest for many material systems [214, 219, 220]. The goal is to obtain a high contrast and dense speckle pattern with a submicron speckle size, which significantly increases the spatial resolution of the DIC analysis. Hoefnagels et al. [221] recently proposed a novel approach allowing for a resolution of a few tens of nanometres, hence justifying the use of the ‘nano DIC’ terminology. The method relies on the ability of some metals to create thin films from the nucleation, growth and coalescence of nanometric clusters or ‘islands’ (Volmer-Weber growth mode). This particular growth mode is observed when adatoms have a high diffusion length on the substrate surface, which may be achieved by depositing a metal (or alloy) with a low melting temperature, while providing high kinetic energy to the deposited atoms via low-pressure deposition methods, e.g. physical vapour deposition (PVD) [221, 222]. Hoefnagels et al. showed that the physical vapour deposition of certain indium-based solder alloys by magnetron sputtering yields the formation of speckle patterns with controlled morphologies (i.e. particle shape, size, and density) on metallic substrates, without requiring substrate heating. This method was used successfully to quantify strain localisation – and thus predict failure location – in polycrystalline iron foils [221].

Nevertheless, a high-resolution speckle is not sufficient to guarantee the overall spatial resolution of DIC measurements, which also depends on the accuracy of the imaging technique. In the case of in-situ mechanical tests performed in a SEM chamber, so-called image distortions – i.e. deviations with respect to the ‘ideal’ image positions [223] – can occur and eventually give rise to spurious displacements and thus invalid strains extraction. SEM-related distortions may be separated into space- and time-dependent effects, as proposed by Sutton et al. [223, 224] and other subsequent studies [225–227]. Spatial distortions (e.g. due to lens aberrations) do not evolve over time, unlike temporal or ‘drift’ distortions. The latter may arise from the components making up the SEM or even charging of the imaged material. Positioning errors of the electron beam during scanning, referred to as ‘scan line shifts’ [214, 223, 225], may also fall under this category, but the impact on DIC measurements has not been extensively studied in the literature – probably because they give rise to highly recognisable line patterns on DIC strain maps.

Spatial distortions have been shown to remain relatively constant throughout a given experiment and to be more prevalent at low magnifications, meaning that the effect on micro or nano DIC should be limited [228]. Drift distortions, however, are more significant at high magnifications, and can induce large overestimations in the measured displacements. Several methods have been proposed to correct for drift distortions, but the simplest approach consists in taking pairs of images at each step during in-situ testing and evaluating the relative shift between them [228]. When the material presents strong stress relaxation, as in polymer glasses, accounting for the effect of stress relaxation on the drift is key and can lead to degraded DIC measurements if not properly dealt with [228]. An alternative approach is to improve the correlation algorithm to take into account such artefacts, as done in [226, 227].

In this study, we combine the latest advances in patterning techniques for micro and nano DIC with in-situ transverse compressions on UD FRPs in order to reveal, for the first time, fine details of the local deformation and failure of the constituents at the fibre/matrix level. This application of nano DIC on FRPs has been made possible by adapting the speckle deposition technique developed by Hoefnagels et al. [221]. Here, we simplify the approach by using electron beam (e-beam) evaporation of pure indium, where only the deposition time (and hence the particle size) can be controlled. The resulting dense and homogeneous nanoscale pattern exhibits particle sizes ranging from 10 nm to a few hundred nm. This pattern is applied to two types of FRPs: a glass fibre-reinforced thermoplastic and a carbon fibre-reinforced thermoset. It allows overcoming the main challenge of low-scale DIC on FRPs, which is the accurate separation of the displacements and strains in each of the constituents. In particular, the size of the matrix-modified interphase region around the fibres can be measured, which was impossible so far due to the averaging within the DIC algorithm linked to an insufficiently fine speckle pattern. The methodology adopted to minimise the impact of SEM-related distortions is also presented in this paper. The results are compared first to AFM data and then to FE predictions made using a continuum model with pre-identified parameters for the matrix.

6.2 Materials and experimental methods

6.2.1 Manufacturing of composite specimens

Glass fibre-reinforced thermoplastic composites

UD glass fibre-reinforced thermoplastic (TP) composite samples were provided by Arkema (France). The thermoplastic matrix comprised a pultrusion-grade methyl methacrylate-based monomer formula, Elium® 591 (Arkema), and 1 part per hundred ratio of the following peroxide thermal initiators: Perkadox® 16 (Nouryon, the Netherlands), Trigonox® 141 (Nouryon) and Luperox® DEC (Arkema). 2400-tex SE 4740 glass rovings (3B-The Fiberglass Company, Belgium) were used as reinforcement. Continuous unidirectional composite profiles with a final thickness equal to 2 mm and fibre volume fraction (V_f) close to 65 % were produced by pultrusion. Parallelepipedic specimens of dimensions $4 \times 2 \times 3 \text{ mm}^3$ were machined using a water-cooled disc milling cutter, as shown in Figure 6.1a.

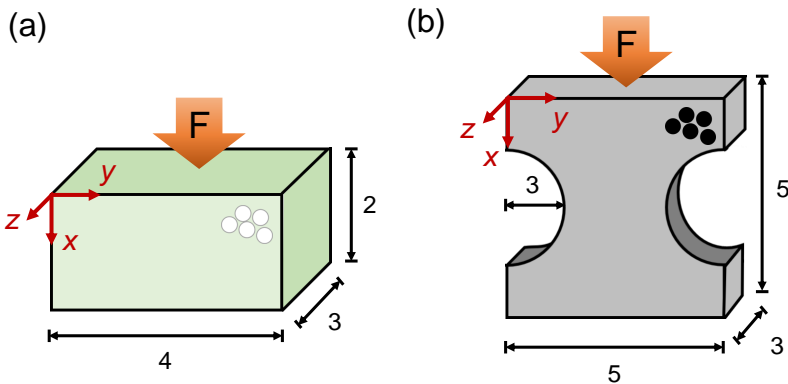


Fig. 6.1 Unidirectional composite specimens for in-situ transverse compression testing: (a) glass fibre-reinforced TP and (b) carbon fibre-reinforced TS. Fibre orientation is parallel to the z -axis and compression is performed in the x -direction. All dimensions are in mm.

The choice of specimen geometry and dimensions was driven by two factors: (1) the limitation associated to the 2 mm-thick UD composite samples manufactured industrially by Arkema and (2) the features of the compression stage and SEM chamber used for in-situ testing, see section 6.2.3. More precisely, the z-dimension was matched with the groove depth of compression jaws (i.e. 3 mm) to optimize electric contact with the metal and minimise working distance during SEM imaging. Additionally, the strength of the specimen had to remain below the load limit of the compression stage, i.e. 2 kN.

Carbon fibre-reinforced thermoset composites

A UD carbon fibre-reinforced thermoset (TS) composite plate was produced by resin transfer moulding according to the procedure described in [197], using the monocomponent HexFlow RTM6 resin from Hexcel (CT, USA) and HTS 12k carbon fibres (Saertex GmbH, Germany). The final V_f value was close to 40 %. Parallelepipeds of dimensions $5 \times 5 \times 3 \text{ mm}^3$ were machined using a water-cooled disc milling cutter, and two notches were drilled parallel to fibre orientation as shown in Figure 6.1b. In this case, specimen geometry and dimensions had already been determined by Chevalier et al. [197] so as to remain within the limits of the compression stage load cell (see section 6.2.3) and induce stress concentration during testing.

Note that different geometries and fibre volume fractions were used for the carbon fibre-reinforced TS and the glass fibre-reinforced TP transverse compression specimens, for the practical reasons mentioned above. However, this should not compromise the comparability of DIC measurements between the two systems, as the nature of nanoscale plastic deformation and failure phenomena occurring between fibres in a given system depends mostly on the local fibre arrangement within the ROI (i.e. inter-fibre distance, fibre diameter and orientation of the inter-fibre matrix strip with respect to the unidirectionally-applied load).

Polishing of composite surfaces

Both types of composite specimens were polished perpendicular to fibre orientation (i.e. z-axis) on a semi-automatic MultiPrep Precision Polishing System (Allied High Tech Products, Inc., CA, USA). Resin-bonded diamond discs with successive grit of 1200 and 4000 (MD-Piano from Struers Inc., OH, USA) were used for grinding, while finishing was performed with a 0.3- μm alumina suspension (AP-D Suspension 0.3 μm , Struers Inc.).

6.2.2 Speckle pattern deposition

The protocol developed by Hoefnagels et al. [221] for depositing nanometric DIC speckles onto metallic specimens by PVD was simplified and applied to polymer composite substrates as follows. Indium deposition was performed by e-beam evaporation, using indium pellets with a purity of 99.99 %. The deposition rate was kept equal to $1 \text{ \AA}\cdot\text{s}^{-1}$ and the operating pressure never exceeded 4×10^{-7} mbar. The influence of the deposition time on speckle pattern morphology was assessed using silicon wafers as the substrate material. More precisely, several deposition times were tested, in order to produce the following target coating thicknesses: 2 nm, 5 nm, 10 nm, 20 nm and 50 nm. The results of this preliminary study are presented in section 6.3.1. Note that indium was selected among the list of commonly evaporated materials for several reasons. First, pure indium has a low melting point under standard temperature and pressure conditions (around $157 \text{ }^\circ\text{C}$ [229]), which should favour the formation of metal ‘islands’ on the substrate material instead of a continuous film during PVD, as mentioned previously [221]. It is also chemically inert to air and water under ambient conditions, which guarantees the stability of the coating between the deposition and imaging steps. Metallic indium is easily available and relatively inexpensive compared to other metals used for e-beam evaporation [230]. Last, human toxicity of metallic indium is low under occupational conditions [231].

6.2.3 SEM imaging and in-situ compression testing

Imaging of indium-coated Si wafers

An Ultra 55 Field-Emission SEM (Zeiss, Germany) was used for imaging the indium speckle patterns deposited onto Si wafers, see section 6.3.1. The acquisition parameters were similar to those applied during the in-situ compression testing of composite specimens, see below.

Preparation of composite specimens for SEM imaging and compression

Unwanted charging effects arise when poor electric conductors, like polymer composites, are imaged by SEM. As detailed in section 6.2.4, charging may be detrimental to image quality (especially at high magnifications) and can ultimately lead to surface degradation, impacting in turn the accuracy of DIC measurements. Following indium deposition, polished composite surfaces were therefore subjected to carbon sputtering, and all other free surfaces were coated with a thin layer of silver lacquer. Composite

specimens were mounted on a microtest compression stage equipped with a 2 kN load cell (Deben UK Ltd., UK) and further placed inside the chamber of an Ultra 55 Field-Emission SEM (Zeiss, Germany). Figure 6.2 shows the experimental setup ready for insertion in the SEM.

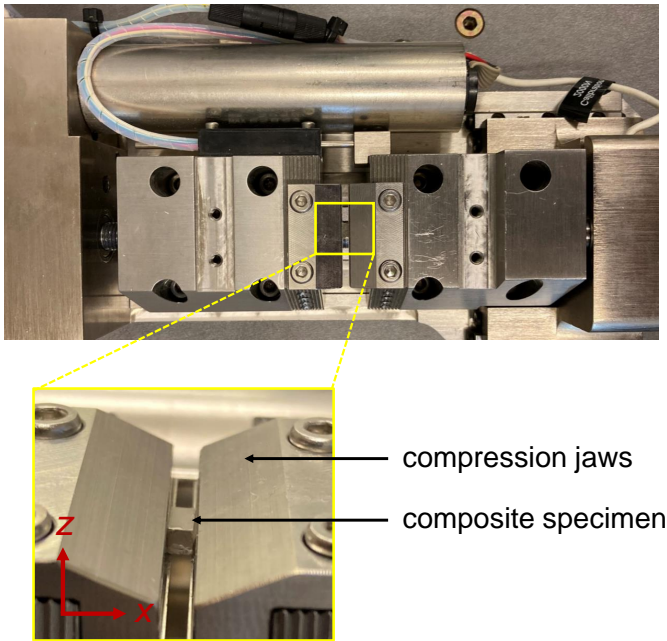


Fig. 6.2 Thermoplastic composite specimen mounted on microtest compression stage.

Compression testing and acquisition of DIC data

For each specimen, one or two zones of interest were selected for DIC measurements and imaged with both a $5.7 \times 4.3 \mu\text{m}^2$ and $11.4 \times 8.6 \mu\text{m}^2$ field of view (i.e. at a magnification of 20,000 and 10,000 in our case), and a pixel size close to 6 and 12 nm, respectively. Acceleration voltage was kept in the 2-4 keV range to limit charging effects. When needed, contrast and brightness values were adapted during the test in order to counter the progressive darkening of SEM images induced by remaining charging effects.

Each region of interest (ROI) was imaged before and during uniaxial compression along the x -axis. Loading was performed using 50 to 100 N increments, in between which the stage motor was stopped. SEM images were taken at each load increment after the specimen was left to relax until the load drop over a two-minute period (i.e. average time to take two successive SEM images) was less than 1 N (see section 6.2.4 for further details). Compression was continued until macroscopic fracture of the specimen.

6.2.4 DIC data processing

Image analysis

The size distribution of indium particles deposited on silicon wafers and composite specimens was assessed using the open-source software ImageJ. SEM images were subjected to binary thresholding, and a watershed segmentation algorithm was applied to separate any spuriously connected particles. The built-in particle analysis tool of ImageJ was run, and the resulting data were processed with MATLAB (R2021b). A sample size of at least 1,000 particles was used for each case.

DIC measurements

The DIC analyses were carried out using the open-source software Ncorr [232], which relies on three input parameters: the subset size, step size and strain radius value. The ‘subset’ refers to a group of pixels in which strains are assumed to be homogeneous, while the ‘step’ denotes the spatial shift between two adjacent subsets. The value of the strain radius indicates the size of the smoothing filter applied when converting displacement fields into strain fields. Note that the choices of subset and step size condition the spatial resolution of calculated displacements, while that of strain radius impacts the level of numerical noise in the final strain maps. The systematic approach of Mehdikhani et al. [212] was followed in order to find a suitable combination of input parameters with respect to (1) the morphology of the speckle pattern and (2) the quality of the SEM images obtained in this work. More precisely, a well-speckled zone of an undeformed TP composite specimen was imaged by SEM at the magnification levels of interest for DIC, i.e. 10,000 and 20,000. The images, of respective dimensions $991 \times 673 \text{ px}^2$ and $828 \times 612 \text{ px}^2$, were then numerically stretched by 10 px in the x -direction using the `lanczos3` tool of Matlab (R2021b). The extracted uniaxial strains ϵ_{xx} were close to the expected values of 0.0101 and 0.0121, respectively. For both levels of magnification, DIC measurements

were performed between the original and stretched SEM images, with different sets of subset size, step size and strain radius values. The values obtained by DIC for the mean strain (and corresponding standard deviation) were compared to the theoretical values of ϵ_{xx} mentioned above. The results of the strain deviation analysis are presented in section 6.3.1.

As mentioned in the introduction, SEM imaging induces spatial and drift (i.e. temporal) distortions. Kammers et al. [228] proposed a straightforward method for addressing both types of artefacts without modifying the DIC algorithm. First, to correct spatial distortions, a series of four overlapping images in the horizontal (u) and four images in the vertical (v) directions are taken over a defined distance. In addition, at each displacement increment, a pair of images is taken to correct for drift distortions (see below). The total applied displacement increment should be selected so that the total displacement in each direction does not exceed $\frac{1}{4}$ of the field of view of the DIC analyses. However, the smallest possible translation within this study was limited to $1\ \mu\text{m}$ due to the SEM stage accuracy limitations. Since the imposed displacement is known (from the rigid body motion principle), it can be subtracted from the calculated displacement fields, resulting in so-called ‘spatial distortion maps’. A linear relationship relating the amplitude of the distortion in the u and v directions and the imposed translation is extracted from the results. This function may be used as a correction tool for spatial distortions, which takes, as input, the u and v displacements at each point of the DIC fields. Second, drift distortions can be measured by taking two consecutive images at each load increment. For each pair of SEM scans, the calculated DIC maps are subtracted from one another. The resulting difference in displacement amplitude over the ROI determines the error related to drift distortions. The horizontal and vertical displacement drift maps are then subtracted from the actual DIC displacement maps to get drift-free maps. Finally, the impact of stress relaxation was determined on the two consecutive images used for drift correction. The evolution of the load as a function of time was monitored during image acquisition. Hence, each pixel may be related to its acquisition time and the corresponding load value, resulting in so-called ‘load maps’. In this study, the composite specimens were systematically left to relax in between load increments, so that the load drop never exceeded 1 N during the acquisition of two consecutive images. The corresponding error on DIC strain measurements was found to be negligible, as shown in Figure 6.20 in the Appendix.

6.2.5 Atomic force microscopy

Micromechanical analysis of the Elium and RTM6 composite systems by AFM was performed on Dimension Icon and MultiMode 8 systems (both from Bruker Corp., USA), using PeakForce Tapping®-QNM mode and a factory-calibrated RTESPA-300-30 probe (Bruker) (see chapter 7). The cantilever spring constant and nominal tip radius values were respectively close to 50 N.m^{-1} and 30 nm . AFM scans of dimensions $6 \times 6 \mu\text{m}^2$ were acquired with a resolution close to 47 nm.px^{-1} . The PeakForce frequency and amplitude parameters were respectively set to 0.5 kHz and 30 nm for Elium, and 1 kHz and 25 nm for RTM6. In both composite systems, the PeakForce setpoint was selected in order to achieve a 2 to 3 nm indentation depth in the resin. In these conditions, the contact radius remained smaller than 10 nm . The selected PeakForce setpoint values were equal to 150 nN for Elium and 100 nN for RTM6. Modulus images were obtained from the built-in Derjaguin-Muller-Toporov (DMT) modulus calculation tool of NanoScope 9.4 (Bruker). More information on the acquisition method is presented in chapter 7 for the Elium composite system.

6.2.6 Finite element modelling

Finite element analyses were carried out using the commercial software Abaqus (Dassault Systèmes Simulia Corp.). The models were created using the exact same geometries as the experimental ROIs. The applied boundary conditions were determined from the displacement profiles measured by DIC on the edges of the respective ROIs. 2D plane stress elements (CPS3) were used for the meshing of the fibres and the matrix. Table 6.1 presents the material properties used for the mechanical modelling of both composite systems. The carbon or glass fibres were considered as linear elastic. The thermoset matrix was modelled as rate-dependent elastoplastic using the constitutive continuum model identified and validated by Morelle for RTM6 [233]. In brief, the pressure-dependent yield criterion for the matrix, used to account for the dependence of the polymer to the hydrostatic stress, was defined by a linear Ducker-Prager model, which writes as

$$F = t + p \tan(\beta) - d = 0, \quad (6.1)$$

where t is the yield stress, $p = \sigma_{kk}/3$ the pressure (with σ_{kk} the trace of the Cauchy stress tensor), β the friction angle and d the cohesion term. β

defines the slope of the yield surface in the $p - t$ plane while t is expressed as

$$t = \frac{\sigma_{\text{eq}}}{2} \left[1 + \frac{1}{K} - \left(1 - \frac{1}{K} \right) \left(\frac{I_3}{\sigma_{\text{eq}}} \right)^3 \right], \quad (6.2)$$

where σ_{eq} is the von Mises equivalent stress, K the stress ratio between the yield stress under triaxial tension and triaxial compression and I_3 the third invariant of the deviatoric stress tensor. The associated flow rule writes as $G = \sigma_{\text{eq}} + \sigma_{\text{kk}}/3 \tan(\phi)$, with G the flow potential and ϕ the dilation angle. The isotropic hardening law was defined as the sum of three contributions: a pre-peak yield non-linearity, a softening term and a re-hardening capacity (the full description can be found in [233]). The strain rate dependence is considered via the coefficients of the hardening law. Following identification over six decades of strain rate, $K = 1$ and thus $t = \sigma_{\text{eq}}$, $\beta = 7.86$ and $\phi = 0$ (assuming plastic incompressibility). A similar model, calibrated for Elium by Maes [234] on four decades of strain rate, was used for the thermoplastic matrix (see Annex 1 in section 9.1). In that case, $K = 1$ and thus $t = \sigma_{\text{eq}}$, $\beta = 26$ and $\phi = 0$. Simulations were performed using Abaqus explicit to overcome convergence issues related to the softening of the matrix, which are difficult to solve with Abaqus Standard (implicit). Perfect interfaces were considered between the fibre and matrix materials, i.e. no damage mechanisms were considered.

	E_{11} (GPa)	E_{22} (GPa)	E_{33} (GPa)	ν_{12}	ν_{23}	ν_{31}	Density (g.cm ⁻³)
Carbon fibres	238	28	28	0.28	0.33	0.02	1.8
Glass fibres	80	-	-	0.22			2.54
RTM6 resin	3	-	-	0.34	-	-	1.14
Elium resin	2.8	-	-	0.35	-	-	1.17

Table 6.1 Elastic properties of the fibre and matrix materials used for the FE modelling of the TP and TS composite systems.

6.3 Results and discussion

6.3.1 Optimisation and validation of the DIC method

Optimisation of speckle pattern

In addition to providing excellent contrast during imaging, the ideal speckle pattern for a given DIC experiment should meet a number of requirements. The particles should be small with respect to the length scale of the mechanical phenomena of interest, while remaining larger than the image pixel size. Additionally, the distribution of particle sizes should be narrow and speckle density should be high, in order to avoid the presence of 'featureless' subsets in DIC. SEM micrographs of the speckle patterns obtained by e-beam evaporation of indium onto Si wafers for different target coating thicknesses (2, 5, 10, 20 and 50 nm, see section 6.2.2) are presented in Figure 6.3, while the associated distributions of particle radii R are displayed as boxplots in Figure 6.4.

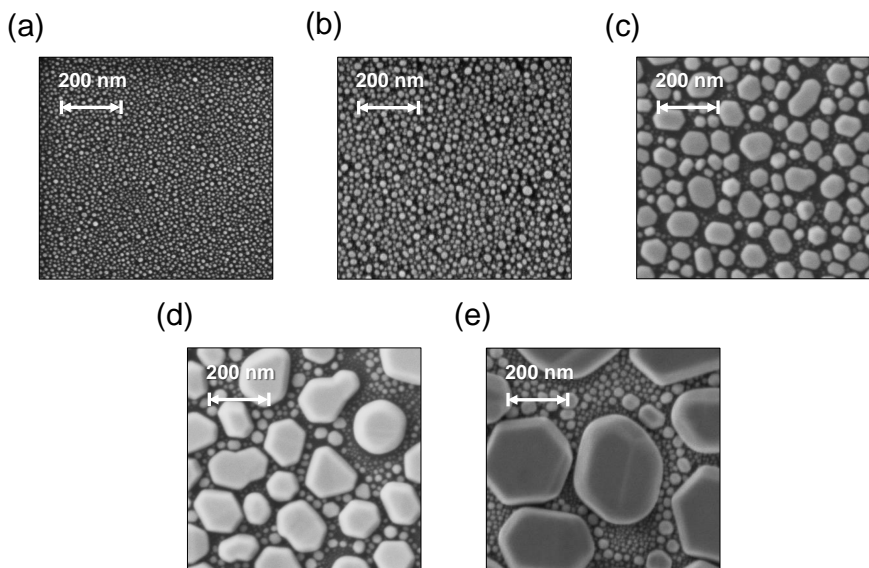


Fig. 6.3 Optimisation of the speckle pattern for DIC measurements: SEM images of a (a) 2 nm, (b) 5 nm, (c) 10 nm, (d) 20 nm and (e) 50 nm-thick indium speckle deposited by e-beam evaporation onto Si wafers.

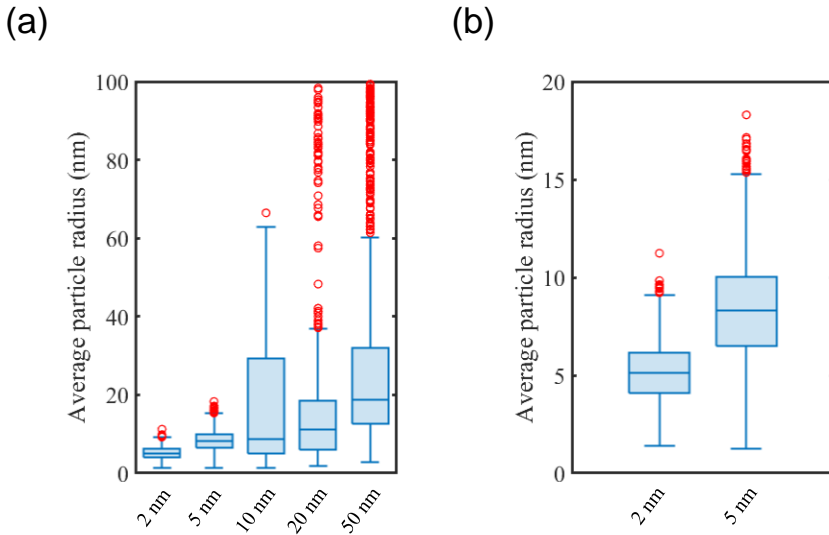


Fig. 6.4 Particle size distribution of indium speckle patterns with target thicknesses of (a) 2 to 50 nm and (b) 2 and 5 nm.

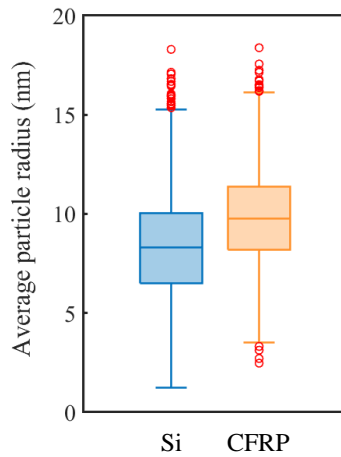


Fig. 6.5 Comparison of particle size distributions obtained for a 5 nm-thick indium speckle pattern deposited onto two different substrates: Si wafer vs. carbon fibre-reinforced TS composite.

Figure 6.3 shows the increase of the average particle size as more metal gets deposited, though the film remains discontinuous. Moreover, for coating thicknesses larger than or equal to 10 nm, the particles segregate into two distinct populations: the ‘large ones’ (for which $R \approx 100$ nm), and the ‘small ones’ (for which $R \approx 10$ nm). Note that the average radius of the larger particles increases from ≈ 50 to ≈ 100 and finally ≈ 300 nm as target coating thickness is raised from 10 to 20 nm and then 50 nm, respectively. Figure 6.4 confirms these trends, while providing quantitative information on the evolution of the statistical distribution of particle radii as coating thickness increases. The plots corresponding to the 2 and 5 nm-thick coatings are short and symmetric (see Figure 6.4b). This indicates a narrow normal distribution for R values in both cases, making both coatings potentially eligible for DIC measurements.

In this work, only the 5 nm-thick coating was used as a DIC speckle pattern. The 2 nm-thick coating was excluded from the study as the mean particle radius (close to 5 nm) was too close to the smallest pixel size used for SEM imaging ($6 \text{ nm}\cdot\text{px}^{-1}$, see section 6.2.4). From coating thicknesses of 10 nm onwards, the boxplots get longer and more skewed towards the high R values. As described previously, this indicates the emergence of a second, more scattered population of ‘large particles’ arising from the coalescence of smaller ones. Note that the lower half of the plots (i.e. lower whisker, first quartile and median R values) only evolves marginally with coating thickness. This suggests that the size distribution of the ‘small particles’ remains relatively unchanged. Finally, the selected deposition method developed on Si wafers was applied to a TS composite sample (CFRP) to assess the reproducibility of the speckle pattern on the substrate of interest. Figure 6.5 shows the corresponding particle size distributions obtained on both materials. The difference in particle size between both substrates remains within the margins of error, consolidating the use of this method on polymer composite specimens.

Choice of DIC input parameters

Table 6.2 shows the results of the strain deviation analysis described in section 6.2.4. In all cases, the mean strain value obtained by DIC matches that of the numerically applied strain, with a standard deviation value at least one order of magnitude smaller. Note that this result also confirms the quality of the speckle pattern after optimisation (see section 6.2.3). The optimum parameters selected for the DIC calculations at both magnification levels were the following: a 10-px subset size (smallest possible size in Ncorr), a 2-px step size and a 5-px strain radius. This combination offers the highest possible spatial resolution for the strain maps, while limiting the amount of noise.

Table 6.2 Strain deviation analysis [212] results obtained for various sets of DIC parameters.

Magnif. level	Subset size (px)	Step size (px)	Strain radius (px)	Mean strain (-)	Standard dev. (-)
10,000	30	2	5	0.0101	5.07E-05
10,000	20	2	5	0.0101	8.33E-05
10,000	10	2	5	0.0101	2.10E-04
10,000	10	2	3	0.0101	3.59E-04
10,000	10	2	1	0.0101	7.99E-04
10,000	10	1	5	0.0101	3.20E-04
10,000	20	1	5	0.0101	1.09E-04
10,000	10	1	3	0.0101	4.90E-04
10,000	10	1	1	0.0101	1.10E-03
20,000	30	2	5	0.0121	4.65E-05
20,000	20	2	5	0.0121	7.47E-05
20,000	10	2	5	0.0121	1.50E-04
20,000	10	2	3	0.0121	2.37E-04
20,000	10	2	1	0.0121	5.40E-04
20,000	10	1	5	0.0121	2.32E-04
20,000	20	1	5	0.0121	9.45E-05
20,000	10	1	3	0.0121	3.38E-04
20,000	10	1	1	0.0121	7.79E-04

Impact of SEM distortions

As mentioned in the introduction, drift and spatial distortions can cause significant errors in the calculated displacements determined by DIC. Figure 6.6 is a SEM micrograph showing a ROI that was subjected to a rigid body motion of $-4 \mu\text{m}$ in the x -direction in order to quantify the amplitude of the distortions described in section 6.2.4. The results of the DIC measurements and corrections are shown in Figure 6.7. The initial DIC measurements shown in Figure 6.7a delivered a displacement of around $-3.5 \mu\text{m}$ over the whole ROI. This represents a $-0.5 \mu\text{m}$ discrepancy with respect to the imposed rigid body motion. First, spatial distortions coming from the SEM stage movements were corrected. The corrected displacement field shown in Figure 6.7b presents an average displacement over the ROI of $-3.863 \mu\text{m}$. The amplitude of spatial distortions is therefore close to $-0.3 \mu\text{m}$. Next, the drift distortion field between the initial and displaced states was determined and subtracted from the corrected field of Figure 6.7b. The resulting distortion-free displacement field is shown in Figure 6.7c. The average displacement over the ROI is now $-3.9 \mu\text{m}$. Comparing Figures 6.7b and c allows quantifying the amplitude of the drift distortion, which is around $0.04 \mu\text{m}$. Typically, drift distortions are dominant at high magnification DIC applications, which Kammers defines as cases where the spatial resolution of the micrographs is finer than $\approx 500 \text{ nm/px}$ [228]. Yet, in the present case, drift distortions are relatively low.

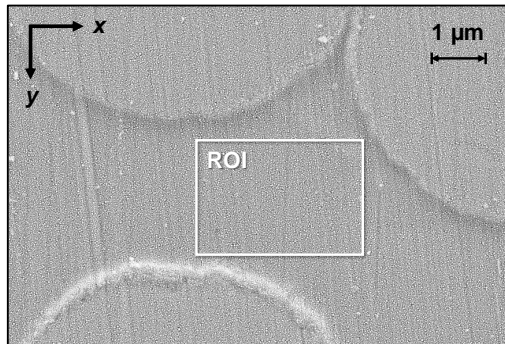


Fig. 6.6 ROI for the quantification of the spatial and drift distortion amplitudes.

This can be related to an excellent grounding of the composite samples via the combination of the conductive carbon coating, evacuating the surface charges, and the silver paste covering the edges of the sample to guide the charges away via the test machine. Thus, proper sample preparation allows overcoming one of the key challenges of nano DIC linked to the excessive amount of drift.

Ultimately, neglecting corrections on DIC measurements for both spatial and drift distortions can induce, at most, an error of around $0.5 \mu\text{m}$ in the present study. In what follows, the presented DIC maps are systematically corrected for both spatial and drift distortions.

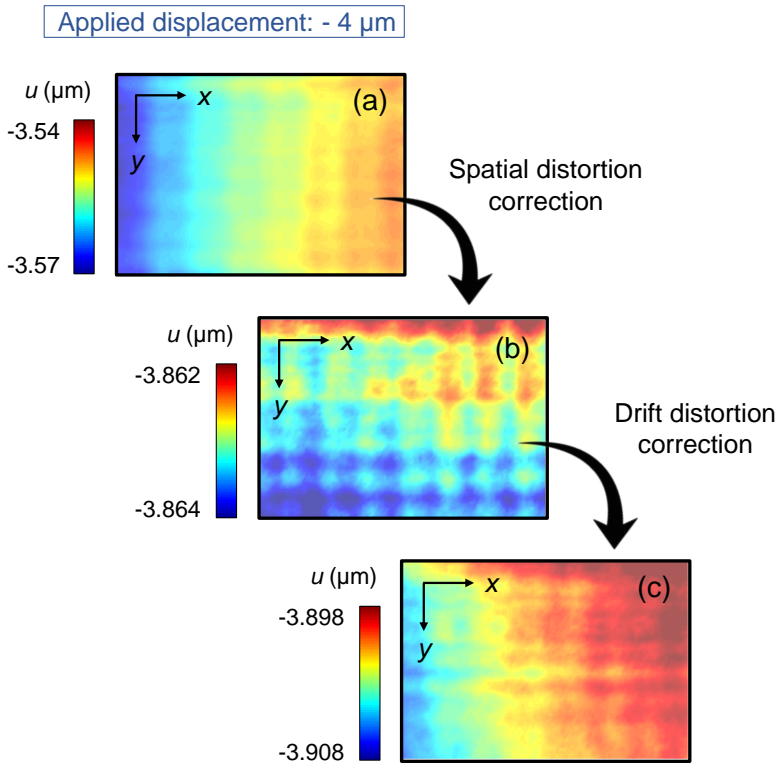


Fig. 6.7 Horizontal displacement field measured by DIC: (a) without any correction, (b) after spatial correction and (c) after spatial and drift corrections.

6.3.2 DIC results

Validation of nano DIC

In order to validate the proposed nano DIC approach, in-situ tests were carried out on the RTM6 and Elium fibre-reinforced systems at a magnification of 20,000. Figures 6.8a and c present the macroscopic load-displacement curves obtained during compression of an RTM6/carbon fibre and an Elium/glass fibre specimen, respectively.

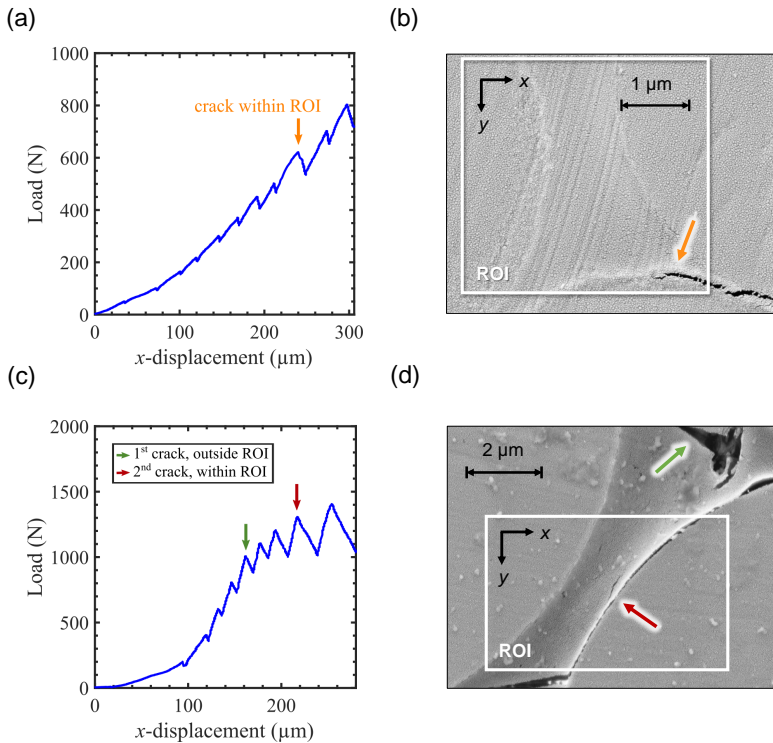


Fig. 6.8 Macroscopic load-displacement curves obtained from the in-situ compression testing and SEM micrographs of the corresponding ROIs used for DIC analysis of: (a) and (b) an RTM6/carbon fibre specimen and (c) and (d) an Elium/glass fibre specimen. Coloured arrows indicate the location of failure events observed within or close to the ROIs during testing, and the same colour code is used to show force-displacement values at these moments.

In both cases, the alternance of peaks and drops results from specimen relaxation following each load increment (see section 6.2.4), while the non-linear behaviour at very low displacements is caused by the compression of the soft layer of silver lacquer present on the lateral and lower surfaces of the specimens, i.e. the surfaces in contact with the compression jaws (see section 6.2.3). Figures 6.8b and d provide a zoomed-out view of the ROIs selected for DIC analysis in both systems. Note that the ROIs are shown *after* failure, whose loci are indicated with coloured arrows. The force value corresponding to each failure event is shown in Figures 6.8a and c. For the RTM6 specimen, failure occurs within the ROI via interface debonding, see Figure 6.8b. For the Elium/glass fibre specimen, however, two subsequent failure events are reported. First, a crack opens in the matrix outside the ROI but close to its boundaries (green arrow), and interface debonding then occurs within the ROI (red arrow), see Figure 6.8d. In this section, only the displacement and strain fields recorded just before each failure event are presented. The corresponding DIC strain maps are presented in Figures 6.9 and 6.10, respectively.

Figures 6.9a and b show the ϵ_{xx} and ϵ_{xy} strain fields for the RTM6 system. Nano DIC clearly distinguishes the fibre and matrix response. Indeed, being much stiffer than the matrix, the average amplitudes of ϵ_{xx} and ϵ_{xy} are close to zero in the fibres. The fibre/matrix interface can also easily be distinguished, which suggests that the resolution of nano DIC is sufficient to avoid smoothing of the fibre and matrix strains. The ϵ_{xx} and ϵ_{xy} strain fields displayed in Figures 6.10a, c and b, d, respectively, show the analogous results for the Elium system. Hence, the combination of a high-quality nanoscale speckle pattern and careful specimen preparation (i.e. grounding, etc.) allows overcoming the main restriction related to the use of micro DIC on FRPs in the literature.

The proper phase separation in the DIC results opens the door to investigate the interphase behaviour of FRPs. To illustrate this, Figures 6.9c and d, as well as Figures 6.10e and f show the strain distribution along different paths (depicted as white dashed lines) for both systems. A transition zone between the fibre and the matrix is systematically present. Within this region, a smooth transition from the quasi-zero strain level of the fibres to the matrix strains is observed. This transition zone spreads over 200 nm to 500 nm (assuming a peak-to-peak width). The literature reports that an interphase layer exists in FRPs that can spread from a few hundreds of nanometres to a few microns depending on the fibre sizing and curing con-

6 | Nanoscale digital image correlation at fibre/matrix level

ditions [208, 210, 235]. Hence, the observed transition zone can be related to the interphase of each system.

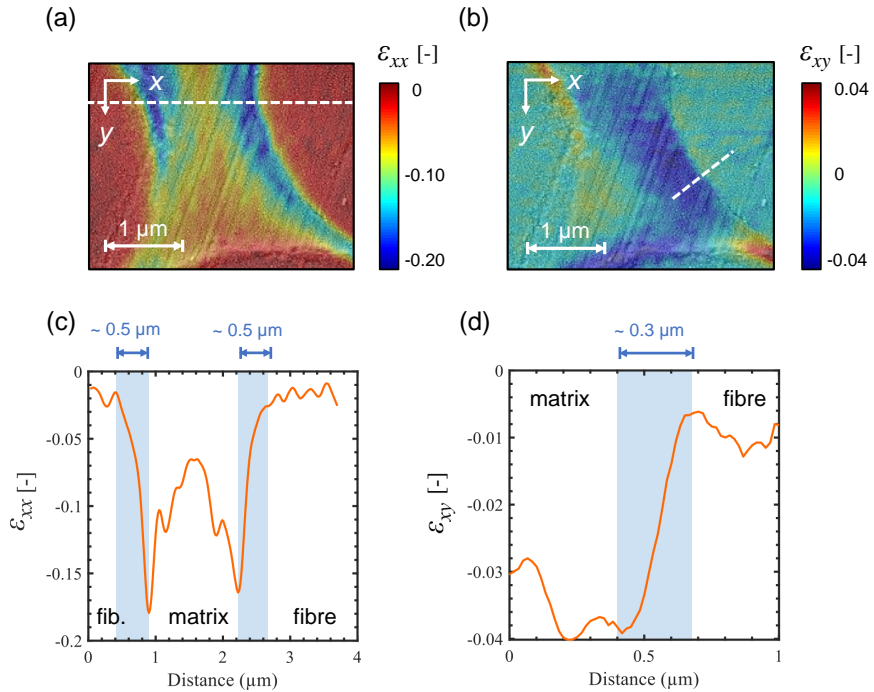


Fig. 6.9 Strain maps and evolution of strain profiles across the carbon fibre-RTM6 matrix interface (white dashed line) obtained by DIC: (a),(c) along the x direction and (b),(d) along the xy direction.

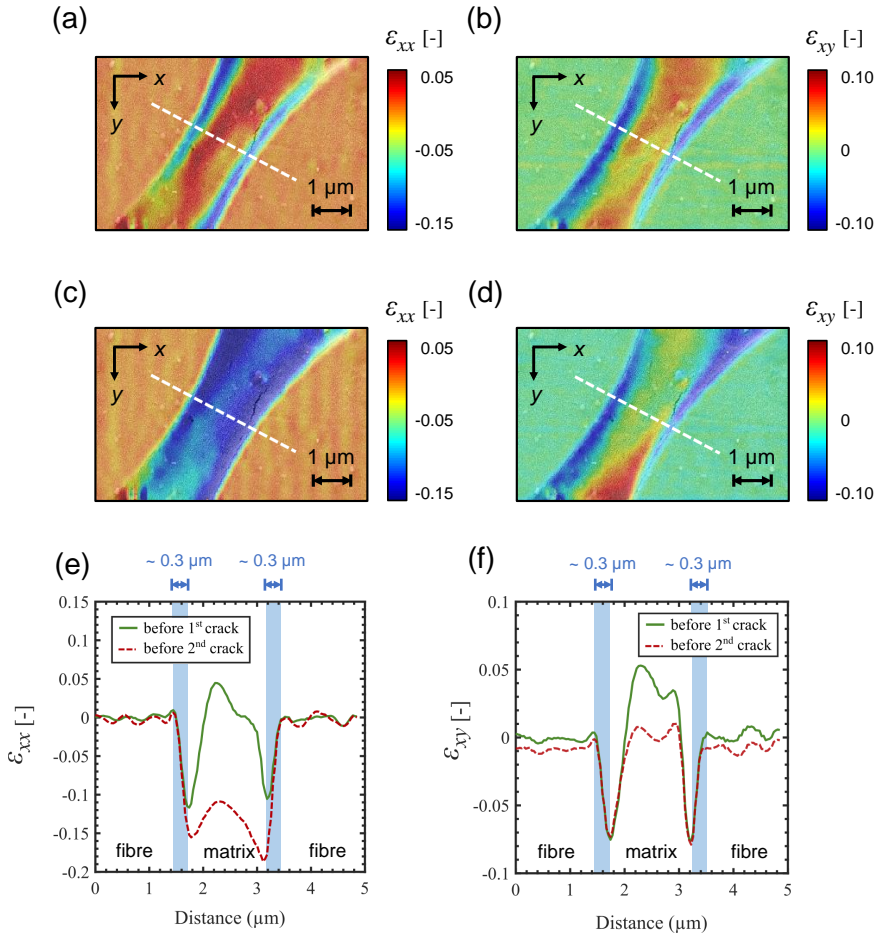


Fig. 6.10 Strain maps obtained by DIC in the Elium/glass fibre specimen along the x direction, (a) before 1st failure event and (c) before 2nd failure event, and along the xy directions (b) before 1st failure event and (d) before 2nd failure event, alongside with corresponding strain profiles across the fibre-matrix interface (white dashed line) in the (e) x and (f) xy directions. The terms ‘1st and 2nd cracks’ refer to the failure events identified in Figure 6.8.

Localised areas of large strain amplitudes in between fibres are captured by DIC, as observed in Figures 6.9 and 6.10 for the RTM6 and Elium systems, respectively. Note that high strain amplitudes are systematically found around fibres, highlighting the importance of getting accurate DIC measurements in both fibre and matrix zones. In particular, shear strain localisation is visible at the bottom right of Figure 6.9b for RTM6 and near the right fibre-matrix interface in Figure 6.10d for Elium. Comparing these two regions with the loci of interface debonding depicted in Figures 6.8b and d for RTM6 and Elium, respectively, large shear strains accumulate exactly where failure ensues. In the case of Elium, DIC also captures the redistribution of strains following a matrix cracking event starting outside the ROI, indicated in Figures 6.8c and d by the green arrows. This is especially clear when comparing Figures 6.10a and c, which show the ϵ_{xx} strain fields before and after the event. One can notice the homogenisation of the matrix strain field in Figure 6.10c, with respect to Figure 6.10a. The same trend is also observed, to a lesser extent, when comparing Figures 6.10b and d in terms of the shear strains ϵ_{xy} . Figure 6.21 in the annex displays the maximum shear strain maps for RTM6 and Elium, which clearly indicate that the maxima of shear coincide with the loci of failure in both systems.

Surprisingly, shear bands propagating between two fibres are not observed in any of the two systems, contrary to what is expected in FRPs subjected to transverse compression [197]. Still, in Figure 6.9b, strain concentrations can be found not only near the bottom of the right-hand fibre (i.e. in the region where a crack follows), but also near the top of the left-hand fibre. This could suggest that a shear band started to develop in the RTM6 ROI, but could not propagate as the induced localisation led the fibre/matrix interface failure first. Hence, the lack of significant shear banding measured by DIC may simply be related to an unfortunate choice of region of interest for a given test. Or, as the observed ROIs are quite small in both systems, it is also possible that large-scale shear band formation events are missed. Therefore, further investigation will require a screening of more regions of interest per specimen during each compression test, in order to identify and quantify the presence and amplitudes of micro shear bands.

In addition to the DIC measurements presented above, post-mortem SEM observations were carried out outside the ROIs to analyse the failure behaviour of both systems. The fracture surfaces are presented in Figure

6.11 for RTM6 and 6.12 for Elium, for different length scales. The micrographs in Figures 6.11a and b suggest that failure initiates suddenly in the RTM6 composite. The crack path follows the fibre/matrix interface, though no sign of progressive damage from interface decohesion or matrix cracking was observed, as demonstrated in Figures 6.11c and d. Still, Figure 6.11c shows that the conductive coating displays a significant amount of micro cracks, confirming that the RTM6 matrix below undergoes strong local plastic deformation via the creation of nano or micro shear bands. These observations are in line with the results of Chevalier et al. [197]. Lastly, a close-up of the fibre/matrix interface in Figure 6.11d shows the absence of crazes, which reinforces the idea of the absence of damage at the interfaces.

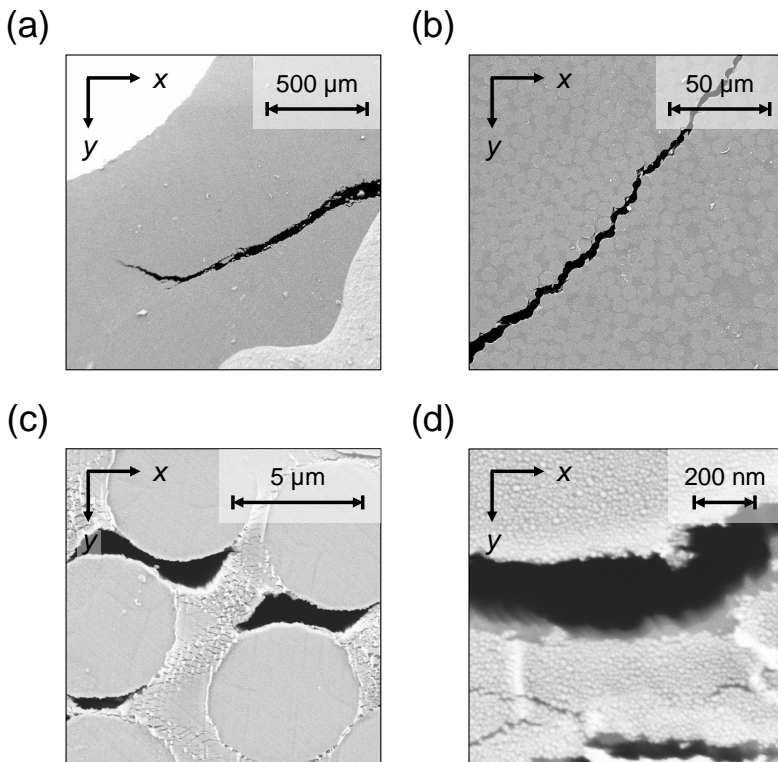


Fig. 6.11 RTM6 – Post-mortem observations of the failed material surface: (a) general overview, (b) main crack, (c) fibre/matrix level interface failure, (d) zoom of the interface failure in (c).

The case of the Elium system in Figures 6.12a and b is different, showing clear signs of damage accumulation all over the matrix. Note that this difference in behaviour between the two composite systems can also be inferred from the load-displacement curves presented in Figures 6.8a and c, which respectively suggest that the RTM6 macroscopically fails in a brittle manner, whereas the Elium system only fails after entering global plasticity. However, these differences as well as those observed on the post-mortem SEM micrographs may partially be explained by the difference in specimen geometry, which leads to different levels of stress triaxiality associated to the barrelling effect.

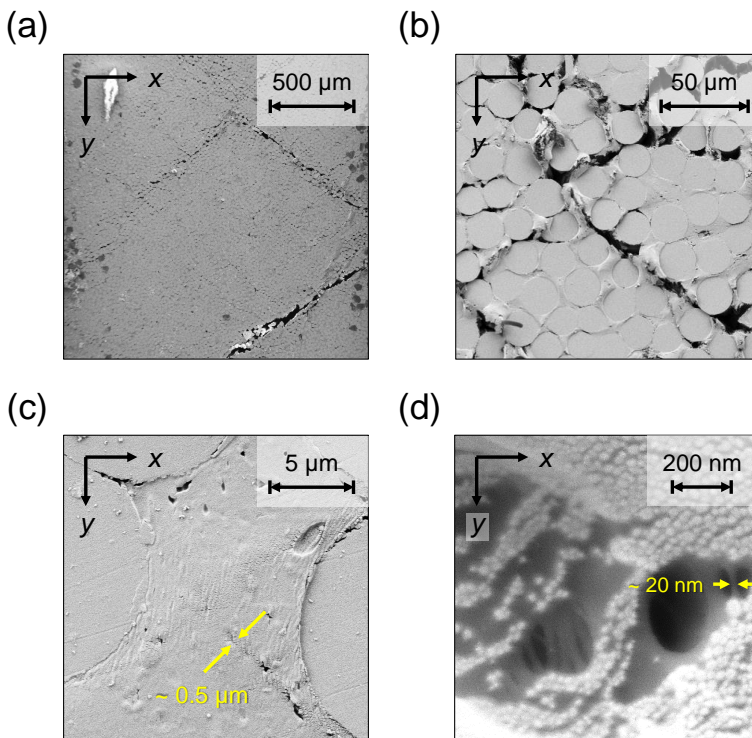


Fig. 6.12 Elium – Post-mortem observations of the failed material surface: (a) general overview, (b) main cracks, (c) fibre/matrix level diffuse cracks and shear bands, (d) zoom of the cracks in (c).

Still, Figure 6.12c clearly indicates strong plastic deformation in the Elium matrix via micro shear bands developing in between fibres. Finally, in Figure 6.12d crazes of around 20 nm in thickness can be observed, confirming that progressive damage accumulates within the Elium matrix during deformation. Ultimately, the DIC analysis is thus able to identify the regions of stress concentration near the fibre/matrix interface that lead to failure for systems that involve progressive damage, such as the Elium/glass fibre composite, and for those that do not, like the RTM6/carbon fibre composite.

Although the above analysis demonstrates the potential of the nano DIC approach, DIC artefacts are still detected in Figures 6.9 and 6.10. The potential sources for these artefacts are presented in Figure 13, using SEM micrographs of both ROIs before and after failure.

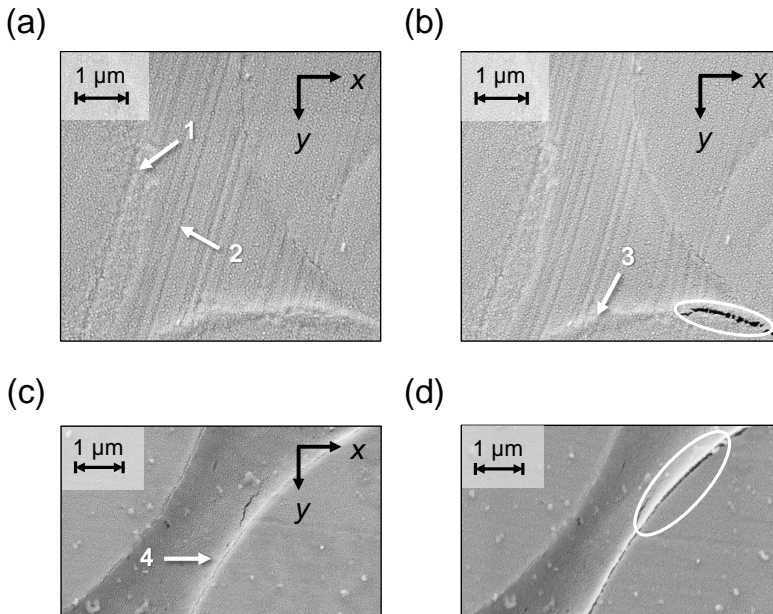


Fig. 6.13 Comparison between initial and final (post-failure) images for two ROIs: RTM6 system (a) in initial state versus (b) after failure, and Elium system (c) in initial state versus (d) after failure. Note that the failure regions are highlighted by white ellipses, while the white arrows represent source of imperfection for the DIC analysis.

In particular, a clustering of indium particles indicated by arrow 1 in Figure 6.13a results in an unclear separation between the fibre and matrix strains in RTM6, see Figures 6.9a and b. This particle clustering is most likely due to differential erosion between the fibre and the matrix that was created during the polishing phase. The presence of shallow leftover polishing scratches on the matrix is made more visible by the indium deposition, as shown by arrow 2. This leads to spurious strain fluctuations in the DIC maps of RTM6, which are most visible in Figure 6.9a. Finally, the combination of deformation around the fibres and repeated observation can lead to some charging of the interfaces, as shown by arrows 3 and 4 where the fibre/matrix interface is whitened. The charging effect decreases the contrast within these whitened zones, potentially leading to a loss of correlation in some cases. Hence, although the novel nano DIC approach allows reaching high resolution and achieving proper DIC characterisation of heterogeneous material systems such as FRPs, careful specimen preparation is crucial to avoid any artefacts.

Investigating the interphase behaviour

The previous section showed that a transition region of a few hundreds of nanometres exists in the strain fields between the fibres and the matrix. It presumably corresponds to the fibre/matrix interphase. To confirm that nano DIC is a viable and relatively direct alternative to measure the interphase size of FRPs, DIC was performed on successive images during a single test. At each load, the current image was compared to the reference image, to avoid propagation of artefacts. The aim was to study whether the transition zone size changes during the test, which would indicate that it does not correspond to the interphase. Figure 6.14 shows the ϵ_{xx} field at different moments during the test for RTM6. Figure 6.15 presents the same for Elium. For each system, the strains were evaluated along paths crossing at least two fibre/matrix interfaces. The results are given in Figure 6.16. In both systems, for all three paths, the amplitude of the maximum strain attained in the transition zone increases during the test. The thickness of the zones grows marginally up until the last load before failure.

For RTM6, path 1 crosses through very thin matrix regions in between fibres whereas path 2 traverses a single large matrix pocket. Yet, the transition zone thickness in paths 1 and 2 is around 300-400 nm. This is in line with the aforementioned results of Figure 6.9. Considering the thin matrix ligaments in path 1, it is questionable whether defining a distinct

interphase is meaningful as the ligament size is roughly 300 nm as well. If the matrix is capable of developing an interphase in such a confined space, then it would imply that in such regions, the mechanical response is entirely dictated by the interphase layer properties (which differ from the bulk matrix). As failure systematically occurs by sudden debonding of the fibre/matrix interface, these findings highlight the importance of studying the interphase surrounding the fibres. For Elixir, the transition zone along path 3 is about 400 nm as well. Again, this result correlates well with the results of Figure 6.10.

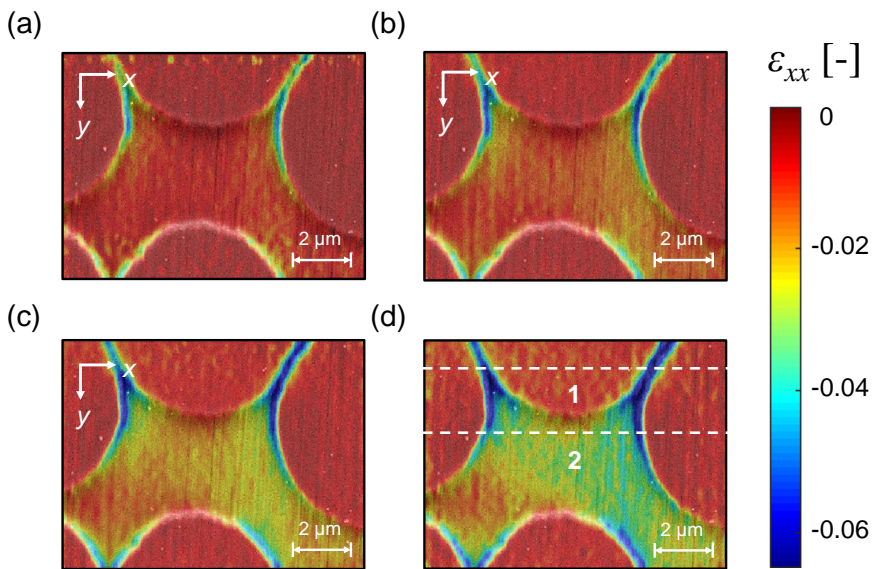


Fig. 6.14 RTM6 - Horizontal ϵ_{xx} strain map at four different stages during the in-situ compression test until the last moment before failure: (a) at 600 N, (b) at 850 N, (c) at 1000 N and (d) at 1150 N.

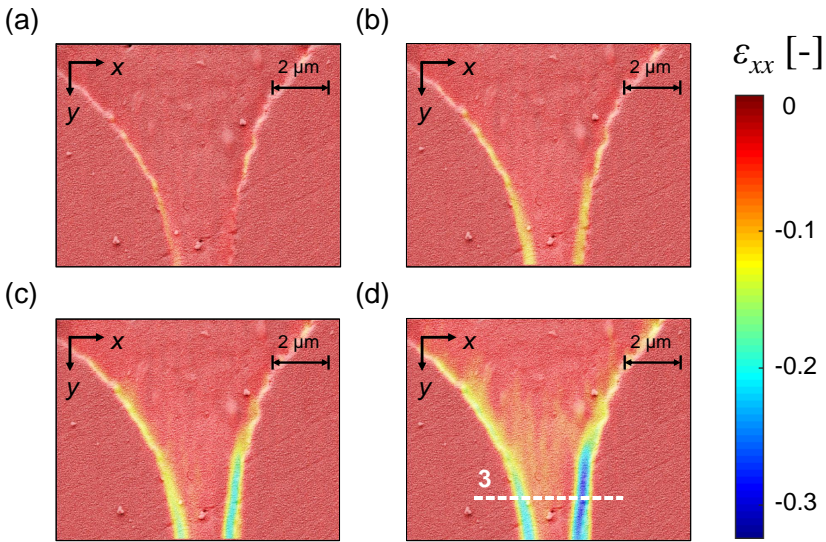


Fig. 6.15 Elium - Horizontal ϵ_{xx} strain map at four different stages during the in-situ compression test until the last moment before failure: (a) at 500 N, (b) at 700 N, (c) at 1000 N and (d) at 1300 N.

To confirm the DIC results, AFM measurements were performed on both composite systems. The AFM modulus map of Figure 6.17a shows two profiles along a path from the carbon fibre to the RTM6 matrix. The evolution of the modulus along these profiles is given in Figure 6.17b. An interphase layer of around 150 nm can be identified for this system. Similarly for Elium, the profiles shown in Figures 6.17c and d indicate the presence of a 200-nm interphase region between the glass fibre and the Elium matrix. For both systems, the interphase thickness measured by AFM is on the same order of magnitude as the width of the transition zone captured by DIC, i.e. a few hundreds of nanometres. This reinforces the idea that nano DIC is capable of capturing interphases in FRPs relatively well.

Ultimately, nano DIC appears as a promising tool to detect the interphase of FRPs. As this technique is simpler to set up than AFM (less tedious sample preparation), it offers a convenient alternative. Furthermore, it provides quantitative data about the deformability while AFM remains semi-quantitative regarding the magnitude of the local stiffness (see Chapter 7). Now, extracting material properties from DIC requires inverse identification through modelling.

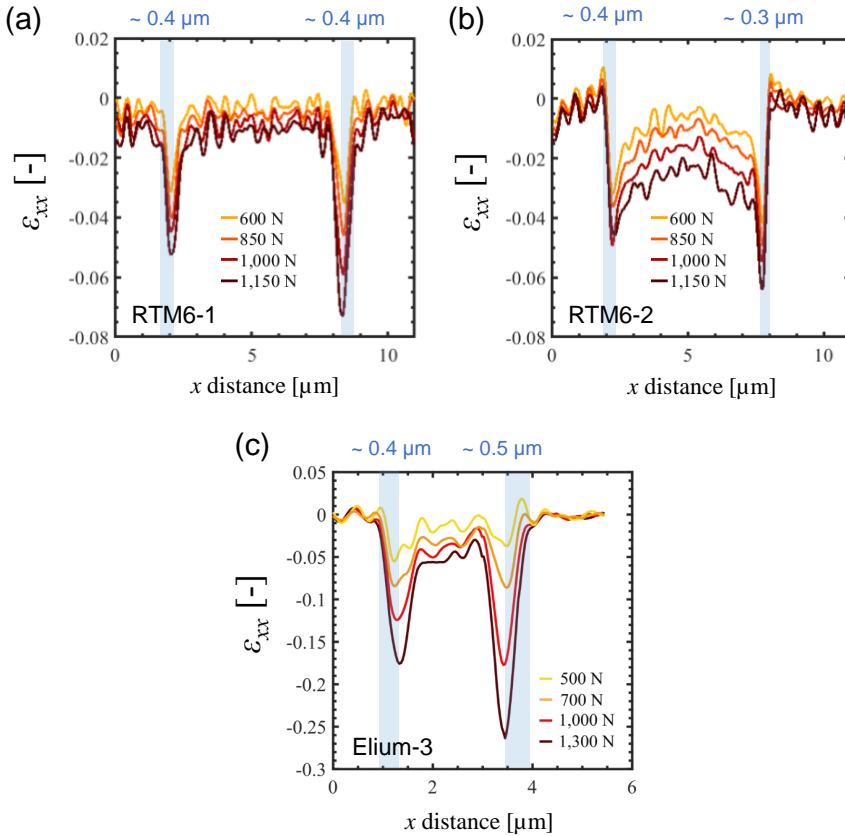


Fig. 6.16 Evolution of the horizontal ϵ_{xx} strain along the three numbered profiles shown in Figures 6.14 and 6.15 at different stages during the in-situ compression test: (a) and (b) profiles 1 and 2 on RTM6, respectively; (c) profile 3 on Elium. An interphase of around 400 nm marked by the shaded area is visible for both systems.

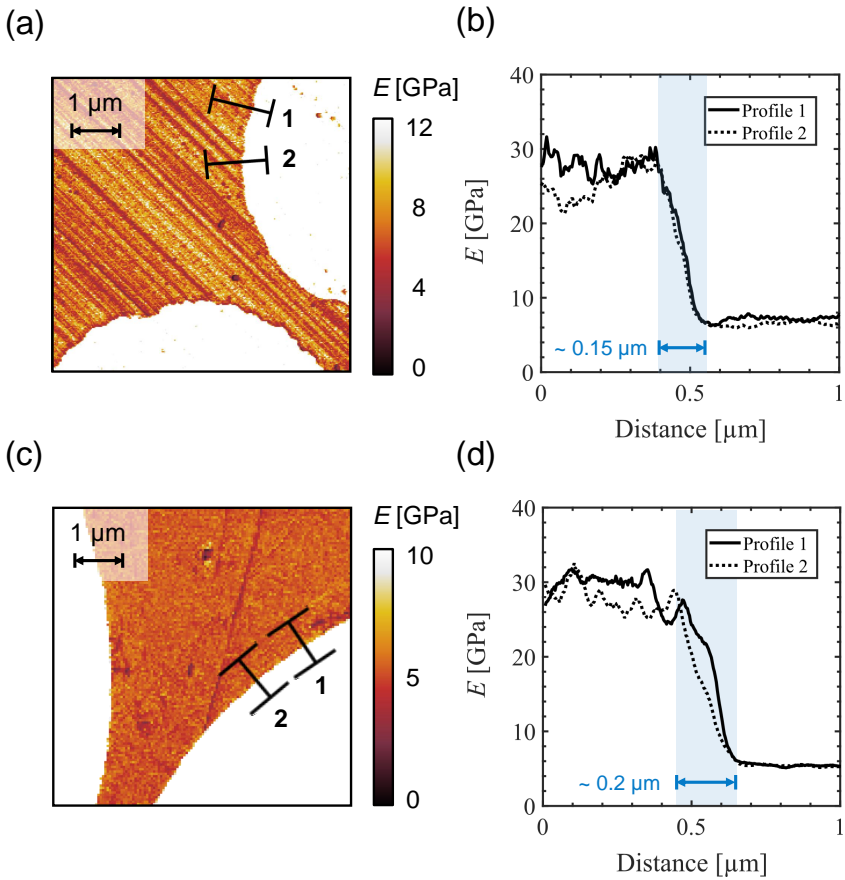


Fig. 6.17 Atomic force microscopy measurements obtained by PeakForce Tapping® on (a), (b) the RTM6/carbon fibre composite, and (c), (d) the Elium/glass fibre composite. DMT modulus maps are presented on Figures (a) and (c), while (b) and (d) show the evolution of the DMT modulus along two profiles extracted from each map.

6.4 Comparison to FE simulations

In an attempt to evaluate the validity of using calibrated continuum models for micro-mechanical analyses, FE simulations were carried out on the ROIs presented in Figures 6.14 and 6.10 for the RTM6 and Elium FRPs, respectively. The ϵ_{xx} and ϵ_{xy} fields measured by DIC and predicted by FEA are compared in Figures 6.18 (RTM6) and 6.19 (Elium).

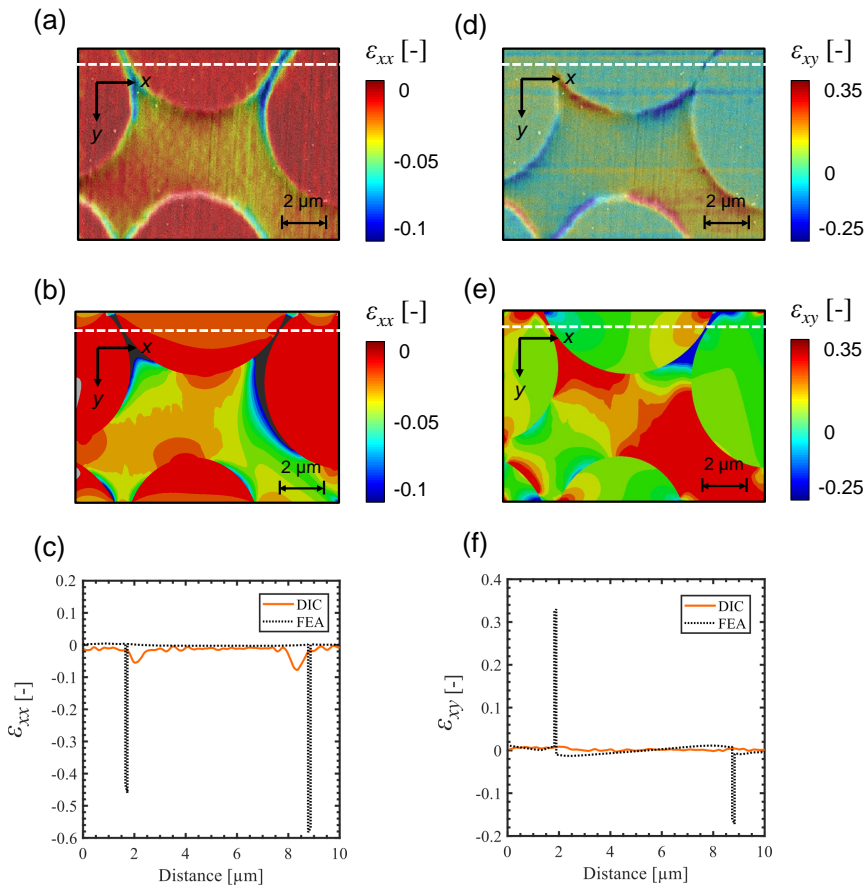


Fig. 6.18 RTM6 – Horizontal ϵ_{xx} strain field (a) measured by DIC versus (b) predicted by FEA using a continuum model, and (c) comparison of strain evolution along the white dashed profile for both DIC and FEA. (d), (e) and (f) show the equivalent in terms of shear strains ϵ_{xy} .

For RTM6, the predicted strain distribution and amplitude within the large matrix pocket fit well with the DIC measurements, in particular for ϵ_{xx} , see Figures 6.18a and b. However, in the thin matrix bands at the top, the model drastically overestimates the strains compared to DIC. Within the ϵ_{xy} map, the opposing diagonal shear pattern around the fibres is also captured by FEA, as shown in Figures 6.18d and e. Yet, the strain amplitude of the shear accumulation around the fibres is, again, largely overestimated. This is further illustrated in Figures 6.18c and f along a path. Furthermore, no transition zone at the interface is predicted by the model. The comparison between FE and DIC analyses for Elium before the 2nd failure event, which is displayed in Figure 6.19, yields the same conclusions. In Figures 6.19b and e, the average ϵ_{xx} and ϵ_{xy} strain distributions within the matrix fit well with the DIC results in Figures 6.19a and d, yet some discrepancies remain as, for example, the presence of a positive shear strain around the left-hand fibre in Figure 6.19e compared to Figure 6.10d. Figures 6.19c and f show the strain variations along a path for both DIC and FEA. At the interfaces, a sharp transition with higher strain amplitudes is once more seen. Furthermore, in Figure 6.19e, the size of the positive strain band in the bottom right extends further, leading to an inversion to positive rather than negative strains along the path.

The validity of the use of the continuum model of Morelle et al. [233] was already questioned by Chevalier et al [197]. The latter demonstrated that the model overestimates the strain amplitudes in matrix pockets, while the overall strain distribution remains close to DIC measurements. The present FE results are therefore not surprising. However, the comparison between FEA and DIC clearly shows that the interphase region around the fibres is crucial. As the presence of the interphase can be confidently confirmed by DIC, assuming a homogeneous matrix within the FE framework limits its ability to accurately model the load transfer at the interfaces. In addition, neglecting the presence of progressive damage is a reasonable assumption for RTM6 (and may be debated for Elium). This suggests that micro-mechanical modelling strategies should consider the presence of an interphase with intrinsic stiffness and hardness larger than the bulk matrix, as indicated by the AFM maps for the Young's modulus. Chevalier et al. pointed out two possibilities to overcome the discrepancy between the DIC and FEA. The first is related to intrinsically different local properties in the matrix, which may arise from difference in curing conditions due to the presence of near fibres. The present

study indeed suggests local variations in the properties of the matrix due the presence of an interphase around the fibres. The second possibility assumes true size-dependent plasticity [236–239]. This last aspect requires further investigations to determine if this second effect plays an important role, in addition to the interphase effect.

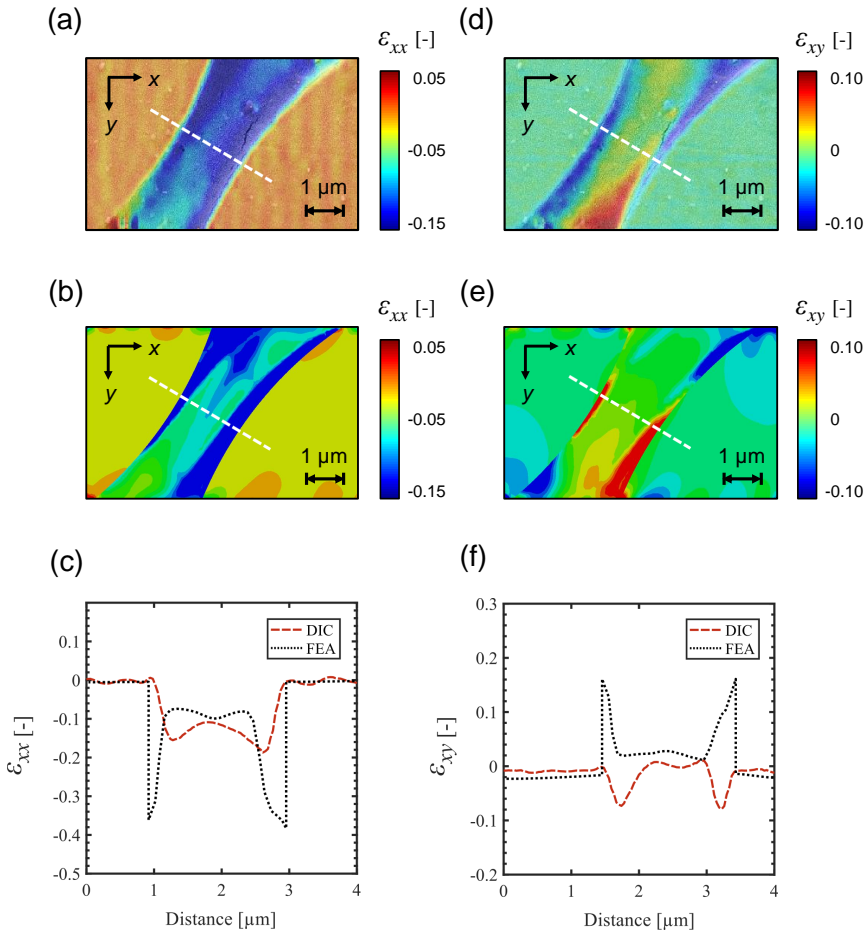


Fig. 6.19 Elium, before 2nd failure event – Horizontal ϵ_{xx} strain field (a) measured by DIC versus (b) predicted by FEA using a continuum model, and (c) comparison of strain evolution along the white dashed profile for both DIC and FEA. (d), (e) and (f) show the equivalent in terms of shear strains ϵ_{xy} .

6.5 Conclusion

The development of predictive micromechanics-based multiscale models requires accurate data about the local fibre/matrix level deformation and failure, as well as a deep understanding of the mechanisms themselves in order to select the right ingredients in the constitutive model. In this study, the use of DIC on FRPs was extended to the nanoscale to determine the deformation behaviour of the matrix in the vicinity of fibres. To this end, a novel nanoscale speckle pattern deposition technique was simplified and used on UD fibre-reinforced thermoplastic and thermoset polymers. In order to assess the robustness of the experimental approach, the quality of the speckle pattern was carefully checked and SEM-induced distortions were quantified. The main challenges associated to the use of nanoscale DIC on FRPs are linked to charging effects in the SEM and related drift distortions. This assessment ensures that the proposed DIC analysis is quantitative. A comparison with FE predictions was performed to determine the differences with DIC. The main findings of this study are the following:

- Careful specimen preparation of FRPs allows minimising spatial and drift distortion-related errors.
- The nano DIC approach accurately determines displacement and strain fields at the local fibre/matrix scale, despite the significant contrast in mechanical properties between the constituents. Hence, the main issue reported in the literature of submicron-level DIC was overcome.
- The local micro shear band formation and interface failure are well captured in the DIC maps within highly confined material regions, even though the strain gradients are very steep.
- DIC data reveal the systematic presence of an interphase around the fibres for both material systems. The measured interphase width perfectly relates to the AFM measurements made on the same material systems.
- The average strain amplitude predicted by FEA in large matrix pockets agrees with DIC. However, the strain distribution and localisation differ, especially in the near fibre region. In particular, the FEA largely overestimates the strain concentration within confined regions and/or at the fibre/matrix interface.

In the end, this study provides a robust method to acquire data about the mechanics of FRPs at submicron levels. The interphase of FRPs can

be easily and reliably measured in comparison to other techniques. The importance of characterising the matrix at this scale is highlighted by the inability of FEA using continuum models to reproduce the experimental results in conditions where the matrix is the main carrier of the deformation. As failure occurs at the fibre/matrix interface, it may be necessary to include an interphase region around the fibres and maybe strain gradient plasticity effects to accurately model the load transfer occurring between the matrix and fibres. Still, this means that quantitative data in the interphase region need to be gathered. The physical reason behind the difference in response of the interphase remains unknown. It may be due to different local curing conditions and strain gradient effects.

6.6 Acknowledgements

The UCLouvain team deeply acknowledges fruitful discussion and guidance from J. Hoefnagels and T. Vermeij from TU Eindhoven, and Y. Swolfs and C. Breite from KULeuven. NK is a research fellow of the Fonds de la Recherche Scientifique de Belgique - FNRS and gratefully acknowledges their support. SG and TP gratefully acknowledge the financial support from Arkema. Computational resources have been provided by the super-computing facilities of the Université catholique de Louvain (CISM/UCL) and the Consortium des Équipements de Calcul Intensif en Fédération Wallonie Bruxelles (CÉCI) funded by the Fonds de la Recherche Scientifique de Belgique (F.R.S-FNRS).

6.7 Appendix

The distortion correction analysis presented in section 6.2.4 stated that the impact of the displacement distortion correction on the strain fields was negligible. Figure 6.20 presents the strain maps obtained after each correction. The strain variations are one order of magnitude below the measured strain amplitudes in the main DIC analysis. Figure 6.21 presents the maximum shear strain maps discussed briefly in section 6.3.2. The maps clearly show that failure coincides with the areas of strain concentration.

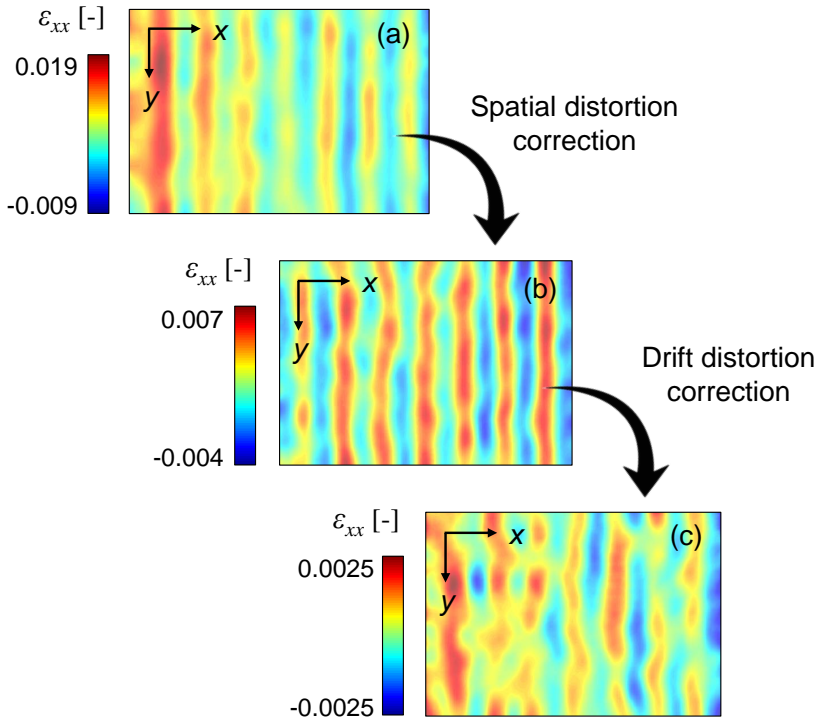


Fig. 6.20 Horizontal ϵ_{xx} strain field measured by DIC: (a) without any correction, (b) after spatial correction and (c) after spatial and drift correction.

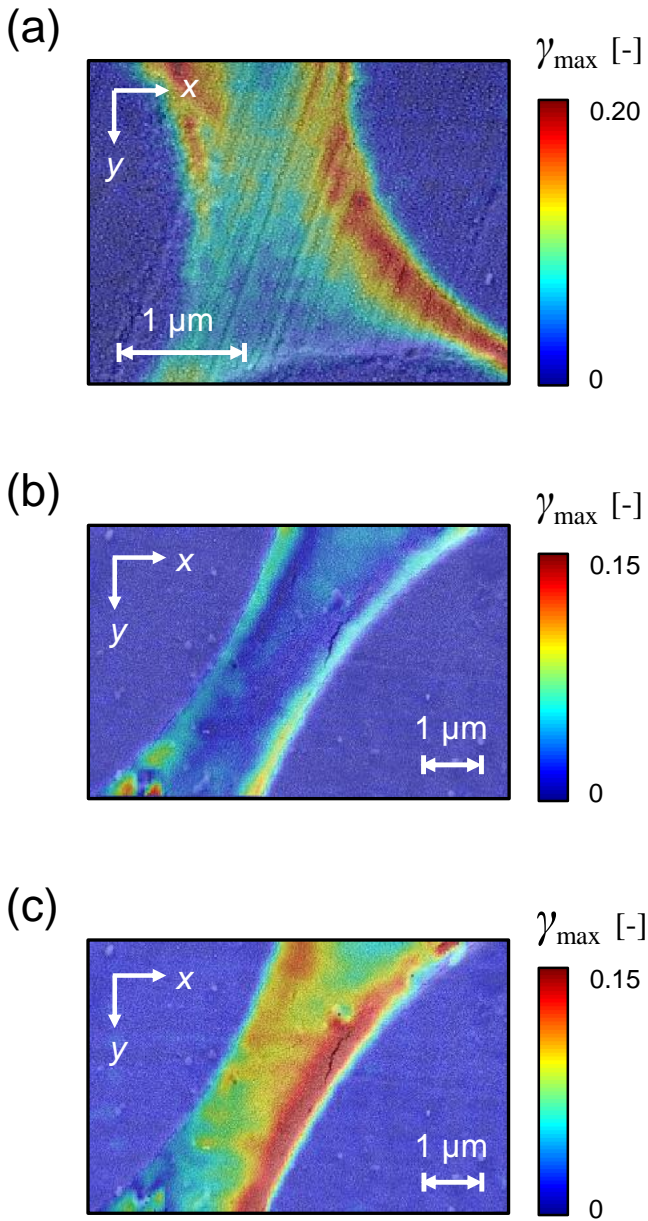


Fig. 6.21 Maximum shear γ_{\max} strain fields obtained by DIC (a) in the RTM6/carbon fibre system and (b), (c) in the Elium/glass fibre system before 1st failure event and before 2nd failure event, respectively

7

Influence of physical ageing and fibre proximity on the local mechanical response of Elium

This chapter is being prepared for publication under the following title: *Influence of physical ageing and fibre proximity on the local mechanical response of a methacrylic composite matrix*, S. F. Gayot, N. Klavzer, A. Guillet, C. Bailly, P. Gérard, T. Pardoën and B. Nysten (2023) [8].

S. F. Gayot was in charge of the conceptualisation/planning, experimental tasks and most FE modelling aspects. N. Klavzer wrote base Python codes for the modelling and output processing of the nanoindentation experiment, and provided guidance for their modification. A. Guillet performed the statistical analysis (model selection and inference analyses).

7.1 Introduction

Multiscale mechanical modelling aims at predicting the failure of macroscopic parts from the deformation and failure mechanisms occurring in the material at smaller length scales. This bottom-up approach simplifies and makes more robust the structural integrity assessment of parts by drastically reducing the need for mechanical testing [195, 240]. This is especially relevant for materials with high production costs, e.g. fibre-reinforced polymer composites. In this case, modelling starts at the micrometre scale and focuses on the behaviour of a single (or a few) elemental fibril(s) embedded in a polymer matrix. The matrix part is assumed to have the same constitutive properties as the bulk, unreinforced polymer, which may not be realistic for two reasons. First, an interphase region has been identified experimentally for a variety of composite systems. Most of these studies relied on various mechanical modes of atomic force microscopy (AFM) [80, 210, 235, 241–252], though a few authors relied on other techniques such as nanoscratch [253, 254], transmission electron microscopy [255, 256], nano dynamic mechanical analysis [257] and more recently nano digital image correlation [7]. The fibre-matrix interphase can be defined as a transition zone which behaves differently from both the polymer and fibre materials, and can extend up to a few micrometres from the fibre surface. Interphase formation results from the chemical reaction and/or interdiffusion phenomena occurring between the fibre sizing and the matrix material during curing. Secondly, beyond this interphase region, the polymer matrix *per se* may also differ from the unreinforced polymer in terms of thermal history, molecular structure (e.g. crosslink density, transcrystallinity, chain length...), residual stress distribution [198, 258–260] and ageing behaviour [261].

To settle the question, the local mechanical properties of the composite matrix must be assessed in-situ and compared to those of the same unreinforced polymer (also referred to as “bulk” or “neat” polymer), which is technically challenging. Indentation techniques may be used, provided the mechanical response of matrix pockets can be decoupled from that of the surrounding fibres. As the polymer matrix is indented, the plastic zone under the tip extends and may interact with the stiffer fibre material: a “constraining effect” arises, leading to an overestimation of the elastic properties of the matrix [210, 235, 243, 252, 253, 258–260, 262–264]. A few authors have attempted to compare the mechanical response of a polymer compos-

ite matrix to those of the unreinforced polymer using instrumented indentation experiments and finite element (FE) simulations [250, 252, 259, 263, 265–268]. The pioneering study by Gregory and Spearing [258] focused on an epoxy resin and the corresponding carbon fibre prepreg laminate. Nanoindentation was used in continuous stiffness measurement (CSM) mode to measure the elastic modulus and hardness of resin pockets in the composite, as a function of penetration depth h . A 2D-axisymmetric FE model of the experiment was designed as follows. A rigid conical punch was pushed into a matrix pocket of radius x , approximated by a cylinder, and whose external surface was subjected to rigid (“encastre”) boundary conditions to simulate the fibre constraining effect. Modulus (and hardness) values obtained from nanoindentation simulations were found to be unconstrained in the cases where $x/h > 25$. By applying this simple geometric criterion to experimental nanoindentation data, the properties of the unconstrained epoxy resin (modulus and hardness) were found to be up to 30 % greater in the composite. However, the minimum indentation depth in this work was equal to 500 nm, meaning that matrix pockets with a radius $x < 12.5 \mu\text{m}$ could not be characterised. A decade later, Hardiman et al. [263] performed a similar study on another epoxy/carbon fibre prepreg system. Lower indentation depths (down to 100 nm) could be achieved, which allowed characterising smaller resin pockets. The modulus and hardness values of the unconstrained composite matrix were found to be up to 20 % higher than in the bulk resin for $x < 15 \mu\text{m}$. No significant difference was observed between the two systems for $x > 15 \mu\text{m}$. Another study focusing on the mechanical properties of a composite polymer matrix *versus* the unreinforced polymer was recently presented by Pecora et al. [260] following a slightly different approach. A 3D-architected carbon fibre/epoxy composite system was produced by liquid moulding instead of prepreg consolidation, leading to the presence of inter-tow matrix pockets with an average radius of hundreds of micrometres. The elastic and time-dependent mechanical properties of the bulk resin were compared to those of the inter-tow composite resin pockets via cyclic nanoindentation testing. An additional distinction was made between resin pockets located at the surface of the composite specimen versus those found in the “core” of the sample. Results showed a small (in the order of a few %) but significant difference in elastic and viscoelastic properties between the three conditions (composite surface, composite core and unreinforced polymer). The properties of the composite core matrix were closer to those of the unreinforced polymer than to those of the surface composite matrix, which

was attributed to differences in thermal history across the thickness of the composite plate during processing.

Yet, none of the three aforementioned studies considered the additional impact of physical ageing on the mechanical response of both the fibre-reinforced and unreinforced polymer specimens. Amorphous solids, including glassy polymers, are not thermodynamically stable: when cooled down from the liquid (or rubbery) state to a temperature T_1 below the glass transition temperature T_g and maintained at this temperature for a period of time Δt , they undergo structural changes marked by a decrease in the mobility of the macromolecular chains as they enter a configuration with lower excess energy (decreased free volume). This phenomenon is referred to as physical ageing, whose rate increases as ageing temperature T_1 increases closer to T_g [269]. Physical ageing may, among others, impact the mechanical properties of glassy polymers (in particular the quasi-static properties, fracture toughness and viscoelastic/viscoplastic behaviour), which may be detrimental to their long-term performances [269, 270]. Contrary to other ageing phenomena, in particular chemical ageing, physical ageing is completely reversible upon heating the material above T_g . The consequences of physical ageing on the mechanical properties of glassy polymers and their composites have been extensively studied [261, 271–276]. To our knowledge, however, the influence of fibre proximity on the rate and extent of physical ageing experienced by glassy polymers has not been explored yet. Acknowledging and accounting for this phenomenon is crucial for interpreting any observed difference in properties between a polymer composite matrix and the equivalent unreinforced polymer.

In this work, the local mechanical response of a thermoplastic methacrylic composite matrix is compared to that of the same, unreinforced polymer. The objective is to assess the dual influence of fibre proximity and physical ageing on the polymer properties. To achieve this goal, micro- and nanomechanical analyses of a methacrylic thermoplastic resin are performed via nanoindentation and AFM. In particular, the properties of the unreinforced resin are compared to those of the inter- and intra-tow matrix pockets of a glass fibre-reinforced composite made of the same resin. The unreinforced resin and composite specimens are subjected to a thermal rejuvenation treatment above T_g , in order to reset the reference t_0 of the ageing time. A first set of nanoindentation measurements is acquired at $t = t_0$, and the experiment is repeated at t_3 , t_5 and t_{17} ,

i.e. after 3, 5 and 17 months of “natural” physical ageing (i.e. ageing under ambient conditions), respectively. A second thermal rejuvenation treatment is applied to the polymer and composite specimens after 18 months, resetting again the ageing time to 0. The final set of nanoindentation measurements is obtained at that moment, which is referred to as t'_0 . The validity of the $x/h > 25$ criterion, established by Gregory and Spearing for obtaining unconstrained nanoindentation measurements in a carbon fibre-reinforced epoxy composite system, is verified in the case of interest using FE simulation of the nanoindentation experiment. A comprehensive statistical comparison of the nanoindentation results is performed to explore the mixed influence of (1) fibre proximity and (2) level of physical ageing on the resin’s modulus and hardness values. Additional AFM analyses are carried out in intra- and inter-tow composite matrix pockets at t_0 and t_5 , and the measured modulus values are confronted to the corresponding nanoindentation results. In parallel, AFM is also used for measuring the thickness and modulus of the fibre-matrix interphase region of the composite material.

7.2 Theoretical background

This section presents a reminder on the main theoretical concepts relevant to the present study.

7.2.1 Instrumented indentation techniques [101]

Indentation testing consists in pushing a rigid punch of known geometry into a flat material surface to determine its mechanical properties. The measurement of the contact area between the indenter and the material during the test enables the extraction of, e.g., the indentation modulus and hardness of the tested material using contact mechanics models. In particular, instrumented indentation techniques (IITs) rely on the indirect estimation of the contact area from force-displacement curves recording the load P applied to the indenter as a function of the penetration depth h of the indenter. Several versions of IITs exist, depending on the order of magnitude of the tip apex radius R , the applied load P or the penetration depth h involved. In this work, both nanoindentation ($R \approx 100$ nm, $P_{\max} \approx 10$ mN, $h \approx 1$ μ m) and nanomechanical AFM ($R \approx 10$ nm, $P_{\max} \approx 0.1$ mN, $h \approx 1$ to 10 nm) measurements were performed, resulting in probed volumes in the μm^3 and nm^3 ranges, respectively.

Nanoindentation

Nanoindentation has been extensively used since the 2000s to determine the indentation hardness H and elastic modulus E of materials, which are given by

$$H = \frac{P}{A_c}, \quad (7.1)$$

$$E^* = \frac{\sqrt{\pi}}{2} \frac{S}{\sqrt{A_c}}, \quad (7.2)$$

where A_c is the projected contact area between the tip and the sample, and $S = \frac{dP}{dH}$ is the unloading contact stiffness. E^* is the reduced indentation modulus related to the elastic moduli E_m and E_p and Poisson ratios ν_m and ν_p of the tested material and the punch material, respectively:

$$\frac{1}{E^*} = \frac{1 - \nu_m^2}{E_m} + \frac{1 - \nu_p^2}{E_p}. \quad (7.3)$$

In the case of measurements on polymer materials, the punch can be considered as infinitely rigid and the reduced elastic modulus only depends on the polymer modulus and Poisson's ratio. The polynomial function relating A_c to the contact depth h_c can be obtained through calibration. The common theoretical approach to extract E and H from load-displacement curves relies on the Oliver and Pharr model [100], which assumes sink-in of the indented material under the tip. The contact depth h_c depends on the penetration depth h via:

$$h_c = h - \varepsilon \frac{P}{S}, \quad (7.4)$$

where ε is a constant describing the indenter geometry. Today, most nanoindentation tests rely on the continuous stiffness measurement (CSM) mode, which enables the continuous monitoring of contact stiffness as a function of indentation depth h by superposing a small amplitude cyclic displacement to the "static" displacement [100].

Semi-quantitative modulus mapping with AFM

The PeakForce Tapping® mode with quantitative nanomechanical mapping (PFT-QNM) of AFM [277] allows semi-quantitative mechanical map-

ping of a surface at the micro- and nano-scales, while also providing topological data. In this mode, the probe is imposed an off-resonance vertical cyclic displacement of a few tens of nanometres at a frequency typically in the kHz range, leading the probe tip to indent the specimen surface periodically. A load (P) versus penetration depth (h) curve is acquired during each “approach-indentation-retraction” cycle, from which various parameters/properties can be extracted such as the maximum indentation depth, the tip-surface adhesion force, the elastic modulus and the energy dissipation. The Derjaguin, Muller and Toporov (DMT) model [278] is often used for modulus calculation, assuming the AFM tip as an infinitely rigid punch with a spherical apex of radius R . In this case, the relationships between the load applied by the probe, P , the radius of the contact area, a , and the tip penetration depth, h , are the following:

$$a^3 = \frac{3}{4} \frac{R}{E^*} (P + F_{\text{adh}}), \quad (7.5)$$

$$h = \frac{a^2}{R}, \quad (7.6)$$

$$P = \frac{4}{3} E^* \sqrt{R} h^{3/2} - F_{\text{adh}}, \quad (7.7)$$

where F_{adh} is the adhesion force due to Van der Waals tip-surface interactions.

In AFM-based nanomechanical techniques, the tip penetration depth, h , is indirectly obtained as the difference between the vertical displacement z imposed to the probe (or the sample), and the cantilever vertical deflection d :

$$h = z - d. \quad (7.8)$$

This imposes to carefully select the AFM probe as a function of the mechanical properties of the analysed material. In particular, the cantilever stiffness, k_C , should be of the same order of magnitude as the contact stiffness k_N [279], which is expressed as

$$k_N = \frac{dP}{dh} = 2aE^* = 2E^* \sqrt{R}h. \quad (7.9)$$

If $k_N \gg k_c$, i.e. if the cantilever is too compliant with respect to the contact stiffness, the probe hardly indents the surface. In this case, the cantilever deflection, d , is almost equal to the vertical displacement, z , and the penetration depth, h , is computed as the difference of two large numbers resulting in a small value with a large uncertainty. If $k_N \ll k_c$, the cantilever deflection values are small with respect to the photodetector limit of detection, leading to low signal-to-noise ratio.

The absolute values of the modulus obtained in PFT-QNM imaging should be considered with caution for several reasons, see e.g. [280–283]. First, errors in the characterisation of tip radius and cantilever stiffness values (during PFT-QNM calibration or at the manufacturer’s) may impact the accuracy of modulus calculations by up to 5 and 10-20 %, respectively [279, 282, 284]. Probe wear, during calibration itself and/or during specimen imaging is also commonly observed [279, 280], adding up to the imprecision on tip radius value. Additionally, surface roughness may interfere with the definition of the contact point and contact radius in two cases: (1) if the root-mean-square (RMS) roughness value is close to that of indentation depth [280] and/or (2) if abrupt slope changes occur [210, 249, 285]. Phenomena related to the viscoelastic and viscoplastic nature of polymeric materials like Elium (i.e. creep, dependency to loading rate) are another well-known source of error [280, 284, 286, 287]. Misestimation of the specimen’s Poisson ratio prior to the AFM experiment may also interfere with modulus calculation, as shown by eq. 7.2 [284]. Consequently, modulus values obtained by PFT-QNM in this work are considered to be relative values, i.e. they are only comparable with data obtained in the same experimental conditions (same probe, same calibration and operating parameters).

7.2.2 Linear mixed models [288] and confidence intervals in statistics

Materials scientists often rely on statistical modelling to assess the influence of one (or several) parameter(s), known as “fixed effects”, on a response variable of interest. Common statistical tests such as correlation tests, t -tests or ANOVA derive from linear regression models, whose applications are restricted to the analysis of fully independent datasets. But one individual may provide multiple observations and/or several individuals can be somehow related (e.g. from the same family), which may introduce bias into the data. One way to artificially restore independence is through the averaging of related data points, which results in a significant loss of in-

formation. The preferred solution is to rely on linear mixed models instead of linear models. Linear mixed models can account for non-independent data via “random effects”, i.e. grouping variables which are known to influence the response alongside the fixed effects. In other words, there are as many fitted models as there are groups of interdependent data. Random-intercept mixed models assume the influence of the fixed effect(s) on the response variable to be the same for each group of data, but allows differences in baseline values between groups. Consequently, all fitted models share the same slope, while intercept values can change. Such models are expressed as:

$$\text{Response variable} \sim \text{Fixed effect} + (1 | \text{Random effect}) \quad (7.10)$$

in the case of one fixed effect and one random effect.

7.3 Materials and methods

7.3.1 Materials

The liquid resin used for producing the bulk and fibre-reinforced polymer specimens comprised a methyl methacrylate-based (MMA) monomer formula, Elium® 191 OSA (Arkema, France) with a peroxide thermal initiator (Luperox® K10, Arkema, France). The composite preform was made from quasi-unidirectional (UD) non-crimp glass fabric plies from Chomarat (France) with an areal weight of 1.03 kg.m^{-2} (85 % warp and 15 % weft). Consumables for composite bagging and vacuum infusion were obtained from Diatex SAS (France).

7.3.2 Preparation of polymer and composite specimens

Manufacturing of composite specimens

A composite plate was manufactured by vacuum infusion of a 90-ply pseudo-UD glass fabric layup. The resin mix was prepared by combining three parts initiator for a hundred parts monomer formula under mechanical stirring. The mixture was degassed for 1 min at 50 mbar and infused at a pressure close to 60 mbar, parallel to the fibre tow orientation. The resin was left to polymerise within the preform after clamping shut the resin inlet and vacuum line. No external heating was applied during the

process. The final part had a total thickness of 73 mm and a fibre volume fraction close to 0.5. Cubic specimens of dimensions $10 \times 10 \times 10 \text{ mm}^3$ were extracted from the core of the plate, according to the sectioning diagram presented in the Supplementary Information.

Manufacturing of resin specimens

A degassed resin mix was prepared as described previously, casted into a $\varnothing 14 \text{ mm}$ borosilicate glass test tube coated with release agent Chemlease 41-90 (Chem-Trend GmbH, Germany), and left to polymerise at room temperature. After cooling, the resin sample was removed from the mould. The first few centimetres below the resin/air interface were cut off and discarded, as peroxide initiators are sensitive to air inhibition. Cylinders with height and diameter both equal to 12 mm were lathed from the remainder of the resin sample.

Thermal rejuvenation

Prior to mechanical testing, the bulk polymer and composite specimens were subjected to thermal rejuvenation through heating at a temperature T_0 slightly above their glass transition temperature T_g until thermodynamic equilibrium is achieved, and then quenching down to a temperature T_1 below T_g as described by Struik [269]. The purpose of a thermal rejuvenation treatment is twofold: (1) relaxing any internal stresses and preferential chain orientations induced by processing and (2) “resetting” the amount of free volume. In practice, the specimens were placed in a laboratory furnace preheated at $100 \text{ }^\circ\text{C}$ (i.e. 3 degrees above the T_g value of Elium 191 OSA as measured by [1]), held at this temperature for 10 min, then taken out and left to cool down to room temperature, i.e. close to $20 \text{ }^\circ\text{C}$. Note that the duration of the heating step (i.e. 10 min) was selected to ensure homogenous heating of the specimens up to $100 \text{ }^\circ\text{C}$ (as verified by solving the heat equation). The time of the quench, referred to as t_0 , was considered as the origin of the ageing time [269, 270] for the measurements performed at t_3 , t_5 and t_{17} . Note that a second, similar thermal rejuvenation treatment was applied to the specimens at $t'_0 \approx t_0 + 18 \text{ months}$, resetting again the origin of the ageing time to zero.

Polishing of composite and bulk specimens

Immediately after each rejuvenation treatment (i.e. around t_0 and t'_0), all specimens were polished on a semi-automatic MultiPrep Precision Polishing System from Allied High Tech Products, Inc., CA, USA. First, polymer

cylinders were polished using resin-bonded diamond discs with successive grit of 1200 and 4000 (MD-Piano from Struers Inc., OH, USA), and finished using a polishing cloth coated with a 0.3- μm alumina suspension (AP-D Suspension 0.3 μm , also from Struers Inc.). Composite specimens were polished perpendicular to fibre tow orientation. The accuracy of indentation-based mechanical measurements being sensitive to surface roughness [198, 210, 249, 285, 289, 290]¹, special care was taken to minimise the differential erosion of polymer and fibre materials during polishing. Diamond lapping films coated with fixed particles of decreasing sizes from 30 down to 0.1 μm (Allied High Tech Products, Inc., CA, USA) were used instead of polishing pastes, and small contact loads were applied to the composite specimens in order to avoid compressing the film material. These precautions were applied to minimise the “nesting” of polishing particles into the softer matrix pockets, leading to the preferential removal of the polymer material. A full description of the composite polishing protocol used in this work is presented in the Supplementary Information.

7.3.3 Micromechanical characterisation by nanoindentation and AFM

Definition of measurement conditions

Figure 7.1 shows a micrograph of the polished surface of a glass fibre-reinforced Elium composite specimen. As mentioned in the introduction, the quasi-UD architecture of the reinforcing fabric gives rise to two categories of matrix pockets in the composite material: (1) intra-tow pockets, whose smallest dimension does not exceed a few tenths of microns, and (2) inter-tow pockets, which are more than ten times larger as illustrated by Figure 7.1. The unreinforced resin is referred to as condition (3), so that the measurement conditions are numbered in the order of the average distance to the closest fibre (unreinforced resin can be considered as an infinitely large matrix pocket).

¹Modulus calculations rely on the estimation of tip-surface contact area, meaning that artifacts may arise from “abrupt” slope changes (with an angle greater than the opening angle of the probe [285]) and/or from imaging “too small” features, whose size is comparable to tip radius or smaller.

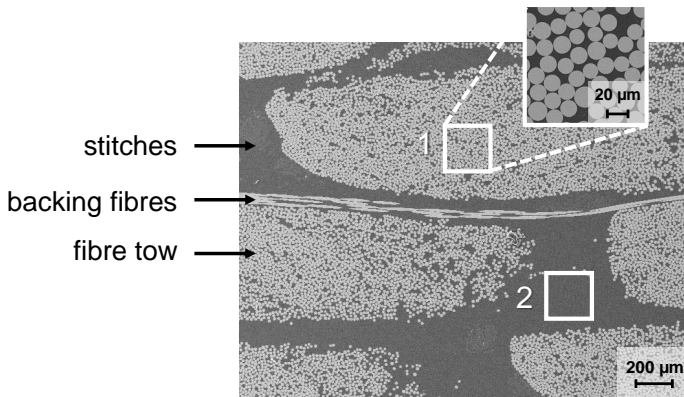


Fig. 7.1 Scanning electron micrograph of the polished surface of a fibre-reinforced Elixir composite specimen after polishing, showing (1) intra-tow and (2) inter-tow matrix pocket morphology.

Nanoindentation

Nanoindentation measurements were performed with an Agilent G200 device equipped with a Berkovich diamond tip and a Dynamic Contact Module (DCM II) head. The CSM mode was used at a frequency of 75 Hz and with an harmonic displacement value of 1 nm. The maximum penetration depth h_{\max} was set to 500 nm, while the strain rate target was equal to 0.05 s^{-1} . Indentation modulus E and hardness H values were directly calculated from raw data by the KLA NanoSuite software (version 6.54.0) via the Oliver and Pharr method [100]. E and H datasets were acquired for conditions (1), (2) and (3) at each of the following ageing times: t_0 , t_3 , t_5 , t_{17} and t'_0 . For each indent performed in condition (1), the distance x between the centre of the residual imprint and the nearest glass fibre was measured from optical micrographs via the open-source software ImageJ [147].

AFM

AFM indentation experiments were carried out on a Dimension Icon and a MultiMode 8 systems (both from Bruker Corp., USA), using the Peak Force Tapping® mode with quantitative nanomechanical mapping (PFT-QNM) mode [277]. The built-in tool of the Nanoscope operating software was used for extracting modulus values from the raw AFM data, via the DMT model [278] described previously. RTESPA-300 and TESPA-300-

30 probes (Bruker) were selected as their nominal cantilever spring constant k_c is around 50 N/m, i.e. close to the contact stiffness k_N of the tip-Elium resin interaction. Indeed, assuming that (1) E and ν are respectively around 3 GPa and 0.35 for Elium resins, (2) R is usually in the 10-30 nm range for PFT-QNM probes and (3) the maximum value of h must not exceed a few nanometres to ensure the validity of the DMT model (typically $h_{\max} \approx 3$ nm), the value of k_N can be estimated around 40 to 60 N/m from eq. 7.9. Calibration of cantilever properties, photodetector sensitivity and PFT-QNM parameters was performed prior to analysis as per the manufacturer's instructions. DMT modulus images of the resin in conditions (1) and (2) (i.e. in the two categories of composite matrix pockets) were acquired at t_0 and t_5 as detailed in Table 7.1. Note that the fibre-matrix interphase region was also imaged at t_0 . In all cases, scan parameters were carefully chosen to ensure that pixel size (i.e. distance between two indented locations) remained larger than contact radius a , so that the probe response was not influenced by adjacent measurement points [291].

The profile extraction tool of the open-source software Gwyddion 2.60 [292] was used to measure interphase thickness in the composite material. Line profiles were manually drawn in several locations across the fibre-matrix interface using 2D property maps obtained in intra-tow areas (condition (1)). Each profile was obtained by averaging the data of 10 neighbouring pixel strips perpendicular to the profile direction in order to reduce noise. Cross-correlation of DMT modulus and PeakForce error data was performed for each profile, and profiles displaying absolute PF error values exceeding 10 % of the applied load were discarded from the study. This kind of artefact indeed suggests a temporary loss of contact between the tip and the surface [285], due to differential erosion of the fibre and matrix materials during polishing. The thickness of the interphase was measured on the remaining profiles using DMT modulus data. More precisely, the width of the transition zone between the modulus value of the fibre and that of the matrix was assessed graphically as follows. Tangents to each of the three modulus domains (i.e. fibre, interphase, matrix) were drawn on all DMT modulus profiles, resulting in two interception points. Interphase thickness was defined as the difference between the coordinates of the two intercepts.

Ageing time of specimens	t_0	t_5
AFM system	Dimension Icon	MultiMode 8
Probe type	RTESPA-300-30	RTESPA-300
Calibrated value of k_N	49,280 N.m ⁻¹ (factory calibration)	≈ 50 N.m ⁻¹ (Söder method)
Calibrated value of R	32 nm (factory calibration)	≈ 10 nm (indirect calibration using ref. sample, see [291])
Probe vibration frequency	0.5 kHz	2 kHz
PF amplitude	30 nm	20 nm
Applied PF setpoint P_{\max}	150 nN	300 nN
Corresponding $l_{t_{\max}}$		2-3 nm
Fit boundaries (for unloading force curve)		Minimum force: 5 % P_{\max} Maximum force: 95 % P_{\max}
Scan parameters		
- Scan size	$6 \times 6 \mu\text{m}^2$ ($128 \times 128 \text{ px}^2$)	$3 \times 3 \mu\text{m}^2$ ($256 \times 256 \text{ px}^2$)
- Pixel size	≈ 47 nm.px ⁻¹	≈ 11 nm.px ⁻¹
- Scan rate	≈ 1 $\mu\text{m.s}^{-1}$	≈ 2 $\mu\text{m.s}^{-1}$
- Contact radius a	≈ 10 nm	≈ 9 nm

Table 7.1 PFT-QNM AFM acquisition parameters used at t_0 and t_5 .

Intra-tow modulus values beyond the interphase region were then compared to inter-tow (condition (2)) modulus values with Igor Pro 8 (WaveMetrics, Inc., USA), via in-house developed routines. Count histograms were generated from all DMT modulus images with a bin width equal to 50 MPa, excluding outliers (which were defined as modulus values below 1 GPa and above 10 GPa). Results were then accumulated into a single frequency histogram for each measurement condition (i.e. (1) or (2)) and ageing time (i.e. at t_0 or t_5), and fitted with a skew normal probability density function for determining the average modulus and standard deviation values.

7.3.4 Statistical analysis of nanoindentation results

Nanoindentation datasets were subjected to multiple comparison tests via repeated resampling using R [293], in order to evaluate the influence of ageing time and distance to nearest fibre on the indentation modulus and hardness of the resin as follows. Let us consider the example of two nanoindentation datasets A and B, consisting of modulus values measured in condition (1) at different ageing times, respectively t_0 and t_3 . Each dataset was first resampled down to 60 measurements, which were randomly selected from 8 indents. Resampled datasets A' and B' were then compared using a random-intercept linear mixed model expressed as

$$E \sim \underbrace{\text{Ageing time}}_{\text{FIXED EFFECT}} + \underbrace{(1 | \text{Indent number}) + (1 | \text{Indent batch number})}_{\text{RANDOM EFFECTS}}, \quad (7.11)$$

where “Ageing time” is the fixed effect, while “Indent number” and “Indent batch number” are random effects. “Indent number” accounts for the fact that each indent yields several modulus measurements in CSM mode. “Indent batch number” is used to illustrate a particulate feature of the nanoindenter operating software, which imposes to perform indents by batches (of about ten indents). Both effects have been found to induce significant variability in the measurements, which is why they have been added to the model as random effects. Possible heteroscedasticity in the compared datasets was also accounted for in the model structure. An estimated difference between datasets A' and B' was obtained from running the model. The resampling/mixed model comparison step was repeated 500 times. The median of the 500 estimated difference values was calcu-

lated as well as the 2.5th and 97.5th percentiles, providing a 95 % confidence interval (CI) for the comparison of datasets A and B. In this example, “Ageing time” was the fixed effect while E (indentation modulus of the resin) was the response variable. Depending on the datasets being compared, indentation hardness H can be the variable response instead of E and/or “Fibre proximity” (i.e. condition (1), (2) or (3)) can be the fixed effect instead of “Ageing time”.

7.4 Results and discussion

7.4.1 Thickness and mechanical properties of the interphase region

A typical 2D modulus image obtained in an intra-tow matrix pocket of the Elium composite is presented in Figure 7.2 alongside with the evolution of topography, DMT modulus and PF error values along two 1 μm -long 1D profiles drawn across the fibre-matrix interface. The modulus profiles in Figure 7.2c exhibit an upper plateau at around 30 GPa and a lower plateau close to 5.5 GPa, which are attributed to the fibre and matrix materials, respectively. Modulus measurements appear more scattered in the glass fibre than in the polymer, and also have significantly lower values than the macroscopic modulus of glass (≈ 70 GPa). As explained previously, the cantilever stiffness of the AFM probe was selected to be close to the contact stiffness between the tip and the polymer. Hence, the probe is too compliant to properly indent the fibre surface, which results in unrealistic modulus measurements in this material and low signal-to-noise ratio as the lower the indentation depth, the larger the impact of surface roughness on modulus measurements [243, 252]. A 150-nm transition zone in which the DMT modulus linearly decreases from 30 to 5.5 GPa is observed between the fibre and matrix phases, as depicted by the yellow area in Figure 7.2c.

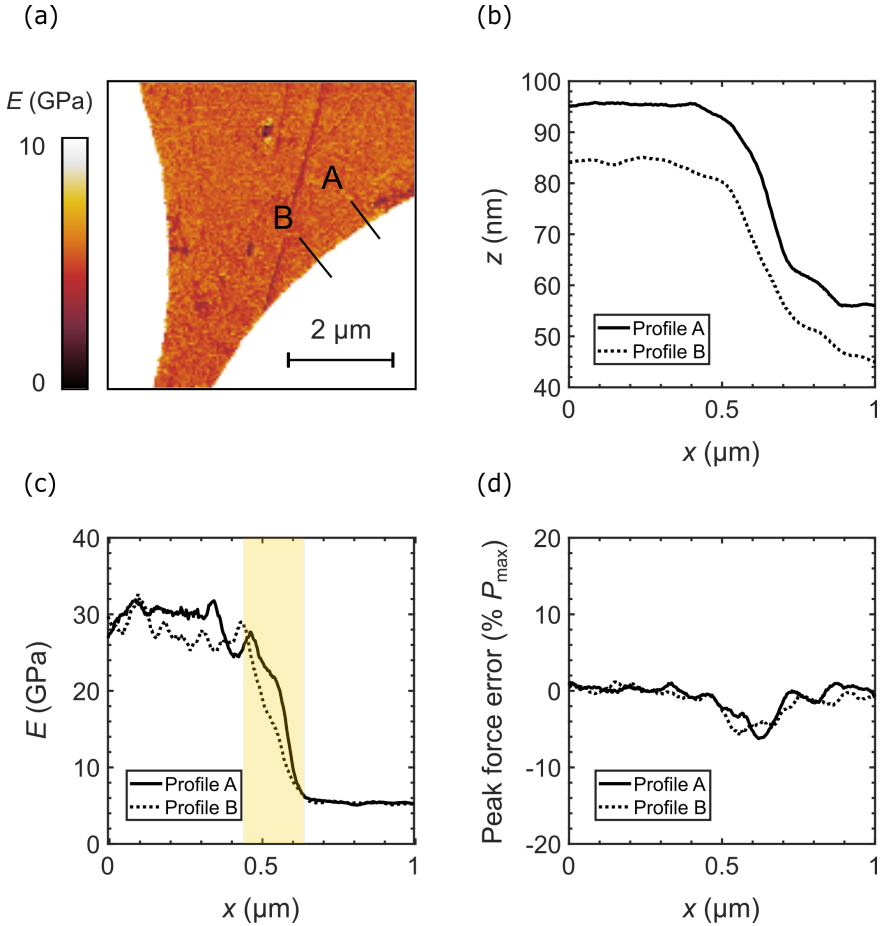


Fig. 7.2 (a) 2D DMT modulus image obtained by AFM in the intra-tow matrix pocket of the E/epoxy composite with location of 1D profiles A and B, and evolution of (b) topography, (c) DMT modulus and (d) PF error values along profiles A and B.

The AFM indentation of the Elium polymer close to a fibre was also modelled via FE simulation, in order to decouple the influence of fibre constraint from that of an actual change in polymer properties close to the fibre-matrix interface. The results of these simulations, which are presented in the Supplementary Information, confirm that this behaviour does not result from a constraining effect from the fibre material. This “third phase”, which appears stiffer than the composite matrix and exhibits a property gradient across the thickness is thus likely to be the interphase region. Note that the drop in DMT modulus observed along the interphase corresponds to a drop in topography as a consequence of differential erosion of the fibre and matrix materials during polishing, see Figure 7.2b. This should not impact the accuracy of the modulus measurements provided the probe tip remains in contact with the surface at all times, which is confirmed by the low PF error values displayed in Figure 7.2d. These do not exceed 6 % of the applied load in the interphase region, which would approximately translate into a 6 % error in the calculated DMT modulus value, see eq. 7.9.

The distribution of interphase thickness values measured by PFT-QNM AFM is shown in Figure 7.3. The box plot is symmetric, which suggests a normal distribution of interphase thickness values (provided the data is unimodal, which is the case here). The median and mean values are both approximately equal to 120 nm, while the calculated standard deviation is around 30 nm. The maximum measured thickness value, including outliers, does not exceed 200 nm. The radius of the glass filaments used as reinforcement in the composite material is approximately 7.5 μm , and the smallest possible matrix pocket could be defined as the closed space between 3 mutually tangent fibres. The cross-sectional area of this “smallest pocket” can be estimated through simple geometric calculations; it is around 9 μm^2 . Considering the extreme case of a 200-nm interphase region extending from the surfaces of the three tangent fibres, less than half of the total area of the “smallest pocket” would be occupied by the interphase. This ratio decreases to around 1/4 if we assume an interphase thickness value of 120 nm. This confirms that even the smallest intra-tow matrix pockets are mostly composed of Elium polymer, not of a continuous interphase region.

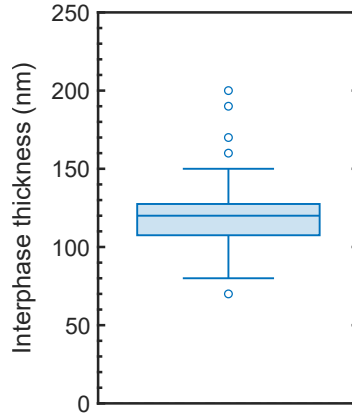


Fig. 7.3 Box plot distribution of interphase thickness values measured by PFT-QNM AFM in the intra-tow matrix pockets of the E/epoxy composite. Whiskers indicate the minimum and maximum values of the distribution, excluding outliers which are depicted by circles. The box extends between the 25th and 75th percentiles, while the central horizontal line indicates the median value.

7.4.2 Influence of fibre proximity and physical ageing on nanoindentation properties

Selection of nanoindentation data for statistical analysis

Indents performed in CSM mode yield one data point for each 1 nm variation of the penetration depth h . This results in a considerable amount of data, which are not all relevant with respect to the present study. In particular, the CSM nanoindentation curves systematically exhibit important fluctuations at low penetration depths for a variety of reasons (see e.g. [259, 294–297]). In the case of interest, the measured values of E and H decrease as h decreases towards 0. The typical evolution of E and H as a function of h is shown in Figure 7.4 for three random indents performed in the bulk E/epoxy specimen. The E and H plots are divided into three domains with respect to the penetration depth h , see Figures 7.4a and b, respectively. In Domain I, i.e. for $0 < h \lesssim 50$ nm, E and H values exhibit very sharp fluctuations. Slighter variations are observed in domain II, which extends from $h \approx 50$ to ≈ 250 nm. In domain III, i.e. for $h > 250$ nm, all E and H curves reach a plateau, meaning that the measurements are no longer dependent on the penetration depth.

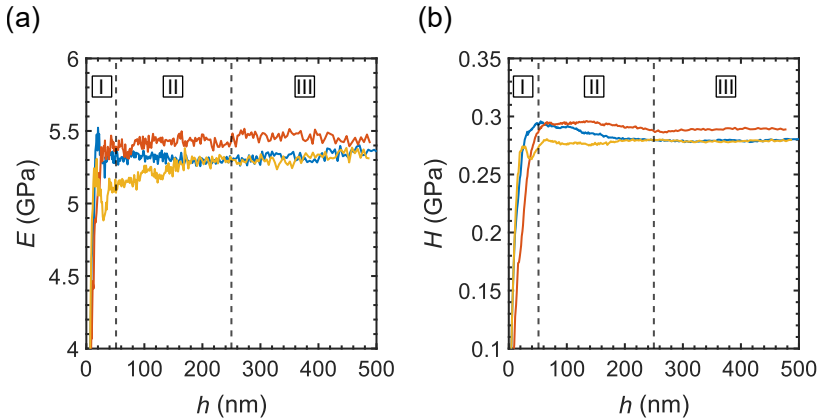


Fig. 7.4 Typical evolution of (a) E and (b) H values measured by nanoindentation in Elium as a function of the penetration depth h . Each colour represents one indent performed in the bulk polymer (i.e. condition(3)) at t_5 .

Note that the behaviour illustrated by Figure 7.4 was observed regardless of fibre proximity (i.e. condition (1), (2) or (3)) and ageing time, in both E and H data. A similar evolution for $h < 100$ nm has already been observed when indenting poly(methyl methacrylate) [297], which is the main constituent of Elium after polymerisation. The phenomenon was attributed to uncertainties in the measured displacements as well as in the contact definition due to tip blunting [297].

In light of these observations, only E and H measurements acquired in the range $400 < h < 450$ nm (i.e. in domain III) were included in the statistical analysis for conditions (2) and (3). For condition (1), however, narrowing down the datasets obtained from each indent was not as straightforward. As mentioned in the introduction, the indentation response of composite matrix pockets may be affected by the proximity of the stiffer reinforcing material. FE models of nanoindentation experiments [258, 259, 263, 268] are classically used to quantify this ‘constraining effect’ as a function of the x/h ratio, where x is the distance between the indenter tip and the closest fibre-matrix interface and h is the penetration depth. The simulation results allow identifying a critical x/h value above which the indentation measurements should no longer be impacted by the fibre response. A similar FE study was performed for the Elium compos-

ite, as described in the Supplementary Information. The simulation results showed that E and H measurements could be considered unconstrained for $x/h > 30$. However, as x/h increases above this critical value, the measurements may become affected instead by the variability observed previously at low indentation depths - whatever its origin may be [258, 259]. Finding the “sweet spot”, i.e. a range of x/h values enabling to avoid both the constraining effect and the low-depth experimental variability, is challenging – if not impossible. As FE simulations like those performed in this work do not capture the variability at low depths, an upper bound for the x/h ratio can only be estimated from the experimental results. In this work, the maximum acceptable value of x/h was set to 40 for the following reason. From image analysis, the minimum radius x of the analysed intra-tow matrix pockets is known to be around $2\ \mu\text{m}$. The variability at low depths is most significant in domain I, i.e. for h values below $50\ \text{nm}$, according to the previous paragraph. Hence, any data point meeting the condition $30 < x/h < 40 (= 2,000/50)$ should not be affected by fibre constraint nor be too impacted by the variability at low depth. In practice, nearly all data points obtained for condition (1) belong to domain II. This is due to the fact that $x < 10\ \mu\text{m}$ for 95 % of the analysed matrix pockets, resulting in unconstrained penetration depths below $300\ \text{nm}$.

Descriptive and inference statistical analysis of nanoindentation results

The distributions of E and H values obtained by nanoindentation in conditions (1), (2) and (3) at different ageing times are presented in Figure 7.5. All box plots appear relatively symmetric, suggesting that each dataset follows a close-to-normal distribution (again, provided the data is unimodal, which has been verified in all cases). In each plot, box height represents the interquartile range, which allows estimating the variability of a dataset. Box height is, on average, twice larger for E and H datasets obtained in condition (1) compared to conditions (2) and (3), indicating a wider dispersion of nanoindentation measurements performed in intra-tow matrix pockets. This results from the fact that most unconstrained data points obtained for condition (1) are slightly impacted by the variability at low depths, as mentioned in the previous section.

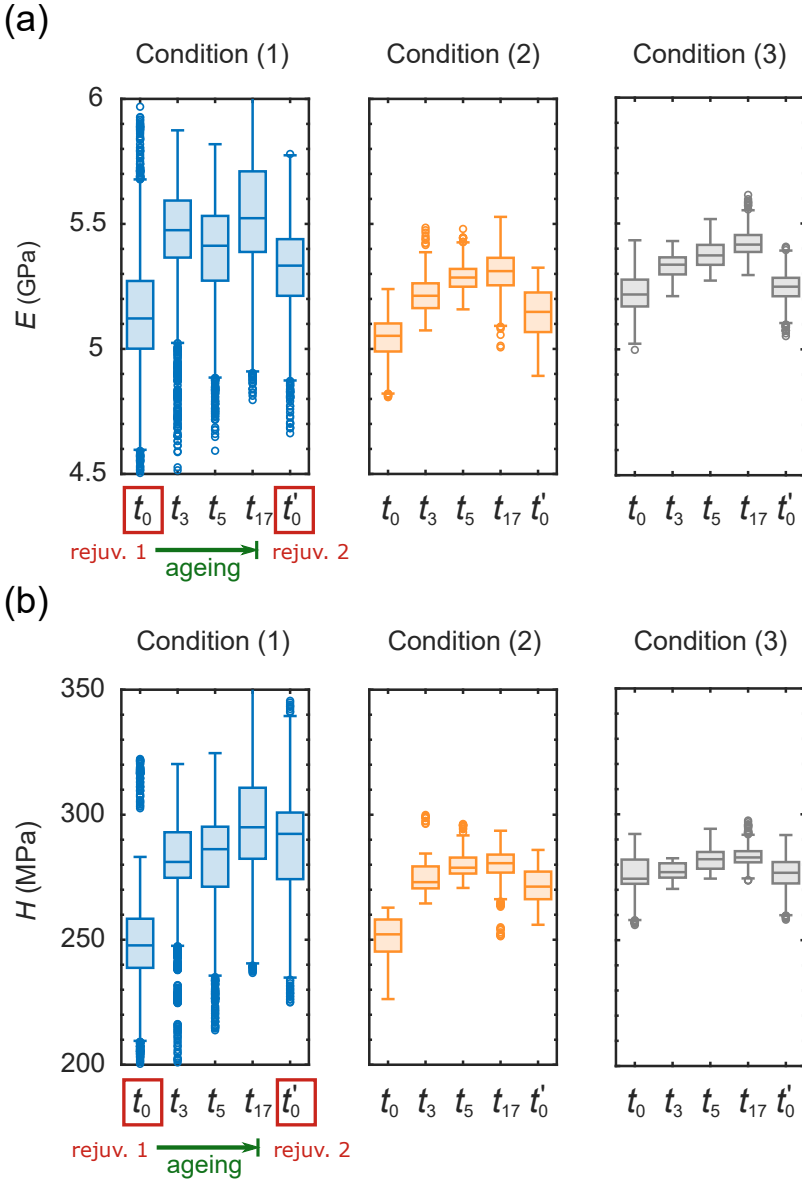


Fig. 7.5 Box plot distributions of (a) E and (b) H values measured by nanoindentation in conditions (1), (2) and (3), for several values of the ageing time. Whiskers indicate the minimum and maximum values of each distribution, excluding outliers which are depicted by circles. Boxes extend between the 25th and 75th percentiles, while the central horizontal line indicates the median value.

Despite this difference in variability, the data shown in Figure 7.5 provide insight into the influence of fibre proximity and physical ageing on the nanoindentation response of the resin. The majority of E and H values in Figures 7.5a and 7.5b lie within the $5.3 \text{ GPa} \pm 10 \%$ and $280 \text{ MPa} \pm 10 \%$ ranges, respectively. Regardless of fibre proximity, a clear trend emerges with respect to the effect of the ageing time on the mechanical properties of the resin. More precisely, E and H values increase as the “physical age” of the resin increases, and drop following the second thermal rejuvenation treatment (which corresponds to t'_0). The largest increase in E and H values occurs during the first 3 months following the initial rejuvenation treatment, i.e. between t_0 and t_3 . There seems to be, however, an influence of fibre proximity on the extent of the observed variations. The largest apparent increase in properties with physical age is respectively observed in condition (1), then (2) and eventually (3). In particular, the median value of H increases by $\approx 20 \%$ between t_0 and t_{17} for condition (1), by $\approx 10 \%$ for condition (2) and by less than 5% for condition (3), see Figure 7.5b. A similar tendency is observed for E values shown in Figure 7.5a, though to a lesser extent. This indicates a higher “physical ageing potential” for the resin located in the close vicinity of fibres. Surprisingly, however, the second rejuvenation treatment induces the same 3% drop in the median value of E and H between t_{17} and t'_0 for all conditions, except in one case (the decrease in the median H value for condition (1) seems more subtle - likely between 0 and 1%). As a consequence, condition (3) is the only one exhibiting the same nanoindentation response at t_0 and t'_0 , i.e. after the first and second rejuvenation treatments. The resin properties in condition (2) and especially (1) remain larger at t'_0 than at t_0 .

The results presented in Figure 7.5 yield interesting but mostly qualitative conclusions, which can be further analysed via inference statistics. Figures 7.6 and 7.7 presents the 95% CIs obtained from multiple pairwise comparisons performed between nanoindentation datasets for assessing the respective influence of fibre proximity (i.e. condition (1), (2) or (3)) and ageing time on the mechanical properties of the resin. CIs should be interpreted as follows: if the interval contains 0 , the corresponding difference is deemed non-significant from a statistical point of view. If a CI does not contain 0 , there is a 95% probability that the two datasets being compared are different: the result is statistically significant. Yet, a statically-significant difference is not always considered “important”, depending on the overall purpose of the study. Here, grey dotted lines in Figures 7.6

and 7.7 indicate a $\pm 5\%$ or $\pm 10\%$ difference with respect to the aforementioned baseline values of 5.3 GPa for E and 280 MPa for H . In this work, any statistically-significant difference whose CI lies completely outside the $\pm 5\%$ range is considered important from a mechanical viewpoint.

The variations in the modulus and hardness of the resin in conditions (1), (2) and (3) as ageing time increases are respectively depicted in the top and bottom parts of Figure 7.6. Inter-tow matrix pockets (condition (2)) do not experience important variations in modulus values due to physical ageing, while hardness values increase by more than 5% between t_0 and t_3 , nearly exceeding the 10% difference threshold by t_{17} . The comparisons made on pure resin (condition (3)), on the other hand, suggest no important changes in neither the modulus nor hardness values with increasing ageing time. The greater dispersion of measurements previously observed in intra-tow matrix pockets translates into larger confidence intervals for condition (1). While this impacts the statistical significance of most of the corresponding CIs, the comparison of nanoindentation datasets obtained at t_0 and t_{17} still clearly shows an increase in hardness values of at least 10% in intra-tow matrix pockets.

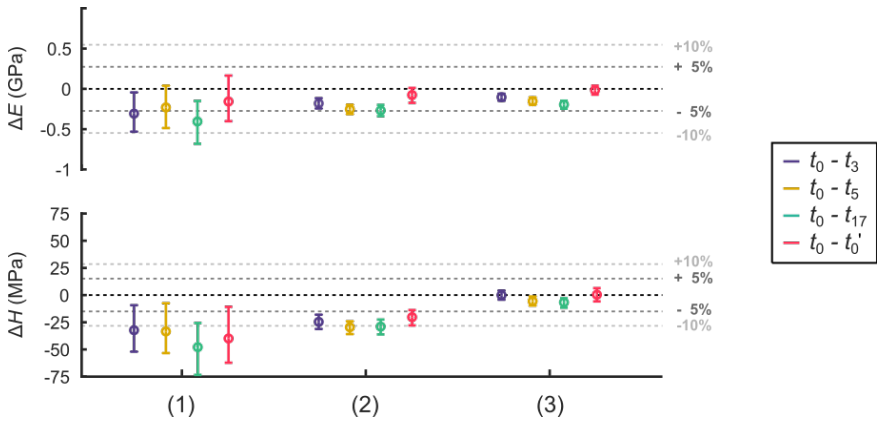


Fig. 7.6 Median differences (circles) and 95% CIs (error bars) in (a) E and (b) H values, obtained from the pairwise comparison of nanoindentation datasets acquired at different aging times for the same measurement condition (i.e. (1), (2) or (3)). The grey dotted lines indicate variations of $\pm 5\%$ and $\pm 10\%$ with respect to the average values of E , i.e. 5.3 GPa and H , i.e. 280 MPa.

We note in passing that the hardness comparisons performed between t_0 and t'_0 for the three conditions confirm the observations made from Figure 7.5, i.e. intra- and inter-tow matrix pockets do not recover their “initial” (t_0) properties after the second thermal rejuvenation treatment. The possible explanations for this are the following. First, despite the precautions taken to ensure a complete relaxation of the polymer, the second treatment may not have been carried out at a sufficiently high temperature and/or for long enough to completely reverse the effects of physical ageing in the composite matrix. Otherwise, part of the increase in hardness values over time may result from another chemical or physical phenomenon which has not been yet identified.

The effect of fibre proximity on the nanoindentation response of the resin is shown in Figure 7.7, for several levels of physical ageing. There is no important effect of fibre proximity on the resin modulus, whatever the ageing time considered.

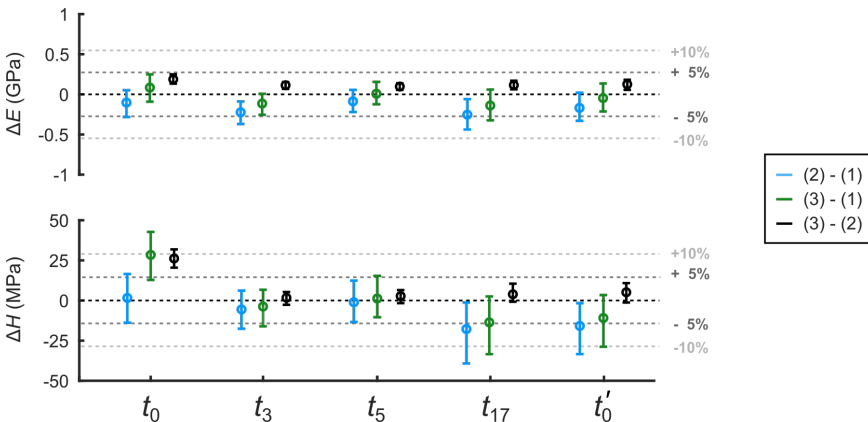


Fig. 7.7 Median differences (circles) and 95 % CIs (error bars) in (a) E and (b) H values, obtained from the pairwise comparison of nanoindentation datasets acquired in conditions (1), (2) and (3) at the same ageing time. The grey dotted lines indicate variations of ± 5 or 10 % with respect to the average values of E , i.e. 5.3 GPa and H , i.e. 280 MPa.

Differences in resin hardness, which are depicted in the bottom part of Figure 7.7, yield mostly the same conclusions. Still, at t_0 , the pure resin (condition (3)) exhibits more than 5 % higher hardness values than the inter-tow composite matrix pockets (condition (2)), and probably also than the intra-tow matrix pockets (condition (1)) although the CI slightly intercepts the +5 % line. This initial mismatch could result from small differences in residual monomer content between the composite and bulk resin specimens and/or from the additional presence of the glass fibre sizing in the case of the composite - both residual methyl methacrylate and glass fibre sizing components having a strong plasticising effect on PMMA-based Elium resins, even at very low concentrations [1]. More interesting is the fact that the difference in hardness between the pure resin and the composite matrix is no longer observed as ageing time increases. We know from Figure 7.6 that the composite matrix (i.e. conditions (1) and (2)) is more affected by physical ageing than pure resin (condition (3)). As physical ageing manifests itself by an increase in hardness and modulus values, the difference in hardness between the bulk resin and the composite matrix at t_0 is thus “smoothed out” as the ageing time increases.

7.4.3 Comparison with PFT-QNM AFM measurements

Histograms showing the distributions of DMT modulus values obtained by AFM in intra-tow (condition (1)) versus inter-tow (condition (2)) matrix pockets at t_0 and t_5 are presented in Figure 7.8 alongside with their fitted skew-normal probability density functions. As explained in section 7.2.1, the modulus values obtained by AFM in this work are considered relative, i.e. only comparable with data obtained in the same experimental conditions (same probe, same calibration and operating parameters). Consequently, the data obtained at t_0 (see Figure 7.8a) and t_5 (see Figure 7.8b) cannot be compared in a quantitative manner, as they correspond to two different sets of experimental conditions (in terms of AFM device, probe type and calibration parameters, see section 7.3.3). From the equations of the fitted probability density functions shown in Figure 7.8a, the mean value and standard deviation of the DMT modulus distributions at t_0 can be estimated. These are respectively equal to 5036 ± 660 MPa for condition (1) and 5164 ± 550 MPa for condition (2). Following the same approach for Figure 7.8b, the calculated values of the mean modulus and standard deviation at t_5 are equal to 3930 ± 600 MPa for condition (1) and to 3950 ± 720 MPa for condition (2).

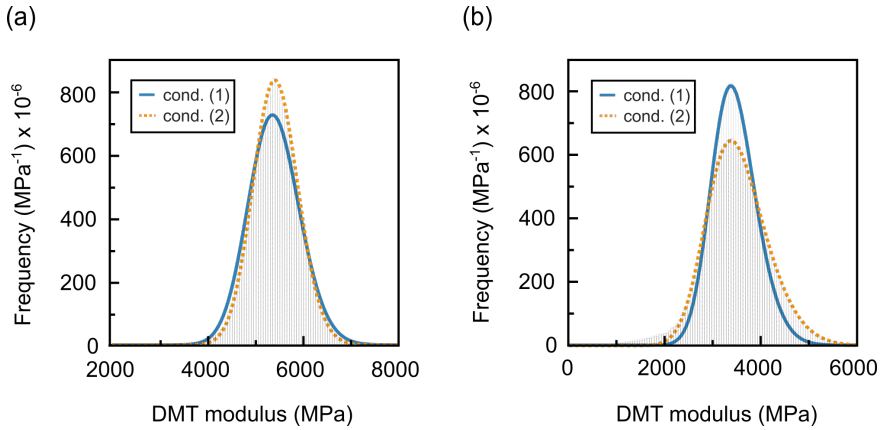


Fig. 7.8 Histogram distribution and skew gaussian fit of DMT modulus values measured by AFM in intra-tow (condition (1)) versus inter-tow (condition (2)) composite matrix pockets at (a) t_0 and (b) t_5 .

These results reinforce one of the conclusions drawn from nanoindentation measurements with respect to the absence of significant differences in modulus values between conditions (1) and (2) at t_0 and t_5 . We note in passing that the dispersion of AFM measurements is in the same order of magnitude for both conditions: AFM is especially designed for providing accurate measurements at very low (or even zero) indentation depths, contrary to nanoindentation measurements whose accuracy at penetration depths below 100 nm is limited, as mentioned above.

7.5 Conclusion

The effects of physical ageing and fibre proximity on the local mechanical response of a methacrylic resin were assessed by CSM nanoindentation and PFT-QNM AFM indentation. The main findings of the present study are the following. First, the modulus and hardness of the resin do not differ significantly as a function of fibre proximity, provided all tested specimens have been subjected to the same level of physical ageing. There seems to be a slight influence of fibre proximity on the rate and extent of physical ageing experienced by the resin, i.e. intra-tow matrix pockets show earlier and stronger signs of ageing (in particular via an increase in hardness) than inter-tow matrix pockets and unreinforced resin, respectively. In the

longer run, this could lead the composite matrix properties to diverge significantly from those of the bulk polymer, as observed by several authors in the case of epoxy resin systems. Further work could therefore focus on the following questions:

- What is the effect of longer periods of natural ageing time (> 18 months) on the mechanical response of unreinforced and reinforced Elium resins? Do their properties stop evolving after a certain amount of time? If they do, this could help determine the best timing for performing the mechanical characterisation of a composite part after it has been manufactured.
- Can the results of accelerated ageing studies (performed at temperatures higher than room temperature) be reliably extrapolated to predict the long-term behaviour of polymers and polymer composites exposed to natural ageing conditions? This matter is still debated in the literature, see e.g. [298].

7.6 Acknowledgements

Financial support from Arkema is gratefully acknowledged. The authors would like to thank the Elium team at Arkema Lacq (France) for their assistance with composite manufacturing, as well as the following people for providing their help and guidance: Dr Audrey Favache and Ms Sophie Ryelandt with nanoindentation, Ms Cécile D'Haese and Pr Philippe Leclère with AFM and Ms Catherine Rasse with statistical analyses.

7.7 Supplementary information

7.7.1 Sectioning diagram of composite plate

The composite plate was machined using a water-cooled disc milling cutter following the sectioning diagram shown in Figure 7.9.

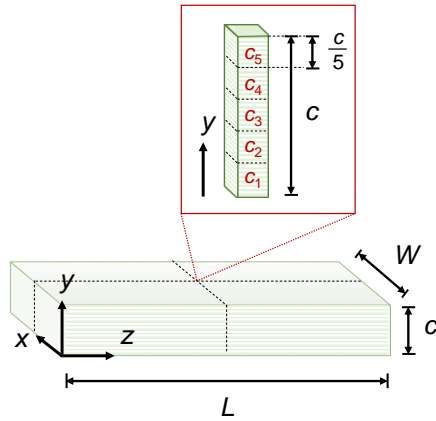


Fig. 7.9 Sectioning diagram for the micromechanical characterisation of the composite plate ($L = 60$ cm, $W = 40$ cm, $c = 73$ mm); the first cuboid was extracted close to $z = L/2$ and $x = W/2$. Note that infusion direction and fibre tow orientation were parallel to the z axis, see [4].

A cuboid of dimensions $10 \times 13 \times 10$ mm³ was extracted from the middle of the plate (close to $z = L/2$ and $x = W/2$) and further divided into 5 equal parts along the y axis in order to obtain specimens C_1 to C_5 . The homogeneity of plate properties in terms of molecular weight, residual monomer content, micromechanical and thermal properties along the y axis was verified, as reported in [1]. Therefore, specimens C_1 to C_5 are considered identical in the present study. Nanoindentation and AFM tests were respectively performed on specimens C_2 and C_4 .

7.7.2 Polishing protocol for composite specimens

Polishing composite surfaces is challenging due to the heterogenous properties of the fibre and matrix materials. The following protocol has been especially developed to minimise differential erosion and allow characterising the intra-tow matrix pockets and interphase region of the composite by AFM. Table 7.2 details the parameters applied to the MultiPrep machine during the various steps of the process. The sample load values indicated in the table range from 0 to 5, referring to the own scale of the MultiPrep machine. These values actually correspond to loads of 0 to 500 g, respectively, excluding the masses of the specimen holder (≈ 300 g in our case) and specimen itself (< 2 g).

Table 7.2 Polishing procedure applied to composite specimens for minimising differential erosion. Each line corresponds to one step of the protocol.

Step no.	Particle size (μm)	Sample load	Platen rotation speed (rpm)	Platen rotation direction
1	30	2	100	
2	15	2	100	Both, alternatively (e.g. change every few min)
3	9	2	100	
4	6	1	50	
5	3	1	50	
6	1	0	50	Counterclockwise (opposite to spindle rotation)
7	0.5	0	10	
8	0.25	0	10	
9	0.1	0	10	

In addition to platen rotation, the spindle holding the specimen was systematically imposed a clockwise rotation on its own axis (“full rotation” mode ON) and subjected to a sweeping motion (“oscillation” mode ON).

7.7.3 FE simulations of AFM and nanoindentation experiments near the fibre-matrix interface

Nanoindentation and AFM indentation experiments were modelled with the finite element software Abaqus 2021 (Dassault Systèmes, France), in order to determine the minimum x/h value leading to unconstrained measurements of the mechanical properties of Elium in the vicinity of glass fibres. A 2D axisymmetric geometry was used for both the AFM indentation and nanoindentation experiments, as illustrated by Figure 7.10. The assumption of axisymmetry may not be realistic with respect to the actual morphology of intra-tow matrix pockets, but it offers a number of advantages. In particular, axisymmetric indentation models have a much lower computational cost than more realistic 3D models, are much easier to implement, and – more importantly – can only overestimate the effect of fibre constraint on the elastic properties of the polymer [252, 263].

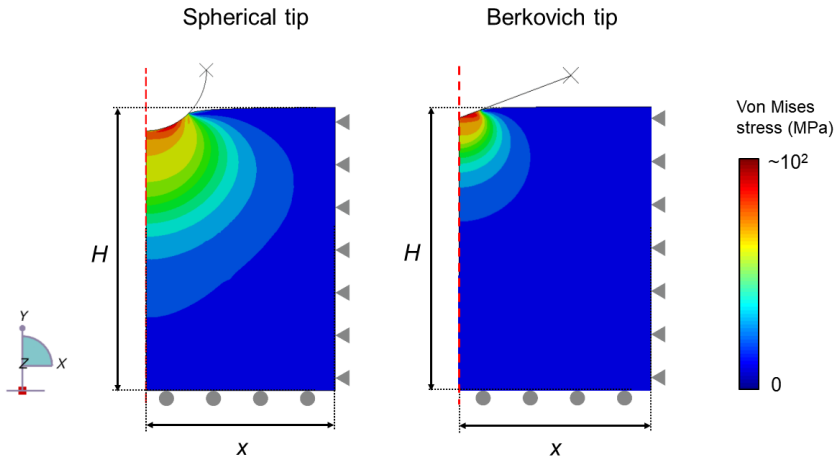


Fig. 7.10 2D axisymmetric FE models of AFM indentation with a spherical tip (left) and nanoindentation with a Berkovich tip (right) with boundary conditions. In this example, the contour plots show the Von Mises stress value at the end of loading.

For all simulations, a 1,000 mass scaling factor was applied to reduce computation times and the *Nlgeom* algorithm was used to account for large deformations.

The AFM and nanoindenter tips were modelled as rigid analytical surfaces, while the indented specimen consisted of CAX4 quadrilateral elements. An elasto-viscoplastic behaviour was assigned to the Elium polymer via a Drucker-Prager hardening law, calibrated from macroscopic compression and tensile tests performed on pure Elium polymer by Maes [234], see Annex 1 in section 9.1. No damage criterion was included in the FE simulations. A friction coefficient of 0.2 was selected for the contact between the polymer and the tip in order to avoid excessive element distortion under the tip (without influencing the overall mechanical response of the indented material) [266, 268]. The bottom of the model was subjected to a roller boundary condition (BC) (i.e. vertical displacements were blocked), while the outer edge of the model was assigned a rigid (“encastre”) BC to simulate the constraining effect of a fibre as suggested by [258, 263]. A fine, uniform mesh was applied in the contact area and made gradually coarser further away from the tip apex, as exemplified by Figure 7.11 for the case of nanoindentation.

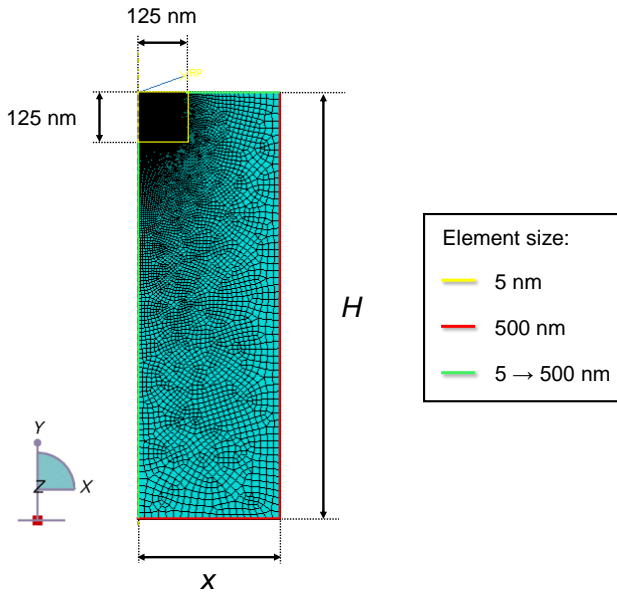


Fig. 7.11 Meshing parameters exemplified in the case of the nanoindentation model, with associated element size. The same meshing parameters were applied for the AFM indentation model with a 0.01 multiplication factor for element size (i.e. 5 nm become 0.05 nm). The edge seeding meshing method by element size was selected; yellow and red lines indicate uniform seeding while green indicates seeding by bias.

Nanoindentation model

The Berkovich tip was modelled as a rigid cone with a half-angle equal to 70.3° . As mentioned by Gregory and Spearing [258], this simplified representation gives the same projected-area-to-depth ratio as the actual Berkovich tip geometry (i.e. a three-sided pyramid). A small (with respect to h_{\max}) 10-nm radius fillet was applied to the tip apex to account for the fact that actual Berkovich tips are not perfectly sharp. Loading and unloading of the Elium polymer were implemented as two subsequent static general steps. Both were performed in displacement-controlled mode, i.e. by imposing a vertical displacement BC to the tip. For the loading step, a non-linear evolution of the displacement between 0 and $-h_{\max}$ (i.e. the selected maximum penetration depth) was imposed, in order to keep the loading rate constant as observed during actual nanoindentation experi-

ments [268]. Unloading was modelled the same way, by imposing a second vertical displacement up to $+h_{\max}$. Indentation modulus E and hardness H were calculated from the predicted load P versus penetration depth h curves following the procedure detailed in [299]. The residual indentation depth h_p (i.e. depth of the residual imprint after unloading) is first obtained by fitting a linear model to the unloading curve in the range 0.5-15 % P_{\max} :

$$P = a_1 h_p + b_1, \quad (7.12)$$

where a_1 and b_1 are the slope and intercept of the model, respectively. The value of h_p is calculated as

$$h_p = -b_1 / a_1. \quad (7.13)$$

The upper part of the unloading curve (comprising P values ranging from 40 to 98 % of P_{\max}) is then fitted by the power law

$$F = \alpha (h - h_p)^m, \quad (7.14)$$

where α and m are fitting parameters. The unloading contact stiffness S is obtained from the following equation:

$$S = \left(\frac{dP}{dh} \right)_{h_{\max}} = \alpha m (h_{\max} - h_p)^{m-1}. \quad (7.15)$$

The contact area A_c is expressed as:

$$A_c = \pi a_c^2, \quad (7.16)$$

where a_c is the contact radius, which may be directly obtained via the CPRESS output in Abaqus. CPRESS measures the contact pressure at the surface nodes; it yields a positive value in the contact area and is equal to zero everywhere else. The reduced indentation modulus E^* can be calculated from A_c and S values via equation 7.2 from the manuscript. Eventually, the value of the indentation modulus E is obtained from equation 7.3 while indentation hardness H is given by equation 7.1. Unlike CSM nanoindentation experiments, which consist in cyclic loading-unloading

steps providing several measurements between $h = 0$ and $h = h_{\max}$, the FE simulation presented here assumes a quasi-static nanoindentation experiment, i.e. one loading step up to h_{\max} followed by one unloading step. Consequently, only one E and H measurement may be obtained from each simulation.

The distance x between the tip apex and the simulated fibre-matrix interface was varied from 3 to 100 times the maximum indentation depth h_{\max} in order to assess the influence of x/h_{\max} on the calculated indentation modulus E and hardness H . Examples of P versus h_{\max} curves obtained from the FE simulations are displayed in Figure 7.12 for the case where $h_{\max} = 1000$ nm. Figure 7.13 shows the final outcomes of the FE simulations, i.e. a plot of E/E_{∞} and H/H_{∞} as a function of x/h_{\max} , where E/E_{∞} (respectively H/H_{∞}) is the ratio of the predicted resin modulus (hardness) divided by the “unconstrained modulus (hardness) value”, which is defined here as the modulus (hardness) of the resin for $x/h_{\max} = 100$. We verified that a change in the value of the tip apex fillet radius R did not impact the model predictions by performing an additional simulation with $R = 50$ nm, whose results are shown as a light blue triangle in both Figures 7.13a and 7.13b.

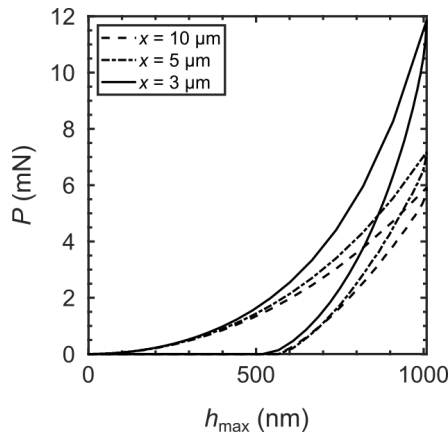


Fig. 7.12 Examples of load P versus penetration depth h_{\max} curves obtained from the FE simulation of nanoindentation experiments for several values of the distance x to the closest fibre.

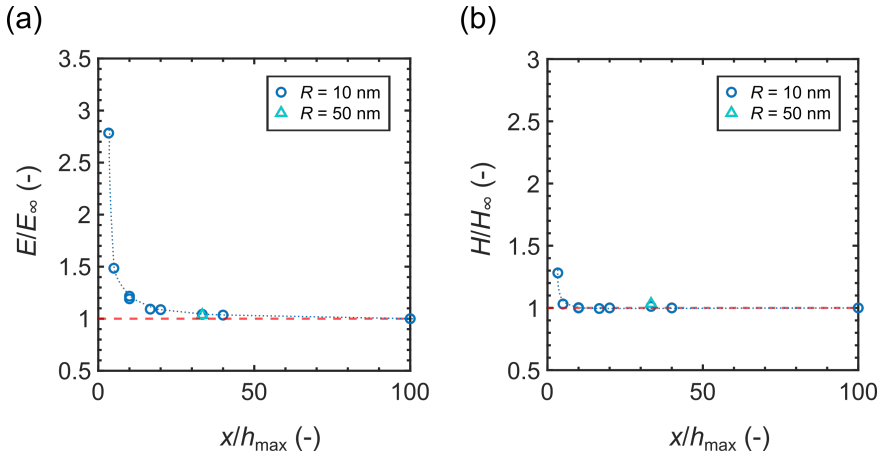


Fig. 7.13 Nanoindentation response of the Elium polymer predicted by FE modelling: evolution of the (a) E/E_∞ and (b) H/H_∞ ratios as a function of x/h_{\max} , for two different values of the tip apex radius R . The blue dotted lines only serve as a guide for the eye. The red dashed lines at $E/E_\infty = 1$ and $H/H_\infty = 1$, respectively, correspond to completely unconstrained resin properties.

We also verified that the predicted values of E/E_∞ and H/H_∞ for a given x/h_{\max} did not depend on the value of h_{\max} , as illustrated by the two overlapping data points in Figure 7.13a corresponding to $x/h_{\max} = 10$. These were respectively obtained for $x = 5 \mu\text{m}$ and $h_{\max} = 500 \text{ nm}$ (lower E/E_∞ value), and for $x = 10 \mu\text{m}$ and $h_{\max} = 100 \text{ nm}$ (higher E/E_∞ value). The two corresponding predicted hardness values completely coincide, see Figure 7.13b.

The FE predictions displayed in Figure 7.13 are in line with those obtained by Gregory and Spearing [258] and Hardiman [263] for a carbon fibre-reinforced epoxy composite using similar 2D axisymmetric models. In particular, the value of the E/E_∞ ratio falls below 1.05 for x/h_{\max} values above 30, i.e. the constraining effect only induces a maximum + 5 % deviation in the predicted modulus value compared to the unconstrained value if $x/h_{\max} > 30$. The predicted hardness values appear less sensitive to the constraining effect than modulus values, consistently with previous observations [268]. More precisely, the value of the H/H_∞ ratio falls below 1.05 for x/h_{\max} values above 5.

In light of the FE simulation results, it was decided that any nanoindentation data point obtained in intra-tow matrix pockets (condition (1)) for x/h values below 30 would be discarded from the comparative study. An additional upper limit for x/h values was introduced for removing the unconstrained data points affected by low-depth variability, see section 7.4.2 of the manuscript.

AFM indentation model

The AFM probe tip was modelled as a rigid sphere with a radius R equal to 32 nm, which is the actual value of the tip radius used for AFM experiments at t_0 , see Table 7.1 in the main manuscript. Loading and unloading of the Elium polymer were implemented as two subsequent static general steps. Both were performed in displacement-controlled mode, i.e. by imposing a vertical displacement BC to the tip. For the loading step, a non-linear evolution of the displacement between 0 and $-h_{\max}$ was imposed in order to keep the loading rate \dot{P}/\dot{p} constant, as mentioned previously for nanoindentation simulations. Unloading was modelled the same way, by imposing a second vertical displacement up to $+h_{\max}$. The indentation modulus E was calculated from the predicted load P versus penetration depth h curves via the DMT contact model described in section 7.2.1 of the manuscript. First, the unloading part of the P versus h curve was fitted by a linear function of $h^{3/2}$ in the range 5-95 % P_{\max} , see equation 7.7. The selected fitting range corresponds to that applied to experimental PFT-QNM force curves for extracting the DMT modulus, see Table 7.1. The reduced modulus E^* of the resin was calculated from the slope a_2 of the fitted model, expressed as

$$a_2 = \frac{4}{3}E^*\sqrt{R}, \quad (7.17)$$

and the modulus E was then obtained via equation 7.3.

In practice, AFM indentation experiments are not displacement-controlled, as assumed in the FE simulation, but load-controlled. This means that a force setpoint (referred to as the PF setpoint in the manuscript) is used as an input, instead of a maximum penetration depth h_{\max} . To circumvent this problem, two subsequent FE simulations were actually performed for each configuration (i.e. each value of the distance x between the indenter tip and the rigid interface). A first simulation was carried out for $h_{\max} = 5$ nm, which is intentionally above the 2-3 nm pen-

etration depth observed experimentally in the Elium polymer. Using the predicted P versus h curve, the h_0 value corresponding to the desired PF setpoint (here 150 nN, see Table 7.1) was identified. A second simulation was performed with h_0 as the target indentation depth for calculating the resin modulus E . Examples of P versus h_0 curves obtained from these FE simulations are displayed in Figure 7.14.

The predicted evolution of the E/E_∞ ratio as a function of x/h_0 is displayed in Figure 7.15a; the unconstrained modulus value E_∞ is defined here as the predicted modulus of the resin in the configuration where $x = 300$ nm. As observed for nanoindentation, the predicted value of the E/E_∞ ratio falls below 1.05 for x/h_0 values above 30. A plot of the same results is shown in Figure 7.15b as a function of x instead of x/h_0 , which allows comparing the FE predictions to one of the DMT modulus profiles measured experimentally in the interphase region. The fibre constraining effect predicted by the simulations is no longer observed beyond ≈ 60 nm from the fibre surface, meaning that the measured values of the interphase thickness (which lied in the 70-200 nm range, with an average value of 120 nm, see Figure 7.3) can be trusted.

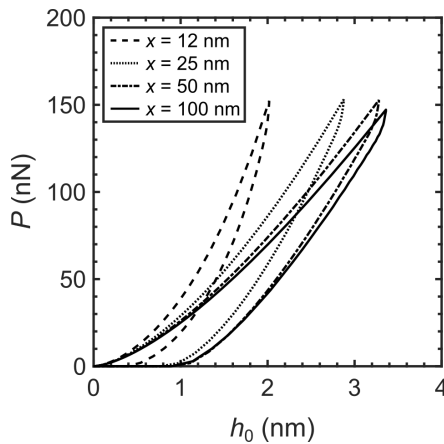


Fig. 7.14 Examples of load P versus penetration depth h_0 curves obtained from the FE simulation of AFM indentation experiments for several values of the distance x to the closest fibre.

Secondly, the increase in DMT modulus values close to $x = 0$ due to the constraining effect is almost negligible with respect to the variations observed experimentally in the interphase region. This confirms the existence of a stiffer interphase region in the Elium composite.

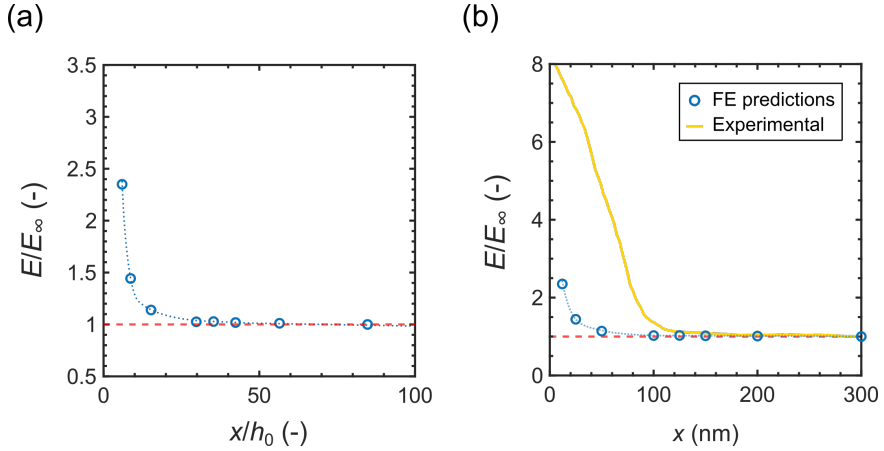


Fig. 7.15 AFM indentation response of the Elium polymer predicted by FE modelling: evolution of the E/E_∞ ratio as function of (a) x/h_0 and (b) x . The blue dotted lines only serves as a guide for the eye. The red dashed lines at $E/E_\infty = 1$ corresponds to completely unconstrained resin properties. An example of experimental measurement close to the fibre-matrix interface is depicted in Fig. (b) with a full yellow line.

8

Conclusions and perspectives

8.1 General conclusions

The general objective of this thesis was to address concrete technological challenges met by the wind industry when manufacturing thick fibre-reinforced Elium composites, while answering scientific questions of interest for the broader composite community.

Mitigating void formation in thick Elium laminates manufactured by vacuum infusion was a first motivation for this work, from an industrial point of view. Based on the existing literature, the main source of void formation in Elium composites was already suspected to be through monomer boiling during the highly exothermic MMA polymerisation step. The problem was first approached from a top-down perspective, i.e. via the phenomenological study of industrially-produced Elium composite samples containing voids described in Chapter 3. The outcomes of this preliminary study marked a turning point in the research, paving the way for the development of the thermokinetic model described in Chapter 4 and for the conception of the in-situ infusion experiment presented in Chapter 5.

The second, more fundamental objective of this thesis was to contribute to the understanding of fibre-reinforced Elium composite proper-

ties at the constituent level. By relying on small-scale indentation techniques (Chapter 7) as well as on a newly-developed nano-DIC method (Chapter 6), the elastic *and* plastic deformation response of the Elium matrix pockets in between glass fibres were characterised, and decoupled from that of the fibre-matrix interphase region. The conclusions lead to questioning the relevance of using continuum laws, calibrated from macroscopic test results, for modelling the microscale behaviour of a polymer within a fibre-reinforced composite material.

The novelty of this work lies, among others, in the methodological developments of three new numerical and experimental tools, which are listed below. Some of these have already been applied to fibre-reinforced polymer systems different than that of interest in this work.



New tools

- **A thermochemical model** [4] for predicting, within a minute, the evolution of temperature across the thickness of Elium laminates during polymerisation for any set of preform, resin and processing parameters. The model was initially validated for vacuum infusion (see Chapter 4), and successfully adapted to the consolidation of carbon fibre/Elium prepregs [300].
- **A 4D-XCT experiment for monitoring void formation** [6] in thick fibre-reinforced laminates produced by infusion. In the proof-of-concept study of Chapter 5, the experiment was conducted within a lab-based XCT device. The progressive growth of macrovoids during the in-situ polymerisation of a miniature glass fibre preform infused with Elium monomer was successfully captured.
- **A nano-DIC method dedicated to composites** [7] for studying the local deformation and fracture mechanisms occurring in Elium laminates at the fibre level. This first-of-a-kind experiment, presented in Chapter 6, also provided accurate nanoscale DIC measurements for a carbon fibre-reinforced epoxy resin.

More importantly, this thesis allowed filling some of the gaps previously identified in the literature. The main topics addressed in this manuscript are presented hereafter, alongside with the corresponding conclusions - many of which were obtained from the newly-developed tools described above.

8.1.1 Mitigating porosity in Elium composites

Monomer boiling: a matter of thermokinetics and preform thickness

Thick Elium laminates manufactured by infusion are sensitive to monomer boiling and subsequent void formation, due to the exothermic and self-accelerating nature of the MMA polymerisation reaction. The competition between heat transfer - within and outside of the laminate - and heat generation via the polymerisation reaction determines whether or not the monomer will boil locally, giving rise to permanent voids in the matrix in the former case. Using the aforementioned model, the influence of preform thickness, fibre volume fraction, fibre material, resin formulation (i.e. nature and amount of initiator, monomer content), external heating parameters applied during processing, mould properties (constitutive material and thickness) and ambient temperature on the formation of thermal porosity could be understood and quantitatively predicted. The computational efficiency of the model allowed generating a large amount of data within a short amount of time, enabling the construction of processing maps. For a given composite application (i.e. for a given set of preform thickness, reinforcing fabric and resin formulation), such maps may, for instance, allow finding the "sweet spot" in terms of external heating parameters for ensuring the shortest possible polymerisation time while avoiding the formation of thermal porosity.

The model also shed light on the heterogenous thermokinetic behaviour along the thickness direction of Elium laminates manufactured by vacuum infusion. In all cases, the polymerisation exotherm occurs first in the lower plies of the laminate, i.e. close to the mould. The heat thus generated in these lower plies diffuses upwards through conduction, triggering the polymerisation exotherm in the upper plies. Due to the self-speeding nature of MMA polymerisation, the exotherm becomes sharper and higher temperatures are reached as one gets closer to the surface of the laminate. This snowballing effect is exacerbated by external heating, which may be applied via the mould to shorten the processing

time. The thicker the preform and the higher the selected heating rate (and maximum setpoint temperature), the more likely the formation of voids from monomer boiling. This phenomenon is responsible for the characteristic, heterogenous void patterns which are sometimes observed in thick Elium composites manufactured by infusion: the closer to the surface of the laminate, the more voids and the larger they are.

Other sources of porosity

Monomer boiling during polymerisation has been identified as the most significant source of voids in the case of Elium composites - but it may not be the only one. Mitigating porosity in thick Elium laminates involves identifying and decoupling *all* the different possible mechanisms leading to void formation over the course of the manufacturing process. Using the dynamic XCT scanning experiment mentioned above, it was found that in the example case of interest, (1) a fraction of the final voids resulted from air entrapment during preform filling, that (2) most of the voids grew during polymerisation (again, starting from the lower plies), and that (3) there was a very slight reduction in void size during the cooling step due to thermal shrinkage. Though more work is needed to extend the study to other systems (e.g. a different reinforcing fabric), these preliminary results demonstrate the potential of the 4D-XCT method for future investigations.

8.1.2 Small-scale mechanical response of Elium matrix and interphase

The deformation and failure mechanisms occurring at the local fibre-matrix level in Elium composites were explored via the newly-developed nano-DIC method. Strain localisation essentially takes place in a thin (less than 0.5 μm wide) crown surrounding the fibres, and failure generally occurs via interface debonding before shear bands can fully develop (and be captured by DIC) across matrix pockets. The 0.3 to 0.5 μm transition zone extending between the near-zero fibre deformation domain and the maximum absolute strain value measured in the matrix was attributed to the interphase region of the composite, and this assumption was confirmed via AFM nanomechanical testing. Note that carbon fibre-reinforced epoxy composite specimens yielded the same observations. Still, the post-mortem comparison of the two composite systems revealed striking differences in terms of damage behaviour. While markers of extensive plastic damage are present in Elium specimens, with the formation of crazes and micro shear bands, epoxy composites fail catastrophically

without any clear sign of damage accumulation at the microscale.

On the other hand, the nanoindentation response of Elium as a composite matrix does not differ significantly from that of the bulk polymer, provided the specimens have experienced the same level of physical ageing (which was performed under ambient conditions for up to 18 months in this work). This means that the composite matrix beyond the interphase region is not *intrinsically* different from the bulk polymer. However, the composite matrix shows earlier and stronger signs of ageing (marked by an increase in hardness and, to a lesser extent, in modulus), especially in the smallest intra-tow pockets. This could lead the composite matrix properties to diverge significantly from those of the bulk polymer in the long term, as observed by several authors in the case of epoxy composites. A plausible explanation could be that the diffusion of free volume “holes” outside of the polymer - which is at the origin of physical ageing - is favoured by the vicinity of fibre-matrix interfaces.

8.2 Recommendations for future work

The main findings of this thesis revolve around processing and microstructural aspects, whose relationships with the macroscopic mechanical properties of Elium composites remain to be explored. In particular, the impact of porosity on the mechanical response of the parts has only been briefly touched upon at the end of Chapter 3, via the macroscopic transverse compression testing of composite specimens containing voids. Future work could focus on the macroscale fatigue and fracture behaviour of thick Elium laminates with and without voids, following again a top-down approach at first. A technical challenge would arise, however, from the fact that no standard test method exists for thick composite materials. After final failure, post-mortem XCT analyses could provide additional insights into the crack propagation path and fracture mechanisms occurring in thick Elium laminates, as compared to those observed in thinner composite panels. The heterogenous void patterns observed in thick Elium composites subjected to monomer boiling and the physical ageing of the matrix are two additional aspects that would be particularly worth studying, in order to understand their impact on crack propagation path and fracture mechanisms.

Nanoscale crack propagation experiments could also be performed via e.g. the nano-DIC method of Chapter 6, both on pure resin and composite

specimens with or without voids. In particular, the interaction of propagating matrix cracks with voids (or other types of manufacturing defects like unbonded interfaces or broken fibres) could be investigated. Similar experiments could be performed on thermosetting composite specimens, which could shed light on the elementary mechanisms responsible for the difference in toughness properties observed between thermoplastic and thermosetting composites at the larger scales.

Finally, the origin of the strain localisation events captured by nano-DIC in the first few hundreds of nanometres away from the fibre-matrix interfaces should be further investigated numerically, for both thermoplastic and thermosetting systems. Is assuming the existence of an interphase of finite thickness, having distinct material properties from those of the matrix, enough to fully predict the extent and distribution of the localisation phenomena observed experimentally? As briefly mentioned in Chapter 6, gradient plasticity effects, occurring in the polymer at the submicron scale, could also be responsible (partially or totally) for the peculiar mechanical response of the composite at the constituent level. In this case, the relative contribution of mechanical and chemical aspects to the observed deformation behaviour in the vicinity of fibres should be determined. Klavzer et al. [301] recently refined the 2D finite element model of Chapter 6, by considering size-dependent plasticity in the matrix material while keeping the hypothesis of a perfect interface between the matrix and fibres. The correlation between the strain fields obtained from nano-DIC experiments and those predicted by the new model was considerably improved, though the 300 to 500 nm-wide transition region observed experimentally between the fibre and matrix strain domains was still not captured. A logical follow-up on this work - beyond adapting the model to the case of a glass fibre-reinforced Elixir composite system - could therefore involve focusing on the implementation of an interphase region of finite thickness between the fibre and matrix materials. To this end, the perfect interface could be replaced by a cohesive surface surrounded by a crown of material whose thickness and mechanical properties match those measured by AFM in Chapter 6. Another option would be to consider the interface and interphase as a single adhesive layer consisting of cohesive elements.

9

Annexes

This chapter contains the following annexes to the main manuscript:

- **ANNEX 1:** Macroscopic characterisation of Elium resins
- **ANNEX 2:** Application for synchrotron beamtime

9.1 ANNEX 1: Macroscopic characterisation of Elium resins

This section presents a non-exhaustive summary of the Master's thesis entitled *Mechanical properties of high performance recyclable thermoplastic based composites for windmill applications* [234], presented in 2020 by Mathieu Maes. This work focused, among others, on the macroscale mechanical characterisation of two grades of Elium: 188 XO and 191 OSA. More precisely, uniaxial compression tests were conducted over four decades of strain rate and at three different temperatures, and additional tensile tests were performed for assessing the influence of the hydrostatic pressure on the mechanical response.

These characterisation results allowed establishing and implementing the elasto-viscoplastic constitutive behaviour of both Elium polymers in the FE software Abaqus, setting the basis for the development of the micromechanical frameworks presented in Chapters 6 and 7. The work of Mathieu Maes also contributes to a better understanding of the mechanical properties of Elium resins at the macroscale.

9.1.1 Materials and methods

Preparation of test specimens

The resin mix was prepared by combining 1.5 parts peroxide initiator Perkadox CH-50X (Nouryon, The Netherlands) for a hundred parts monomer formula (Elium 188 XO or Elium 191 OSA of Arkema, France) under mechanical stirring. The mixture was degassed for 1 min at 50 mbar, casted into a borosilicate glass test tube (inner diameter 14 mm) coated with release agent Chemlease 41-90 (Chem-Trend GmbH, Germany), and left to polymerise at room temperature. After cooling, the resin samples were demoulded. Cylindrical compression specimens with height and diameter both equal to 12 mm were lathed from the samples, as described by Morelle [102]. For the tensile tests, cylindrical dogbones were machined according to the sectioning diagram shown in Figure 9.1, taken from [268].

Mechanical testing

Compression and tensile tests were performed on a screw-driven Zwick-Roell universal testing machine, equipped with a 250 kN loading cell. A Wyoming Test Fixture subpress was used for compression tests. Axial displacements values were obtained via a compliance-corrected crosshead

displacement method. A minimum of 3 specimens were tested for each set of experimental conditions. Compression tests were carried out at the following true strain rates: $\dot{\epsilon} = 10^{-4}, 10^{-3}, 10^{-2}$ and 10^{-1} s^{-1} and at three different temperatures: $T = -10, 23$ and $55 \text{ }^\circ\text{C}$. The tests at -10 and $55 \text{ }^\circ\text{C}$ were performed in an isolated casing. As advised by Morelle [102], Teflon films were inserted between each specimen and the subpress platens in order to minimise friction. Tensile tests were only performed at $T = 23 \text{ }^\circ\text{C}$ with a true strain rate equal to 10^{-4} s^{-1} .

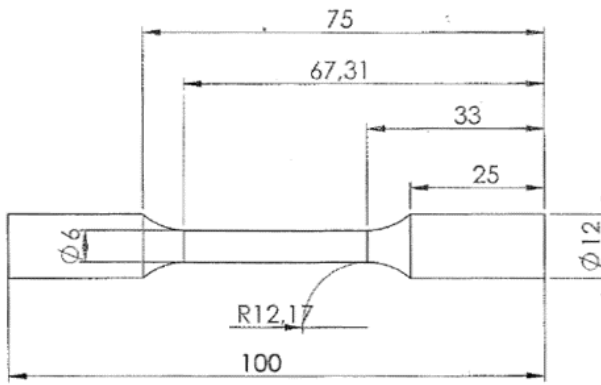


Fig. 9.1 Sectioning diagram of cylindrical tensile test specimens [268].

9.1.2 Results and discussion

Compressive behaviour of Elium 188 XO and Elium 191 OSA

The stress-strain curves obtained from the compression testing of Elium 188 XO and 191 OSA specimens are shown in Figures 9.2a and b, respectively. For the sake of clarity, only one representative curve is presented for each set of experimental conditions. The mechanical response of both grades of Elium is typical of glassy polymers, i.e. the following domains are successively observed as the strain ϵ increases: elastic regime, yield transient, strain softening and strain hardening. An increase in the peak (or upper) yield stress value σ_y with increasing strain rate $\dot{\epsilon}$ and decreasing temperature T is clearly visible for both grades of Elium, as expected from the literature (see e.g. the work of Richeton [302]). The slope of the stress-strain curves in the hardening regime increases as T decreases, which is

also consistent with the literature [302]. The influence of $\dot{\epsilon}$ on the hardening slope is less obvious, mostly because of the so-called adiabatic heating effect [302–305] observed for $\dot{\epsilon} \geq 10^{-2} \text{ s}^{-1}$ in PMMA [302].

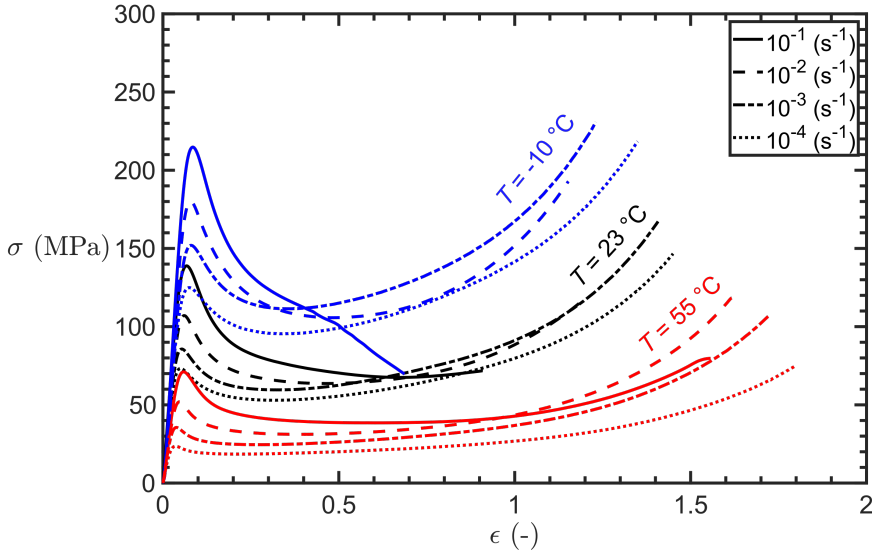


Adiabatic heating affects glassy polymers subjected to high strain rates, due to the low thermal diffusivity of these materials. This results in a decrease of the strain hardening rate or the complete absence of strain hardening, if the polymer reaches its glass transition temperature T_g [302]. PMMA is particularly affected by adiabatic heating [302] due to its relatively low T_g compared to other glassy polymers (e.g. polycarbonate). This phenomenon is addressed in more details in the full version of the thesis [234]. In particular, the stress-strain curves impacted by adiabatic heating are successfully corrected into isothermal curves via thermomechanical modelling [303].

Regardless of adiabatic heating, the stress-strain curves corresponding to $\dot{\epsilon} = 10^{-1} \text{ s}^{-1}$ exhibit lower fracture strain values ϵ_f at a given temperature, compared to those obtained at smaller strain rates. This trend is more marked as the temperature decreases, especially for Elium 188 XO. This behaviour is characteristic of the ductile-to-brittle (D-B) transition experienced by glassy polymers subjected to high strain rates and low temperatures. The D-B transition likely results from intense strain localisation phenomena occurring at the microscale, which may be favoured, among others, by a high extent of strain softening [102, 306, 307]. However, it is difficult to identify clear differences in the softening behaviour of Elium 188 XO and 191 OSA from Figure 9.2 alone.

The evolution of the Young's modulus E , peak yield stress σ_y and yield drop (i.e. difference between peak yield stress and lower yield stress observed in the softening regime) as a function of temperature and strain rate is detailed in Figure 9.3 for both grades of Elium, and confirms the qualitative observations mentioned above. Moreover, Elium 191 OSA appears marginally stiffer and more resistant than Elium 188 XO: for a given temperature, a consistent difference of 130 MPa (5 %) in E values and of 10 MPa (8 %) in σ_y is observed between the two grades of Elium. Larger yield drop values are also observed for Elium 188 XO, which may explain why this material experiences a more marked D-B transition at low temperatures and high strain rates.

(a)



(b)

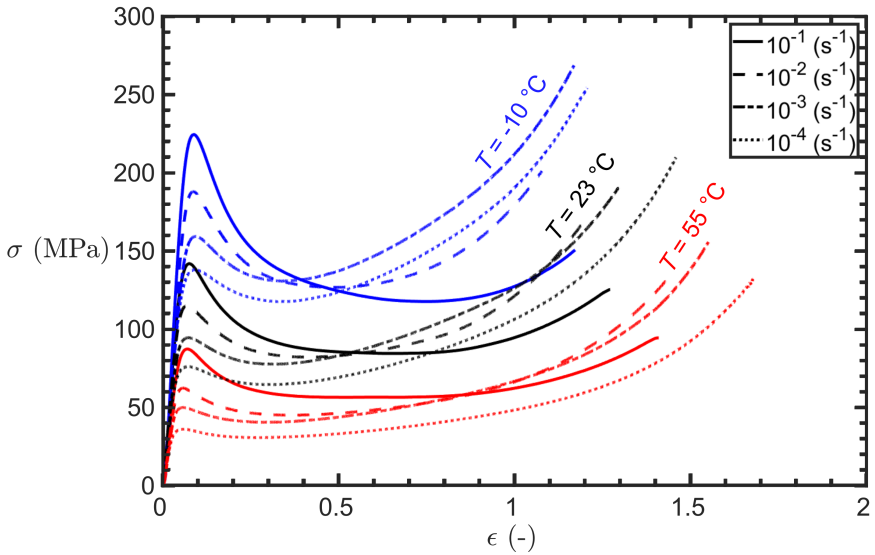


Fig. 9.2 Compression tests results obtained for (a) Elium 188 XO and (b) Elium 191 OSA.

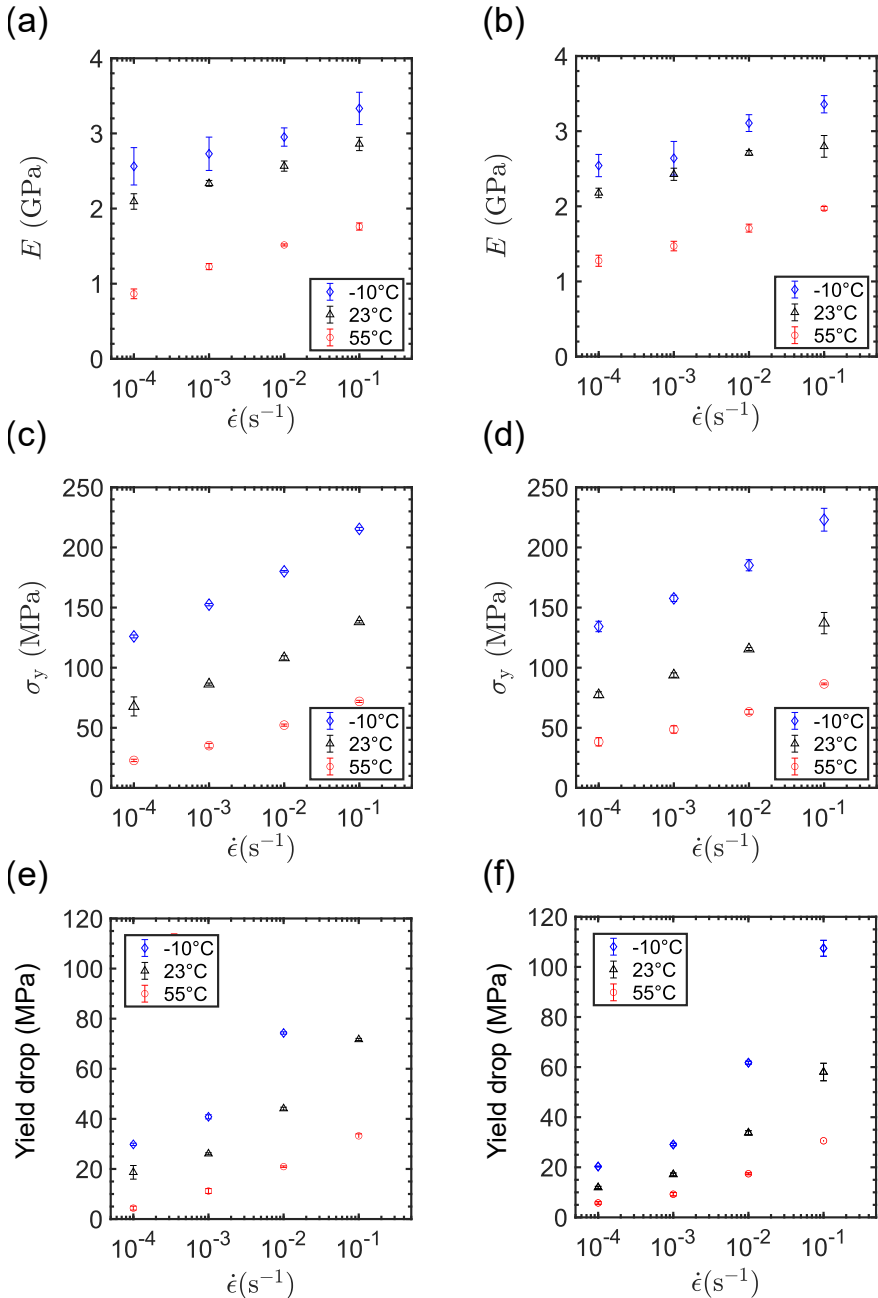


Fig. 9.3 Evolution of the mean mechanical properties of Elium 188 XO (left) and 191 OSA (right) as a function of $\dot{\epsilon}$: (a), (b) Young's modulus E , (c), (d) peak yield stress σ_y and (e), (f) yield drop. Error bars represent standard deviation values.

The strain rate sensitivity m , which is expressed as

$$m = \frac{d \ln(\sigma)}{d \ln(\dot{\epsilon})} \Big|_{\sigma=\sigma_y} \quad (9.1)$$

can be estimated from the results shown in Figure 9.3c and d. The values of m , calculated for both grades of Elium at each of the three test temperatures, are presented in Table 9.1. While most m values are in the same order of magnitude (i.e. close to 0.1), Elium 188 XO clearly exhibits overall higher strain rate sensitivity than 191 OSA. Both polymers experience an increase in rate sensitivity as the temperature increases, which is consistent with the literature for PMMA [302, 304].

Figure 9.4 shows the evolution of the fracture strain ϵ_f values as a function of strain rate and temperature. Elium 188 XO specimens seem to be more ductile at $T = 55^\circ\text{C}$, with ϵ_f values 6% higher on average than those of Elium 191 OSA specimens; however, the trend reverses at lower temperatures and high strain rates (i.e. for $\dot{\epsilon} \geq 10^{-2} \text{ s}^{-1}$) as a consequence of the D-B transition mentioned above. Note that no values of yield drop (Figure 9.3e) nor failure strain (Figure 9.4a) are available for Elium 188 XO at $T = -10^\circ\text{C}$ and $\dot{\epsilon} = 10^{-1} \text{ s}^{-1}$ due to the premature failure of the specimens before reaching the hardening regime.

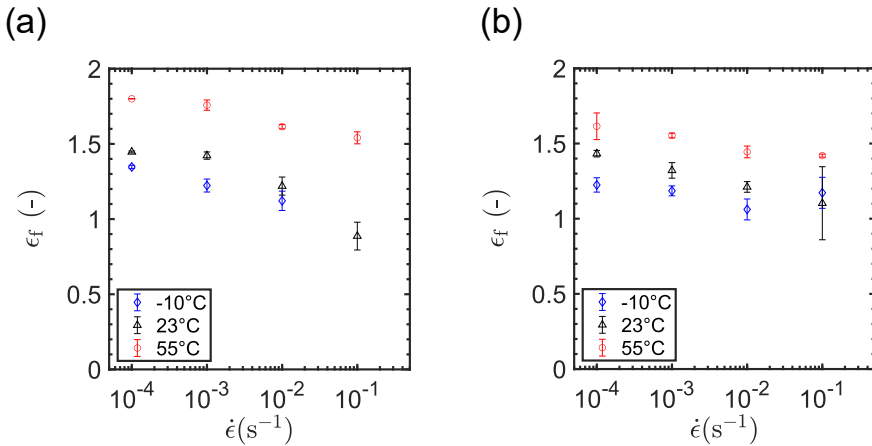


Fig. 9.4 Evolution of the fracture strain ϵ_f of Elium (a) 188 XO and (b) 191 OSA as a function of the true strain rate $\dot{\epsilon}$. Error bars represent standard deviation values.

Table 9.1 Strain-rate sensitivity m of Elium 188 XO and 191 OSA at 3 different temperatures.

T (°C)	Elium 188 XO	Elium 191 OSA
-10	0.08	0.07
23	0.10	0.08
55	0.17	0.12

A summary of the compressive properties of Elium 188 XO and 191 OSA is presented in Table 9.2 for $T = 23$ °C and $\dot{\epsilon} = 10^{-3} \text{ s}^{-1}$, i.e. in conditions where adiabatic heating does not impact their mechanical behaviour. Results obtained on actual PMMA in similar testing conditions by [308] are also shown for the sake of comparison. The compressive properties of all three polymers are in the same order of magnitude, which confirms - once again - that Elium resins behave similarly to PMMA, see Chapter 2.

Table 9.2 Intrinsic compressive properties of Elium 188 XO, Elium 191 OSA and PMMA [308] obtained at $T = 23$ °C and $\dot{\epsilon} = 10^{-3} \text{ s}^{-1}$. No fracture strain value ϵ_f is available for PMMA, as the specimen was unloaded before failure in [308].

	E (GPa)	σ_y (MPa)	Yield drop (MPa)	ϵ_f (-)
Elium 188 XO	2.34	86	26	1.42
Elium 191 OSA	2.43	94	17	1.32
PMMA	2.45	108	26	/

9.1.3 Tensile test results

Tensile peak yield stress $\sigma_{y,t}$ values, which were extracted from the tensile curves of both grades of Elium, are displayed in Table 9.3 alongside with the compressive peak yield stress $\sigma_{y,c}$ values obtained in the same experimental conditions.

Table 9.3 Tensile $\sigma_{y,t}$ and compressive $\sigma_{y,c}$ peak yield stress values measured at $T = 23\text{ }^{\circ}\text{C}$ and $\dot{\epsilon} = 10^{-4}\text{ s}^{-1}$ for both grades of Elium.

	$\sigma_{y,t}$ (MPa)	$\sigma_{y,c}$ (MPa)
Elium 188 XO	47	68
Elium 191 OSA	60	78

9.1.4 Identification of Drucker-Prager model parameters

As mentioned in Chapter 6 and briefly in Chapter 7, a Drucker-Prager hardening law was used for modelling the mechanical behaviour of Elium. In Abaqus, three input parameters are required for defining a Drucker-Prager hardening behaviour, namely the friction angle β , the flow stress ratio K and the dilation angle φ . This section explains how the values of these parameters were determined for both grades of Elium.

The friction angle β of a material is expressed as

$$\tan\beta = \frac{3 - 3r}{1 + r}, \quad (9.2)$$

where r is the uniaxial symmetry ratio, which may be defined as

$$r = \left| \frac{\sigma_{y,t}}{\sigma_{y,c}} \right|. \quad (9.3)$$

The value of r can be estimated from the results shown in Table 9.3. The resulting values of β are close to 28° for Elium 188 XO, and to 21° for Elium 191 OSA.

The values of K and φ are respectively assumed to be equal to 1 and 0 for both grades of Elium, which is a common simplifying assumption used e.g. by Morelle [102] and Chevalier [268]. If the value of K is set to 1, the yield surface in the deviatoric principal plane becomes the von Mises yield surface. Likewise, setting the value of φ to 0 means that we assume plastic incompressibility [102, 268]).

9.2 ANNEX 2: Application for synchrotron beamtime

Below is a copy of the application form sent to the Swiss Light Source synchrotron facility in September 2022 for requesting beamtime at the TOMCAT X-ray source. The following persons were listed as co-proposers: Prof Y. Swolfs, Dr J. Soete and Mr J. Vanhulst from the Department of Materials Engineering at KU Leuven, Belgium, as well as Prof T. Pardoen, Dr F. Hannard and Ms S. Gayot (main proposer/principal investigator) from the Institute of Mechanics, Materials and Civil Engineering at UCLouvain.

9.2.1 Goal of the experiment

An innovative time-resolved X-ray computed tomography (4D-XCT) method was developed for the in-situ dynamic monitoring of void evolution during the curing of fibre-reinforced polymer composites (FRPCs) produced by vacuum infusion [6]. The method aims to identify the origin(s) of voids, which are the most studied manufacturing defects in FRPCs. We will achieve this through real-time observation and subsequent quantification of void nucleation, growth, transport, and coalescence mechanisms occurring in the polymer matrix during processing. Void size ranges from a few μm (microvoids) to a few mm (macrovoids) and their evolution in a viscous liquid occurs in a matter of seconds [193]. Lab-based XCT cannot fulfill the corresponding requirements in terms of spatial and temporal resolution due to, amongst others, insufficient beam brightness. We would, therefore, like to request beamtime at TOMCAT to image the central part of specimens of approximate dimensions $30 \times 30 \times 5 \text{ mm}^3$ during curing.

9.2.2 Background

FRPCs offer a unique combination of high strength, high stiffness and low density, making them ideal candidates for producing lightweight and high-performance structures. However, FRPCs produced by liquid moulding contain voids, which can have detrimental and unpredictable effects on the physical and thermomechanical properties of the component. There are still many uncertainties about void formation mechanisms as well as difficulties in their suppression in modern manufacturing techniques [127]. This has slowed down the adoption of FRPCs for structural applications and emphasises the importance of the proposed research.

Voids may have various origins: incomplete degassing of the resin, air entrapment during preform filling, volatilisation of resin components, or matrix shrinkage. Mitigation methods can only be applied if the involved mechanism(s) of void nucleation, growth and transport are known. Post-mortem non-destructive analysis of porosity in FRPCs by, e.g., lab-based XCT or ultrasonic inspection makes it possible to characterise void patterns in the final parts, but they do not allow reconstructing the timeline of events and hence cannot identify the root causes of porosity nucleation. Some authors have relied on 4D-XCT synchrotron-based methods to investigate void formation during liquid moulding composite processing. However, these studies provided no insight into the void formation mechanisms involved in real-scale processes, as (1) dynamic scanning was only performed during the impregnation step, and (2) the setup consisted of a single fibre tow [184, 186, 189]. To fill this gap in the literature, we developed a new 4D-XCT stage allowing in-situ dynamic monitoring of void formation during the curing of FRPCs produced by vacuum infusion [6]. The principle of the experimental infusion setup, presented in Figure 9.5, was inspired by the pioneering work of Hemmer [191].

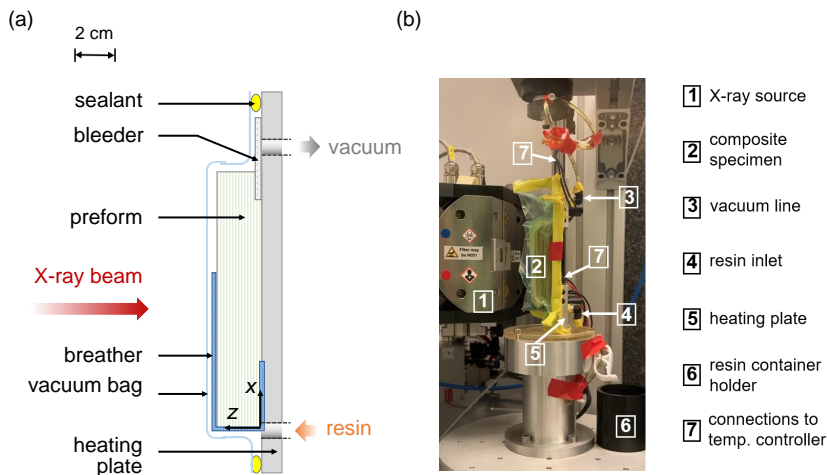


Fig. 9.5 Infusion setup used for the preliminary in-situ experiments: (a) simplified side-view of the mould with vacuum bag and (b) full rig within the XCT scanner.

Preliminary dynamic experiments were performed in a lab-based TESCAN UniTOM XL tomograph, using a 2 cm-thick glass fibre preform infused with a methacrylic monomer (Elium of Arkema, France). This thermoplastic resin system allows producing FRPCs by vacuum infusion followed by in-situ polymerisation. Using our new 4D-XCT stage, the formation of macrovoids could be successfully observed in Elium composites, see Figure 9.6. Void growth almost exclusively occurred at the end of the curing phase (i.e. within 20 min after infusion), and was observed in between fibre bundles. However, the shortest scan time achievable in the lab with this in-situ stage (≈ 2 min 15 per volume) did not make it possible to grasp nor decouple the void nucleation and growth mechanisms involved. Besides, the spatial resolution was not sufficient to capture microvoids within the bundles.

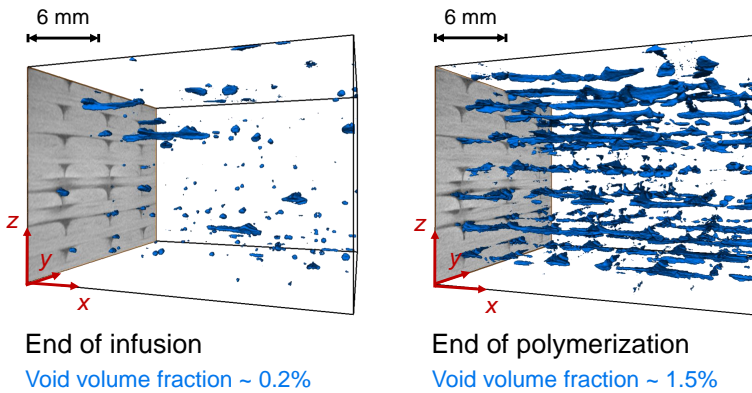


Fig. 9.6 Void patterns captured with the TESCAN UniTOM XL in Elium.

Repeating these experiments at TOMCAT, while benefiting from the knowledge acquired in a laboratory setting, should allow overcoming these temporal and spatial resolution limitations. The in-house expertise at the KU Leuven XCT Core Facility regarding 4D-XCT and image processing (image registration, digital volume correlation, etc.) guarantees scientific results and publications. Note that we are in the process of modifying our infusion rig to best suit the TOMCAT setting, see Figure 9.7. In particular, any unnecessary elements (e.g. tubing, metal plate) will be removed from the field of view of the scanner.

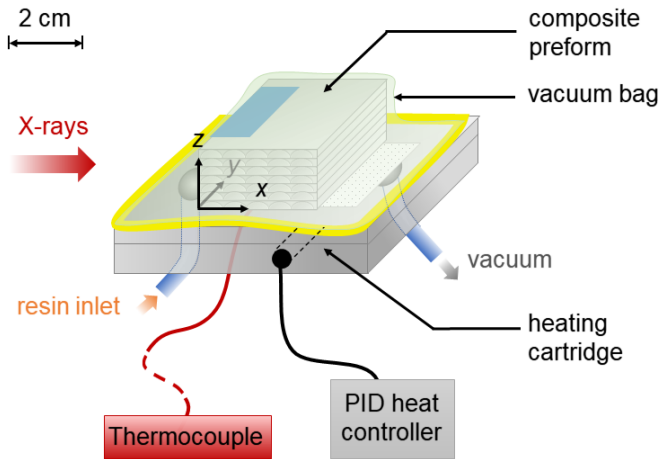


Fig. 9.7 Proposed design for the new infusion setup, better suited for synchrotron experiments. Rotation axis along the vertical direction.

9.2.3 Experimental method and specific requirements

We would like to perform a series of 5 in-situ infusion and curing experiments, to assess the influence of the following parameters on void formation: heating parameters (applied to the specimen to trigger polymerisation), resin formulation (via the chemical nature and amount of peroxide initiator) and preform geometry, (via the glass fabric architecture and preform thickness).

The GigaFRoST high-speed detector and white beam will be used to scan the full volume of interest every few seconds. Appropriate beam filtering will allow minimising the heat load on the specimen, so as to avoid any unwanted bubble formation events. If the voids after a full cure while being exposed to a filtered white beam are different from those without exposure, we will switch to monochromatic beam and consider compromises on the time resolution. Each of the 5 planned experiments will be performed twice, with different microscopes: microscope 2 for characterising macrovoids with the largest possible field of view, and then microscope 5 ($\times 4$) for zooming in on one fibre bundle and capturing microvoid formation. The switch between microscopes 2 and 5 would only be made once, i.e., halfway through the requested beamtime.

Prior to our visit to SLS, we will prepare 10 identical infusion moulds with the preforms already laid up and sealed as shown in Figure 9.7. Each mould can be quickly plugged into the rig and connected to the vacuum/resin tubes, in order to optimise experiment turnover and thus maximise the efficiency of our beamtime.

4D-XCT experiment

Each scanning session will take around 2h35 and will be performed as follows:

- Mounting of the mould onto the rotation table inside the hutch, connection to electric line via slipring (for allowing heating of the mould), connection to vacuum pump and last seal check (≈ 1 h 15).
- Start of vacuum pumping, in parallel with resin mix preparation (≈ 15 min).
- Resin infusion into preform, and clamping of resin and vacuum tubes (≈ 5 min)
- Immediately after: initiation of specimen heating (if applicable), followed by dynamic scanning in time-lapse mode for ≈ 30 min, depending on experimental parameters. Scanning will cover the in-situ polymerisation phase and onset of cooling. A thermocouple will be used for the real-time monitoring of specimen temperature: a sharp exotherm marks the end of in-situ polymerisation.
- Dismantling of used mould (≈ 30 min).

Note that 6 calibration experiments are planned before conducting the in-situ experiments of interest. The first 2 will focus on optimising beam filtering parameters to minimise self-heating of the specimen, which will be monitored via the thermocouple. Then, as it is not possible to decouple void nucleation and growth with lab-based XCT (cf. section 9.2.2), 2 calibration experiments for both resolutions will help optimise the scanning parameters and sequence (within the 30-min curing/cooling window), ensuring that void nucleation events are captured.

Specific requirements

- Possibility to use liquid resin inside the hutch. Note that, as an extra precaution, a thin, X-ray transparent protective case will surround the infusion rig and a catchment basin will be placed below the sample to avoid resin spilling.

- Access to a chemistry lab with the following equipment: fridge (for peroxide storage), scale and fume hood (for resin mix preparation).

9.2.4 Results expected

The combination of high imaging speed and spatial resolution of TOMCAT will enable new capabilities not possible in lab-based XCT by providing (1) resolved intra- and interbundle voids (micro- to macroscale) and (2) insights into nucleation AND growth mechanisms of these voids. This should lead to a better understanding of the sources of porosity in FRPCs produced by liquid moulding and their sensitivity to certain sample and/or process parameters. Ultimately, the experiments performed at TOMCAT should enable the design of tailored mitigation methods for composite manufacturers.

9.2.5 Estimate and justification of the beamtime

We estimate that we require 48 hours to conduct our experiments, i.e., 6 shifts of 8 hours. The first 4 hours will be used for tuning the beamline and installing the first rig and mould. The remainder of the beamtime will be dedicated to the 16 in-situ polymerisation experiments (6 calibration experiments + 5 experiments at both resolutions) mentioned above, with a microscope switch after the first 5 experiments. Each experiment should take a maximum of 2 h 35 min (see section 9.2.3), which corresponds to a total time just under 48 hours.

List of publications and awards

Publications in scientific journals

S. F. Gayot, C. Bailly, T. Pardoën, P. Gérard and F. Van Loock, *Processing maps based on polymerisation modelling of thick methacrylic laminates*, *Materials and Design* 196, 109170 (2020) [4].

T. Pardoën, N. Klavzer, S. F. Gayot, F. Van Loock, J. Chevalier, X. Morelle, V. Destoop, F. Lani, P. Camanho, L. Brassart, B. Nysten, and C. Bailly, *Nanomechanics serving polymer-based composite research*, *Comptes Rendus de Physique* 22, 331–352 (2021) [198]

N. Klavzer and S. F. Gayot, M. Coulombier, B. Nysten, and T. Pardoën, *Nanoscale digital image correlation at elementary fibre/matrix level in polymer-based composites*, *Composites Part A: Applied Science and Manufacturing* 168, 107455 (2023) [7].

S. F. Gayot, N. Klavzer, A. Guillet, C. Bailly, P. Gérard, T. Pardoën and B. Nysten, *Influence of physical ageing and fibre proximity on the local mechanical response of a methacrylic composite matrix*, (in preparation for submission in 2023) [8].

Publications in conference proceedings

S. F. Gayot, C. Bailly, T. Pardoën, and P. Gérard, *Relationship between processing parameters and mechanical properties of thick glass fibre reinforced thermoplastic methacrylic composites*, in *Proceedings of the 7th ECCOMAS Thematic Conference on the Mechanical Response of Composites* (2019) [1].

S. F. Gayot, C. Bailly, T. Pardoën, P. Gérard, and F. Van Loock, *A computationally efficient thermomechanical model for the in-situ polymerization of a methyl methacrylate-based resin in a thick glass fiber laminate.*, in Proceedings of the 35th ASC Annual Technical Conference (2020) [3].

S. F. Gayot, J. Soete, J. Vanhulst, C. Bailly, P. Gérard, and T. Pardoën, *Monitoring Void Formation during Liquid Composite Molding by in-Situ X-Ray Computed Tomography*, in Proceedings of the 37th ASC Annual Technical Conference (2022) [5].

S. F. Gayot, N. Klavzer, E. Van Vlierberghe, B. Nysten, Y. Swolfs and T. Pardoën, *Local Deformation and Fracture Mechanisms in Methacrylic Composites at the Fiber-Matrix Level: Insights from Nanoscale Digital Image Correlation*, in Proceedings of the 38th ASC Annual Technical Conference (2023).

Awards

EUROMECH Young Researcher Award 2022 (awarded at the 11th European Solid Mechanics Conference in Galway, Ireland)

Bibliography

- [1] S. F. Gayot, C. Bailly, T. Pardoën, and P. Gérard, “Relationship between processing parameters and mechanical properties of thick glass fibre reinforced thermoplastic methacrylic composites”, in Proceedings of the 7th ECCOMAS Thematic Conference on the Mechanical Response of Composites (Sept. 2019).
- [2] S. F. Gayot, *Comparative study of two thick Elium/pseudo-UD glass fibre composite plates produced by vacuum infusion*, Technical report (confidential) (UCLouvain/Arkema, 2019), pp. 1–51.
- [3] S. F. Gayot, C. Bailly, T. Pardoën, P. Gérard, and F. Van Loock, “A computationally efficient thermomechanical model for the in-situ polymerization of a methyl methacrylate-based resin in a thick glass fiber laminate.”, in Proceedings of the 35th ASC Annual Technical Conference (2020).
- [4] S. F. Gayot, C. Bailly, T. Pardoën, P. Gérard, and F. Van Loock, “Processing maps based on polymerization modelling of thick methacrylic laminates”, en, *Materials & Design* **196**, 109170 (2020).
- [5] S. F. Gayot, J. Soete, J. Vanhulst, C. Bailly, P. Gérard, and T. Pardoën, “Monitoring Void Formation during Liquid Composite Molding by in-Situ X-Ray Computed Tomography”, in Proceedings of the 37th ASC Annual Technical Conference (2022).
- [6] S. F. Gayot, J. Soete, J. Vanhulst, C. Bailly, P. Gérard, F. Hannard, and T. Pardoën, “4D-XCT monitoring of void formation in thick thermoplastic composites produced by infusion”, Manuscript in preparation for submission (2023).
- [7] N. Klavzer, S. F. Gayot, M. Coulombier, B. Nysten, and T. Pardoën, “Nanoscale digital image correlation at elementary fibre/matrix level in polymer-based composites”, en, *Composites Part A: Applied Science and Manufacturing* **168**, 107455 (2023).

- [8] S. F. Gayot, N. Klavzer, A. Guillet, C. Bailly, P. Gérard, T. Pardoën, and B. Nysten, "Influence of physical ageing and fibre proximity on the local mechanical response of a methacrylic composite matrix", Manuscript in preparation for submission (2023).
- [9] A. P. Votinov, P. P. Kobeko, and F. Marei, "Polymer studies. VII. Depolymerization of linear polymers", *Russ Zhurnal Fiz Khim* **16** (1942).
- [10] N. Grassie and H. Melville, "The Thermal Degradation of Polyvinyl Compounds. I. A New Type of Molecular Still", *Proceedings of The Royal Society A: Mathematical, Physical and Engineering Sciences* **199**, 1–13 (1949).
- [11] J. Charnley, "Anchorage of the femoral head prosthesis to the shaft of the femur", en, *The Journal of bone and joint surgery. British* volume **42-B**, Publisher: J Bone Joint Surg Br, 28–30 (1960).
- [12] M. Arora, E. K. Chan, S. Gupta, and A. D. Diwan, "Polymethylmethacrylate bone cements and additives: A review of the literature", en, *World Journal of Orthopedics* **4**, 67–74 (2013).
- [13] M. S. Zafar, "Prosthodontic Applications of Polymethyl Methacrylate (PMMA): An Update", *Polymers (Basel)* **12**, 2299 (2020).
- [14] G. G. Odian, *Principles of polymerization*, en, 4th ed., OCLC: ocm53393894 (Wiley-Interscience, Hoboken, NJ (USA), 2004).
- [15] G. I. A. Inc., *Global Polymethyl Methacrylate (PMMA) Market to Reach \$5.9 Billion by 2026*, en, June 2022.
- [16] C. L. Beyler and M. M. Hirschler, "Chapter 1-7: Thermal Decomposition of Polymers", en, in *SFPE Handbook of Fire Protection Engineering*, Third Edition (National Fire Protection Association, Inc., One Batterymarch Park Quincy, Massachusetts 02269, USA, 2002), pp. 110–131.
- [17] R. G. W. Norrish and E. F. Brookman, "The mechanism of polymerization reactions. I. The polymerization of styrene and methyl methacrylate", *Proceedings of the Royal Society of London. Series A. Mathematical and Physical Sciences* **171**, Publisher: Royal Society, 147–171 (1939).
- [18] R. G. W. Norrish and R. R. Smith, "Catalyzed polymerization of methyl methacrylate in the liquid phase", *Nature* **150**, 336–337 (1942).
- [19] V. E. Trommsdorff, H. Köhle, and P. Lagally, "Zur polymerisation des methacrylsäuremethylesters", de, *Die Makromolekulare Chemie* **1**, 169–198 (1948).

- [20] N. Friis and A. E. Hamielec, "Gel-Effect in Emulsion Polymerization of Vinyl Monomers", en, in *Emulsion Polymerization*, Vol. 24, edited by I. Piirma and J. L. Gardon (American Chemical Society, Washington, D.C. (USA), June 1976), pp. 82–91.
- [21] S. Sehajpal and V. Sood, "Effect of metal fillers on some physical properties of acrylic resin", en, *The Journal of Prosthetic Dentistry* **61**, 746–751 (1989).
- [22] M. M. Gad, S. M. Fouda, F. A. Al-Harbi, R. Nöpänkangas, and A. Raustia, "PMMA denture base material enhancement: a review of fiber, filler, and nanofiller addition", *Int J Nanomedicine* **12**, 3801–3812 (2017).
- [23] I. Tacir, J. Kama, M. Zortuk, and S. Eskimez, "Flexural properties of glass fibre reinforced acrylic resin polymers", en, *Australian Dental Journal* **51**, 52–56 (2006).
- [24] A. Vandenberghe and P. Tardieu, *ETIPWind Roadmap*, en, tech. rep., <https://etipwind.eu/files/reports/ETIPWind-roadmap-2020.pdf> (ETIPWind, 2020), p. 32.
- [25] Y. Liu, M. Farnsworth, and A. Tiwari, "A review of optimisation techniques used in the composite recycling area: State-of-the-art and steps towards a research agenda", en, *Journal of Cleaner Production* **140**, 1775–1781 (2017).
- [26] J. Beauson, B. Madsen, C. Toncelli, P. Brøndsted, and J. Ilsted Bech, "Recycling of shredded composites from wind turbine blades in new thermoset polymer composites", en, *Composites Part A: Applied Science and Manufacturing* **90**, 390–399 (2016).
- [27] N. Papadakis, C. Ramírez, and N. Reynolds, "Designing composite wind turbine blades for disposal, recycling or reuse", in *Management, Recycling and Reuse of Waste Composites* (Dec. 2010), pp. 443–457.
- [28] I. Komusanac, G. Brindley, Fraile, and L. Ramirez, *Wind energy in Europe: 2021 statistics and the outlook for 2022-2026*, tech. rep. (WindEurope, Feb. 2022).
- [29] Gurit, *Core materials - product overview*.
- [30] K. van Rijswijk, "Thermoplastic composite wind turbine blades - vacuum infusion technology for anionic polyamide-6 composites", NL, PhD thesis (Technische Universiteit Delft, Delft, The Netherlands, 2007).

- [31] R. E. Murray, J. Roadman, and R. Beach, "Fusion joining of thermoplastic composite wind turbine blades: Lap-shear bond characterization", en, *Renewable Energy* **140**, 501–512 (2019).
- [32] S. K. Bhudolia, G. Gohel, K. F. Leong, and R. J. Barsotti, "Investigation on Ultrasonic Welding Attributes of Novel Carbon/Elium® Composites", en, *Materials* **13**, Number: 5 Publisher: Multidisciplinary Digital Publishing Institute, 1117 (2020).
- [33] S. K. Bhudolia, G. Gohel, L. Kah Fai, and R. J. Barsotti, "Fatigue response of ultrasonically welded carbon/Elium® thermoplastic composites", en, *Materials Letters* **264**, 127362 (2020).
- [34] M. Bodaghi, C. H. Park, and P. Krawczak, "Reactive Processing of Acrylic-Based Thermoplastic Composites: A Mini-Review", en, *Front. Mater.* **9**, 931338 (2022).
- [35] P. Mallon and C. M. Ó Brádaigh, "Compliant Mold Techniques for Thermoplastic Composites", in *Comprehensive Composite Materials* (Talreja, R. and J.A.E. Manson, Amsterdam, The Netherlands, Dec. 2000), pp. 873–913.
- [36] K. van Rijswijk and H. E. N. Bersee, "Reactive processing of textile fiber-reinforced thermoplastic composites – An overview", en, *Composites Part A: Applied Science and Manufacturing* **38**, 666–681 (2007).
- [37] *The world's first offshore wind farm is retiring*, <https://orsted.com/en/media/newsroom/news/2017/03/the-worlds-first-offshore-wind-farm-is-retiring>, 2017.
- [38] C. Legaard, *Approval - Middelgrunden*, <https://www.middelgrunden.dk/approval/>, 2021.
- [39] *Power plants: Thanet Offshore Wind Farm - Vattenfall*, <https://powerplants.vattenfall.com/thanet/>.
- [40] *Anholt Offshore Wind Project*, <https://www.renewable-technology.com/projects/anholt-offshore-wind-project/>.
- [41] *Burbo Bank Extension Offshore Wind Farm, Liverpool Bay*, <https://www.power-technology.com/projects/burbo-bank-extension-offshore-wind-farm-liverpool-bay/>, 2017.
- [42] *About the project*, <https://oceanwindone.com/about-the-project>.
- [43] I. Chang and J. Lees, "Recent Development in Thermoplastic Composites: A Review of Matrix Systems and Processing Methods", en, *Journal of Thermoplastic Composite Materials* **1**, 277–296 (1988).

- [44] D. Cousins, "Advanced thermoplastic composites for wind turbine blade manufacturing", PhD thesis (Colorado School of Mines, Golden, Colorado, USA, 2018).
- [45] D. Bank, P. Cate, and M. Shoemaker, "pCBT: A New Material for High Performance Composites in Automotive Applications", en, in SAE Technical Paper Series (Oct. 2004).
- [46] J.-C. Fontanier, "Développement d'un système réactif pour composites acryliques par procédé RTM", fr, PhD thesis (Institut National des Sciences Appliquées de Lyon, 2017).
- [47] C. Edwards, "Thermoplastic pultrusion promises new synergies", en, *Reinforced Plastics* **45**, 34–39 (2001).
- [48] P. P. Parlevliet, "Residual Strains in Thick Thermoplastic Composites an Experimental Approach", en, PhD thesis (Technische Universiteit Delft, The Netherlands, 2010).
- [49] J. J. E. Teuwen, A. A. v. Geenen, and H. E. N. Bersee, "Temperature Evolution During Processing of Thick-Walled Anionic Polyamide 6 Composites: Experiment and Simulation", en, *Macromolecular Materials and Engineering* **298**, 722–729 (2013).
- [50] Z. Boufaïda, "Analyse des propriétés mécaniques de composites taffetas verre/matrice acrylique en relation avec les propriétés d'adhésion des fibres sur la matrice", fr, PhD thesis (Université de Lorraine, Nancy, France, 2015).
- [51] Q. Charlier, "Adhesion phenomena in thermoplastic composites based on acrylic matrices obtained by free radical polymerization", PhD thesis (Institut National des Sciences Appliquées de Lyon, 2015).
- [52] J. Beguinel, "Interfacial adhesion in continuous fiber reinforced thermoplastic composites: from micro-scale to macro-scale", PhD thesis (Université de Lyon, Lyon, France, 2016).
- [53] G. R. Kinvi-Dossou, "Etude de la résistance à l'impact et de l'endommagement des composites stratifiés à matrice Elium acrylique: caractérisation expérimentale et modélisation numérique multi-échelle", fr, PhD thesis (Université de Lorraine, Metz, France, 2018).
- [54] L. Cadieu, "Effets de chargements thermocinétiques sur le comportement mécanique d'un composite stratifié à résine thermoplastique.", fr, PhD thesis (Université de Bordeaux, Bordeaux, France, 2019).

- [55] W. Kaminsky, "Monomer Recovery by Pyrolysis of Poly(Methyl Methacrylate)", *J Anal Appl Pyrol* **19**, 311–318 (1991).
- [56] W. Kaminsky and C. Eger, "Pyrolysis of Filled PMMA for Monomer Recovery", *J Anal Appl Pyrol* **58**, 781–787 (2001).
- [57] C.-C. M. Ma and C.-H. Chen, "Pultruded fiber reinforced thermoplastic poly(methyl methacrylate) composites. Part I. Correlation of processing parameters for optimizing the process", *en, Polym. Eng. Sci.* **31**, 1086–1093 (1991).
- [58] R. Brouwer, *Composite Applications using Coir Fibres in Sri Lanka - Final Report*, tech. rep. (Delft University of Technology, the Netherlands, 2003).
- [59] J. Beguinel, J.-F. Gérard, F. Lortie, P. Gérard, and J. Maupetit, "New Continuous Fiber Reinforced Thermoplastic Composites: An analysis of Interfacial Adhesion from the micro scale to the macro scale", *en*, (2015).
- [60] Q. Charlier, F. Lortie, P. Gerard, and J.-F. Gerard, "Interfacial adhesion between glass fibers and acrylic-based matrices as studied by micromechanical testing", *en*, in *Proceedings of the 20th International Conference on Composite Materials (July 2015)*.
- [61] T. Lorriot, J. E. Yagoubi, J. Fourel, and F. Tison, "Non-conventional Glass fiber NCF composites with thermoset and thermoplastic matrices.", *en*, (2015).
- [62] A. Zoller, D. Gignes, and Y. Guillaneuf, "Simulation of radical polymerization of methyl methacrylate at room temperature using a tertiary amine/BPO initiating system", *Polym Chem* **6**, 5719–5727 (2015).
- [63] W. Obande, C. M. Ó Brádaigh, and D. Ray, "Continuous fibre-reinforced thermoplastic acrylic-matrix composites prepared by liquid resin infusion – A review", *en, Composites Part B: Engineering* **215**, 108771 (2021).
- [64] A. Zoller, P. Escalé, and P. Gérard, "Pultrusion of Bendable Continuous Fibers Reinforced Composites With Reactive Acrylic Thermoplastic ELIUM® Resin", *Frontiers in Materials* **6** (2019).
- [65] C. Baley, M. Lan, A. Bourmaud, and A. Le Duigou, "Compressive and tensile behaviour of unidirectional composites reinforced by natural fibres: Influence of fibres (flax and jute), matrix and fibre volume fraction", *en, Materials Today Communications* **16**, 300–306 (2018).

- [66] W. Fan, Q. Zhou, J. Sun, and S. Zhang, "Density, Excess Molar Volume, and Viscosity for the Methyl Methacrylate + 1-Butyl-3-methylimidazolium Hexafluorophosphate Ionic Liquid Binary System at Atmospheric Pressure", *J. Chem. Eng. Data* **54**, Publisher: American Chemical Society, 2307–2311 (2009).
- [67] M. Stickler, D. Panke, and W. Wunderlich, "Solution properties of poly(methyl methacrylate) in methyl methacrylate, 1. Viscosities from the dilute to the concentrated solution regime", *en, Makromol. Chem.* **188**, 2651–2664 (1987).
- [68] R. E. Murray, D. Swan, D. Snowberg, D. Berry, R. Beach, and S. Rooney, "Manufacturing a 9-Meter Thermoplastic Composite Wind Turbine Blade", *en, in American Society for Composites 2017* (Nov. 2017).
- [69] R. Matadi Boumbimba, M. Coulibaly, A. Khabouchi, G. Kinvi-Dossou, N. Bonfoh, and P. Gerard, "Glass fibres reinforced acrylic thermoplastic resin-based tri-block copolymers composites: Low velocity impact response at various temperatures", *en, Composite Structures* **160**, 939–951 (2017).
- [70] T. Pini, "Fracture behaviour of thermoplastic acrylic resins and their relevant unidirectional carbon fibre composites: rate and temperature effects", *en, PhD thesis* (Politecnico Milano, Milan, Italy, 2017).
- [71] A. Zoller, "Développement et modélisation cinétique de résines pour des matériaux composites avancés à base de polymères thermoplastiques", *PhD thesis* (Université d'Aix Marseille, 2016).
- [72] O. de Andrade Raponi, B. Righetti de Souza, L. C. Miranda Barbosa, and A. C. Ancelotti Junior, "Thermal, rheological, and dielectric analyses of the polymerization reaction of a liquid thermoplastic resin for infusion manufacturing of composite materials", *en, Polymer Testing* **71**, 32–37 (2018).
- [73] O. d. A. Raponi, L. C. M. Barbosa, B. R. de Souza, and A. C. Ancelotti Junior, "Study of the influence of initiator content in the polymerization reaction of a thermoplastic liquid resin for advanced composite manufacturing", *en, Advances in Polymer Technology* **37**, 3579–3587 (2018).
- [74] D. S. Achilias and I. D. Sideridou, "Kinetics of the Benzoyl Peroxide/Amine Initiated Free-Radical Polymerization of Dental Dimethacrylate Monomers: Experimental Studies and Mathematical Modeling for TEGDMA and Bis-EMA", *en, Macromolecules* **37**, 4254–4265 (2004).

- [75] M. F. Ashby, *Materials selection in mechanical design*, en, 4th ed. (Butterworth-Heinemann, Oxford (England), 2010).
- [76] A. Chilali, W. Zouari, M. Assarar, H. Kebir, and R. Ayad, “Analysis of the mechanical behaviour of flax and glass fabrics-reinforced thermoplastic and thermoset resins”, *J Reinf Plast Comp* **35**, 1217–32 (2016).
- [77] H. F. Li, Q. Q. Duan, P. Zhang, X. H. Zhou, B. Wang, and Z. F. Zhang, “The quantitative relationship between fracture toughness and impact toughness in high-strength steels”, en, *Engineering Fracture Mechanics* **211**, 362–370 (2019).
- [78] P. Davies, P.-Y. Le Gac, and M. Le Gall, “Influence of Sea Water Aging on the Mechanical Behaviour of Acrylic Matrix Composites”, en, *Appl Compos Mater* **24**, 97–111 (2017).
- [79] D. S. Cousins, Y. Suzuki, R. E. Murray, J. R. Samaniuk, and A. P. Stebner, “Recycling glass fiber thermoplastic composites from wind turbine blades”, en, *Journal of Cleaner Production* **209**, 1252–1263 (2019).
- [80] J.-K. Kim and Y.-W. Mai, *Engineered Interfaces in Fiber Reinforced Composites*, 1st edition (Elsevier Science, 1998).
- [81] B. Miller, P. Muri, and L. Rebenfeld, “A microbond method for determination of the shear strength of a fiber/resin interface”, en, *Compos. Sci. Technol.* **28**, 17–32 (1987).
- [82] L. H. Sharpe, “The Interphase in Adhesion”, *The Journal of Adhesion* **4**, 51–64 (1972).
- [83] P. Davies and M. Arhant, “Fatigue Behaviour of Acrylic Matrix Composites: Influence of Seawater”, en, *Appl Compos Mater* **26**, 507–518 (2019).
- [84] W. Obande, D. Mamalis, D. Ray, L. Yang, and C. M. Ó Brádaigh, “Mechanical and thermomechanical characterisation of vacuum-infused thermoplastic- and thermoset-based composites”, en, *Materials & Design* **175**, 107828 (2019).
- [85] W. Obande, D. Ray, and C. M. Ó Brádaigh, “Viscoelastic and drop-weight impact properties of an acrylic-matrix composite and a conventional thermoset composite – A comparative study”, en, *Materials Letters* **238**, 38–41 (2019).
- [86] S. K. Bhudolia, P. Perrotey, and S. C. Joshi, “Experimental investigation on suitability of carbon fibre thin plies for racquets”, en, *Proceedings of the Institution of Mechanical Engineers, Part P: Journal of Sports Engineering and Technology* **230**, 64–72 (2016).

- [87] S. K. Bhudolia and S. C. Joshi, "Low-velocity impact response of carbon fibre composites with novel liquid Methylmethacrylate thermoplastic matrix", en, *Composite Structures* **203**, 696–708 (2018).
- [88] S. K. Bhudolia, P. Perrotey, and S. C. Joshi, "Mode I fracture toughness and fractographic investigation of carbon fibre composites with liquid Methylmethacrylate thermoplastic matrix", en, *Composites Part B: Engineering* **134**, 246–253 (2018).
- [89] S. K. Bhudolia, S. C. Joshi, A. Bert, G. R. Gohel, and M. Raama, "Energy Characteristics and Failure Mechanisms for Textile Spread Tow Thin Ply Thermoplastic Composites under Low-velocity Impact", en, *Fibers Polym* **20**, 1716–1725 (2019).
- [90] S. K. Bhudolia, S. C. Joshi, A. Bert, B. Yi Di, R. Makam, and G. Gohel, "Flexural characteristics of novel carbon methylmethacrylate composites", en, *Composites Communications* **13**, 129–133 (2019).
- [91] L. C. M. Barbosa, D. B. Bortoluzzi, and A. C. Ancelotti, "Analysis of fracture toughness in mode II and fractographic study of composites based on Elium® 150 thermoplastic matrix", en, *Composites Part B: Engineering* **175**, 107082 (2019).
- [92] A. Chilali, W. Zouari, M. Assarar, H. Kebir, and R. Ayad, "Effect of water ageing on the load-unload cyclic behaviour of flax fibre-reinforced thermoplastic and thermosetting composites", en, *Composite Structures* **183**, 309–319 (2018).
- [93] M. Haggui, A. El Mahi, Z. Jendli, A. Akrouf, and M. Haddar, "Damage Analysis of Flax Fibre/Elium Composite Under Static and Fatigue Testing", en, in *Design and Modeling of Mechanical Systems—III*, Lecture Notes in Mechanical Engineering (2018), pp. 681–691.
- [94] M. Haggui, A. El Mahi, Z. Jendli, A. Akrouf, and M. Haddar, "Static and fatigue characterization of flax fiber reinforced thermoplastic composites by acoustic emission", en, *Applied Acoustics, Special Issue on Design and Modelling of Mechanical Systems conference CMSM'2017* **147**, 100–110 (2019).
- [95] S. K. Bhudolia, P. Perrotey, and S. C. Joshi, "Enhanced vibration damping and dynamic mechanical characteristics of composites with novel pseudo-thermoset matrix system", en, *Composite Structures* **179**, 502–513 (2017).
- [96] H. Moulinec and P. Suquet, "A numerical method for computing the overall response of nonlinear composites with complex mi-

- crostructure”, en, *Computer Methods in Applied Mechanics and Engineering* **157**, 69–94 (1998).
- [97] Y. Suzuki, D. S. Cousins, J. Wassgren, B. B. Kappes, J. Dorgan, and A. P. Stebner, “Kinetics and temperature evolution during the bulk polymerization of methyl methacrylate for vacuum-assisted resin transfer molding”, en, *Compos. Part A Appl. Sci. Manuf.* **104**, 60–67 (2018).
- [98] J. Hemmer, “Rapport intermédiaire d’expériences”, fr,
- [99] “Synthesites Innovative Technologies”, en, *Reinforced Plastics* **59**, 180–181 (2015).
- [100] W. Oliver and G. Pharr, “An improved technique for determining hardness and elastic modulus using load and displacement sensing indentation experiments”, en, *J. Mater. Res.* **7**, 1564–1583 (1992).
- [101] A. C. Fischer-Cripps, *Nanoindentation*, en, 3rd edition (Springer Science & Business Media, Aug. 2011).
- [102] X. Morelle, “Mechanical characterization and physicsbased modeling of highly-crosslinked epoxy resin”, PhD thesis (Université catholique de Louvain, Louvain-la-Neuve, Belgium, 2015).
- [103] S. Arrhenius, “On the Reaction Velocity of the Inversion of Cane Sugar by Acids”, *Zeitschrift für Physikalische Chemie* **4**, 226–(1889).
- [104] H. B. Lee and D. T. Turner, “Influence of crosslinking on the tensile strength and fractography of poly(methyl methacrylate)”, en, *Polymer Engineering and Science* **19**, 95–98 (1979).
- [105] F. L. Marten and A. E. Hamielec, “High Conversion Diffusion-Controlled Polymerization”, en, in *Polymerization Reactors and Processes*, ACS Symposium Series, Vol. 104, edited by J. N. Henderson (July 1979), pp. 43–70.
- [106] L. Rebenfeld, G. P. Desio, and J. C. Wu, “Effects of fibers on the glass transition temperature of polyphenylene sulfide composites”, en, *Journal of Applied Polymer Science* **42**, 801–805 (1991).
- [107] N. A. Rahman, A. Hassan, R. Yahya, and R. A. Lafia-Araga, “Impact properties of glass-fiber/polypropylene composites: The influence of fiber loading, specimen geometry and test temperature”, en, *Fibers and Polymers* **14**, 1877–1885 (2013).
- [108] R. L. Gorowara, W. E. Kosik, S. H. McKnight, and R. L. McCullough, “Molecular characterization of glass fiber surface coatings for thermosetting polymer matrix/glass fiber composites”, en, *Composites Part A: Applied Science and Manufacturing* **32**, 323–329 (2001).

- [109] J. D. Eshelby and R. E. Peierls, "The determination of the elastic field of an ellipsoidal inclusion, and related problems", *Proc. R. Soc. Lond. A* **241**, 376–396 (1957).
- [110] B. Klusemann and B. Svendsen, "Homogenization methods for multi-phase elastic composites: Comparisons and benchmarks", *Technische Mechanik* **30**, 374–386 (2010).
- [111] F. Becker and C. Hopmann, "Stiffness Estimates for Composites with Elliptic Cylindrical Voids", en, *Materials* **13**, Number: 6 Publisher: Multidisciplinary Digital Publishing Institute, 1354 (2020).
- [112] T. Mori and K. Tanaka, "Average stress in matrix and average elastic energy of materials with misfitting inclusions", en, *Acta Metallurgica* **21**, 571–574 (1973).
- [113] J. R. Martin, J. F. Johnson, and A. R. Cooper, "Mechanical Properties of Polymers: The Influence of Molecular Weight and Molecular Weight Distribution", en, *Journal of Macromolecular Science, Part C* **8**, 57–199 (1972).
- [114] J. J. Murray, C. Robert, K. Gleich, E. D. McCarthy, and C. M. Ó Brádaigh, "Manufacturing of unidirectional stitched glass fabric reinforced polyamide 6 by thermoplastic resin transfer moulding", en, *Materials & Design* **189**, 108512 (2020).
- [115] D. Mamalis, W. Obande, V. Koutsos, J. R. Blackford, C. M. Ó Brádaigh, and D. Ray, "Novel thermoplastic fibre-metal laminates manufactured by vacuum resin infusion: The effect of surface treatments on interfacial bonding", en, *Materials & Design* **162**, 331–344 (2019).
- [116] S. K. Bhudolia, P. Perrotey, and S. C. Joshi, "Optimizing Polymer Infusion Process for Thin Ply Textile Composites with Novel Matrix System", en, *Materials* **10**, Number: 3 Publisher: Multidisciplinary Digital Publishing Institute, 293 (2017).
- [117] M. E. Kazemi, L. Shanmugam, D. Lu, X. Wang, B. Wang, and J. Yang, "Mechanical properties and failure modes of hybrid fiber reinforced polymer composites with a novel liquid thermoplastic resin, Elium®", en, *Composites Part A: Applied Science and Manufacturing* **125**, 105523 (2019).
- [118] N. Judd and W. Wright, "Voids and their effects on the mechanical properties of composites - an appraisal", *SAMPE Journal* **14**, 10–15 (1978).

- [119] L. Maragoni, P. A. Carraro, M. Peron, and M. Quaresimin, “Fatigue behaviour of glass/epoxy laminates in the presence of voids”, en, *Int J Fatigue* **95**, 18–28 (2017).
- [120] T. Hayashi and J. Takahashi, “Influence of void content on the flexural fracture behaviour of carbon fiber reinforced polypropylene:” en, *J Compos Mater* **51**, 4067–4078 (2017).
- [121] F. Van Loock, M. Thouless, and N. Fleck, “Tensile fracture of an adhesive joint: the role of crack length and of material mismatch”, *J Mech Phys Solids* **130**, 330–348 (2019).
- [122] M. Mehdikhani, N. A. Petrov, I. Straumit, A. R. Melro, S. V. Lomov, and L. Gorbatikh, “The effect of voids on matrix cracking in composite laminates as revealed by combined computations at the micro- and meso-scales”, en, *Compos. Part A Appl. Sci. Manuf.* **117**, 180–192 (2019).
- [123] J. Kardos, R. Dave, and N. Dudukovic, “Voids in composites”, in *The manufacturing Science of Composites, Proceedings of Manufacturing International '88, Vol. 4* (1988), pp. 41–48.
- [124] T. Lundstrom, B. Gebart, and C. Lundemo, “Void Formation in RTM”, *J Reinf Plast Comp* **12**, 1339–1349 (1993).
- [125] N. Patel, V. Rohatgi, and L. J. Lee, “Micro scale flow behavior and void formation mechanism during impregnation through a unidirectional stitched fiberglass mat”, en, *Polym Eng Sci* **35**, 837–851 (1995).
- [126] M. Afendi, W. Banks, and D. Kirkwood, “Bubble free resin for infusion process”, *Compos. Part A Appl. Sci. Manuf.* **36**, 739–746 (2005).
- [127] M. Mehdikhani, L. Gorbatikh, I. Verpoest, and S. V. Lomov, “Voids in fiber-reinforced polymer composites: A review on their formation, characteristics, and effects on mechanical performance”, en, *J. Compos. Mater.* **53**, 1579–1669 (2019).
- [128] N. Patel and L. J. Lee, “Modeling of void formation and removal in liquid composite molding. Part I: Wettability analysis”, en, *Polym Compos* **17**, 96–103 (1996).
- [129] L. Labat, J. Bréard, S. Pillut-Lesavre, and G. Bouquet, “Void fraction prevision in LCM parts”, en, *Eur Phys J Appl Phys* **16**, 157–164 (2001).
- [130] J. Bréard, Y. Henzel, F. Trochu, and R. Gauvin, “Analysis of dynamic flows through porous media. Part I: Comparison between saturated and unsaturated flows in fibrous reinforcements: Analysis of Dynamic Flows. I”, en, *Polym Compos* **24**, 391–408 (2003).

- [131] A. Hamielec, "Recent developments in free-radical polymerization at high conversion - Diffusion-controlled termination and propagation", en, *Chem Eng Commun* **24**, 1–19 (1983).
- [132] S. Zhu and A. E. Hamielec, "Chain-length-dependent termination for free radical polymerization", en, *Macromolecules* **22**, 3093–3098 (1989).
- [133] D. Achilias and C. Kiparissides, "Modeling of diffusion-controlled free-radical polymerization reactions", en, *J. Appl. Polym. Sci.* **35**, 1303–1323 (1988).
- [134] D. S. Achilias and C. Kiparissides, "Development of a general mathematical framework for modeling diffusion-controlled free-radical polymerization reactions", en, *Macromolecules* **25**, 3739–3750 (1992).
- [135] A. W. Hui and A. E. Hamielec, "Thermal polymerization of styrene at high conversions and temperatures. An experimental study", en, *J. Appl. Polym. Sci.* **16**, 749–769 (1972).
- [136] N. Tefera, G. Weickert, and K. R. Westerterp, "Modeling of free radical polymerization up to high conversion. I. A method for the selection of models by simultaneous parameter estimation", en, *J. Appl. Polym. Sci.* **63**, 1649–1661 (1997).
- [137] J. S. Sangwai, S. A. Bhat, S. Gupta, D. N. Saraf, and S. K. Gupta, "Bulk free radical polymerizations of methyl methacrylate under non-isothermal conditions and with intermediate addition of initiator: Experiments and modeling", en, *Polymer* **46**, 11451–11462 (2005).
- [138] A. C. Loos and G. S. Springer, "Curing of Epoxy Matrix Composites", en, *J. Compos. Mater.* **17**, 135–169 (1983).
- [139] T. A. Bogetti and J. W. Gillespie, "Two-Dimensional Cure Simulation of Thick Thermosetting Composites", en, *J. Compos. Mater.* **25**, 239–273 (1991).
- [140] T. Twardowski, S. Lin, and P. Geil, "Curing in Thick Composite Laminates: Experiment and Simulation", *J. Compos. Mater.* **27**, 216–250 (1993).
- [141] M. K. Telikicherla, M. C. Altan, and F. C. Lai, "Autoclave curing of thermosetting composites: process modeling for the cure assembly", en, *Int Commun Heat Mass* **21**, 13 (1994).
- [142] D. Blest, B. Duffy, S. McKee, and A. Zulkifley, "Curing simulation of thermoset composites", en, *Compos. Part A Appl. Sci. Manuf.* **30**, 1289–1309 (1999).

- [143] E. Ruiz and F. Trochu, "Numerical analysis of cure temperature and internal stresses in thin and thick RTM parts", en, *Compos. Part A Appl. Sci. Manuf.* **36**, 806–826 (2005).
- [144] S. Anandan, G. S. Dhaliwal, Z. Huo, K. Chandrashekhara, N. Apretre, and N. Iyyer, "Curing of Thick Thermoset Composite Laminates: Multiphysics Modeling and Experiments", en, *Appl Compos Mater* **25**, 1155–1168 (2018).
- [145] M. Ren, Q. Wang, J. Cong, and X. Chang, "Study of one-dimensional cure simulation applicable conditions for thick laminates and its comparison with three-dimensional simulation", en, *Sci Eng Compos Mater* **25**, 1197–1204 (2018).
- [146] A. Borzacchiello, L. Ambrosio, L. Nicolais, E. J. Harper, K. E. Tanner, and W. Bonfield, "Isothermal and non-isothermal polymerization of a new bone cement", en, *J. Mater. Sci. Mater. Med* **9**, 317–324 (1998).
- [147] C. A. Schneider, W. S. Rasband, and K. W. Eliceiri, "NIH Image to ImageJ: 25 years of image analysis", en, *Nat Methods* **9**, 671–675 (2012).
- [148] N. A. Dotson, R. Galvan, R. L. Laurence, and M. Tirrell, *Polymerization process modeling* (VCH Publishers, Inc., New York, NY (USA), 1996).
- [149] H. Fujita, "Diffusion in polymer-diluent systems", en, *Fortschr. Hochpolym. Forsch.* **3**, 1–47 (1961).
- [150] J. S. Vrentas and J. L. Duda, "Diffusion in polymer–solvent systems. II. A predictive theory for the dependence of diffusion coefficients on temperature, concentration, and molecular weight", en, *J Polym Sci Pol Phys* **15**, 417–439 (1977).
- [151] R. Greiner and F. R. Schwarzl, "Thermal contraction and volume relaxation of amorphous polymers", en, *Rheol Acta* **23**, 378–395 (1984).
- [152] J. E. Mark, ed., *Physical properties of polymers handbook*, en, 2nd ed. (Springer, New York, NY (USA), 2006).
- [153] M. Karabaev, A. Saidov, T. Abduzhaminov, and M. Kenisarin, "Heat capacity and molecular kinetic processes of condensed phase acrylates and methacrylates", *Izv. Akad. Nauk UzSSR, Ser. Fiz.-Mat. Nauk* **6**, 51–54 (1985).
- [154] J. Brandrup, E. H. Immergut, and E. A. Grulke, eds., *Polymer handbook*, en, 4th ed. (Wiley, New York, NY (USA), 1999).

- [155] M. Baucchio, *ASM Engineered Materials Reference Book*, 2nd ed. (Ed. ASM International, Materials Park, OH (USA), 1994).
- [156] J. N. Cardenas and K. F. O'Driscoll, "High-conversion polymerization. I. Theory and application to methyl methacrylate", en, *J Polym Sci Pol Chem* **14**, 883–897 (1976).
- [157] G. T. Russell, D. H. Napper, and R. G. Gilbert, "Termination in free-radical polymerizing systems at high conversion", en, *Macromolecules* **21**, 2133–2140 (1988).
- [158] W. M. Haynes, *CRC Handbook of Chemistry and Physics*, en, 97th ed. (CRC Press, Taylor & Francis Group, Boca Raton, FL (USA), 2017).
- [159] S. Beuermann, M. Buback, T. Davis, R. Gilbert, R. Hutchinson, O. Olaj, G. Russell, J. Schweer, and A. van Herk, "Critically evaluated rate coefficients for free-radical polymerization, 2.†. Propagation rate coefficients for methyl methacrylate", *Macromol. Chem. Phys.* **198**, 1545–1560 (1997).
- [160] D. R. Taylor, K. Y. v. Berkel, M. M. Alghamdi, and G. T. Russell, "Termination Rate Coefficients for Radical Homopolymerization of Methyl Methacrylate and Styrene at Low Conversion", en, *Macromol. Chem. Phys.* **211**, 563–579 (2010).
- [161] S. S. Meadows, M. V. Hosur, A. Tcherbi-Narteh, and S. Jeelani, "Kinetic analysis of different peroxide initiators on the cure behavior of bio-based and recycled unsaturated polyester Envirez resins", en, in *CAMX Conference Proceedings* (Oct. 2015), p. 14.
- [162] J. H. Lienhard and J. H. Lienhard, *A Heat Transfer Textbook*, 5th ed. (Phlogiston Press, Cambridge, MA (USA), 2019).
- [163] E. T. Denisov, T. G. Denisova, and T. S. Pokidova, *Handbook of free radical initiators*, en, 1st ed. (Wiley-Interscience, Hoboken, NJ (USA), 2003).
- [164] D. L. Kurdikar and N. A. Peppas, "A Kinetic Model for Diffusion-Controlled Bulk Crosslinking Photopolymerizations", en, *Macromolecules* **27**, 4084–4092 (1994).
- [165] B. W. Grimsley, P. Hubert, X. Song, R. J. Cano, A. C. Loos, and R. B. Pipes, "Flow and Compaction During the Vacuum Assisted Resin Transfer Molding Process", en, in *Proceedings of 33rd ISTC* (2001), pp. 1–14.
- [166] M. Moghaddam, A. Breede, C. Brauner, and W. Lang, "Embedding Piezoresistive Pressure Sensors to Obtain Online Pressure Profiles Inside Fiber Composite Laminates", en, *Sensors* **15**, 7499–7511 (2015).

- [167] P. Hayden and H. Melville, "The kinetics of the polymerization of methyl methacrylate. I. The bulk reaction", en, *J Polym Sci* **43**, 201–214 (1960).
- [168] S. Zhu, Y. Tian, A. Hamielec, and D. Eaton, "Radical concentrations in free radical copolymerization of MMA/EGDMA", en, *Polymer* **31**, 154–159 (1990).
- [169] A. G. Gibson and J. A. Manson, "Impregnation technology for thermoplastic matrix composites", en, *Composites Manufacturing* **3**, 223–233 (1992).
- [170] P. Brøndsted, H. Lilholt, and A. Lystrup, "Composite materials for wind power turbine blades", en, *Annu. Rev. Mater. Res.* **35**, 505–538 (2005).
- [171] J. D. Ferry, *Viscoelastic properties of polymers*, 3rd ed. (John Wiley & sons, New York, NY (USA), 1980).
- [172] M. Rubinstein and R. H. Colby, *Polymer Physics* (Oxford University Press, Oxford (England), 2003).
- [173] R. Helmus, J. Kratz, K. Potter, P. Hubert, and R. Hinterhölzl, "An experimental technique to characterize interply void formation in unidirectional prepregs", en, *Journal of Composite Materials* **51**, 579–591 (2017).
- [174] W. Hu, L. K. Grunenfelder, T. Centea, and S. Nutt, "*In situ* monitoring and analysis of void evolution in unidirectional prepreg", en, *Journal of Composite Materials* **52**, 2847–2858 (2018).
- [175] A. Hautefeuille, S. Comas-Cardona, and C. Binetruy, "Mechanical signature and full-field measurement of flow-induced large in-plane deformation of fibrous reinforcements in composite processing", en, *Composites Part A: Applied Science and Manufacturing* **118**, 213–222 (2019).
- [176] L. Salvo, M. Suéry, A. Marmottant, N. Limodin, and D. Bernard, "3D imaging in material science: Application of X-ray tomography", en, *Comptes Rendus Physique* **11**, 641–649 (2010).
- [177] S. Garcea, Y. Wang, and P. Withers, "X-ray computed tomography of polymer composites", en, *Composites Science and Technology* **156**, 305–319 (2018).
- [178] T. Centea and P. Hubert, "Measuring the impregnation of an out-of-autoclave prepreg by micro-CT", en, *Composites Science and Technology* **71**, 593–599 (2011).
- [179] T. Centea, G. Peters, K. Hendrie, and S. Nutt, "Effects of thermal gradients on defect formation during the consolidation of partially

- impregnated prepregs”, en, *Journal of Composite Materials* **51**, 3987–4003 (2017).
- [180] J. Torres, M. Simmons, F. Sket, and C. González, “An analysis of void formation mechanisms in out-of-autoclave prepregs by means of X-ray computed tomography”, en, *Composites Part A: Applied Science and Manufacturing* **117**, 230–242 (2019).
- [181] J. Dewanckele, M. Boone, F. Coppens, D. Van Loo, and A. Merkle, “Innovations in laboratory-based dynamic micro-CT to accelerate *in situ* research”, en, *Journal of Microscopy* **277**, 197–209 (2020).
- [182] J. Kratz, P. Galvez-Hernandez, L. R. Pickard, J. Belnoue, and K. Potter, “Lab-based in-situ micro-CT observation of gaps in prepreg laminates during consolidation and cure”, en, *Composites Part A: Applied Science and Manufacturing* **140**, 106180 (2021).
- [183] T.-H. Le, P. Dumont, L. Orgéas, D. Favier, L. Salvo, and E. Boller, “X-ray phase contrast microtomography for the analysis of the fibrous microstructure of SMC composites”, en, *Composites Part A: Applied Science and Manufacturing* **39**, 91–103 (2008).
- [184] J. Vilà, F. Sket, F. Wilde, G. Requena, C. González, and J. LLorca, “An in situ investigation of microscopic infusion and void transport during vacuum-assisted infiltration by means of X-ray computed tomography”, en, *Composites Science and Technology* **119**, 12–19 (2015).
- [185] D. Ferré Sentis, L. Orgéas, P. Dumont, S. Rolland du Roscoat, M. Sager, and P. Latil, “3D in situ observations of the compressibility and pore transport in Sheet Moulding Compounds during the early stages of compression moulding”, en, *Composites Part A: Applied Science and Manufacturing* **92**, 51–61 (2017).
- [186] N. M. Larson and F. W. Zok, “Insights from in-situ X-ray computed tomography during axial impregnation of unidirectional fiber beds”, en, *Composites Part A: Applied Science and Manufacturing* **107**, 124–134 (2018).
- [187] B. de Parscau du Plessix, P. Lefébure, N. Boyard, S. L. Corre, N. Lefèvre, F. Jacquemin, V. Sobotka, and S. Rolland du Roscoat, “In situ real-time 3D observation of porosity growth during composite part curing by ultra-fast synchrotron X-ray microtomography”, en, *Journal of Composite Materials* **53**, 4105–4116 (2019).
- [188] Y. Lakroune, L. Orgéas, P. Dumont, F. Martoia, S. R. D. Roscoat, F. Jacquemin, P. Casari, and O. Guiraud, “Analyse 3D en temps réel et in situ des mécanismes de (dé)consolidation dans les composites

- thermoplastiques renforcés lors de leur thermo-estampage”, fr, in (2019), p. 7.
- [189] N. M. Larson, C. Cuellar, and F. W. Zok, “X-ray computed tomography of microstructure evolution during matrix impregnation and curing in unidirectional fiber beds”, en, *Composites Part A: Applied Science and Manufacturing* **117**, 243–259 (2019).
- [190] J. Hemmer, A. S. Dharmalingam, A.-S. Lectez, C. Burtin, S. Comas-Cardona, C. Binetruy, and T. Savart, “Compaction behaviour of tow at meso-scale: experimental investigations of morphological evolution at dry, lubricated and saturated states”, en, *IOP Conf. Ser.: Mater. Sci. Eng.* **406**, 012020 (2018).
- [191] J. Hemmer, C. Burtin, S. Comas-Cardona, C. Binetruy, T. Savart, and A. Babeau, “Unloading during the infusion process: Direct measurement of the dual-scale fibrous microstructure evolution with X-ray computed tomography”, en, *Composites Part A: Applied Science and Manufacturing* **115**, 147–156 (2018).
- [192] B. Palmieri, A. Petriccione, G. De Tommaso, M. Giordano, and A. Martone, “An Efficient Thermal Cure Profile for Thick Parts Made by Reactive Processing of Acrylic Thermoplastic Composites”, en, *J. Compos. Sci.* **5**, 229 (2021).
- [193] K. Yamada, H. Emori, and K. Nakazawa, “Time-evolution of bubble formation in a viscous liquid”, en, *Earth Planet Sp* **60**, 661–679 (2008).
- [194] E. Maire and P. J. Withers, “Quantitative X-ray tomography”, *International Materials Reviews* **59**, 1–43 (2014).
- [195] J. LLorca, C. González, J. M. Molina-Aldareguía, and C. S. López, “Multiscale Modeling of Composites: Toward Virtual Testing ... and Beyond”, en, *JOM* **65**, 215–225 (2013).
- [196] A. Melro, P. Camanho, F. Andrade Pires, and S. Pinho, “Micromechanical analysis of polymer composites reinforced by unidirectional fibres: Part I – Constitutive modelling”, en, *Int. J. Solids Struct.* **50**, 1897–1905 (2013).
- [197] J. Chevalier, P. Camanho, F. Lani, and T. Pardoën, “Multi-scale characterization and modelling of the transverse compression response of unidirectional carbon fiber reinforced epoxy”, en, *Compos. Struct.* **209**, 160–176 (2019).
- [198] T. Pardoën, N. Klavzer, S. Gayot, F. Van Loock, J. Chevalier, X. Morelle, V. Destoof, F. Lani, P. Camanho, L. Brassart, B. Nysten,

- and C. Bailly, "Nanomechanics serving polymer-based composite research", en, *Comptes Rendus. Physique* **22**, 331–352 (2021).
- [199] M. Hardiman, T. Vaughan, and C. McCarthy, "A review of key developments and pertinent issues in nanoindentation testing of fibre reinforced plastic microstructures", *Compos. Struct.* **180**, 782–798 (2017).
- [200] C.-S. Han, "Influence of the molecular structure on indentation size effect in polymers", en, *Mater. Sci. Eng. A* **527**, 619–624 (2010).
- [201] G. Z. Voyiadjis and A. Samadi-Dooki, "Constitutive modeling of large inelastic deformation of amorphous polymers: Free volume and shear transformation zone dynamics", en, *J. Appl. Phys.* **119**, 225104 (2016).
- [202] F. Naya, C. González, C. Lopes, and J. Llorca, "Combined multi-scale simulations in fiber-reinforced composites", in *Proceedings of the 20th International Conference on Composite Materials* (July 2015).
- [203] P. Nikaen, A. Samadi-Dooki, G. Voyiadjis, P. Zhang, W. Chirdon, and A. Khattab, "Effect of plastic deformation on the nanomechanical properties of glassy polymers: An experimental study", *English, Mechanics of Materials* **159**, 103900 (2021).
- [204] W. Tan, F. Naya, L. Yang, T. Chang, B. Falzon, L. Zhan, J. Molina-Aldareguía, C. González, and J. Llorca, "The role of interfacial properties on the intralaminar and interlaminar damage behaviour of unidirectional composite laminates: Experimental characterization and multiscale modelling", en, *Comp. Part B Eng.* **138**, 206–221 (2018).
- [205] F. Alisafaei and C.-S. Han, "Indentation Depth Dependent Mechanical Behavior in Polymers", en, *Adv. Condens. Matter. Phys.*, 1–20 (2015).
- [206] M. Rodríguez, J. Molina-Aldareguía, C. González, and J. Llorca, "Determination of the mechanical properties of amorphous materials through instrumented nanoindentation", en, *Acta Mater.* **60**, 3953–3964 (2012).
- [207] T. A. Bogetti, T. Wang, M. VanLandingham, and J. W. Gillespie, "Characterization of nanoscale property variations in polymer composite systems: 2. Numerical modeling", *Compos. Part A Appl. Sci. Manuf.* **30A**, 85–94 (1999).
- [208] M. Munz, H. Sturm, E. Schulz, and G. Hinrichsen, "The scanning force microscope as a tool for the detection of local mechanical

- properties within the interphase of fibre reinforced polymers”, en, *Compos. Part A Appl. Sci. Manuf.* **29**, 1251–1259 (1998).
- [209] R. M. Winter and J. E. Houston, “Interphase mechanical properties in an epoxy-glass fiber composite as measured by interfacial microscopy”, in *Proceedings of the SEM Spring Conference on Experimental and Applied Mechanics and Experimental/Numerical Mechanics in Electronic Packaging III* (1998), pp. 355–358.
- [210] T. D. Downing, R. Kumar, W. M. Cross, L. Kjerengtroen, and J. J. Kellar, “Determining the interphase thickness and properties in polymer matrix composites using phase imaging atomic force microscopy and nanoindentation”, en, *J. Adhes. Sci. Technol.* **14**, 1801–1812 (2000).
- [211] L. Canal, C. González, J. Molina-Aldareguía, J. Segurado, and J. LLorca, “Application of digital image correlation at the microscale in fiber-reinforced composites”, en, *Compos. Part A Appl. Sci. Manuf.* **43**, 1630–1638 (2012).
- [212] M. Mehdikhani, M. Aravand, B. Sabuncuoglu, M. G. Callens, S. V. Lomov, and L. Gorbatikh, “Full-field strain measurements at the micro-scale in fiber-reinforced composites using digital image correlation”, en, *Compos. Struct.* **140**, 192–201 (2016).
- [213] M. Bornert, F. Brémand, P. Doumalin, J.-C. Dupré, M. Fazzini, M. Grédiac, F. Hild, S. Mistou, J. Molimard, J.-J. Orteu, L. Robert, Y. Surrel, P. Vacher, and B. Wattrisse, “Assessment of Digital Image Correlation Measurement Errors: Methodology and Results”, en, *Exp. Mech.* **49**, 353–370 (2009).
- [214] F. Lagattu, F. Bridier, P. Villechaise, and J. Brillaud, “In-plane strain measurements on a microscopic scale by coupling digital image correlation and an in situ SEM technique”, en, *Mater. Charact.* **56**, 10–18 (2006).
- [215] E. Totry, C. González, J. LLorca, and J. M. Molina-Aldareguía, “Mechanisms of shear deformation in fiber-reinforced polymers: experiments and simulations”, en, *Int. J. Fract.* **158**, 197–209 (2009).
- [216] G. Catalanotti, P. Camanho, J. Xavier, C. Dávila, and A. Marques, “Measurement of resistance curves in the longitudinal failure of composites using digital image correlation”, *Compos. Sci. Technol.* **70**, 1986–1993 (2010).
- [217] S. V. Lomov, D. S. Ivanov, I. Verpoest, M. Zako, T. Kurashiki, H. Nakai, J. Molimard, and A. Vautrin, “Full-field strain measurements

- for validation of meso-FE analysis of textile composites”, en, *Compos. Part A Appl. Sci. Manuf.* **39**, 1218–1231 (2008).
- [218] M. Mehdikhani, A. Matveeva, M. A. Aravand, B. L. Wardle, S. V. Lomov, and L. Gorbatikh, “Strain mapping at the micro-scale in hierarchical polymer composites with aligned carbon nanotube grafted fibers”, en, *Compos. Sci. Technol.* **137**, 24–34 (2016).
- [219] J. L. W. Carter, M. D. Uchic, and M. J. Mills, “Impact of Speckle Pattern Parameters on DIC Strain Resolution Calculated from In-situ SEM Experiments”, en, in *Fracture, Fatigue, Failure, and Damage Evolution, Volume 5*, edited by J. Carroll and S. Daly (Springer International Publishing, Cham, Switzerland, 2015), pp. 119–126.
- [220] C. Montgomery, B. Koohbor, and N. Sottos, “A robust patterning technique for electron microscopy-based digital image correlation at sub-micron resolutions”, en, *Exp. Mech.* **59**, 1063–1073 (2019).
- [221] J. Hoefnagels, M. van Maris, and T. Vermeij, “One-step deposition of nano-to-micron-scalable, high-quality digital image correlation patterns for high-strain *in-situ* multi-microscopy testing”, en, *Strain* **55**, 12330 (2019).
- [222] Y. Jung, D. Lee, and D. Jeon, “Influence of dc magnetron sputtering parameters on surface morphology of indium tin oxide thin films”, English, *Applied Surface Science* **221**, 136–142 (2004).
- [223] M. A. Sutton, N. Li, D. Garcia, N. Cornille, J. J. Orteu, S. R. McNeill, H. W. Schreier, X. Li, and A. P. Reynolds, “Scanning Electron Microscopy for Quantitative Small and Large Deformation Measurements Part II: Experimental Validation for Magnifications from 200 to 10,000”, en, *Exp. Mech.* **47**, 789–804 (2007).
- [224] M. A. Sutton, N. Li, D. C. Joy, A. P. Reynolds, and X. Li, “Scanning electron microscopy for quantitative small and large deformation measurements part I: SEM imaging at magnifications from 200 to 10,000”, en, *Exp. Mech.* **47**, 775–787 (2007).
- [225] S. Maraghechi, J. P. M. Hoefnagels, R. H. J. Peerlings, and M. G. D. Geers, “Correction of scan line shift artifacts in scanning electron microscopy: An extended digital image correlation framework”, en, *Ultramicroscopy* **187**, 144–163 (2018).
- [226] S. Maraghechi, J. P. M. Hoefnagels, R. H. J. Peerlings, O. Rokoš, and M. G. D. Geers, “Correction of Scanning Electron Microscope Imaging Artifacts in a Novel Digital Image Correlation Framework”, en, *Exp Mech* **59**, 489–516 (2019).

- [227] A. Mello, T. Book, A. Nicolas, S. Otto, C. Gilpin, and M. Sangid, “Distortion Correction Protocol for Digital Image Correlation after Scanning Electron Microscopy: Emphasis on Long Duration and Ex-Situ Experiments”, English, *Experimental Mechanics* **57**, 1395–1409 (2017).
- [228] A. D. Kammers and S. Daly, “Digital image correlation under scanning electron microscopy: methodology and validation”, en, *Exp. Mech.* **53**, 1743–1761 (2013).
- [229] R. Street and S. Clara, *Thin Film Evaporation Guide*, en, 2017.
- [230] *Evaporation Materials*, https://heegermaterials.com/34_evaporation-materials.
- [231] T. N. I. for Occupational Safety and Health (NIOSH), *NIOSH Pocket Guide to Chemical Hazards*, English.
- [232] J. Blaber, B. Adair, and A. Antoniou, “Ncorr: Open-Source 2D Digital Image Correlation Matlab Software”, en, *Exp Mech* **55**, 1105–1122 (2015).
- [233] X. P. Morelle, J. Chevalier, C. Bailly, T. Pardoën, and F. Lani, “Mechanical characterization and modeling of the deformation and failure of the highly crosslinked RTM6 epoxy resin”, en, *Mech. Time-Depend. Mater.* **21**, 419–454 (2017).
- [234] M. Maes, “Mechanical properties of high performance recyclable thermoplastic based composites for windmill applications”, MA thesis (UCLouvain, Louvain-la-Neuve, Belgium, 2020).
- [235] M. R. Vanlandingham, S. H. McKnight, G. R. Palmese, T. A. Bogetti, R. F. Eduljee, and J. W. Gillespie, “Characterization of Interphase Regions Using Atomic Force Microscopy”, en, *MRS Proc.* **458**, 313 (1996).
- [236] A. C. M. Chong and D. C. C. Lam, “Strain gradient plasticity effect in indentation hardness of polymers”, en, *J. Mater. Res.* **14**, 4103–4110 (1999).
- [237] G. Chandrashekar and C.-S. Han, “Length scale effects in epoxy: The dependence of elastic moduli measurements on spherical indenter tip radius”, en, *Polym. Test.* **53**, 227–233 (2016).
- [238] F. Alisafaei, C.-S. Han, and N. Lakhera, “Characterization of indentation size effects in epoxy”, en, *Polym. Test.* **40**, 70–78 (2014).
- [239] M. Jebahi and S. Forest, “Scalar-based strain gradient plasticity theory to model size-dependent kinematic hardening effects”, English, *Continuum Mechanics and Thermodynamics* **33**, 1223–1245 (2021).

- [240] J. LLorca, C. González, J. M. Molina-Aldareguía, J. Segurado, R. Seltzer, F. Sket, M. Rodríguez, S. Sádaba, R. Muñoz, and L. P. Canal, “Multiscale Modeling of Composite Materials: a Roadmap Towards Virtual Testing”, en, *Adv. Mater.* **23**, 5130–5147 (2011).
- [241] M. VanLandingham, R. Dagastine, R. Eduljee, R. McCullough, and J. Gillespie, “Characterization of nanoscale property variations in polymer composite systems: 1. Experimental results”, en, *Compos. Part A Appl. Sci. Manuf.* **30**, 75–83 (1999).
- [242] S. A. Syed Asif, K. J. Wahl, R. J. Colton, and O. L. Warren, “Quantitative imaging of nanoscale mechanical properties using hybrid nanoindentation and force modulation”, en, *J. Appl. Phys.* **90**, 1192–1200 (2001).
- [243] S.-L. Gao and E. Mader, “Characterisation of interphase nanoscale property variations in glass fibre reinforced polypropylene and epoxy resin composites”, en, *Compos. Part A Appl. Sci. Manuf.* **33**, 559–576 (2002).
- [244] J. He and Y. Huang, “AFM Characterization of Interphase Properties of Silver-Coated Carbon Fibre Reinforced Epoxy Composites”, en, *Polymers and Polymer Composites* **14**, 123–134 (2006).
- [245] Y. Wang and T. H. Hahn, “AFM characterization of the interfacial properties of carbon fiber reinforced polymer composites subjected to hygrothermal treatments”, en, *Compos. Sci. Technol.* **67**, 92–101 (2007).
- [246] S. Q. Wang, S. D. Nair, D. Hurley, and S. H. Lee, “Characterizing Interphase Properties in Fiber Reinforced Polymer Composite with Advanced AFM Based Tools”, en, *Adv Mat Res* **123-125**, 403–406 (2010).
- [247] M. Qu, F. Deng, S. M. Kalkhoran, A. Gouldstone, A. Robisson, and K. J. Van Vliet, “Nanoscale visualization and multiscale mechanical implications of bound rubber interphases in rubber–carbon black nanocomposites”, en, *Soft Matter* **7**, 1066–1077 (2011).
- [248] V. Cech, E. Palesch, and J. Lukes, “The glass fiber–polymer matrix interface/interphase characterized by nanoscale imaging techniques”, en, *Compos. Sci. Technol.* **83**, 22–26 (2013).
- [249] X. Cheng, K. W. Putz, C. D. Wood, and L. C. Brinson, “Characterization of Local Elastic Modulus in Confined Polymer Films via AFM Indentation”, en, *Macromol. Rapid Commun.* **36**, 391–397 (2015).
- [250] P. F. Brune, G. S. Blackman, T. Diehl, J. S. Meth, D. Brill, Y. Tao, and J. Thornton, “Direct Measurement of Rubber Interphase Stiffness”,

- Macromolecules **49**, Publisher: American Chemical Society, 4909–4922 (2016).
- [251] M. Zhang, Y. Li, P. V. Kolluru, and L. C. Brinson, “Determination of mechanical properties of polymer interphase using combined atomic force microscope (AFM) experiments and finite element simulations”, en, *Macromolecules* **51**, 8229–8240 (2018).
- [252] L. K. Babu, “The use of AFM indentation to quantify mechanical properties of the interphase region in fiber-reinforced composites”, en, PhD thesis (Oklahoma State University, Oklahoma City, OK, USA, July 2019).
- [253] A. Hodzic, Z. Stachurski, and J. Kim, “Nano-indentation of polymer–glass interfaces Part I. Experimental and mechanical analysis”, en, *Polymer* **41**, 6895–6905 (2000).
- [254] J.-K. Kim, M.-L. Sham, and J. Wu, “Nanoscale characterisation of interphase in silane treated glass fibre composites”, en, *Compos. Part A Appl. Sci. Manuf.* **32**, 12 (2001).
- [255] Q. Wu, M. Li, Y. Gu, Y. Li, and Z. Zhang, “Nano-analysis on the structure and chemical composition of the interphase region in carbon fiber composite”, en, *Composites Part A: Applied Science and Manufacturing* **56**, 143–149 (2014).
- [256] Q. Wu, M. Li, Y. Gu, S. Wang, and Z. Zhang, “Imaging the interphase of carbon fiber composites using transmission electron microscopy: Preparations by focused ion beam, ion beam etching, and ultramicrotomy”, en, *Chinese Journal of Aeronautics* **28**, 1529–1538 (2015).
- [257] Y. Gu, M. Li, J. Wang, and Z. Zhang, “Characterization of the interphase in carbon fiber/polymer composites using a nanoscale dynamic mechanical imaging technique”, en, *Carbon* **48**, 3229–3235 (2010).
- [258] J. Gregory and S. Spearing, “Nanoindentation of neat and polymers in polymer-matrix composites”, en, *Compos. Sci. Technol.* **65**, 595–607 (2005).
- [259] M. Hardiman, T. Vaughan, and C. McCarthy, “Fibrous composite matrix characterisation using nanoindentation: The effect of fibre constraint and the evolution from bulk to in-situ matrix properties”, en, *Compos. Part A Appl. Sci. Manuf.* **68**, 296–303 (2015).
- [260] M. Pecora, O. Smerdova, and M. Gigliotti, “In-situ characterization of the local mechanical behaviour of polymer matrix in 3D carbon

- fiber composites by cyclic indentation test”, en, *Composite Structures* **244**, 112268 (2020).
- [261] T. Gates, “The physical and chemical ageing of polymeric composites”, en, in *Ageing of composites*, 1st edition, Composites Science and Engineering (Woodhead Publishing, 2008).
- [262] S. B. Yedla, M. Kalukanimuttam, R. M. Winter, and S. K. Khanna, “Effect of Shape of the Tip in Determining Interphase Properties in Fiber Reinforced Plastic Composites Using Nanoindentation”, *Journal of Engineering Materials and Technology* **130**, 1–15 (2008).
- [263] M. Hardiman, T. Vaughan, and C. McCarthy, “The effect of fibre constraint in the nanoindentation of fibrous composite microstructures: A finite element investigation”, en, *Comput. Mater. Sci.* **64**, 162–167 (2012).
- [264] A. M. Díez-Pascual, M. A. Gómez-Fatou, F. Ania, and A. Flores, “Nanoindentation Assessment of the Interphase in Carbon Nanotube-Based Hierarchical Composites”, en, *J. Phys. Chem. C* **116**, 24193–24200 (2012).
- [265] Y. Li, M. Li, Y. Gu, Z. Zhang, and P. Guan, “Investigation of the nanoscale mechanical properties of carbon fiber/epoxy resin interphase. I. analysis of fiber-stiffening effect during the nanoindentation process based on numerical simulation”, en, *Polymer Composites* **33**, 1387–1394 (2012).
- [266] Z. Hu, K. J. Lynne, S. P. Markondapatnaikuni, and F. Delfanian, “Material elastic–plastic property characterization by nanoindentation testing coupled with computer modeling”, en, *Materials Science and Engineering: A* **587**, 268–282 (2013).
- [267] Z. Hu, M. Farahikia, and F. Delfanian, “Fiber bias effect on characterization of carbon fiber-reinforced polymer composites by nanoindentation testing and modeling”, en, *J. Compos. Mater.* **49**, 3359–3372 (2015).
- [268] J. Chevalier, “Micromechanics of an epoxy matrix for fiber reinforced composites : experiments and physics-based modelling”, PhD thesis (Université catholique de Louvain, Louvain-la-Neuve, Belgium, 2018).
- [269] L. C. E. Struik, “Physical aging in amorphous polymers and other materials”, PhD thesis (Technische Hogeschool Delft, Delft, The Netherlands, 1977).

- [270] A. Flory and G. B. McKenna, "Physical aging behavior of the normal force and torque in polymer glasses", en, *Mech Time-Depend Mater* **14**, 347–357 (2010).
- [271] R. L. Hastie and D. H. Morris, "The effect of physical aging on the creep response of an off-axis thermoplastic composite", in, Vol. 1 (1992), pp. 183–91.
- [272] J. Sullivan, E. Blais, and D. Houston, "Physical aging in the creep behavior of thermosetting and thermoplastic composites", en, *Composites Science and Technology* **47**, 389–403 (1993).
- [273] G. McKenna, "On the physics required for prediction of long term performance of polymers and their composites", en, *J. Res. Natl. Inst. Stan. J.* **99**, 169 (1994).
- [274] D. Leveque, A. Schieffer, A. Mavel, and J. Maire, "Analysis of how thermal aging affects the long-term mechanical behavior and strength of polymer?matrix composites", en, *Composites Science and Technology* **65**, 395–401 (2005).
- [275] R. Martin, *Ageing of Composites*, 1st Edition, Pages: 517 (Woodhead Publishing In Materials, Aug. 2008).
- [276] G. M. Odegard and A. Bandyopadhyay, "Physical aging of epoxy polymers and their composites", en, *J. Polym. Sci. B Polym. Phys.* **49**, 1695–1716 (2011).
- [277] S. Minne, Y. Hu, S. Hu, B. Pittenger, and C. Su, "NanoScale Quantitative Mechanical Property Mapping Using Peak Force Tapping Atomic Force Microscopy", en, *Microsc Microanal* **16**, 464–465 (2010).
- [278] B. V. Derjaguin, V. M. Muller, and Y. P. Toporov, "Effect of contact deformations on the adhesion of particles", en, *Journal of Colloid and Interface Science* **53**, 314–326 (1975).
- [279] C. A. Clifford and M. P. Seah, "Quantification issues in the identification of nanoscale regions of homopolymers using modulus measurement via AFM nanoindentation", en, *Applied Surface Science* **252**, 1915–1933 (2005).
- [280] G. Moeller, "AFM nanoindentation of viscoelastic materials with large end-radius probes", en, *J Polym Sci Pol Phys* **47**, 1573–1587 (2009).
- [281] S. S. Nair, C. Wang, and K. J. Wynne, "AFM Peakforce QNM mode for measurement of nanosurface mechanical properties of Pt-cured silicones", en, *Progress in Organic Coatings* **126**, 119–128 (2019).

- [282] M. R. VanLandingham, J. S. Villarrubia, and G. Meyers, “Nanoindentation of Polymers: Tip Shape Calibration and Uncertainty Issues”, en, *41(2)*, 1412–1413 (1999).
- [283] M. R. VanLandingham, J. S. Villarrubia, W. F. Guthrie, and G. F. Meyers, “Nanoindentation of polymers: an overview”, en, *Macromol. Symp.* **167**, 15–44 (2001).
- [284] M. E. Dokukin and I. Sokolov, “On the Measurements of Rigidity Modulus of Soft Materials in Nanoindentation Experiments at Small Depth”, en, *Macromolecules* **45**, 4277–4288 (2012).
- [285] P. Eaton and P. West, *Atomic Force Microscopy*, en (Oxford University Press, Oxford, England, Mar. 2010).
- [286] L. Vande Putte, “Caractérisation mécanique de matériaux souples à plusieurs échelles de mesure différentes”, MA thesis (UCLouvain, Louvain-la-Neuve, Belgium, 2021).
- [287] N. Myshkin, A. Kovalev, D. Spaltman, and M. Woydt, “Contact mechanics and tribology of polymer composites”, en, *Journal of Applied Polymer Science* **131**, 39870 (2014).
- [288] B. Winter, *Linear models and linear mixed effects models in R with linguistic applications*, en, <http://arxiv.org/pdf/1308.5499.pdf>, Aug. 2013.
- [289] S. K. Khanna, P. Ranganathan, S. B. Yedla, R. M. Winter, and K. Paruchuri, “Investigation of Nanomechanical Properties of the Interphase in a Glass Fiber Reinforced Polyester Composite Using Nanoindentation”, en, *Journal of Engineering Materials and Technology* **125**, 90–96 (2003).
- [290] S. K. Khanna, R. M. Winter, P. Ranganathan, S. Yedla, M. Kalukanimuttam, and K. Paruchuri, “Sample preparation techniques for nano-mechanical characterization of glass fiber reinforced polyester matrix composites”, en, *Composites Part A: Applied Science and Manufacturing* **34**, 53–65 (2003).
- [291] A. Bahrami, C. Bailly, and B. Nysten, “Spatial resolution and property contrast in local mechanical mapping of polymer blends using AFM dynamic force spectroscopy”, en, *Polymer* **165**, 180–190 (2019).
- [292] D. Nečas and P. Klapetek, “Gwyddion: an open-source software for SPM data analysis”, en, *Centr Eur J Phys* **10**, 181–188 (2012).
- [293] R Core Team, *R: a language and environment for statistical computing*, R Foundation for Statistical Computing (Vienna, Austria, 2023).

- [294] G. Z. Voyiadjis and R. Peters, “Size effects in nanoindentation: an experimental and analytical study”, en, *Acta Mech* **211**, 131–153 (2010).
- [295] G. M. Pharr, E. G. Herbert, and Y. Gao, “The Indentation Size Effect: A Critical Examination of Experimental Observations and Mechanistic Interpretations”, *Annual Review of Materials Research* **40**, 271–292 (2010).
- [296] D. R. Tadjiev, R. J. Hand, and S. A. Hayes, “Calibrating a nanoindenter for very shallow depth indentation using equivalent contact radius”, en, *Philosophical Magazine* **90**, 1819–1832 (2010).
- [297] G. Guillonneau, G. Kermouche, S. Bec, and J.-L. Loubet, “Extraction of Mechanical Properties with Second Harmonic Detection for Dynamic Nanoindentation Testing”, *Experimental Mechanics* **52**, 933–944 (2012).
- [298] M. Frigione and A. Rodríguez-Prieto, “Can Accelerated Aging Procedures Predict the Long Term Behavior of Polymers Exposed to Different Environments?”, *Polymers (Basel)* **13**, 2688 (2021).
- [299] A. C. Campbell, R. Šlesinger, and P. Grolich, 5. *Oliver and Pharr*.
- [300] C. Ghnatios, P. Gérard, and A. Barasinski, “An advanced resin reaction modeling using data-driven and digital twin techniques”, en, *International Journal of Material Forming* **16**, 5 (2023).
- [301] N. Klavzer, M. Abatour, J. Chevalier, S. Forest, and T. Pardoën, “On the use of strain gradient plasticity to predict the deformation and failure of unidirectional composites”, *Manuscript in preparation for submission* (2023).
- [302] J. Richeton, S. Ahzi, K. S. Vecchio, F. C. Jiang, and R. R. Adharapurapu, “Influence of temperature and strain rate on the mechanical behavior of three amorphous polymers: Characterization and modeling of the compressive yield stress”, en, *International Journal of Solids and Structures* **43**, 2318–2335 (2006).
- [303] M. Nasraoui, P. Forquin, L. Siad, and A. Rusinek, “Influence of strain rate, temperature and adiabatic heating on the mechanical behaviour of poly-methyl-methacrylate: Experimental and modelling analyses”, en, *Materials & Design* **37**, 500–509 (2012).
- [304] P. Moy, C. Gunnarsson, T. Weerasooriya, and W. Chen, “Stress-Strain Response of PMMA as a Function of Strain-Rate and Temperature”, in *Conference Proceedings of the Society for Experimental Mechanics Series*, Vol. 1, Journal Abbreviation: Conference

- Proceedings of the Society for Experimental Mechanics Series (Jan. 1970), pp. 125–133.
- [305] E. M. Arruda, M. C. Boyce, and R. Jayachandran, “Effects of strain rate, temperature and thermomechanical coupling on the finite strain deformation of glassy polymers”, en, *Mechanics of Materials* **19**, 193–212 (1995).
- [306] L. C. A. van Breemen, T. A. P. Engels, E. T. J. Klompen, D. J. A. Senden, and L. E. Govaert, “Rate- and temperature-dependent strain softening in solid polymers”, en, *Journal of Polymer Science Part B: Polymer Physics* **50**, 1757–1771 (2012).
- [307] H. Van Melick, L. Govaert, and H. Meijer, “Localisation phenomena in glassy polymers: influence of thermal and mechanical history”, en, *Polymer* **44**, 3579–3591 (2003).
- [308] V. Srivastava, S. A. Chester, N. M. Ames, and L. Anand, “A thermo-mechanically-coupled large-deformation theory for amorphous polymers in a temperature range which spans their glass transition”, en, *Int. J. Plast.* **26**, 1138–1182 (2010).